Cheng, Weiqing (2024) *High-sensitivity optical biochemical sensors.* PhD thesis.

https://theses.gla.ac.uk/84216/

High-sensitivity optical biochemical sensors

Weiqing Cheng
October 2023

A thesis submitted for the degree of
Doctor of Philosophy (Ph.D.)

in the
Faculty of Engineering
Department of Electronics and Electrical Engineering

Declaration of Authorship

I, Weiqing Cheng, declare that this thesis titled, *High-sensitivity optical biochemical sensors* and the work presented in it are my own. I confirm that:

☐ This work was done wholly or mainly while in candidature for a research degree at this University.

☐ Where any part of this thesis has previously been submitted for a degree or any other qualification at this University or any other institution, this has been clearly stated.

☐ Where I have consulted the published work of others, this is always clearly attributed.

☐ Where I have quoted from the work of others, the source is always given, with the exception of such quotations, this thesis is entirely my own work.

☐ I have acknowledged all main sources of help.

☐ Where the thesis is based on work done by myself jointly with others, I have made clear exactly what was done by others and what I have contributed myself.

Signed: Weiqing Cheng

Date: 01/06/2023

Abstract

Label-free biochemical sensors enable direct detection of biomolecules and analytes based on their physical properties. In addition to their applications in solutions and gas detection, these sensors can serve as affinity-based biosensors, with receptors attached to the sensor surface that interact with analytes. Emerging applications encompass point-of-care blood tests, disease diagnostics, drug testing, environmental monitoring, and food security. Point-of-care systems can be developed to process clinical samples with various biomarkers in diverse working environments.

In this thesis, I have designed, simulated, fabricated, and measured integrated optical label-free biochemical sensors. Four distinct compact sensor designs have been proposed to address sensitivity limitations and the free spectral range (FSR) effect in microring resonators (MRRs), which have significantly advanced the field. I have measured the transmission losses of fabricated optical waveguides, including strip and slot waveguides. Experimental verification of sensitivity performance has been conducted across various parameters.

One of the key contributions is the demonstration of the inner-wall grating double slot micro ring resonator (IG-DSMRR) with a 6.72 µm radius, based on the silicon-on-insulator (SOI) platform. This sensor has demonstrated a high measured refractive index (RI) sensitivity in glucose solutions (563 nm/RIU) with a limit of detection (LOD) value of 3.7×10^{-6} RIU. The achieved bulk sensitivity is more than two times that of optimized designed single strip SOI-based quasi-transverse magnetic (TM) mode MRRs. The concentration sensitivity for sodium chloride solutions reaches 981 pm/%, with a minimum concentration detection limit of 0.02%. The detection range has been significantly extended to 72.62 nm, with a measured Q-factor of 1.6×10^{4}. Transmission losses for straight strip, slot, and double slot waveguides are 0.9 dB/cm, 5.2 dB/cm, and 20.2 dB/cm, respectively.

Another significant contribution is the novel sidewall grating slot microring resonator (SG-SMRR) with a compact size (5 µm centre radius) on the silicon-on-insulator (SOI) platform. This sensor demonstrates a measured refractive index (RI) sensitivity of 620 nm/RIU and a LOD value of 1.4×10^{-4} RIU. The concentration sensitivity and minimum concentration detection limit are 1120 pm/% and 0.05%, respectively. Notably, the detection range, based on a grating structure, has been significantly enlarged to 85.8 nm, four times the free spectral range of conventional slot MRRs, with a measured Q-factor of 5.2×10^{3}.

The subwavelength grating cascaded microring resonator (SWG-CMRR) structure has been developed, demonstrating high measured sensitivity at 810 nm/RIU, with a LOD value of 2.04×10^{-4} and a measured Q-factor of 7.7×10^{3}.

Additionally, the double slot microring resonator (DSMRR) structure has been fabricated

and verified in this project, showcasing a measured RI sensitivity of 600 nm/RIU, a LOD value of 1.15×10^{-6}, and a measured Q-factor of 2.6×10^{4}.

Furthermore, I have undertaken the design, simulation, and fabrication of surface plasmonic sensing structures, such as nanodots and nano rings. These structures enable the detection of hybrid photons and mapping of anapole-like electronic modes using the Polarization Indirect Microscopic Imaging (PIMI) technique.

List of publication papers

Journal papers

1.**W. Cheng**, X. Sun, S. Ye, B. Yuan, J. Xiong, X. Liu, Y. Sun, J. H. Marsh, and L. Hou, "Double slot micro ring resonators with inner wall angular gratings as ultra-sensitive biochemical sensors," Optics Express **31**(12), 20034-20048 (2023).

2. **W. Cheng**, X. Sun, S. Ye, B. Yuan, Y. Sun, J. H. Marsh, and L. Hou, "Sidewall grating slot waveguide microring resonator biochemical sensor," Optics Letters **48**(19), 5113-5116 (2023).

3. B. Yuan, Y. Fan, S. Zhu, **W. Cheng,** Y. Zhang, X. Chen, S. Ye, S. Liang, Y. Huang, R. Zhang, J. Akbar, J.H. Marsh, and L. Hou, "Millimetre-wave generation based on a monolithic dual-wavelength DFB laser with four phase-shifted sampled gratings and equivalent chirp technology," Optics Letters **48**(19), 5093-5096 (2023).

4. X. Sun, S. Liang, **W. Cheng**, S. Ye, Y. Sun, Y. Huang, R. Zhang, J. Xiong, X. Liu, J. H. Marsh, and L. Hou, "Regrowth-free AlGaInAs MQW polarization controller integrated with sidewall grating DFB laser," Photonics Research **11**(4), 622-630 (2023).

5. X. Jin, L. Xue, S. Ye, **W. Cheng**, J. Hou, L. Hou, J. H. Marsh, M. Sun, X. Liu, J. Xiong, and B. Ni, "Asymmetric Parameter Enhancement in the Split-ring Cavity Array for Virus-like Particle Sensing," Biomed. Opt. Express **14**(3), 1216-1227 (2023).

6. B. Yuan, Y. Fan, S. Ye, Y. Zhang, Y. Sun, X. Sun, **W. Cheng**, S. Liang, Y. Huang, R. Zhang, J. Wang, J. H. Marsh, and L. Hou, "Dual-wavelength DFB Laser Array Based on Sidewall Grating and Lateral Modulation of the Grating Coupling Coefficient," Journal of Lightwave Technology **41**(9), 2775-2784 (2023).

7. X. Jin, S. Ye, **W. Cheng**, J. J. Hou, W. Jin, T. Sheng, L. Hou, J. H. Marsh, Y. Yu, M. Sun, B. Ni, X. Liu, and J. Xiong, "Sub-wavelength Visualization of Near-Field Scattering Mode of Plasmonic Nano-Cavity in the Far-Field," Nanophotonics **12**(2), 297-305 (2023).

8. X. Sun, **W. Cheng**, S. Liang, S. Ye, Y. Huang, R. Zhang, B. Qiu, J. Xiong, X. Liu, J. H. Marsh, and L. Hou "Stepped-height ridge waveguide MQW polarization mode converter monolithically integrated with sidewall grating DFB laser," Optics Letters **48**(2), 359-362 (2023).

9. Y. Sun, B. Yuan, X. sun, S. Liang, Y. Huang, R. Zhang, S. Ye, Y. Fan, **W. Cheng**, J. H. Marsh, and L. Hou, "DFB laser array based on four phase-shifted sampled Bragg grating with precise wavelength control," Optics Letters **47**(23), 6237-6240 (2022).

10. X. Sun, **W. Cheng**, Y. Sun, S. Ye, A. Al-Moathin, Y. Huang, R. Zhang, S. Liang, B. Qiu, J. Xiong, X. Liu, J. H. Marsh, and L. Hou, "Simulation of an AlGaInAs/InP electro-absorption

modulator monolithically integrated with sidewall grating distributed feedback laser by quantum well intermixing," Photonics **9**(8), 564 (2022).

11. X. Sun, S. Ye, **W. Cheng**, S. Liang, Y. Huang, B. Qiu, Z. Li, J. Xiong, X. Liu, J. H. Marsh, and L. Hou, "Monolithically Integrated AlGaInAs MQW Polarization Mode Converter using a Stepped Height Ridge Waveguide," IEEE Photonics Journal **14**(3), 1-6 (2022).

Conferences

1. **W. Cheng**, X. Sun, S. Ye, B. Yuan, X. Liu, J. Marsh, and L. Hou, "Inner-wall grating double slot microring resonator for high sensitivity and large measurement range label-free biochemical sensing," in Conference on Lasers and Electro-Optics (CLEO) (2023).

2. B. Yuan, Y. Fan, **W. Cheng**, M. Al-Rubaiee, Y. Zhan, X. Chen, J. Marsh, and L. Hou, "Monolithic dual-wavelength laser array based on four phase-shifted grating and equivalent chirp technology," accepted by European Conference on Optical Communications (ECOC) (2023).

3. X. Jin, L. Xue, J. Xiong, S. Ye, **W. Cheng**, L. Hou, J. Marsh. Ni, B. Xu, and X. Liu, "Scattering field enhanced biosensing based on sub-wavelength split-ring plasmonic cavity with high Q-factor." in Plasmonics in Biology and Medicine XX **12396**, SPIE (2023), pp. 34-40.

4. X. Sun, **W. Cheng**, S. Liang, S. Ye, Y. Huang, Y. Sun, R. Zhang, J. Xiong, X. Liu, J. Marsh, and L. Hou, “Monolithic MQW Polarization Mode Controller Integrated with Sidewall Grating DFB Laser,” in Conference on Lasers and Electro-Optics (CLEO) (2023).

5. X. Sun, S. Ye, J. H. Marsh, **W. Cheng**, Y. Sun, and L. Hou, "AlGaInAs/InP EML with Sidewall Grating Distributed Feedback Laser and Quantum Well Intermixing Technology," in IEEE Photonics Conference (IPC) (2022), pp. 1-2.

6. **W. Cheng**, S. Ye, X. Sun, B. Yuan, J. H. Marsh, and L. Hou, “Double Slot Micro Ring Resonators with Inner Wall Angular Gratings as Ultra Highly Sensitive Biochemical Sensors,” in IEEE Photonics Conference (IPC) (2022), pp. 1-2.

Acknowledgements

In my whole PhD study, many people provided help and encouragement for me. Here, I want to profoundly express my deepest gratitude to them:

First and foremost, I would like to thank my supervisors, Prof. Lianping Hou and Prof. John Marsh, for having made this Ph.D. possible. Their continuous suggestions, advice, and psychological support during my whole PhD study constituted immeasurable value for me. Both helped me mature from a scientificpoint of view. Thanks a lot.

Dr. Shengwei Ye has been a model for me. I still remember the first time he took me to the clean room, the first time he gave me the tweezers and the first sample fabrication. Many thanks to Dr Zhibo Li who helped me with device measurement, really appreciate Xiao Sun who helped me with device measurement also helped me a lot in my PhD study. Also, thanks to Bocheng Yuan who helped me with the measurement platform.

Thanks to the help from many other researchers who helped me with fabrications in JWNC and measurement in our lab.

Thanks to all staff in JWNC, who helped me with the device fabrication. Their continuous help made my design idea could be achieved in fabrication.

Thanks to all my friends who made my three-year PhD period full of happiness and helped me to achieve a work-life balance.

Thanks to my family for the continuous support in every momentof my life. Thanks for all your love and support for me with every decision I made and every dream I chase.

Thanks to the U.K. Engineering and Physical Sciences Research Council and the Chinese Ministry of Education collaborative project for funding my project.

To all I have thanked above, I wish you all have a perfect life full of happiness.

Contents

List of Figures

Acronyms

Symbol	**Description**	**Symbol**	**Description**
PIC	Photonic integrated circuit	ICP	Inductively Coupled Plasma
FSR	Free spectral range	CMOS	Complementary Metal-Oxide-Semiconductor
MRR	Microring resonator	FDE	Finite Difference Eigenmode
IG-DSMRR	Inner-wall grating double slot microring resonator	WDM	Wavelength division multiplexed
SG-SMRR	Sidewall grating slot microrirng resonator	MMI	Multi-mode interference
SWG-CMRR	Subwavelength grating cascaded microring resonator	RIE	Reactive ion etching
DSMRR	Double slot microring resonator	SMF	Single-mode fibre
SOI	Silicon on insulator	CE	Coupling efficiency
RI	Refractive index	BW	Bandwidth
LOD	Limit of detection	EBL	Electron Beam Lithography
TM	Transverse magnetic	FWHM	Full-width at half-maximum
TE	Transverse electronic	FSR	Free spectral range
Q	Quality factor	FDTD	Finite-difference time-domain
PIMI	Polarization Indirect Microscopic Imaging	AFM	Atomic force microscopy
SLD	Superluminescent Diode	SEM	Scanning electron microscopy
LED	Light-emitting diode	PMMA	Polymethyl methacrylate
HSQ	Hydrogen silsesquioxane		

List of Tables

Chapter 1 Introduction

1.1 Objectives and aims

In this PhD project, we studied and developed label-free biosensors with high sensitivity and large detection range based on a silicon-on-insulator photonic chip. The sensors consist of grating couplers, microring resonators, sidewall grating, slot waveguides, subwavelength waveguides, and strip-to-slot coupler structures. This integrated optical resonator could respond when analytes cladding layer changes or biomolecules interact at the surface. This interdisciplinary project combines different research fields such as chemistry, microfluidics, and optics to obtain a sensitive multiple-use biochemical chip for multiplexed analytes and molecules detection. These devices are fabricated in James Watt Nanofabrication Centre (JWNC). This first chapter mainly sets the background of this project work. Section 1.1 will introduce what is label-free optical biochemical sensors, why and where we use it, and current development status and limitation. The structures we designed and fabricated to overcome current limitations, and their potential application areas are stated in section 1.2. The outline of the thesis is shown in section 1.3.

1.1.1 Label-based and label-free optical biochemical sensors

In the biochemical sensing area, the main method of analytes and molecules detection relies on analytes indirect detection by attaching easily measurable labels to them, such as some visible signals fluorescent dyes, and enzymes. The instance of the label-based detection method is using the enzyme-linked immunosorbent (ELIS) to measure antigens in the sample [1]. The illustration of label based biosensing method is shown in Figure 1.1 (a). The antigen in a liquid test sample (probably an unknown amount) is immobilized on the sensor surface. Then, specific antibodies are bonded to the immobilized antigen for detection. The antibodies are recognized by enzymatic labels which could produce a visible signal indicating the presence and quantity of antigens. This detection method can be applied to disease diagnosis areas like human immunodeficiency virus infection (HIV) tests [2]. Generally, in disease diagnosis, labelling is performed in test tubes and positive results can be interpreted through colour change or light transmittance measurement. The labelled detection method based on the basic platform only allows single-type proteins or molecule detection. Some techniques, for instance, protein microarrays with different capture antibodies, and the surface of microbeads labelling in solutions are developed for highly multiplexed measurements [3-4].

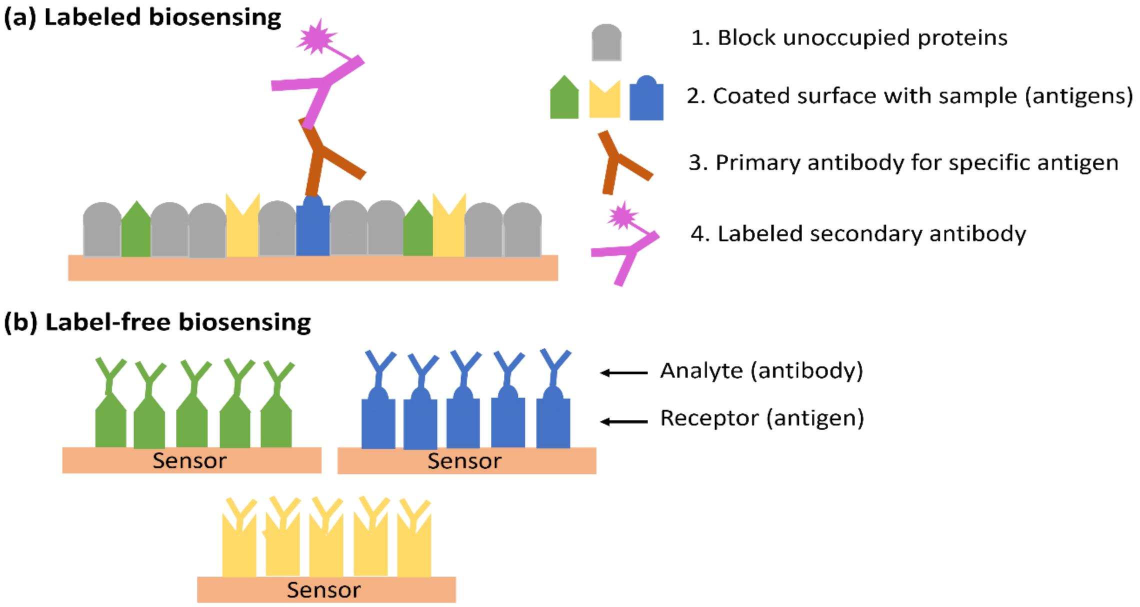

Fig. 1.1 Illustration of (a) labelled and (b) label-free biosensors.

Although labelling techniques enable detection limits down to the single-molecule level, they have some practical disadvantages [5]. First, the label assays only show endpoint readouts without continuous, real-time monitoring of molecular interactions [6], thereby some information on kinetics and affinities binding is lost. Second, some assays require two high-affinity capture agents for distinct and non-overlapping target identification, which limits highly multiplexed assay development and increases cost and development time [7, 8]. Third, the cleaning process between different assay steps often increases the sample preparation complexity and reduces efficiency.

Therefore, label-free affinity biosensors have recently become popular and received more attention. As the label-free biosensing method shown in Figure 1.1 (b), the receptor molecules are immobilized on the sensor surface, which directly performs the selective affinity interaction between the analyte molecules and the immobilized receptor molecules through the intrinsic optical, electrical, or mechanical properties of the analyte effect. The highly multiplexed assay could be achieved in a simple way by integrating multiple sensors with different receptor molecules. Also, many label-free methods allow continuous monitoring of affinity reactions, providing highly quantitative measurements of concentration, affinity, and binding kinetics. Additionally, label-free assays require a few sample preparation steps, reducing costs and increasing throughput. The assay development is also significantly simplified, only one recognition element is required for each analyte in highly multiplexed arrays.

There are many investigated label-free technologies, and a general review of the most promising ones is shown in [8-9]. Some prominent ones will be briefly discussed in this section. The recent widespread label-free method is surface plasmon resonance (SPR) [10-11]. It directly detects the local refractive index (RI) change induced by plasmon waves and biomolecular interactions on metal surfaces when the charge density oscillations are optically excited. The improved limit of detection (LOD) value (about 0.1 pg/mm^2 for protein interactions [12]) is measured using angular or wavelength spectroscopy interrogation. However, it allows only up to ten measurements to be performed simultaneously, which limits the multiplicity and throughput degree. Intensity interrogation is developed to overcome this limit. It could perform SPR imaging, where the broadband reflectance change of the gold surface could be monitored by cameras with a spatial resolution down to 4 µm, making it possible to achieve tens of thousands of parallel measurements [12-13]. However, SPR imaging has more than an order of magnitude worse LOD compared with SPR spectroscopy (5 pg/mm^2 for protein interactions [9, 10]), making it limited to high quantitative measurement applications. Many companies develop SPR label-free sensor systems, including GenOptics, Biorad, and Biacore.

Many methods are investigated to deliver LOD values that could rival SPR spectroscopy and allow high throughput and multiplicity with small analyte consumption. One optical technology is reflectometric interference spectroscopy (RIFS), which measures biomolecular interactions on the surface through the induced RI change using the Michelson interferometer system. This self-reference structure makes it noise-tolerant, and the flexible readout makes it easier for system integration. While it reaches the multiplexing and throughput as SPR imaging, it does not highly improve the LOD

(1pg/mm^2 for protein interactions [9]). The optical diffraction gratings can also measure RI changes induced by analyte interactions through the shift of diffraction wavelength in a fixed direction. It could be mass-produced by imprinting [14]. Commercial high multiplicity and throughput cell-based assays and drug systems are developed by SRU Biosystems, Corning, etc. companies. However, this system encounters problems monitoring end-point read-out and real-time binding curves in simultaneous interrogation for binding kinetics and affinity analysis, and no clinically relevant LOD has been reported from up-to-date references. Electrochemical label-free sensors like electrochemical impedance spectroscopy and field effect transistor sensors in silicon nanowires and carbon nanotube structures are well-suited for massively integrated systems. However, the performance will deteriorate at physiological ionic strengths and requires desalting before measurement [15-16]. Microcantilever structures could transfer molecular interactions to mechanical motion on the nanometre scale and allow highly multiplexed label-free biosensing [6]. The best performance with clinical LOD values (0.2 ng/ml) in static measurements, and even down to 10 pg/ml for the dynamic mechanical resonance frequency change measurement [17-18]. Some arrays of microcantilever label-free biosensors are commercially provided by companies like Cantion and Concentris. However, optical interrogation through fluidic system might be complicated, and practical electrical interrogation could not achieve the same level LOD.

1.1.2 State-of-art of silicon MRR biochemical sensors

Like well-developed electronic integrated circuits, photonic integrated circuits combine and miniaturize optical functions (laser sources, filters, sensors, and detectors) on one single chip, which could be mass-produced at high quality using photolithography or electron beam lithography and etching. These photonic chips are highly required and commonly used in fibre optic communication networks. The principal component is the photonic waveguides that guide light over the entire chip by total internal reflection. It consists of a high-refractive-index core surrounded by low-refractive-index cladding and substrate layers. Thus, the guided mode is mainly confined in the core and the exponentially decaying evanescent tail is in the claddings. The photonic microring resonator consists of a self-folding waveguide to form a closed loop cavity where the light resonates at an effective wavelength that fits in the integer number times of the loop length.

Then the bus waveguides (at least one) are positioned proximate to the microring resonators to achieve light coupling between the microring and bus waveguide through evanescent wave coupling. The grating coupler structures connect the microring resonator structures with on-chip or off-chip light sources and detectors. The light in the bus waveguide interferes with the light coupled back from the ring resonator at the resonance wavelengths, which causes sharp dips in the transmission spectrum. The microring resonator structures are well-known photonic components [19-26] that could be used as delay elements for optical buffers [22], filters for wavelength division multiplexed circuits [23], modulators [24], and lasers cavities when fabricated on active material layer wafers [25-26]. The MRR structure used for label-free biochemical sensing could measure selective affinity interactions between analyte and receptor molecules immobilized on the MRRs waveguide surface.

For MRR sensing structures, intensity interrogation, and wavelength interrogation are the two typical interrogation approaches that have been widely utilized [27]. The former suffers from a narrow detection range and unstable accuracy. Wavelength interrogation has therefore become a popular detection method, meeting the requirements of a large detection range and easy-to-identify sensing. The analyte solutions cladding layer or binding biological molecules (proteins and DNA) will locally increase the RI in the range of the evanescent field. This will cause the resulting waveguide modes transitions and lead to measurable changes in the ring resonance wavelength. This wavelength shift could be monitored continuously and provide information on analyte concentrations, molecules affinities results, and biochemical reaction kinetics.

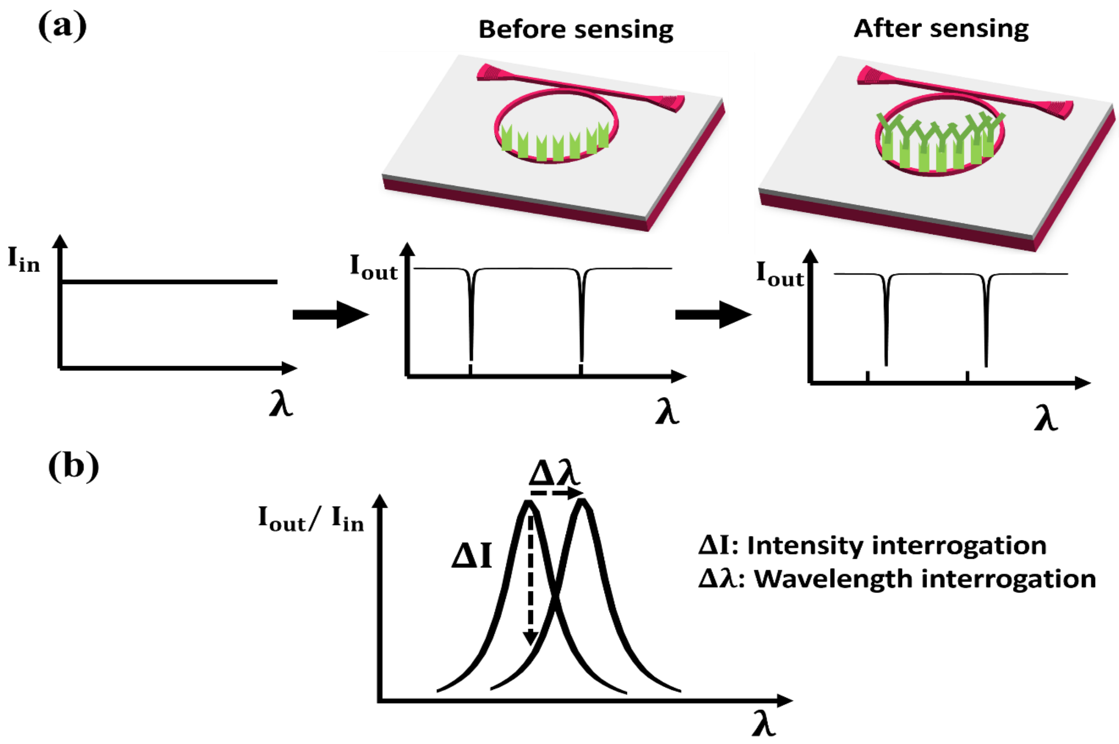

Fig. 1.2 MRR sensing using (a) wavelength interrogation method, (b) comparison of intensity and wavelength interrogation method [95].

The label-free biosensors based on silicon microring resonator structures have many advantages. First, the silicon core waveguides have high RI contrast between the silicon and buried oxide layer (3.47 for Si and 1.44 for SiO_2 at 1.55 μm wavelength which is within telecom C-band). Thus, the microring resonator sensors could be made in a very compact size (typically micro size diameter, possibly down to 5 μm diameter) to construct a high-density label-free sensor array with high throughput and multiplexed sensing. Second, the penetration depth of the microring waveguide’s fast-decaying evanescent field is 50 nm (hundreds of nm for SPR sensors) [28]. This overlaps well with biomolecular interaction areas, leading to a high signal-to-noise ratio. Third, the access waveguides and broadband grating couplers with high coupling efficiency allow light coupling from any area on the sample surface, providing a lot of flexibility in structure design. Fourth, the SOI MRRs are highly manufacturable, and silicon is the consumer electronic material and is heavily invested in industries. Silicon photonics circuits can be fabricated using mature technologies (photolithography and dry etching) [29, 30], which can be massively produced at full wafer levels. Therefore, the sensor chips could achieve high-quality and budget friendly at the same time. The fabrication is even cheap enough for single use, this will avoid the complicated cleaning process of the sensor. These SOI

MRRs with high quality factors (Q factors), large extinction ratio, and low insertion loss could be fabricated with reliable, high yield and repetition rate. Fifth, it’s highlighted that the inherent silicon oxide serves as a conventional glass material, facilitating a mild oxidation of the sensor surface. This property enables its integration with microfluidic channels for biosensing applications. Sixth, silicon photonics circuits enable further light sources, filters, and detectors integration. This opens the prospect of portable instruments capable of high-end point-of-care diagnostics.

However, some drawbacks cannot be ignored when using SOI MRRs structures for biochemical sensing. Firstly, silicon is only transparent to light with wavelengths in near infrared, where sources and detectors are more expensive compared with visible light devices. Secondly, the water absorption loss should be considered and analysed in this wavelength range (typically dominates the propagation loss in ring resonator waveguides). Third, the high RI of the silicon waveguide core could lead to scattering loss in the sidewall roughness of fabricated waveguides and may raise aberrations in the transmission spectrum [31].

The Idea of using micro disk resonators for label-free biomolecules detection is introduced by R. W. Boyd and J. E. Heebner [32] in 2001. Then some research groups reported SOI MRRs structures to improve biochemical sensors performance with experiment demonstration. The MRR sensor using glass material for model protein label-free detection was first demonstrated by A. Yalcin et al. in 2006 [33] and followed by a demonstration of SOI MRR sensors concepts by K. De Vos et al. [34-35]. After that, several groups proposed different approaches to multiplex label-free detection of proteins in an array format that does not compromise each senso’'s performance [36-38]. At present, the company Genalyte investigated multiplexed label-free biosensor platforms based on silicon microring resonators [39-40]. Some research groups collaborated with the company to make contributions to platform characterization [41-48]. The high-quality factor photonics biosensors including silicon MRRs are reviewed by M.S. Luchansky et al. [49]. The state-of-the-art results reported by Luchansky et al. [28] shows measured slightly improved LOD 1.5 pg/mm^2 (compared with SPR imaging 5 pg/mm^2). However, the low absolute mass LOD (125 ag) proves that only small fluidic samples are required for sensor measurement. The direct label-free quantification of cancer biomolecules (carcinoembryonic antigen) using silicon MRRs was demonstrated by Washburn et al. [41]. But this non-specific binding method lowered the LOD in undiluted serum to 25 ng/ml, which is still insufficient for clinical use. But the total assay time compared favourably with that of the ELISA (less than 30 minutes compared with 3 hours) and could be extended to multiplex measurements of five biomarkers without compromising sensor performance [36]. Small proteins like cytokines (size: 5-40 kDa) are important to intercellular communication which are more difficult for quantification compared with antibodies (size: 150 kDa) due to their smaller size and lower concentrations (pg/mL to ng/mL) [49-50]. The T-cells temporal secretion patterns are measured using 4-plex real-time binding analyses in MRR arrays with sensor signal amplification [34]. Some groups employed the real-time binding curve of sensors to distinguish single nucleotide polymorphism by differences in the dissociation kinetics [52-53]. The virus detection in agricultural areas using MRRs sensors is demonstrated by McClellan and Bailey [54].

The sensing method based on MRR transmission spectrums are shown in Figure 1.2. For the sensing of chemical analyte solutions based on SOI MRRs structures using the wavelength shift interrogation method. There are some limitations that need to be overcome based on the reported reference. First is the sensitivity limitation, this could be improved by changing the structures design to allow more light intensity that could interact with analytes. Second is the detection range limitation. Sometimes the analyte concentration range could be large with large RI change, so the resonant wavelength will be shifted over the entire free spectral range (FSR) of the MRR sensor. Therefore, the measurement range of a conventional wavelength shift dependent MRR sensor is limited and affected by its FSR range. Some schemes have been proposed to enlarge FSR and detection range such as Mach–Zehnder interferential coupled MRRs [55], serially coupled double MRRs [56], grating-coupled silicon MRRs [57], and angular grating (AG) MRRs [58] have been proposed to enlarge the FSR. Although these schemes could improve the detection range, their bulk sensitivities are at traditional single-strip waveguide MRR sensors (around 70 nm/RIU [59]) level, and even specially designed quasi-TM MRR, the maximum bulk sensitivity of a traditional strip waveguide MRR sensor based on wavelength shifting is only 270 nm/RIU [60]. Thus, their sensitivities are much lower than those of multi-slot microring resonator (SMRR) schemes, since these SMRR sensing structures based on the SOI platform could enhance light-analyte interaction. The experimentally demonstrated sensitivities reported are up to 298 nm/RIU (5 μm bend radius) [61] and could reach 476 nm/RIU with larger radius structures (30 μm bend radius) [62].

1.1.3 Application areas

The silicon MRRs label-free biochemical sensors have many application fields. Firstly, it could be used in health care research. This includes identifying disease biomarkers in patients' samples (proteins, DNA, RNA, and viruses), and using real-time high throughput could differentiate molecules. Secondly, silicon MRR biosensors could support drug development. The cycle time, competitiveness and R&D costs in pharmaceutical industries could be improved using advanced high-throughput equipment, and the early process of biomolecular identify could provide time and cost efficiency in the discovery stages. Thirdly, biochemical measurement could be used for blood tests and personalized medical treatment indication in hospitals [63]. Fourthly, silicon MRRs sensors are ideal for lab-on-chip integration and can be designed in arrays for high throughput multiple diagnosis. This sample with microfluidic channel technologies could achieve point-of-care biochemical sensing in portable devices. Finally, these sensors can also be applied in areas other than healthcare, like on-site continuous environment monitoring and food safety control [64-65].

1.2 Sensors to overcome current limitations.

This section mainly provides a brief introduce of our designed novel sensor structures to overcome the current limitations on photonics sensors we talked about before in the background view. The structures are illustrated in each small section. Some measured MRR performance data like waveguide loss and quality factor, and some photonic MRR biochemical sensors performance parameters based on the measured optical transmission spectrum are also stated in this section.

The high sensitivity biochemical sensors we demonstrated are compared with the current reported biochemical SOI sensors in many references to understand our novelty and improvement stage. The measured slot waveguide based microring resonator on SOI platform with similar radius is reported in [152] with sensitivity 298 nm/RIU. Thus, our slot waveguide MRR sensors (IG-DSMRR and SG-SMRR) shows two times than this measured sensitivity in reference. For the multi-slot subwavelength grating structures, we can compare our results with the measured subwavelength grating straight waveguide and microring resonator structures reported in [150, 151], the sensitivities are 579.5 nm/RIU and 730 nm/RIU respectively. Therefore, we could conclude that our designed SWG-CMRR shows a sensitivity improvement than the current reported subwavelength grating biochemical sensor on SOI platform.

1.2.1 Inner-Wall Grating Double Slot Microring Resonator (IG-DSMRR)

Currently, novel structures are proposed to solve some main limitations of SOI MRR sensors, like the sensitivity limitation and the detection range limitation. From the references reported and discussed in section 1.1.2, when using the wavelength shift interrogation method for MRR sensing, the resonant wavelength peaks will be shifted over the entire free spectral range (FSR) and overlapped together when the analyte concentration range is large and the corresponding RI change is large as well. Therefore, the measurement range of a conventional MRR sensor using wavelength interrogation method is limited and affected by its FSR range. Some schemes like Mach–Zehnder interferential coupled MRRs, serially coupled double MRRs, grating-coupled silicon MRRs, and angular grating (AG) MRRs have been proposed to enlarge FSR and detection range. Also, the sensitivity limitation of current MRR sensors is mainly based on the MRR waveguide and structure design. The slot waveguide structure could improve the sensitivity to four times than the traditional strip waveguide structure, and this waveguide also enable tight bending structure.

The inner-wall grating double slot microring resonator (IG-DSMRR) sensor was designed, simulated and demonstrated based on silicon-on-insulator (SOI) platform. This structure has compact size with a centre slot ring radius of 6.72 µm. The double slot waveguide structure could improve the measured refractive index (RI) sensitivity to 563 nm/RIU with the limit of detection (LOD) value being 3.7×10^{-6} RIU (refractive index units) in different concentrations of glucose solutions. The measured concentration sensitivity can reach 981 pm/% with a minimum concentration detection limit of 0.02% in different concentrations of sodium chloride solutions. The detection range is significantly enlarged to 72.62 nm with sidewall IG structure inside the DSMRR waveguide, which is three times than the FSR of conventional SMRR. The measured straight strip and double slot waveguide transmission losses are 0.9 dB/cm and 20.2 dB/cm respectively. The measured Q-factor is 1.6×10^4. This novel sensor combines the merits of micro ring resonators, slot waveguides, and angular inner wall gratings. It offers an ultra-high sensitivity and large measurement range which makes it highly desirable and competitive in analytes, liquids, and gases biochemical sensing. This sensor is the first fabricated and demonstrated double-slot micro ring resonator with an inner sidewall grating structure.

1.2.2 Sidewall Grating Slot Microring Resonator (SG-SMRR)

The silicon-on-insulator (SOI) platforms are well-known candidates for photonic integrated circuits (PICs) because of their compatibility of Complementary Metal-Oxide-Semiconductor (CMOS) fabrication technologies. Besides, the high refractive index (RI) contrast in SOI wafers (silicon RI 3.47, silica RI 1.44 at 1.55 µm wavelength which is within telecom C-band) could provide strong optical mode field confinement and realize tight bending designs. The MRR structures on SOI platform are promising candidates for high-quality and high-performance on-chip photonics sensors.

This work includes a novel and compact size sidewall grating slot microring resonator (SG-SMRR, 5 µm centre radius) designed on the SOI platform and is fabricated and demonstrated experimentally. The measurement refractive index (RI) sensitivity is 620 nm/RIU with the limit of detection value of 1.4×10^{-4} RIU. The measured concentration sensitivity is 1120 pm/% and the related minimum concentration detection limit is 0.05%. The sidewall grating on the slot microring resonator waveguide makes this sensor not be affected by its FSR, which will cause peaks overlapping when measuring the transmission spectrum under high concentration solution with large rIs. So, the sensitivity measurement transmission spectrum of this sensor is free of FSR limitations on sensitivity measurement. The measured detection range is significantly extended to 84.5 nm, four times the FSR of conventional SMRRs. The measured Q-factor is 5.2×10^3 and the straight slot waveguide transmission loss is 24.2 dB/cm under sensing circumstance (water absorption loss counted). The measured results show the potential of small form factor silicon photonics sensors, also makes it essential for high sensitivity and large detection range application areas. This is the first reported fabricated and measured SG-SMRR based on the SOI wafer structures providing FSR free limitation on sensitivity measurement and high sensitivity at the meantime.

1.2.3 Subwavelength Grating Cascaded Microring Resonators (SWG-CMRR) & Double Slot Microring Resonator (DSMRR)

The other two structures are proposed to improve the make sensitivity. Based on the current MRR sensing structures reported, we decide to use optimized structure design for ultra-high sensitivity sensor instead of suspended structure because this will lead to complex and unstable fabrication process. Thus, the subwavelength grating cascaded microring resonators (SWG-CMRR) and the double slot microring resonator (DSMRR) are proposed. For the SWG-CMRR sensor, it utilizes both sub wavelength multi-box straight waveguides and sub wavelength grating micro ring resonator structure to enable more light analyte interaction to enhance the sensitivity. The measured sensitivity is 810 nm/RIU. For the novel DSMRR sensor. It consists of double slot waveguide and microring resonator. The measured sensitivity of this structure is 600 nm/RIU.

1.2.4 Application domains

As pointed in section 1.1.3, the application areas of silicon MRRs label-free biochemical photonics sensors are disease diagnosis in healthcare, drug development, biochemical measurement (blood or analyte test, medical treatment), point-of-care biochemical sensing, food security control, and environment monitoring. Thus, our proposed sensing could be utilized in all the applications above. Moreover, they have the advantage of ultra-high sensitivity and ultra-large detection range. These merits make them more competitive in miniature molecules and analyte detection in a large RI change range. Also, the large detection range makes a large concentration of solutions or analyte detection possible. This is highly desirable in biochemical sensing areas.

1.3 Thesis overview

The thesis comprises eight chapters, each contributing to a comprehensive exploration of the subject matter.

In Chapter 1, Section 1.1 provides a comprehensive overview of the state-of-the-art, objectives, and application areas of the research. Section 1.2 delves into the design of sensing structures while considering current limitations, and in Section 1.3, readers are introduced to a brief overview of the thesis.

Chapter 2 is dedicated to the theoretical analysis of various components of the sensing structures, such as silicon waveguides, microring resonators, sidewall gratings, and grating couplers. Furthermore, it delves into the sensing theory of silicon photonics microring resonator sensors, encompassing sensitivity and limit of detection (LOD) value definitions.

Chapter 3 details the measurement setup used in the laboratory, including descriptions of the light source, detector, measurement platform, and methods for calculating refractive indices in analytical solutions.

Chapters 4 through 8 provide an in-depth examination of the IG-DSMRR, SG-SMRR, SWG-CMRR, DSMRR, and gold nanodots plasmonic sensing structures. These chapters encompass the design, simulation results, fabrication processes, measurement results, and thorough analysis of each of these sensing structures.

Chapter 9 is dedicated to summarizing the thesi''s conclusions and research findings. Additionally, it offers insights into potential future work, building upon the current processes and results.

Chapter 2 Theory

This chapter is dedicated to the main silicon photonic components in this PhD project: the theory of single microring resonator operating principle, and multiple applications including a sensor. In section 2.1, we investigate the different structures of photonics waveguides that are widely used for photonic circuit designs, the single-mode regime, loss and dispersion, and bend waveguides. The 2.2 section contains the theory of all-pass microring resonator and add-drop resonators. The silicon-on-insulator (SOI) microring resonators focusing on their sensing capabilities are examined. Meanwhile, the general design guidelines for microring filters theory are provided. All devices in this project are fabricated using electron-beam lithography (EBL) and dry etching. The 2.3 section mainly focused on grating couplers theory introduction, which are the components for light coupling into and out of chips. Section 2.4 contains the theory for plasmonic sensors, which is the collaboration work we did with other universities. In section 2.5, the evanescent field sensing theory is illustrated when using microring resonator as a sensor, like tracking wavelength shifts caused by refractive index changes of sensor's surrounding environment. The sensitivity parameters (RI sensitivity, concentration sensitivity, surface sensitivity, limit of detection) are studied and detailed in sections 2.6 and 2.7.

2.1 Silicon wire waveguides

Nowadays, many silicon photonic components are investigated and developed for the wavelength range near 1.55 µm, since the propagation loss in silica fibres becomes minimal there [64], making this wavelength region special interest to telecommunication applications. To profit from this advantage, all devices presented in this thesis were also developed to operate near a wavelength of 1.55 µm. The refractive index contrast between the silicon (3.47) and silica (1.44) material at this wavelength is very high, which allows confining light in very compact structures, and the silicon waveguides can be bent with very small radii (a few micrometre) without significant bending loss, this merit enable creation of very dense photonic circuits. This section introduces the silicon wire waveguide that can be used for most photonics circuits and discusses its basic properties such as single-mode regime, loss, and dispersion.

2.1.1 Silicon photonic waveguides

Over the last few years, photonics has been developed on multiple material platforms. The most well-known material platforms are silica-on-silicon, III-V semiconductor materials, lithium niobate ($LiNbO_3$), silicon nitride on insulator (Si_3N_4), and silicon-on-insulator (SOI). The basic design of photonic wafer material has a core and cladding material layers, both layers materials should be transparent in the operating wavelength region, and the core material always has a higher refractive index (RI) than the cladding material. The relative difference between the refractive index of the core and cladding is called refractive index contrast.

Silica-on-silicon, also known as Planar Lightwave Circuits (PLC), is one of the most mature platforms for photonic circuits. Today, silicon is the mainstay material for photonic chips in telecommunications and data communications areas. The optical waveguides based on this platform have germanium (Ge)-doped silicon core and undoped silica cladding on top of a silicon substrate. The refractive index of the core is 0.8%- 3.5% higher than the cladding material. This platform has advantages like well-developed manufacturing technology, low waveguide loss, and better coupling with optical fibres. However, waveguides designed for low-loss propagation always have large bend radii. This makes optical components based on this platform less suitable for applications require high-density integration, such as on-chip interconnects.

The III-V semiconductor material platforms are important photonics materials due to their direct bandgap, which makes them suitable for active photonics components design like integrated laser, modulator, and photodetectors. This materials platform is also used for passive photonics components, but due to high cost, low-yield fabrication technology, and lower integration density, the use of these materials is limited mainly to active photonics components.

The lithium niobate (LiNbO3) platform has been used commercially for optical modulators. Apart from modulation, $LiNbO_3$ is unlikely to be used in laser or photodetectors. Although some passive photonic components (AWGs) have been demonstrated in this waveguide platform [67], $LiNbO_3$ is limited to light modulation due to large bending radii, high cost, and unstable manufacturing process repeatability and reliability. Typically, $LiNbO_3$ modulators are integrated with silicon passive components for optical communication applications.

In the past few years, the silicon nitride (Si_3N_4) platform has attracted interest for photonics applications due to its interesting refractive index and CMOS compatibility (Si_3N_4 waveguides can be fabricated using well-established electronics fabrication facilities). At a wavelength of 1550 nm, Si_3N_4 (waveguide core) has a refractive index near 2 and silica (cladding) has a refractive index of 1.44. Therefore, Si_3N_4 is neither a high refractive index contrast platform like silicon-on-insulator (SOI), nor a low index contrast platform like silicon dioxide on silicon. The merits are that it does not suffer from high loss or low coupling to the fibre like silicon waveguides and supports compact device design due to the achievable small bending radius. The main disadvantage is that the platform does not have a mature manufacturing process, problems like high stress and low quality appear when the Si_3N_4 layer thickness is over 400 nm.

In SOI, the silicon waveguide layer acts as the core on top of the buried oxide acts as the cladding. For a wavelength of 1550 nm, the refractive indices of silicon and silicon dioxide are 3.47 and 1.44 respectively. The main benefits of this platform are CMOS compatibility, a high refractive index contrast waveguides that allow for less bending radius with smaller footprint. Silicon is capable of multiple devices with different functions on a single chip due to its high integration level. The small device footprint significantly increases the achievable chips numbers per wafer, which considerably reduces the cost per chip. The main disadvantage in silicon photonics is that they are highly sensitive to fabrication imperfections, waveguide sidewall roughness increases losses and causes phase errors, also silicon waveguides are strongly birefringent, have significant temperature dependence, and high coupling losses to optical fibres.

The brief waveguide definition is a structure used for efficient electromagnetic power transfer from one point to another. In practice, based on the wafer materials and operating wavelength requires, various waveguides geometries are used. In this section, we mainly discuss the waveguide geometries used for integrated photonics and use the waveguides designed based on SOI platform as examples to derive basic waveguide functionalities. The general geometry of optical waveguides is a higher refractive index material as core

(η_{core}) surrounded by a lower refractive index material as cladding ($\eta_{cladding}$). The refractive index of the waveguide determines the number of guided optical modes in the waveguide. In general, the optical mode is a time-harmonics solution of Maxwell equations, and these modes can be TE or TM polarized. The two basic properties of optical mode are effective refractive index (η_{eff}) and group index (η_{group}). The effective refractive index can be determined from the mode phase velocity (ν_p), which is the phase velocity of any frequency component of the mode propagating through the waveguide. The related calculated formula is shown below,

$$\eta_{eff} = \frac{c_0}{v_p} \tag{1}$$

Thus, the effective index of waveguides is a wavelength-dependent property. The effective index provides the confinement of the mode into the waveguide core and this value should not be higher than the core refractive index and lower than the cladding refractive index. The mode will be guided if the effective index satisfies $\eta_{core} > \eta_{eff} > \eta_{cladding}$. The light is tightly confined in the core is the effective index is close to the core index ($\eta_{eff} \sim \eta_{core}$) and poorly confined if the effective index is closed to the cladding index ($\eta_{eff} \sim \eta_{cladding}$).

The group velocity (ν_g) is the velocity of the wave packets propagating through the waveguide. It determines the waveguide group index. The calculated formula is shown as Eq (2); the group index can be higher than the core index.

$$\eta_{group} = \frac{c_0}{v_g} \tag{2}$$

In one of the SOI platform, a 220 nm thick silicon layer is used as a waveguide core on top of a 2 μm thick thermal silicon dioxide on a 675 μm thick bottom silicon substrate. In most designs and applications, silicon dioxide or air is used as top cladding layer materials for the SOI photonics waveguides.

The different schematic of waveguide geometries is shown in Figure 2.1. The silicon slab waveguide geometry is shown in Figure 2.1(a). Both TE and TM polarization light can be propagated in a slab waveguide. The waveguide geometry is invariant along the X-axis and the propagation direction is the Z-axis. In TE polarization, there are only electric field components along the X-axis and only electric field components along the Y-axis in TM polarization.

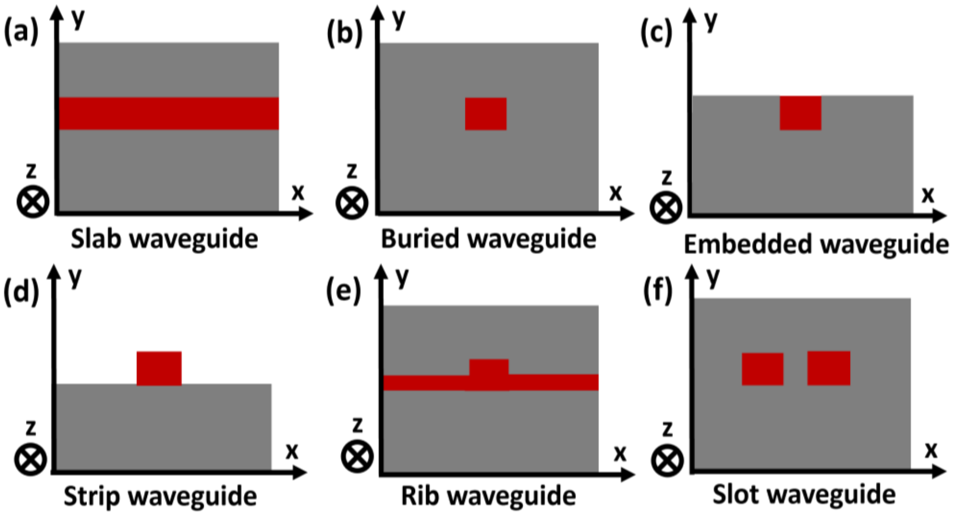

Fig. 2.1 Schematic of waveguides geometry.

The typical ridge waveguide geometry focused on 1550 nm wavelength is 500 nm wide in SOI wafer. The cladding material is varied based on the application demands. The structure of the ridge waveguide with silicon dioxide cladding and air cladding is shown in Figure 2.1(b) as a buried waveguide and Figure 2.1(d) as a strip waveguide respectively. The geometry of the buried waveguide is in the x and y directions, but strip waveguide geometry is only in the x direction. The electric field along the X, Y, and Z axis is denoted as E_x, E_y and E_z respectively. E_x is the dominant field component for TE polarization light and E_y is the dominant field component for TM polarization.

The mode electric field distribution of buried and stirp waveguide are simulated using MODE Finite Difference Eigenmode (FDE) solver in Lumerical FDTD software. The E_x field of TE polarized, and Ey field of TM polarized buried ridge waveguide are shown in Figure 2.1(a) and (c), the Ex field of TE polarized and Ey field of TM polarized strip waveguide are shown in Figure 2.1(b) and (d). The TE polarized E_x field for both waveguide structures is symmetric along the X-axis. However, there is a discontinuity at the sidewalls and stronger near the waveguide boundary, this makes any fabrication imperfection in these interfaces like sidewall roughness will lead to high waveguide transmission loss and phase error for TE polarized light. For TM polarization, E_y field distribution of the two waveguides is strong at the waveguide top and bottom area. Thus, in TM polarization sidewall roughness will not have an obvious influence on the waveguide loss or phase error. However, the effective index of this polarization is very sensitive to effective width and height alteration. The buried waveguide has field symmetry along Y-axis while the strip waveguide does not. The confinement near the waveguide top is much better compared to the bottom area as the refractive index contrast at the silicon-air boundary is higher compared to the silicon-silica boundary.

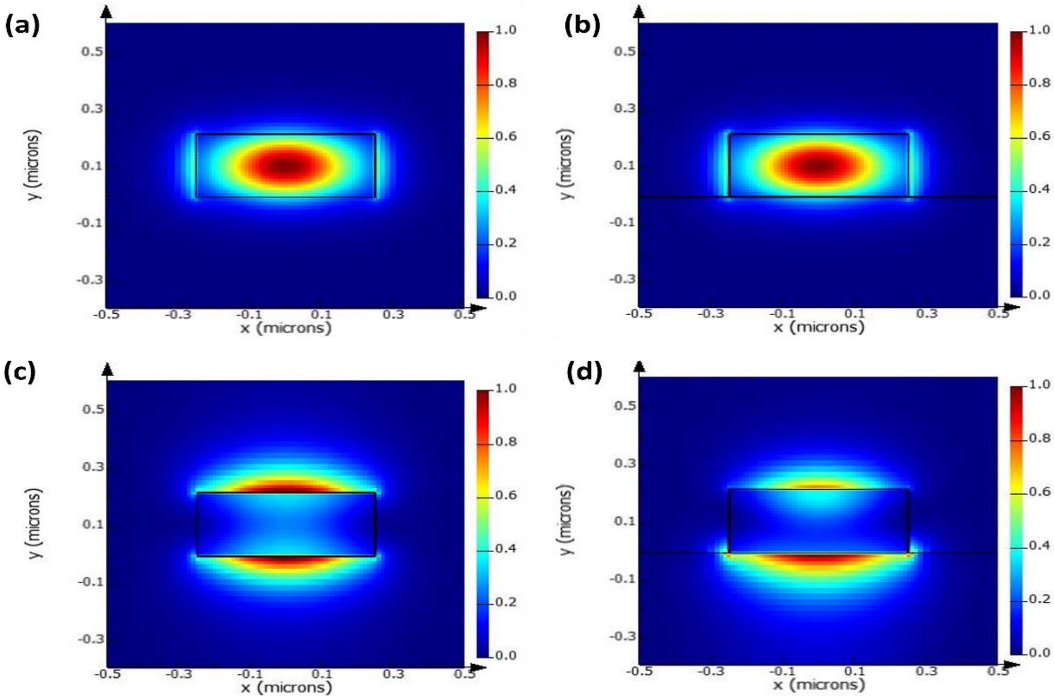

Fig. 2.2 (a) The E_x field of TE polarized buried ridge waveguide, (b) The E_x field of TE polarized strip waveguide, (c) The E_y field of TM polarized buried ridge waveguide, (d) The E_y field of TM polarized strip waveguide.

The rib waveguide geometry structure shown in Figure 2.I), the commonly used rib waveguide geometry in integrated photonics circuits is 450 nm wide with 150 nm slab thickness. The E_x-field component of the TE-like mode is confined in the slab region but has strong boundary discontinuity. As this is a shallow etch waveguide structure, the sidewall roughness is smaller compared with ridge waveguide which leads to lower waveguide loss and phase error. However, as the confinement is mainly in the slab region, the bend radius of the waveguide structure design is large. Also, it has been experimentally proved that TM-like modes in rib waveguides are leaky inherently because the effective index of the TM-like mode is in the same range as the higher-order TE slab modes. These modes propagate in the slab at arbitrary random angles, which allows phase matching with the guided TM-like modes, and these modes will couple to the slab modes. For fundamental TE-like mode, the mode will be pushed to the slab region, and it will no longer be guided when the waveguide width decreases.

The slot waveguide is also a widely used waveguide structure with the geometry shown in Figure 2.1(f). It consists of two or more silicon ridge waveguides placed close to create slot waveguides. For our simulation, we used two 210 nm-wide ridge waveguides separated by a 100 nm gap with silicon dioxide cladding.

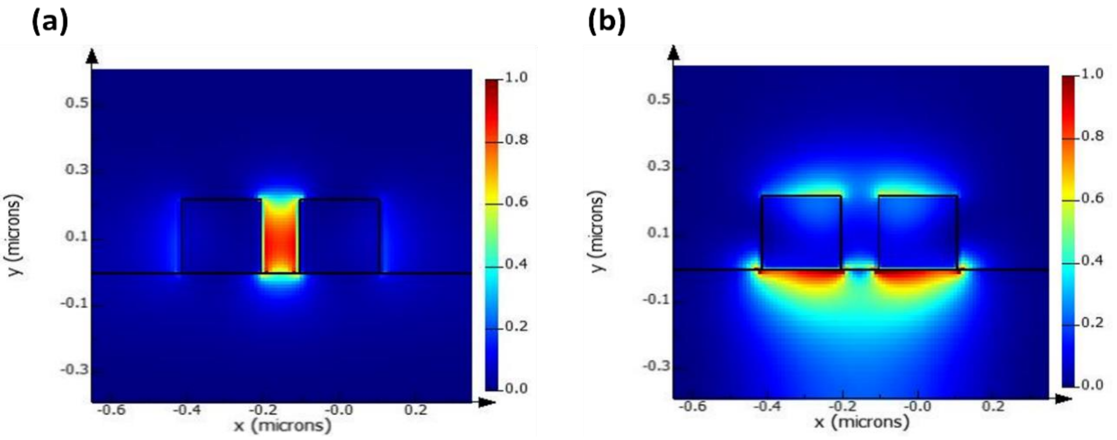

Fig. 2.3 (a) E_x field of TE polarized light, (b) E_y field of TM polarized light in SOI slot waveguide.

From Figure 2.3 (a) and (b), it is clear to see that E_x field is highly confined in the gap for TE polarization light and the E_y field components are highly confined at the top and bottom of the waveguide in TM polarization. In TE polarization, the E_x-field strongly confined in the slot region makes this slot waveguide structure highly suitable for sensing applications. In sensing applications, samples like analyte, solutions, and gas can be used instead of oxide cladding, the refractive index changes of these cladding materials will cause the wavelength shift of the transmission spectrum. The unknown gas or liquid could be detected using prior calibration. The mode will be guided by the gap if the waveguide is small enough, otherwise the light will propagate through the individual silicon ridge waveguide working as directional couplers. The main challenge to fabricate these waveguides is to fabricate the high precision ultra-narrow gap. The TE-like mode polarized light is highly confined in the gap, therefore the fabrication imperfection like sidewall roughness will cause a high loss and phase error.

2.1.2 Single-mode regime

The SOI wafer structure we use in our design is shown in the picture below. The substrate material system is silicon on an insulator wafer with the thickness of the top silicon layer 220 nm, the thickness of the silicon dioxide BOX layer is 2 μm, and the thickness of the Si substrate layer is 675 μm.

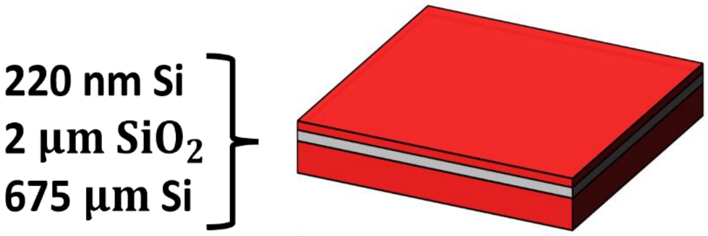

Fig. 2.4 The SOI wafer structure.

Some simulations using Lumerical FDTD have been done based on the straight strip silicon waveguide. The height of the strip waveguide is fixed at 220 nm which is the top silicon layer thickness. In our sensing design, we focused on single-mode TE transmission waveguide width limits for silicon straight strip waveguides. From the references about single mode strip silicon waveguide with 220 nm thickness in [68-69], which says the single-mode transmission is between waveguide width 305 nm and 677 nm. The waveguide width between this range could realize the single-mode transmission with lower transmission loss. To determine the appropriate single-mode transmission waveguide width, we did single mode waveguide simulation based on the SOI wafer structure and the simulation results are shown in Figure 2.5. For 1550 nm wavelength, only the modes above the black dotted lines (SiO2 refractive index) are guided. To obtain a single TE-like mode polarization at 1550 nm, a strip waveguide with a height of 220 nm and width below 560 nm is required, as shown in the red dot line is the single TE mode cut-off waveguide width value. In this case, the waveguide supports one TE-like and one

TM-like mode. For wider waveguides, a second TE-like mode is present, and above 760 nm, a second TM-like mode appears. The simulated waveguides do not operate in a pure TE or TM polarization, thus the waveguide polarization is shown as a polarization fraction (with 1 representing a pure TE mode).

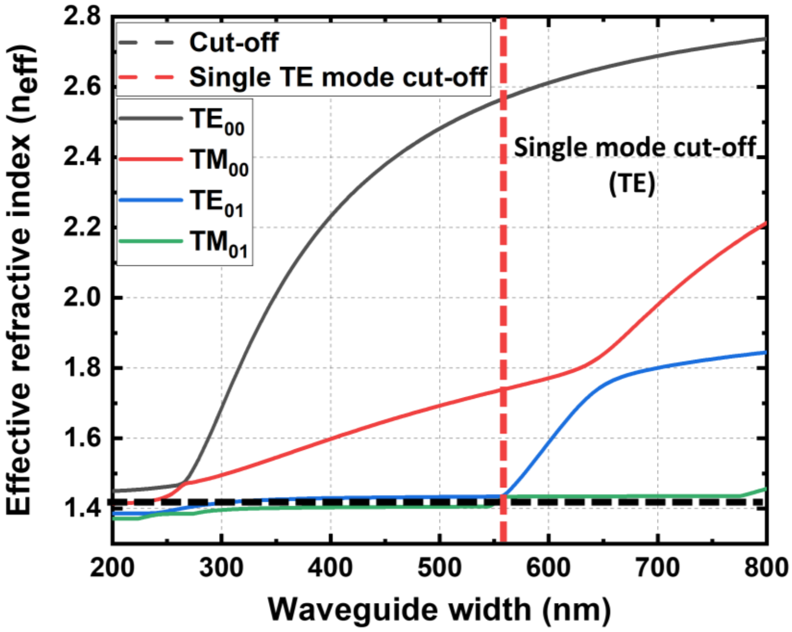

Fig. 2.5 The transmission modes of different waveguide widths.

2.1.3 Loss and dispersion

The silicon wire waveguides based on SOI platform with low propagation loss are the key components of integrated photonics circuits. In this section, we analysis the categories of waveguide loss and the measured low propagation loss waveguides reported based on different fabrication methods. In the following chapter, we will show measured results of different waveguide structures transmission loss in our lab measurement. The simulated transmission loss with strip waveguide dimension 500 nm × 220 nm is simulated with different wavelength shown in Figure 2.6 (a), the loss values are 0.01 dB/cm at 1550 nm. The simulated transmission loss with different waveguide width is simulated in Figure 2.6 (b), with maximum loss value reaching 0.058 dB/cm.

The origin for the silicon wire waveguides propagation loss can be classified into four categories: (1) the absorption in silicon cores like bulk absorption, (2) interface scattering between the silicon core and the cladding layer, (3) absorption of impurities in the interface and clad, and (4) light leakage to the silicon substrate through BOX. For the bulk absorption of non-doped silicon at 1550 nm is quite small. While some studies have reported impurity absorption due to metal residue at the interface or cladding, leading to a decrease in propagation properties [70-71], these can be avoided by careful cleaning post fabrication. For the substrate leakage, the leakage of propagating light for low-order TE mode propagation to the substrate was estimated as negligible for BOX thickness more than 1.5 μm (value less than 1×10^{-4} dB/cm) [72].

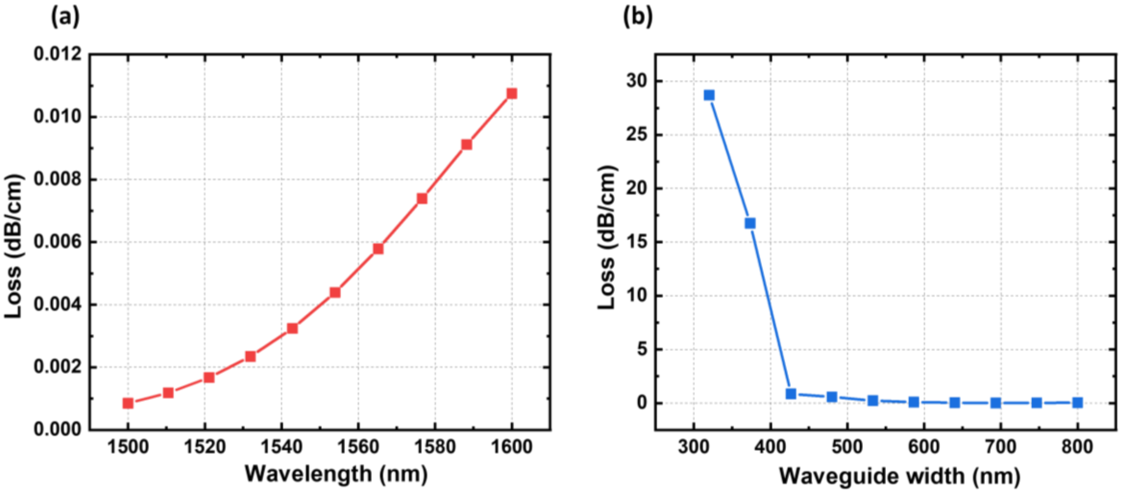

Fig. 2.6 The simulated strip waveguide loss with (a) different wavelengths and (b) different waveguide widths.

Therefore, the scattering at the interface between the silicon core and cladding is the main cause of propagation loss. The analysis of Barwicz and Haus's theory shows that sidewall scattering is the main cause of propagation loss even in low loss waveguide structures. The silicon waveguide on SOI wafers is fabricated by resist pattern with lithography on the top silicon layer following anisotropic dry etching the top silicon layer. This fabrication flow was established in 2005 [73-77]. During this period, some research groups verified that scattering of propagating light with line edge roughness (LER) is the main cause of propagation loss [73,75], and the sidewall roughness was found to be the origin of LER. Table 2.1 compares the main measured results of propagation loss reported. The transverse electric (TE) mode waveguide loss <2 dB/cm with thermal oxidation for sidewall smoothing was first reported by IBM in 2006 [78]. The loss <1 dB/cm was first reported by the UoG group. The hydrogen silsesquioxane (HSQ) was used as a negative-tone Electron-beam lithography (EBL) resist and Si ridge waveguide dry etching mask as well [79]. The IMEC group reported a reduced propagation loss of <1 dB/cm using ArF immersion lithography in 2012 [80]. Recently the propagation loss of less than 2 dB/cm is widely achieved in most silicon photonics fabrication platforms including foundries [81]. However, loss below 1 dB/cm was only reported by some research groups (the group mentioned above). The lithography process could greatly influence the propagation loss.

Table 2.1 Comparison of propagation losses for fundamental TE mode Si wire waveguides.

Dimension (nm × nm)	λ (nm)	Lithography	α (dB/cm)	Ref.
630 × 220	1550	KrF	1.9	[75]
460 × 220	1550	ArF	2.7	[82]
457 × 220	1550	ArF-I	0.71	[80]
500 × 260	1520-1525	EB	0.92	[79]
440 × 220	1550	EB	1.2-1.8	[83]
500 × 220	1550	ArF-I	0.5	[84]

2.1.4 Bend waveguides

The strong mode confinement in SOI photonics wires allows very sharp bends (radius down to 3 µm) with still low radiation as compared to bends in conventional waveguides (radius down to 100 µm). This brings advantages to tight integrated optics circuit design. In the microring resonator structure, the ring resonator part consists of silicon bend waveguides. The propagation loss in a straight SOI waveguide is from the fabricated waveguide sidewall roughness. The two major propagation loss sources for a 90-degree bending waveguide structure are: 1) the mode propagation losses in the bent region, 2) mode overlap losses between the waveguide straight and bend sections, 3) The extra coupling to TM or higher modes in bend section should considered if happened. The bend waveguide propagation loss is simulated in this section. The simulation uses waveguide dimensions of 500 nm × 220 nm with a 5 µm bending radius as an example in Mode FDE Lumerical. The two main causes of bending waveguide loss are 1) the propagation loss of the mode in bending region, 2) the mode overlap losses between the waveguide bent and straight sections. The simulated E_x field of TE polarized strip bend waveguide is shown in Figure 2.7 (a) and the monitor position is shown in Figure 2.7 (b). The propagation loss of the bend waveguides versus different wavelength, different waveguide width, and different bend radius are shown in Figure 2.8 (a), (b), and (c) respectively. The bend region propagation loss and the mode overlap losses of the 90-degree bend can be calculated by combining simulation and formulas (3) and (4). The simulated bend region propagation loss is 0.213 dB/cm and the overlap between the two modes is 99.94%. Thus, the calculated loss per bend for 500 nm × 220 nm waveguide with 5 µm bending radius is 0.0104 dB.

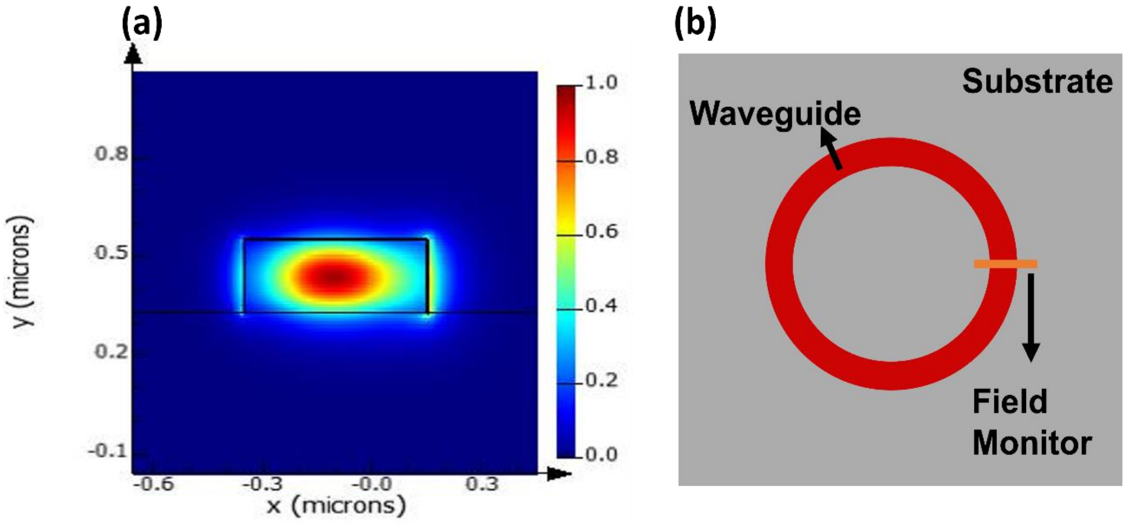

Fig 2.7 (a) The simulated E_x field of TE polarized strip bend waveguide with dimensions of 500 nm × 220 nm and a 5 µm bending radius, (b) The top view of simulated waveguide with mode field monitor position.

$$Loss = -2 \times 10 \times log_{10}(Overlap) + LossPerBend(i) \quad (3)$$

$$LossPerBend = Loss(dB/um) \times \pi \times R(um) \quad (4)$$

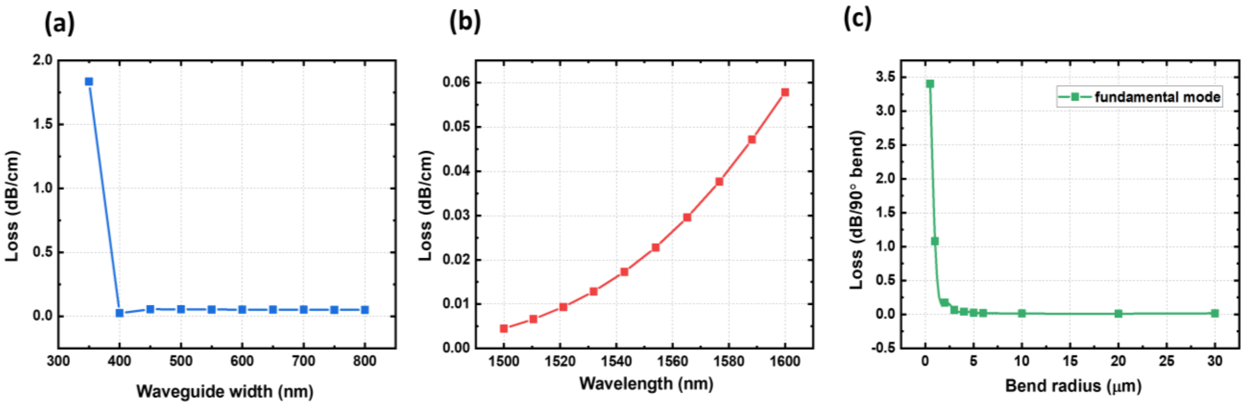

Fig. 2.8 The simulated bend waveguide propagation loss with (a) different waveguide width at 1550 nm operation wavelength, (b) different wavelength at 500 nm waveguide width, and (c) different bend radius at 1550 nm wavelength and 500 nm ridge waveguide width.

The strong mode confinement in SOI wires allows for very sharp bends (radius down to 3 μm) with still low radiation as compared to bends in conventional waveguides (radius down to 100 μm).

In practical applications, the fabrication of bending waveguides introduces challenges related to both substrate leakage and scattering losses, primarily due to the mode being slightly displaced outward. For 500 nm wide SOI wire waveguides with a 4.5 μm radius microring resonator, bending losses are as low as 0.01 dB/90° when employing deep-UV lithography. However, as the bend radius decreases to 1 μm, these losses escalate to 0.071 dB/90° [85].

2.2 Microring resonators (MRRs)

Microring resonators (MRRs) are widely used photonic components that can be used as delay elements in optical buffers, filters in wavelength division multiplexed (WDM) networks, modulators, and laser cavities using active material wafers. One of the first published articles for integrated microring resonators simulation as a bandpass filter was published by E. A. Marcatili in 1969 [86]. The standard structure configuration of an integrated MRR channel drop filter consists of two straight bus waveguides coupled by directional couplers (evanescent field) or multimode interference couplers to the MRR. A simpler configuration is achieved if the second bus or port waveguide is removed, and it acts like a notch or all-pass filter. In the following section, the microring resonator theory and simulation model are described beginning with the basic notch configuration and add-drop configurations, and some theory and performance parameters when using MRRs as biochemical sensors are detailed.

2.2.1 Coupling sections

After the analysis of the photonics waveguide structure, some complex structures could be developed. The coupler section is important for structures like coupled waveguides, Mach Zender interferometers and microring resonators. The two basic structures of couplers are the multi-mode interference (MMI) coupler [87] and the directional coupler [88]. The MMI couplers are used for coupling ratios apart from 50-55% and tuning requirement. This coupler structure could only achieve coupling ratio 50-55% by altering MMI coupler geometry (tiny angle, tiny etched gap and waveguide local RI variation) for the interference pattern modification [89-91]. The structure design should be careful to avoid the production of spurious back-reflection. Although MMIs can provide 50% coupling with high dimensional variations tolerance [92], they become instable for very low coupling required for near critical coupling situations in low loss microring resonators. Moreover, their sizes are typically larger than directional couplers and require two-step etch process in fabrication [93].

The power coupling coefficients control may be needed in multiple microring coupling structures (like CROW structures) which are repeatable and controllable in directional couplers. The directional coupler is constructed by two parallel waveguides in proximity. This close distance between two waveguides makes the optical modes in pristine waveguides being disturbed and independent. The evanescent fields in two waveguides interact with results as coupled and mutual interfere. The spatial dependence of each mode amplitude is affected by the other modes. The coupling coefficients between two optical modes are affected by the gap distance between the waveguides *Gc* and the coupling length *Lc*. The schematic demonstration of the directional waveguide coupler is shown in Figure 2.9.

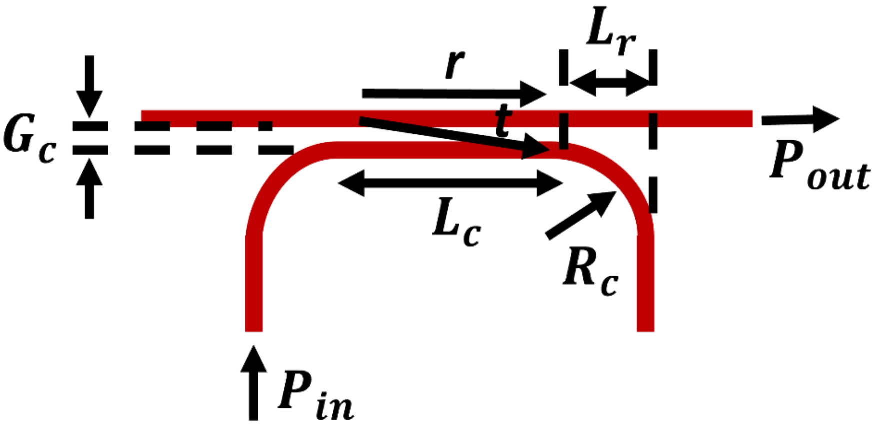

Fig. 2.9 The schematic of directional waveguide coupler.

Microring resonators are widely used photonic components that can be used as delay elements in optical buffers, filters in wavelength division multiplexed (WDM) networks, modulators, and laser cavities using active material wafers.

The formulas for self-couplI (*r*) and cross-coupling (*t*) coefficients of the directional coupler are shown in equation (5), The parallel section is characterized by its coupling coefficient per unit distance κ [1/µm] (the coupling constant obtained from simulation of the coupled system equation [94]) and the two bent regions together cause an offset coupling κ_0.

$$r = cos(\kappa L_c), r^2 = 1 - sin^2(\kappa z) \tag{5}$$

$$t = -jsin(\kappa L_c), \tag{6}$$

The power cross coupling *t* of the directional coupler can be formulated as equation (7) [95].

$$K = \frac{P_{out}}{P_{in}} = t^2 = sin^2(\kappa \cdot L_c + \kappa_0) \tag{7}$$

The interaction region consists of both straight region *Lc* and two transition regions *Lr* corresponding to the input bending and output bending regions, and these two transition regions contribute additional effect to the coupling coefficients. The effective length of interaction is $L_{eff} = L_C + 2L_r$, and the value of L_r could be described as an evanescent field with an exponential decay (ς) in equation (8) [94].

$$L_r = \int_0^{\infty} exp\big(-\varsigma(d(z) - G)\big)dz = \frac{1}{2}\sqrt{\frac{\pi R}{\varsigma}} \tag{8}$$

In this formula, *d(z)* represents the relative distance between the two waveguides at a particular section, *G* represents the gap width between the two waveguides. L_r is dependent on the bend radius *R* before and after the coupler straight section, a bigger radius will have a longer interaction length.

In FDTD simulation, the coupling coefficient is the fraction of power that couples from the fundamental TE-mode in the straight waveguide to the fundamental TE-mode of the curved waveguide. Its value can be controlled by the gap distance between the bus waveguide and the ring resonator. The quality factor is a key parameter in different applications and is inversely proportional to the coupling coefficient. The coupling coefficient with different wavelength and the power cross coupling coefficient versus the gap dimension for different values of length of the coupler *Lc* (the waveguide dimension in the simulation is 500 nm × 220 nm with 5 µm bending radius) are shown in Figure 2.10. In Figure 2.10(a), the coupling coefficient κ is simulated based on silicon strip waveguide dimension 500 nm× 220 nm microring resonator with 100 nm gap. The coupling coefficient increase with wavelength. In Figure 2.10(b), the simulation results show that to obtain a higher coupling coefficient, a larger value of coupling length may be required when the fabrication gap length is fixed. To reduce the coupling length it needs a reduction of the gap length. Also, when looking at the curve with fixed *Lc* value, power coupling coefficient K is the fraction of power that couples from the fundamental TE-mode in the straight waveguide to the fundamental TE-mode of the curved waveguide. Its value can be controlled by the gap distance between the bus waveguide and the ring resonator. The first increases to a peak then decrease, this can be explained in formula (7) with sin^2 function and *Lc* as one variable.

Here we need to point out, because of the reactive ion etching (RIE) lag effect, it is a challenge to get a high quality gap smaller than 100 nm.

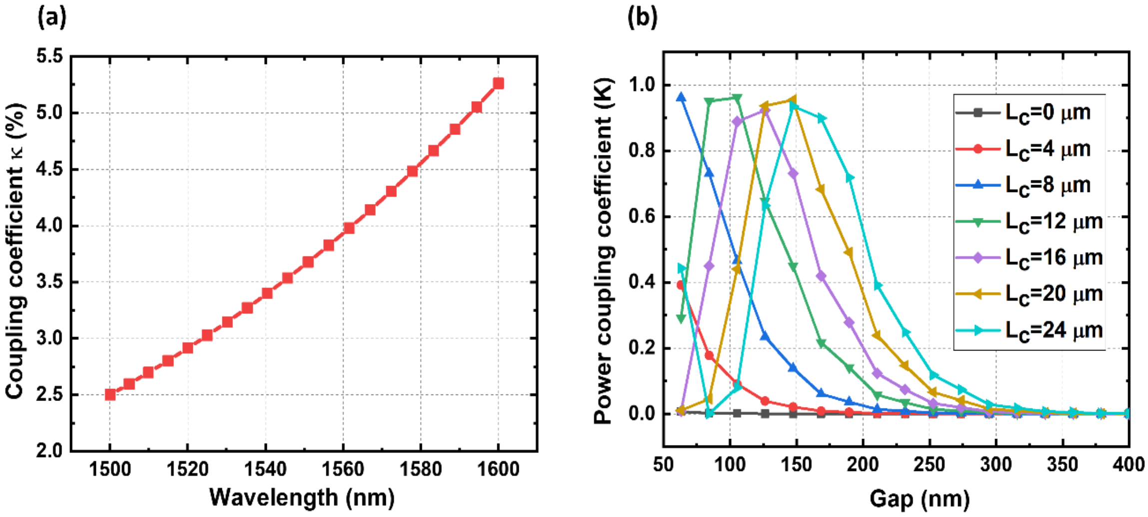

Fig. 2.10 (a) The coupling coefficient vs operation wavelength with a 100 nm gap and (b) the power cross coupling coefficient versus the gap dimensions for different length of the coupler, denoted as L_C.

2.2.2 All-pass MRRs

The all-pass microring resonator structures consists of the single bus waveguide and the microring resonator structure, which is shown in Figure 2.11. The fundamental transmission spectral properties of an all-pass filter (APF) microring resonator can easily be obtained by assuming continuous wave (CW) operation and matching fields. In this APF structure, the reflections back into the bus waveguide are negligible (which is not necessarily the case in a silicon wire). The ratio of the output (transmitted) and input (incident) field in the single bus waveguide could be described in formula (9) [96],

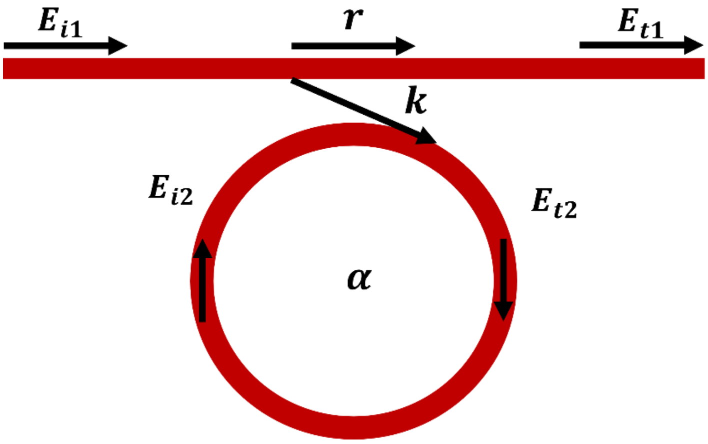

Fig.2.11 Structure of all-pass microring resonator.

$$\frac{E_{pass}}{E_{input}} = e^{i(\pi+\emptyset)} \frac{a-re^{-i\emptyset}}{1-rae^{i\emptyset}} \tag{9}$$

where $\emptyset=\beta L$ is the single-pass phase shift, L is the round-trip length, β is the propagation constant of the circulating mode . The single-pass amplitude transmission including both propagation loss in the ring and loss in the couplers, which is defined as a and is related to the power attenuation coefficient α [1/cm] as a^2=exp(-αL). The intensity transmission T_n is the squaring of Eq. (9),

$$T_n = \frac{I_{pass}}{I_{input}} = \frac{a^2-2racos\emptyset+r^2}{1-2arcos\emptyset+(ra)^2} \tag{10}$$

where r and k are the self-coupling coefficient and the cross-coupling coefficient respectively. The power splitting ratios of the coupler are r^2 and k^2, and they satisfy $r^2+k^2=1$, which means there are no losses in the coupling section.

The microring resonator is on resonance when the phase $\emptyset$ is a multiple of $2\boldsymbol{\pi}$ or when the light wavelength fits a whole number of times inside the optical length of the microring:

$$\lambda_{res} = \frac{n_{eff}L}{m},\ m = 1,2,3\ ... \tag{11}$$

For ideal cavities with zero attenuation, a =1. Under critical coupling, when the coupled power is equal to the power loss in the ring, $1-a^2=k^2$ or $r=a$, the transmission at resonance drops to zero.

From Eq. (9) the effective phase shift φ induced by the ring resonator can be calculated,

$$\varphi = \pi + \emptyset + arctan\frac{rsin\emptyset}{a-rcos\emptyset} + arctan\frac{rasin\emptyset}{1-racos\emptyset} \tag{12}$$

For ideal cavities with zero attenuation, a=1. Under critical coupling, when the coupled power is equal to the power loss in the ring, $1-a^2=k^2$ or $r=a$, the transmission at resonance drops to zero. The phase parameter of field transmission varies periodically with frequency. All-pass resonators delay the input signal by temporarily storing light energy within the resonator.

2.2.3 Add-drop MRRs

The add-drop microring resonator structures consists of one input and one output bus waveguides and the microring resonator structure, which is shown in Figure 2.12. For add-drop microring resonator structures where the microring resonator is coupled to two waveguides, the incident field is transmitted to both pass and drop port. The transmission to the pass T_p and the drop port T_n are:

$$T_p = \frac{I_{pass}}{I_{input}} = \frac{r_2^2 a^2 - 2 r_1 r_2 a cos\emptyset + r_1^2}{1 - 2 r_1 r_2 a cos\emptyset + (r_1 r_2 a)^2}. \tag{13}$$

$$T_d = \frac{I_{pass}}{I_{input}} = \frac{(1 - r_1^2)(1 - r_2^2) a}{1 - 2 r_1 r_2 a cos\emptyset + (r_1 r_2 a)^2}. \tag{14}$$

If the attenuation is negligible (a≈1), critical coupling status occurs when symmetric coupling ($k_1 \approx k_2$). For a lossy resonator, critical coupling occurs when the losses match the coupling $r_2 a = r_1$, where $r_1$is the amplitude self-coupling coefficient of the input channel waveguide and r_2 is the amplitude self-coupling coefficient of the drop channel waveguide.

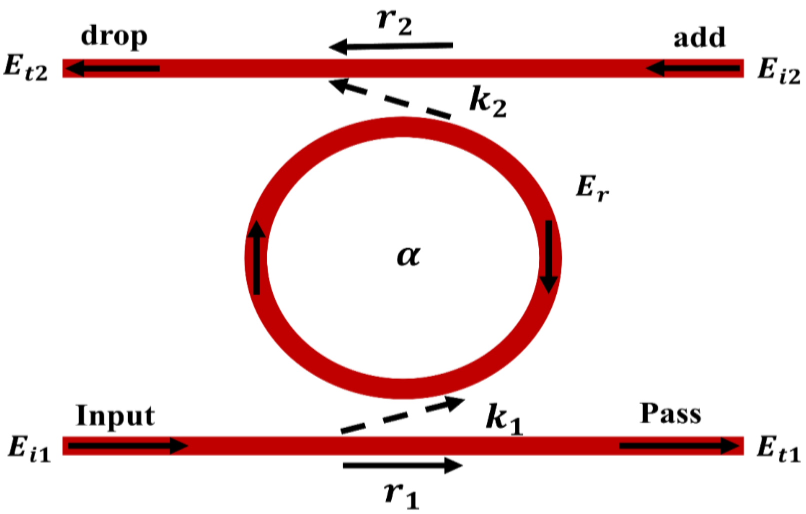

Fig.2.12 Structure of add-drop microring resonator.

2.2.4 Spectral characteristics of MRRs

The characteristic parameters of all pass MRR and add drop MRR structures depend on the losses and coupling coefficients and can be extracted directly from the transmission formulas (10), (13), and (14). The full width at half maximum (FWHM) of the resonance spectrum for an all-pass ring resonator:

$$\mathrm{FWHM} = \frac{(1-ra)\lambda_{res}^2}{\pi n_g L\sqrt{ra}} \tag{15}$$

And the FWHM for an add-drop ring resonator configuration is:

$$\mathrm{FWHM} = \frac{(1-r_1 r_2 a)\lambda_{res}^2}{\pi n_g L\sqrt{r_1 r_2 a}} \tag{16}$$

The wavelength range between two resonance dips or free spectral range (FSR) can be calculated in the function of wavelength equals:

$$\mathrm{FSR} = \frac{\lambda^2}{n_g L} \tag{17}$$

where L is the round-trip length. The strong confinement based on the high RI contrast in SOI wafers allows very sharp bends and greatly increases the potential FSR of SOI ring resonators.

The group index considering the dispersion of the waveguide is defined as

$$n_g = n_{eff} - \lambda_0 \frac{dn_{eff}}{d\lambda} \tag{18}$$

The corresponding group velocity $v_g = \frac{c}{n_g}$, shows the velocity at which the envelope of a propagating pulse travels and is a characteristic of a dispersive medium (or waveguide).

The on-off extinction ratio of each resonance dip is equal to $\frac{\boldsymbol{T_{max}}}{\boldsymbol{R_{min}}}$. For an APF ring configuration, the T_{max} and R_{min} are:

$$T_{max} = \frac{(r+a)^2}{(1+ra)^2} \tag{19}$$

$$R_{min} = \frac{(r-a)^2}{(1-ra)^2} \tag{20}$$

For an add-drop configuration, the same $ER = \frac{T_{max}}{R_{min}}$ for the drop transmission. At resonance, the ER between through and drop port of an add-drop resonator is given by $\frac{T_{max}}{R_{min}}$. T_t, R_{min}, T_{max} and T_d are defined and shown in Figure 2.13 and Figure 2.14 as follows,

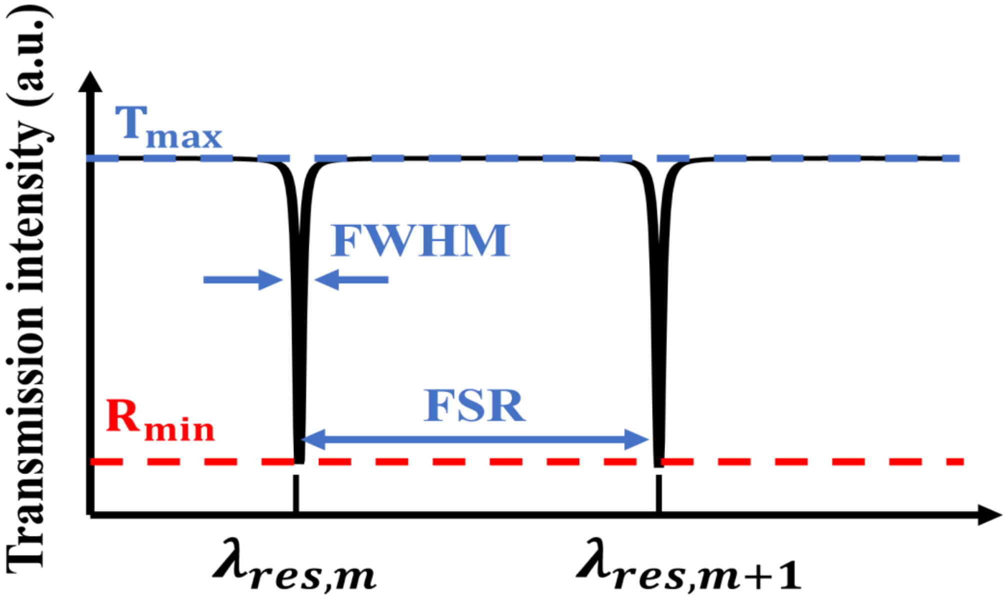

Fig.2.13 The power transmission spectrum of an all-pass ring resonator resonance dips characterized by full-width at half-maximum (FWHM) and on-off extinction (T_{max} /R_{min}) and free spectral range (FSR).

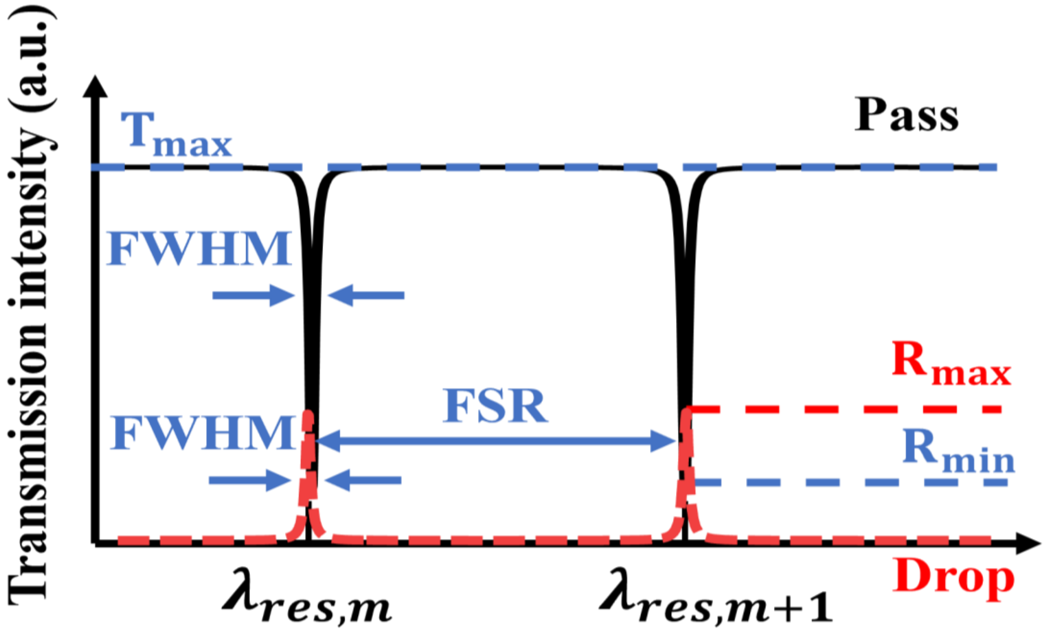

Fig.2.14 The power transmission spectrum of an add-drop ring resonator resonance dips characterized by full-width at half-maximum (FWHM) and on-off extinction (T_{max} /R_{min}) and free spectral range (FSR).

$$T_t = \frac{(r_2a+r_1)^2}{(1+r_1r_2a)^2} \tag{21}$$

$$R_{min} = \frac{r_2^2a^2-2r_1r_2a+r_1^2}{(1-r_1r_2a)^2} \tag{22}$$

$$T_{max} = \frac{(1-r_1^2)(1-r_2^2)a}{(1-r_1r_2a)^2} \tag{23}$$

$$T_d = \frac{(1-r_1^2)(1-r_2^2)a}{(1+r_1r_2a)^2} \tag{24}$$

The finesse is defined as the ratio of FSR and resonance width,

$$\text{Finesse} = \frac{\text{FSR}}{\text{FWHM}} \tag{25}$$

It is thus a measure of the sharpness of resonances relative to their spacing. The quality factor (Q-factor) is a measure of the sharpness of the resonance relative to its central frequency,

$$\mathrm{Q-factor} = \frac{\lambda_{\mathrm{res}}}{\mathrm{FWHM}} \tag{26}$$

The physical meaning of the finesse and Q-factor relates to the number of roundtrips can be made by the energy inside the microring resonator before being lost to internal loss and the bus waveguides. This is a temporal phenomenon and must be checked with the transient response. Mathematics is described in many books and publications [97]. The fineness, the study found, is a factor of 2π, which represents the number of times light travels back and forth in the ring before its energy drops to 1/e of its initial value. The Q factor represents the number of oscillations of the field before the cyclic energy is depleted to 1/e of the initial energy. To define the Q-factor, the microring is excited to a certain level and the power decay rate is considered. From this perspective, it can be understood that the round-trip loss, as well as the coupling in the directional coupler, is the loss factor that needs to be reduced to obtain a high-Q resonance. Therefore, an all-pass resonator will exhibit a higher Q-factor than a split resonator (when both devices are operating close to critical coupling).

We distinguish between loaded Q-values and unloaded Q-values. The unloaded-load Q value of a resonator is the Q-factor of the resonator when it is not coupled to the waveguide. When coupled into a waveguide, additional losses are introduced in the cavity. Therefore, the loaded Q-value is always smaller than the unloaded Q-value. Unless specifically stated otherwise, when referring to the Q-factor we always mean the loaded Q-value.

2.3 Grating coupler

The promising solution for high-performance and low-cost photonic and complementary metal-oxide-semiconductor (CMOS) compatible silicon photonics systems is using integrated photonics elements. For instance, the silicon-on-insulator (SOI) platforms, have become the most significant solution for new generation on-chip optical interconnect technology. Many optical components are implemented on silicon platforms like light sources, wavelength division multiplexers (WDM), modulators, and optical switches. In addition to data communication areas, silicon photonic devices could also be used in biosensing and light detection areas.

Some key challenges appear after these developed high-performance optical components on SOI. One of the challenges is the efficient light coupling to and from optical fibres. The ordinary fibre dimension for single-mode fibre (SMF) has a mode field diameter (MFD) near 10 μm at 1550 nm wavelength. However, the dimension size of silicon photonic waveguides is about 500 nm × 220 nm, and this large modal size mismatch makes it a challenge for efficient coupling form SMF to waveguide. This problem is usually solved using two methods, in plane butt edge coupling and off plane vertical grating coupling [98-100]. In edge coupling, the fibre is placed at the chip edge facet and horizontally aligned with the silicon waveguide on chip. The edge couplers always consist of the inverse tapered waveguide which has the waveguide width gradually decrease along the light propagation to the edge. As the taper size decreases, optical confinement decreases, and the mode size becomes larger, comparable to that of a SMF mode. The opposite is true for fibre-to-chip propagation where the Gaussian fibre mode distribution is confined to the tapered waveguide as its size increases. Edge couplers have several advantages. It enables high coupling efficiency (CE), large bandwidth (BW), and low polarization-dependent loss (PDL) [98]. But this coupling method requires a properly cleaved and polished facet with strict controlled smoothness, this may increase extra fabrication cost and difficulty considering mass manufacturing, also raise the cost per sample (chip) and accuracy requirement for sample packaging and testing. The vertical grating couplers (GCs) structures are more flexible compared to the edge coupling. This method allows arbitrary coupling position on chip, brings advantages like compact size, less complexity fabrication and wafer-scale testing ability. In grating coupler light coupling, the fibre is placed above the diffractive grating coupler structures on the top of the chip. The grating coupler could change the off-plane light wave-vector direction and couples the light into the silicon waveguide through spot-size converter. Even though the grating couplers have many advantages mentioned above, they also have drawbacks because of their operation principles. Firstly, they have lower coupling efficiency (CE) compared with specially designed edge couplers, and many research works are focused on changing GC design structures for CE improvement. Secondly, gratings are inherently sensitive to both wavelength and polarization variations. In the following, we mainly illustrated the theory of focused grating couplers since this structure is used in our MRR biochemical sensors for light coupling between fibres and chips.

The grating couplers structures interface the fibre mode directly, thus the grating width at y-direction is always comparable to the MFD size near 10 µm. The light transition from grating section to the single-mode waveguide (400-500 nm width) section is achieved by tapered waveguides. The energy is conserved if propagating mode only changes its size and shape in this transition without waveguide radiation or higher-order waveguide mode conversion. It could be considered as an adiabatic transition in this case. In the linear tapered waveguide that allows adiabatic transition, the geometric parameters satisfy [100],

$$\theta_{taper} < \frac{\lambda}{2Wn_{eff}} \tag{15}$$

where θ_{taper} is the taper angle, W is the varying waveguide width and n_{eff} is the corresponding mode effective index. The adiabatic waveguide structure (usually 300-500 µm in length) are adopted in order to achieve high coupling efficiency. However, this large size waveguide may occupy much space on chip. The focused design of grating couplers is usually used to reduce the footprint. The structure of the focused grating couplers is shown in Figure. 2.15 and the grating lines are curved to [102],

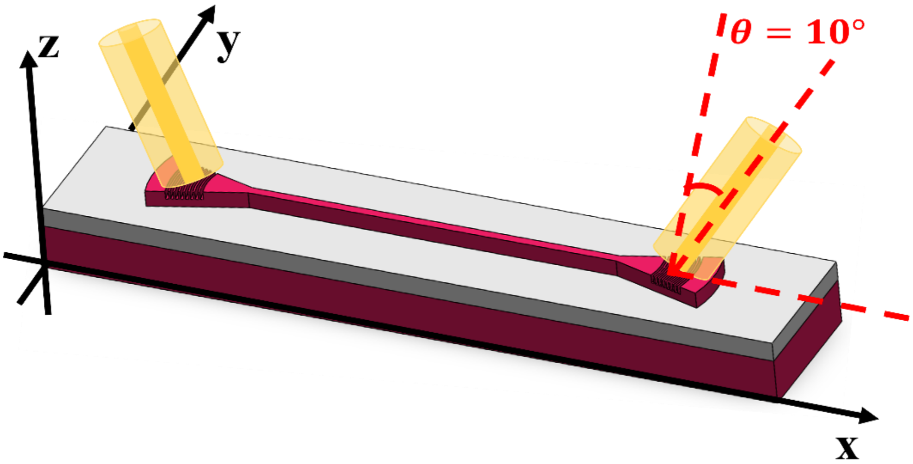

Fig.2.15 Structure of focused grating couplers with bus waveguide.

$$m\lambda = n_{eff}\sqrt{x^2 + y^2} - xn_0 sin\theta \tag{16}$$

where the focal point is origin, m is each grating line integer, θ is the tilt angle of fibre, n_0 is the refractive index of cladding layer and n_{eff} is the effective index of GC. These curved grating lines form ellipses with collaborative focal points. In this structure, the coupled wavefront will be curved and light from fibre will be focused as it propagates, thereby eliminating the full-length adiabatic taper requirement. For a focusing GC with grating lines curved, light diffracted from different positions is expected to interfere constructively at the focal point. However, since the dry etch of the grating depths may not be very stable, so the simulation of the effective refractive index n_{eff} may not be evaluated precisely. The 2D and 3D Lumerical FDTD simulation [103] are used for the GC structure parameters optimization and CE improvement. The grating coupler design is based on the simulation using FDTD first to optimize the grating coupler parameters based on the wafer structure. The optimized parameters include the grating pitch, duty cycle and fibre position. Also, a balance is required considering fabrication limitations and the footprint. The detailed simulation fabrication, and measured results are illustrated with the sensors performance in Chapter 3.

2.4 Polarization parametric indirect microscopic imaging (PIMI) system

In nowadays biosensor design, plasmonic structures are widely adopted. The plasmonic resonant cavities could efficiently achieve high quality factor and local field intensity, this could enhance surface-enhanced Raman scattering (SERS) or photoluminescence. Moreover, the biological particle detection method is used for sensing viruses or particles in plasmonic structures. This method has a significant influence on the scattering spectrum and field when adding molecules to the structure which is highly desirable for high sensitivity detection. The detection of far-field mode distribution under the resonant wavelength is using Polarization Indirect Microscopic Imaging (PIMI) technique.

In the simulation, the resonant peaks could be demonstrated in the spectrum of visible light wavelength range. The scattering distribution is evidently changed because of energy exchange between particles and split-ring cavity, indicating a promising possibility for biosensing. The plasmonic excitation could be categorized as surface plasmon resonances (SPR) and localized surface plasmon resonances (LSPR). The guided modes in SPR are propagating along flat planar and grating metal/dielectric interfaces. The harmonic oscillation of conduction electrons in metallic nanostructures under electric field background is LSPR [104-105]. One plasmonic structures application is sensing surrounding RIs or biological layers with different RI. The plasmonic structure could provide high sensitivity of the resonant wavelength to the refractive index (RI) such as bulk and surface sensitivity. Another type of method uses surface-enhanced fluorescence (SEF), which exploits fluorescence amplification at localized hotspots [106-107]. The surface enhanced Raman scattering (SERS) is similar to SEF, the signals of Raman scattering could be enhanced by 10^3 to 10^6 times. Also, the infrared absorption could be enhanced in the surface enhanced infrared absorption (SEIRA) spectroscopy using direct mid-IR excitation of molecules on metal structures. Currently, most plasmonic structures for sensing applications focus on the change of reflection or scattering spectrum for biochemical particles detection.

The optical Iystem is constructed based on the PIMI method to measure the orientation angle of the polarization ellipsoid and the phase difference between two orthogonal directions of light transmitted, reflected, or scattered by the sample. The main optical path is based on the Olympus BX51 microscope in this system. The liquid crystal tuneable filter (Thorlabs KURIOS-WB1) and a quarter-wave plate were added together in front of the halogen light source to select the illumination wavelength with a 35 nm bandwidth. In the PIMI system, the light source is modulated continuously with 18° polarization angle steps by the polarizer rotation. The quarter-wave plate and linear analyser are placed in the reflected light path at angles of 45° and 90° to the X-axis respectively. The light intensity images are recorded using a 5-megapixel high-sensitivity charge-coupled sensor (CCD, PiA2400-17gm, Basler) combined with a 100× objective lens (NA = 0.9) under different polarization states [108]. The diagram of the PIMI system for measurement is shown in Figure 2.16.

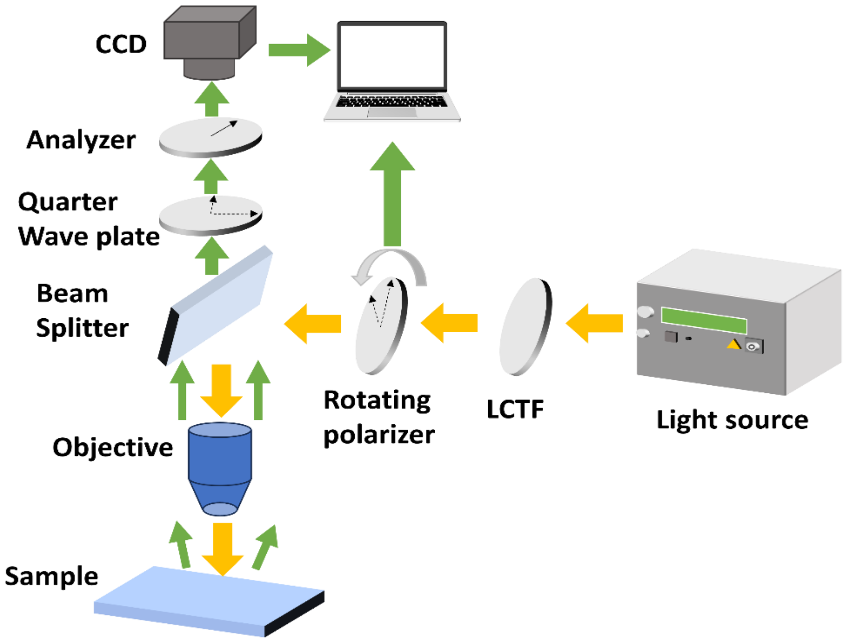

Fig.2.16 Diagram of the measurement using PIMI system [108].

The PIMI system [108] is a method for large-scale observation of sample birefringence and image indirect parameters. Considering the birefringent position on the sample, the phase difference between the fast and slow axes is [108],

$$\delta = 2\pi L\Delta n/\lambda \tag{17}$$

Where L is the light path and λ is the wavelength, and ϕ is the polarization ellipse orientation angle which defined as angle between fast axis and X axis. In PIMI system, a rotating polarizer with angle of θ_i is placed before the sample, with reflected light from the sample sequncingly go through a quarter wave plate and a 45° polarizer. The output Intensity are calculated as

$$I_i = \frac{1}{2}I_0[1 + sin\delta sin2(\theta_i - \phi)] \tag{18}$$

where I_i indicates the pixel intensity of different number of polarization rotation angles, I_0 is the average intensity under all polarization states, $sin\delta$ represents the sine of the phase difference between two orthogonal polarization components, θ_i is the polarization angle of the linearly polarized incident beam and ϕ is the polarization ellipse orientation angle of the reflected beam from the sample. The reformulation of Eq. (18 is trigonometrically expanding in the following form, and a_0, a_1 and a_2 can be calculated as follows:

$$I_i = a_0 + a_1 sin2\theta_i + a_2 cos2\theta_i \tag{19}$$

$$a_0 = \frac{1}{2} I_0 = \sum_{i=1}^{N} \frac{1}{N} I_i \tag{20}$$

$$a_1 = \frac{1}{2} I_0 sin\delta cos2\phi = \sum_{i=1}^{N} \frac{2}{N} I_i sin\alpha_i \tag{21}$$

$$a_2 = -\frac{1}{2} I_0 sin\delta sin2\phi = \sum_{i=1}^{N} \frac{2}{N} I_i cos\alpha_i \tag{22}$$

Thus, the PIMI parameters $sin\delta$ and ϕ can be calculated using the Equations (18-22),

$$sin\delta = \frac{\sqrt{a_1^2 + a_2^2}}{a_0} \tag{23}$$

$$\phi = \frac{1}{2} arccos\left(\frac{a_1}{\sqrt{a_1^2 + a_2^2}}\right) \tag{24}$$

2.5 Evanescent field sensing with MRRs

The working principle of microring resonator label-free biosensors is directly measuring the selective affinity interactions between analyte and receptor molecules immobilized on the waveguides surface as shown in Figure 2.17. The refractive index (RI) value of most biological molecules (proteins, DNAs, etc.) are around 1.45 which is larger than the aqueous solutions (about 1.31). The molecular binding could increase the refractive index in the evanescent field range of the waveguide mode locally with the graph show in Figure 2.18. This mode phase transitions lead to measurable microring resonance wavelength changes. It can be continuously monitored and shows information on analyte concentrations, molecules affinities, and biochemical kinetics reactions.

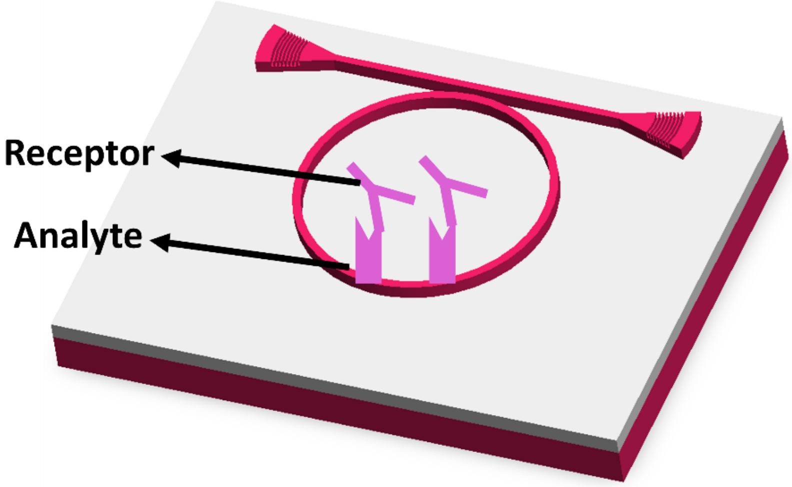

Fig.2.17 The microring resonator biochemical sensor working principle.

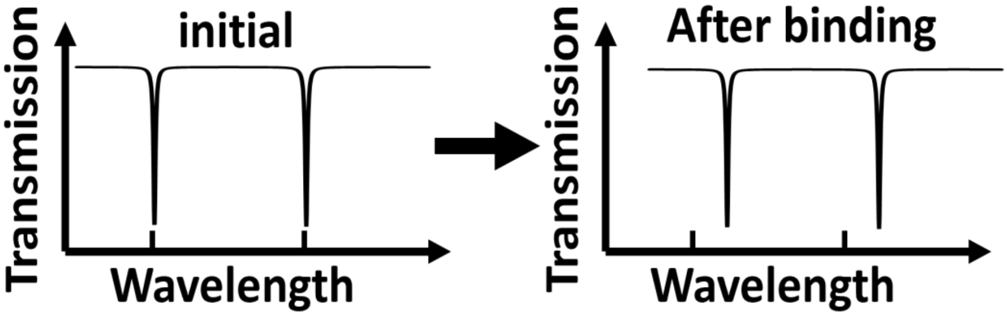

Fig.2.18 The wavelength shifts of the transmission spectrum when sensing.

2.5.1 Evanescent field

The evanescent field of the guided mode is the part extending in the cladding. It decays exponentially with distance from the core-cladding interface. The electric field in the cladding $|\vec{E}(d)|$ could be calculated as a function of d which is the distance from the interface, the formula is shown in]q. (25) [109]:

$$|\vec{E}(d)| = |\vec{E}(0)| \cdot \exp{(-\gamma d)} \tag{25}$$

The decay constant γ can be formulated as Eq. (26) [110]:

$$\gamma = \frac{2\pi}{\lambda}\sqrt{n_{eff}^2 - n_w^2} \qquad (26)$$

where n_{eff} is the effective refractive index of the waveguide mode and n_w is the refractive index of the analyte solution cladding. From the formula, it could be indicated that larger refractive index contrast leads to a faster decay.

The fundamental quasi-TE mode of the basic strip waveguide structure (cross section waveguide dimension 500 nm × 220 nm) is simulated with the decay constant as 8.3 /µm with water as cladding layer material. The electric field energy density distribution is shown in Figure. 2.16. This silicon wire waveguide structure field decays exponentially with the distance from the waveguide surface with a penetration depth of only a few tens of nanometres. This mode is therefore highly selective for refractive index changes occurring tens of nanometres from the waveguide surface, making it very selective towards refractive index changes caused by molecular binding near that surface. This is a large asset for photonics biosensors because the structure decreases the interaction with refractive index changes in the analyte away from the surface, and therefore enhances the signal-to-noise ratio. Even though the evanescent field is distributed ununiformly over the waveguide surface as shown in Figure 2.19, the effect for sensing is negligible when the working condition is far enough from single-molecule detection limits.

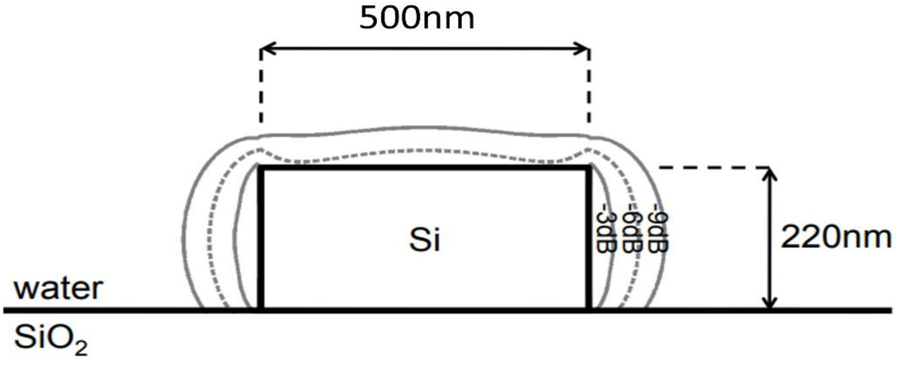

Fig.2.19 The energy density of the evanescent electric field of the quasi-TE mode of basic silicon wire waveguide structure [95].

2.5.2 Resonance wavelength interrogation

As mentioned in section 1.1.2 before, the two widely used typical interrogation methods for MRR biochemical sensing structures are intensity and wavelength interrogation. The intensity interrogation method always suffers from narrow detection range and unstable accuracy problems. Therefore, the wavelength interrogation approach has become popular and widely applied. It meets the large detection range and easy identification requirements in sensing. The analyte or binding biological molecule solutions, such as proteins and DNAs, serve as a cladding layer on the sensor, leading to a localized increase in the refractive index within the evanescent field range of the waveguide. This leads to the waveguide modes transitions and measurable microring resonance wavelength changes. The shift of resonance wavelength could be continuously monitored with information about analyte concentrations, molecules affinities, and biochemical kinetics reaction.

The shift of the resonance wavelength λ_{res} caused by the resonant mode effective index change n_{eff} could be described as [95],

$$\Delta\lambda = \frac{\Delta n_{eff} L}{m}, m = 1,2,3 \ldots \tag{27}$$

where m is the resonant mode order. n_{eff} represents the effective index of the resonant mode, which is subject to variation based on the refractive index of the cladding layer, a parameter that may change depending on the specific sensing conditions. The waveguide dispersion loss could be ignored because of the large index contrast of SOI wafer. The change in n_{eff} will alter λ_{res} and will back influence n_{eff} because of the non-zero slope of $\frac{\partial n_{eff}}{\partial \lambda}$. The compact formula for the resonance wavelength shifts with first order dispersion at $\lambda = \lambda_{res}$,

$$\boldsymbol{\Delta\lambda} = \frac{\boldsymbol{\Delta_{env} n_{eff} \cdot \lambda_{res}}}{\boldsymbol{n_g}}, \tag{28}$$

where $\Delta_{env}n_{eff}$ is the effective index shift when the environment background change, with value as $\Delta_{env}n_{eff} = \left(\frac{\partial n_{eff}}{\partial n_{env}}\right)_{\lambda_{res,n_{env}^{0}}} \Delta n_{env}$. The waveguides variational theorem shows $\Delta_{env}n_{eff}$ caused by the local change of dielectric constant $\Delta\epsilon(x,y)$, this could be expressed as [110],

$$\Delta_{env}n_{eff} = c\int \Delta\epsilon E_v \cdot E_v^{*}dxdy, \tag{29}$$

where $E_v(x,y)$ is the normalized modal electric field vector microring resonator waveguide mode.

The sensor response is proportional to the square of the magnitude of the electric field at the time of the perturbation, and therefore proportional to the proportion of the total modal power contained in the volume of the surface where the permittivity changes. This fraction can be increased by reducing the waveguide core size to delocalize the waveguide modes or by expanding the waveguide modes, thereby increasing the interaction with the surrounding cladding material. In the case of surface layer sensing, it is advantageous if the electric field decays quickly near the surface, since a relatively large part of the field will be located where the layer forms. Therefore, the sensitivity of the adsorbed layer increases with increasing refractive index contrast. The sensitivity of n_{eff} of slab waveguides to environmental changes was rigorously derived by Tiefenthaler in [111].

2.5.3 Optical biomolecular sensing model

The change in the refractive index will happen when there is a biomolecular interaction between the complementary analyte molecules (previously deposited on the waveguide surface) and receptor molecules, this will induce a variation in the optical properties of the guided light in the evanescent field. The interaction between the biomolecular layer and waveguide surface is shown in Figure 2.20. The biomolecular layer performed in the simulation is optically modelled as a uniform layer with variation thickness t_L with certain refractive index n_L. The refractive index of the layer is between the index value of dry molecules and index value of the analyte solvent. N_L relates to the molecular density in the layer $\boldsymbol{\rho}_L$ [g/cm3] as [112], the optical model of waveguide and biomolecular layer interaction is shown in Figure 2.20:

$$\rho_L = \rho_{protein} \frac{n_L - n_B}{n_{protein} - n_B} \tag{30}$$

n_B is the refractive index of the bulk cover medium (mostly buffer and solvent). $\rho_{protein}$ is the dry proteins density ($\mathrm{g/cm^3}$), this formula mainly focuses on proteins but suitable for DNA or other molecules. We use a literature density of dry proteins $\rho_{protein}$ which is 1.33 $\mathrm{g/cm^3}$ [113]. The refractive index of the dry molecules $n_{protein}$ is used as 1.45 and 1.48 as reported in [114].

The mass of the layer M_L ($\mathrm{g/cm^3}$) can be calculated with information on the thickness and the index of the layer based on using formula (30),

$$M_L = t_L \rho_L \tag{31}$$

Several researchers have quantified the molecular layers density, the combinatorial techniques are used mostly. 1) In some research, molecular layers are 66hermos66 as fixed-height adsorbed layers whose refractive index varies linearly from bulk solution refractive index to saturation refractive index of monolayer [114]. 2) Also, the refractive index of the adsorbed layer can be assumed to be fixed typically at n = 1.45, and the measured output relates to the effective thickness [115]. Ultimately, both methods are approximations and require calibration using ostensibly known biomolecule concentrations. Accurate information about the conformational situation of the protein in this layer can only be obtained using a combination of techniques or using a system that can resolve n_L and t_L independently. We will perform a theoretical system characterization using a model with a fixed layer refractive index n_L = 1.45.

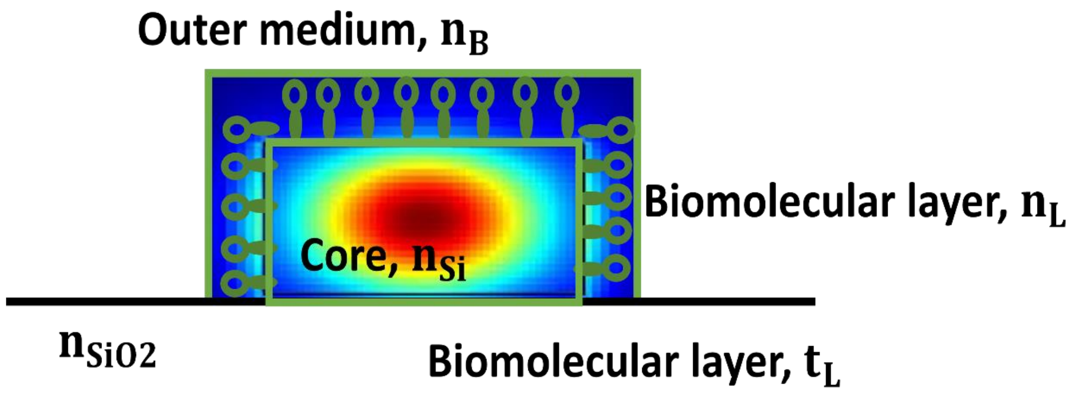

Fig.2.20 Optical model interaction with the biomolecular layer on the waveguide surface [95].

2.6 Sensitivities

Some performance parameters are used to assess the performance of the different MRR structures we designed and fabricated for biochemical sensing. We will introduce parameters refractive index (RI) sensitivity, concentration sensitivity, surface sensitivity, and the related limit of detection (LOD) values definition values. In the following chapters, these parameters will be used for performance evaluation for the MRR photonic biochemical sensor performance.

2.6.1 Refractive index (RI) sensitivity

The effective refractive index of the waveguide mode changes as the refractive index of the cladding layer changes within its evanescent field range. It can be described in follows based on [116]:

$$\Delta n_{eff} \propto n_g \cdot \frac{\iint_{-\infty}^{\infty} n(x,y)\cdot\Delta n(x,y)\cdot\left|\vec{E}(x,y)\right|^2 dxdy}{\iint_{-\infty}^{\infty} n^2(x,y)\cdot\left|\vec{E}(x,y)\right|^2 dxdy} \tag{32}$$

where Δn_{eff} is the effective refractive index change and n_g is the mode group index, $n(x,y)$ is the refractive index profile of the waveguide, $\Delta n(x,y)$ is the change of the waveguide refractive index profile, and $\vec{E}(x, y)$ is the electric field phasor. This formula indicates that the change in effective refractive index due to a change in refractive index is proportional to the product of the factor (n_g) associated with temporal confinement and the factor associated with spatial confinement of the electric field energy density. It should be noted that the latter is different from the power confinement in high-index-contrast material systems like silicon-on-insulator because the electric and magnetic field distributions are not proportional. This is due to the large electric field discontinuities at the waveguide interfaces.

The resonance wavelength of a ring resonator mode will shift when Its effective refractive index changes:

$$\Delta\lambda = \frac{\lambda \cdot \Delta n_{eff}}{n_g} \tag{33}$$

When a molecule of volume V_{mol} and refractive index n_{mol} binds at the waveguide surface location (x, y) in the watery top cladding environment with refractive index n_w, the resonance wavelength shift could be described as,

$$\Delta\lambda(x, y) \propto \frac{\left|\vec{E}(x,y)\right|^2}{\iint_{-\infty}^{\infty} n^2(x,y) \cdot \left|\vec{E}(x,y)\right|^2 dxdy} \tag{34}$$

assuming the molecule is small enough to ignore electric field variations over its volume. A large temporal confinement with large n_g value could directly increase the light-matter interaction but has no direct impact on the sensor sensitivity. Thus, slowing down light transmission has no direct improvement it could only have an impact through a change of the spatial mode profile.

The sensitivity could improve from the large field enhancement at the waveguide surface because of the large refractive index contrast. The normal component of the electric displacement field must be continuous at the dielectric interface, so the value of the normal component of the electric field on the cladding side of the core-cladding interface is enhanced by a factor $n_{core}^2/n_{cladding}^2$ compared to its value at the core-side. For the high-index-contrast interface between silicon (3.47) and water (1.31) in the sensing condition, this corresponds to a sevenfold enhancement of the electric field component normal to the waveguide surface. The main electric field component of the quasi-TE mode of a line waveguide is perpendicular to the waveguide sidewalls, so the main field discontinuities occur there. Although the horizontal limit of the waveguide is lower than its vertical limit (cross section waveguide dimension 500 nm × 220 nm), its quasi-TE mode is on average twice higher as sensitive to refractive index changes at sidewalls than the top surface (Fig. 2.2. The sensitivity to increase upon decreasing waveguide core width.

For comparative purposes, the universal RI sensitivity (S_V) can be written as:

$$S_V = \Delta\lambda_{res}/\Delta n \tag{35}$$

where Δn is the RI variation of the aqueous solution. This sensitivity, with the unit of nm/RIU, means the resonant wavelength shift induced by unit change in the RI.

2.6.2 Concentration sensitivity

The other parameter is concentration sensitivity S_c, also important for MRR biochemical sensor performance determination in this research. The different concentrations of sodium chloride and glucose solutions are utilized for sensitivity measurement. The concentration sensitivity [28] of the optical sensor can be defined as:

$$S_c = \Delta\lambda_{res}/\Delta C \tag{36}$$

where ΔC and $\Delta\lambda_{res}$ are the variations in the sample (gas or liquid) concentration and resonant wavelength, respectively. This concentration sensitivity means the resonant wavelength shift induced by 1% mass concentration change.

2.6.3 Surface sensitivity

The wavelength shift when molecular interaction occurs on the waveguide surface can be simulated with the above optical model. The wavelength shift corresponding to the effective index change are simulated using Lumerical FDTD. The refractive index of different analyte as cladding layers near 1550 nm wavelength light are detailed in the following chapter 3 (RI value range from 1.31 to 1.48). The sensor response is linear for layer thicknesses up to 40 nm. This thickness far exceeds the thickness of the molecular layer and does not constitute a limitation. In fact, reducing the waveguide core size will enlarge the waveguide modes, thereby increasing interaction with the surrounding cladding material and increasing sensitivity. However, as the mode expands further in a water base analyte environment, propagation losses due to water absorption will increase. The resulting reduction in Q-factor may reduce the minimum detectable wavelength shift and ultimately the overall detection limit of the system. In this research, we mainly focus on achieving high sensitivity in optimal single TE mode configuration.

The surface RI sensitivity (S_s) is a measure of the wavelength shift per unit change in refractive index within the first few tens of nanometres (adlayer thickness) above the waveguide and is important in biosensing applications [117]:

$$S_s = \frac{\Delta\lambda_{res}}{\Delta t_{ad}} = \frac{\lambda_{res}}{n_g}\left(\frac{\partial n_{eff}}{\partial t_{ad}}\right) \tag{37}$$

where ng is the group index, t_{ad} is the uniform thickness of the adsorbed molecule layer with refractive index n_{ad}. For most proteins, the refractive index is about n_{ad} = 1.48 [117].

2.7 Limit of detection (LOD)

When the biochemical sensor (using RI interrogation method) contact with an analyte sample, the resonance condition for the device changes when the refractive index of the cladding layer analyte changes, and the resonant mode sifts to a new wavelength as a result. The sensitivity of the device is the magnitude of the wavelength shift divided by the change in RI. It could be calculated as the slope of the generated trend for several changes in RI. The unit of sensitivity is given in nm/RIU.

However, the magnitude of the spectral shift (i.e., sensitivity) does not fully describe the devic''s ability to detect and quantify sample. The ability to accurately measure the spectral shifts produced by the sample is also important. Thus, we bring into the concept of sensor resolution which characterizes the smallest possible spectral shift that can be accurately measured. As discussed as follows, this term takes into account the spectral resolution of the system and a number of noise parameters. Sensitivity (S) and sensor resolutionI) together form the device's detection limit (DL) [119]:

$$DL = \frac{R}{S} \tag{38}$$

The DL value reports the smallest sample RI change that can be accurately measured for refractive sensing, it describes the minimum amount of analyte that can be accurately quantified by the RI sensor for biomolecule sensing.

Due to the method of measuring the spectral shift of the response sample, the spectral resolution and system noise factor are incorporated into the DL. In most resonance-based RI sensors, the resonance mode has a Lorentz spectral profile. A simple way to monitor spectral shifts is to track the locations of extreme values (i.e., minimum or maximum, depending on the measurement configuration). The total sensor response is the spectral difference between the final extreme and the initial extreme. If infinitely high spectral resolution is available and absolutely zero system noise is available, sensor performance can be characterized by sensitivity alone. However, spectral resolution and system noise reduce the precision and accuracy from which the true centre of the resonant mode can be located. Minimal error in determining the actual mode spectral position results in limited sensor resolution and subsequent need for sensor DL.

There are two types of noise that can cause errors in determining the location of resonant modes: amplitude changes and spectral changes. Amplitude noise refers to the cumulative noise added to the spectral pattern profile. Noise sources include thermal and shot noise in the photodetector, laser relative intensity noise, and quantization error. In a typical system, extreme values are quickly and automatically located by the system processor (e.g., a computer). Due to the added amplitude noise, the actual extremum is unlikely to be located exactly at the centre frequency of the Lorentzian shape. Therefore, amplitude noise processes lead to random spectral deviations in the measured spectral positions of the resonant modes.

It is important to analyse the stochastic process of this deviation and its dependence on the noise amplitude and mode linewidth. Although noise processes can be well characterized by normalized statistical distributions, extreme value operations prevent a direct analytical solution to the statistical distribution of the resulting spectral changes at actual extreme values. However, the system can be studied numerically using Monte Carlo simulation. Here, we use this technique to determine the statistical variance of the extrema of a Lorentz-shaped pattern when a random noise signal is added to the amplitude of the pattern. For simplicity, we plot each amplitude noise data point from a white Gaussian distribution (actually, shot noise is generated by a Poisson process). It shows that a high-quality factor is beneficial to reducing the spectral noise of the sensor. This phenomenon can be explained by the fact that the noise signal causes a finite probability that samples within the optical bandwidth of the resonant mode are identified as extrema. Resonant modes with narrower linewidths filter spectral noise more effectively, thereby reducing spectral deviations from the actual centre of the mode. Therefore, the Q factor plays an important role in the DL of the sensor.

Although an analytical solution for the statistical variance of the position of the mode amplitude maximum is not available, the Monte Carlo simulation results provide an opportunity to approximate the relationship between Q-factor, SNR, and spectral variation of the mode maximum. It is revealed that a linear dependence of standard deviation on linewidth and an exponential relationship with SNR. It is found that within the parameter range considered here, the numerical results can be approximated as [119]:

$$\sigma \approx \frac{\Delta\lambda}{4.5(SNR^{0.25})} \tag{39}$$

where σ is the standard deviation of the resulting spectral variation and $\Delta\lambda$ is the full-width-half-max of the mode amplitude and the Q-factor relates to these values is calculated by $Q = \lambda/\Delta\lambda$ (SNR is in linear units). This equation is generally applicable to any RI sensor technology in which the measured extremum value is used to identify the spectral location of the resonant mode.

In addition to amplitude noise, there are some spectral noise factors that also affect changes in the spectral position of the resonant mode, thereby affecting sensor resolution. The first is the thermal change of the system. All RI sensors are susceptible to thermally induced fluctuations because the sensor material and sample have non-z73hermosermo-optical and thermal expansion coefficients. Therefore, slight changes in temperature lead to changes in the RI of the material and sample, causes a shift in the spectral position of the resonant mode. This results in another source of noise creating errors in determining the spectral shift produced by the analyte.

The spectral resolution of the system setup may also limit the accuracy with which resonant mode locations can be identified. Depending on the measurement setup, laser or optical detection mechanisms may limit resolution. In the common setup for very narrow resonant mode linewidth RI sensors, the laser is tuned over a very small spectral range (on the pm order) while a photodetector measures the amplitude of the system output. The processing unit in this device is expected to be able to sample the photodetector voltage at a very high rate compared to the laser tuning speed. The limitation in this case is due to the linewidth of the laser, which is typically less than 1 MHz (equivalent to 8 fm at 1550 nm).

In the common setup for relatively large resonant mode linewidth RI sensors, a broadband optical source (like SLD) and an optical spectrum analyser (OSA) or spectrometer are used to record the resonant mode. In this circumstance, it is clear that the spectral resolution of the detection device provides the limitation may be on the 1 pm order. The resulting error due to spectral limitations of the detection device can be modelled as quantization error. As an example, for a device with a spectral resolution of 1 pm, the error in determining the position of the resonant mode is uniformly distributed from -0.5 pm to 0.5 pm, and has a resulting standard deviation of σ is 0.29 pm.

Once the statistical properties of all noise sources are known, sensor resolution can be determined. Here we use the typical convention of determining resolution as 3σ of the noise in the system. The total system noise variance can be approximated by summing all individual noise variances.

The limit of detection (LOD) is another widely used parameter to evaluate the sensing capability of a device, and is defined as the resonance wavelength resolution 3σ divided by the sensitivity (S_c or S_v), where σ is the standard deviation of the resulting spectral variation and can be calculated using the method in [119]:

$$LOD = 3\sigma / S_C \text{ or } LOD = 3\sigma / S_V \tag{40}$$

Chapter 3 Measurement system

This chapter aimed to provide detailed information about the measurement system we built according to the project for photonics biochemical sensors (using grating couplers for light coupling into and out of the chip) transmission spectrum measurement. The detailed information about the measurement setup, including the 6-axis adjustment platform, the monitoring system, the light source, the detector device, and the automated measurement system using LabVIEW software based on the general-purpose interface bus (GPIB). Also, some basic information related to biochemical sensing like RI values for different concentrations of sodium chloride and glucose, biochemical surface binding, and microfluidics are introduced in this chapter.

3.1 Setup

In this section, the setup for the photonics sensors measurement in our photonic integrated circuit group lab is shown in detail and in pictures. This setup contains the 6-axis adjustment platform, the monitoring system, the light source, the detector device, and the automated measurement system using LabVIEW software based on the general-purpose interface bus (GPIB). This measurement setup is constructed mainly focus on the photonic biochemical sensors utilising grating couplers structures to couple the light between the chips and fibres from the light source. But with the 6-axis adjustment stage and the angle adjustment stage for fibre-coupler alignment, this stage could be used in many other sensors or lasers measurement. Thus, a versatile measurement system was built in this PhD research project.

3.1.1 Light sources and detectors

As mentioned in section 2.7 before, In the common setup for relatively large resonant mode linewidth photonics refractive index sensors, a broadband optical source (like SLD) and an optical spectrum analyser (OSA) or spectrometer are used to record the resonant mode and the spectrum. Therefore, in our measurement setup, we decided to use the broadband light source as the light source in our photonic sensor’s spectrum measurement, which is a Super Luminescent Diode (SLD, THORLABS S5FC1005P – PM Benchtop SLD Source). This broadband light source we use for spectral response measurement has a central wavelength at 1550 nm, the maximum output power is 22 mW and the 3 dB bandwidth is 50 nm. The optical transmission spectrum detection is using an optical spectrum analyser (OSA) with a resolution bandwidth of 0.06 nm through output single mode fibre (SMF). The detailed pictures for the SLD and OSA devices are shown in Figure 3.1(a) and Figure 3.1(b) below.

Here we need to include a small discussion of different light sourcees into consideration. They are 1. LD (Laser Diode): A laser diode is a semiconductor device that emits coherent light when an electric current is applied to it. Laser diodes are commonly used in various applications, including optical communication, barcode readers, laser pointers, and more. They are known for their efficiency and precision. 2. SLD (Superluminescent Diode): Similar to a laser diode, a superluminescent diode is a semiconductor device that emits broad-spectrum light, but unlike lasers, it doesn't exhibit full coherence. SLDs are often used in applications where a combination of high brightness and broad spectral width is required, such as in optical coherence tomography (OCT) systems used in medical imaging. 3. LED (Light-Emitting Diode): An LED is another type of semiconductor device that emits light when an electric current passes through it. Unlike laser diodes, LEDs emit incoherent light over a broad spectrum. LEDs are commonly used for lighting applications, display backlighting, indicators, and various other lighting purposes. In summary, LD and SLD are both types of diodes that emit light, with laser diodes having coherent light emission and superluminescent diodes emitting broad-spectrum light with reduced coherence, thus could be used as the light source for MRR transmission spectrum measurement. LEDs, on the other hand, emit incoherent light over a broad spectrum and find widespread use in lighting and display applications.

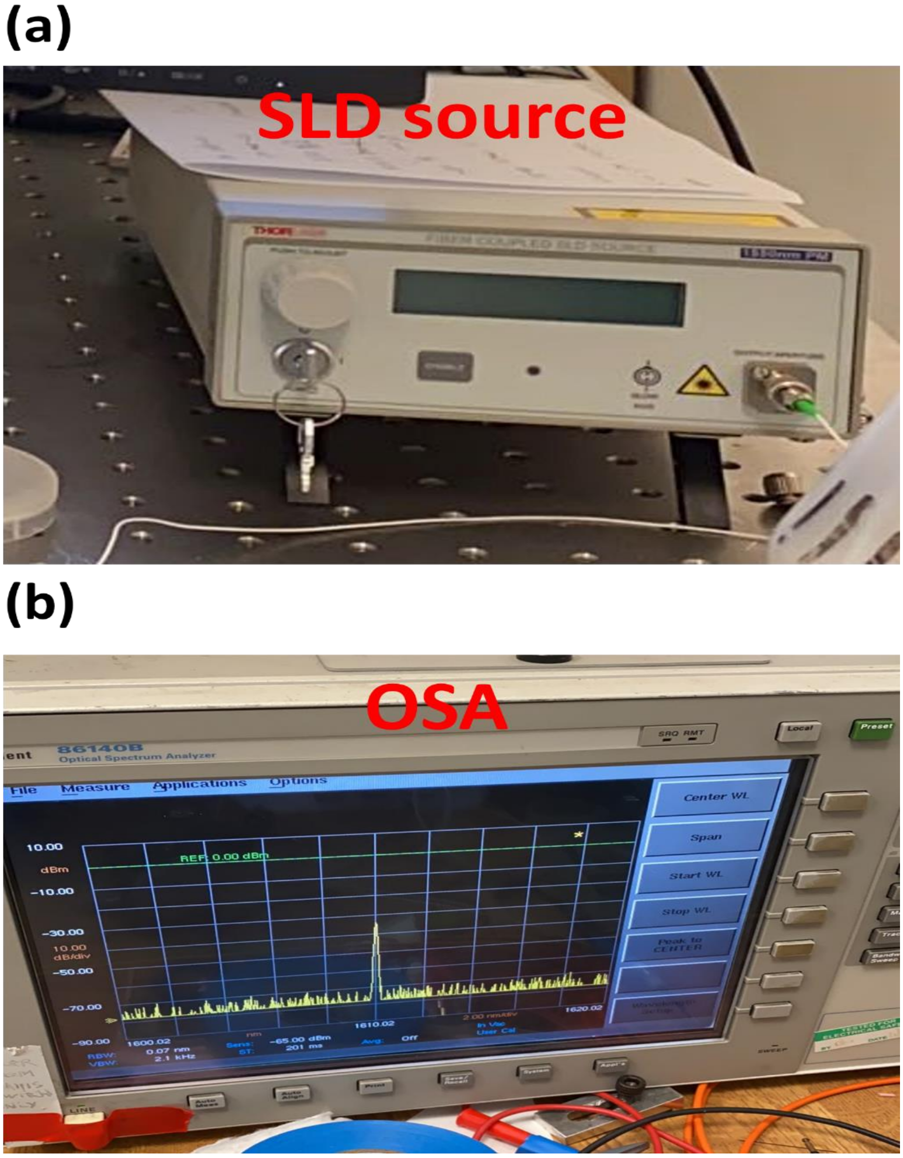

Fig.3.1 The photos of (a) the Super Luminescent Diode (SLD) broadband light source, and (b) the optical spectrum analyzer (OSA) for the measurement system.

3.1.2 Measurement setups

The measurement setups are designed and constructed based on the coupling angle and position for coupling between fibres and grating couplers. The fibre-based setup generally consists of two single-mode fibres which are aligned to the grating couplers to transfer the input and output optical signal between light sources and sensing devices. From Figure 3.2 illustration it is clear that only one pair of grating couplers can be addressed at the time. Therefore, the achievable multiplexing is limited. The output fibre can guide the signal to the bus waveguide, which couples the light to multiple ring resonators. To determine the maximum number of MRRs that could achieve in one cascaded microring sensors array, the free spectral range (FSR) and the separated distance of their resonances to avoid spectral overlap and achieve shifting upon molecular detection should be considered. Post-processing involves separating individual signals from the common port signal, fitting a Lorentzian to each resonance spectrum, storing the resonance wavelengths, and tracking the resonance wavelengths of all signals over time. When measuring a ring resonator sensor array simultaneously, light from multiple output gratings must be detected in parallel. One possible mechanism is the arrangement of fibre arrays. However, the outer diameter of the single-mode fibre cladding is about 125 μm, so the gratings need to be spaced at least this distance apart. This is a space-consuming and fragile solution. If fine packaging is used, multiple optical fibres can be packaged together with the chip. However, the fibre then becomes part of the disposable product, which increases its cost unacceptably. The constructed measurement stage in our photonic integrated circuit group lab is shown in Figure 3.3. It consists of the 6-axis adjustment stage and the angle adjustment stage to achieve high precision fibre alignment and improve the coupling efficiency of light coupling between fibres and grating couplers in the measurement.

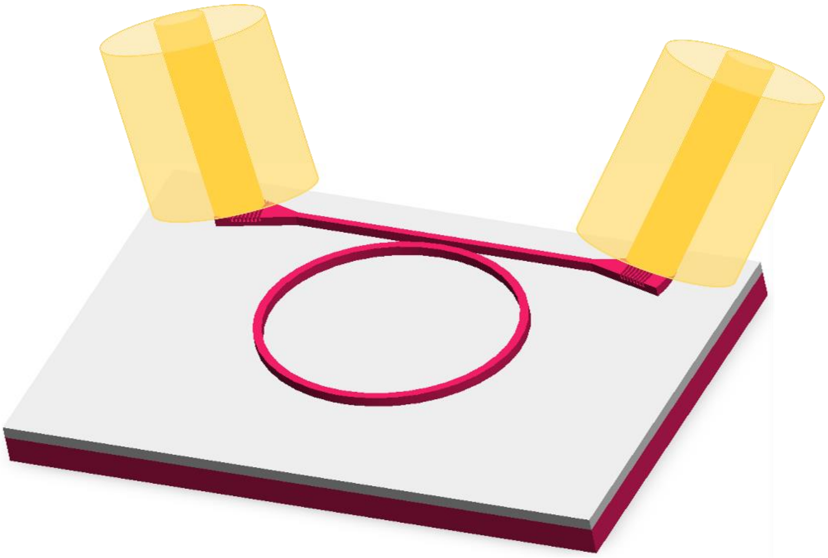

Fig.3.2 Setup with Fibre and Grating Coupler.

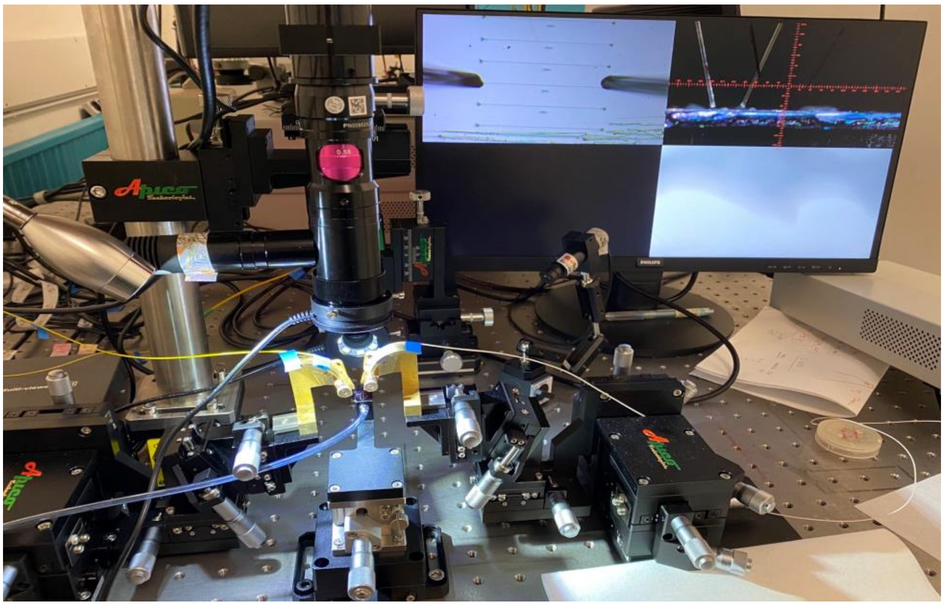

Fig.3.3 Optical biochemical sensor measurements setup in our laboratory.

The second option for simultaneous multiple output signals measurement is to use a camera-based measurement setup to monitor the light from the grating coupler by imaging the output light from the grating coupler with an infrared (IR) camera: one input light signal grating coupler is addressed with a single-mode fibre and the output light signal is captured from the outcoupling gratings with an IR camera. As in the reference, the InGaAs camera was mounted on the microscope with an operation wavelength from 0.9 to 1.7 µm range, has 320 × 256 pixels with a pixel pitch of 30 µm, and captures a frame rate of 60 Hz. Exposure time can be set from 1 µs to 400 s. To image a 15 × 20 µm output grating on approximately 5 × 5 pixels, with the magnification set to 15x [95]. The linear pixel array was used to reduce system cost while maintaining similar performance. The input light signal is coupled into the photonic integrated circuit through a single-mode optical fibre.

Here, we also need to mention the thermoelectric cooler (TEC) module is used for room temperature control as a fixed factor in our sensor performance measurement. But we should discuss the thermal optic effect in silicon photonics. The thermal optic effect in silicon refers to the phenomenon where the refractive index of silicon undergoes changes in response to variations in temperature. Silicon, being a semiconductor material commonly used in electronic and photonic devices, exhibits a temperature-dependent refractive index. As the temperature of silicon increases, its lattice structure experiences thermal expansion, leading to changes in the density of the material. This, in turn, affects the speed of light passing through silicon, influencing its refractive index. The thermal optic effect is particularly relevant in the design and performance of devices such as integrated circuits, sensors, and optical components, where precise control and understanding of the optical properties of silicon are crucial for their proper functioning.

The thermo-optic effect is quantified by the thermo-optic coefficient or thermo-optic factor, which represents how much the refractive index of silicon changes with temperature. The thermo-optic coefficient (dn/dT) is defined as the rate of change of refractive index (n) with respect to temperature (T). For silicon, this coefficient is typically negative, indicating that as the temperature increases, the refractive index decreases. The specific value of the thermo-optic coefficient for silicon can vary depending on factors such as the wavelength of light and the temperature range of interest. Typically, for silicon at room temperature, the thermo-optic coefficient is in the range of approximately -1.8×10^{-4} per degree Celsius (°C) for the telecom wavelength range (around 1550 nm).

It's important to note that these values can be wavelength-dependent, and for precise applications or specific temperature ranges, more accurate coefficients may be used. Researchers and engineers working with silicon-based photonic devices often consider these factors to account for the thermal effects on the optical properties of silicon in their designs.

3.1.3 Noise

In addition to wavelength resolution, alignment tolerance and degree of multiplexing, noise is also an important characteristic of sensing device measurement. The limit of detection is defined by the ratio of measurement resolution and sensitivity (as mentioned in Chapter 2). If infinitesimal resonance widths can be used and there is absolutely zero system noise, sensor performance can be characterized by sensitivity alone. However, in measurement, the resonant resolution and system noise could reduce the accuracy of true resonant wavelength location. The intensity changes and spectral changes are the two types of noise that could cause errors in determining the resonant modes' locations. Intensity noise is the cumulative noise added to the spectral transmission characteristics.

Noise sources include thermal and shot noise in the photodetector, laser relative intensity noise, quantization errors, and possible fibre-to-chip coupling variations. In addition to intensity noise, there are also spectral noise factors that also affect the change in the spectral position of the resonant mode, thereby affecting the measurement resolution. The first is the thermal change of the system. Also, the spectral resolution is limited by the wavelength accuracy of the laser or optical detection mechanism. Since the Q-factor of the SOI microring resonator is relatively low (around 10^4 magnitude), the effect of noise on the limit of detection is dominated by the intensity noise. In the case of high-Q sensors (10^7 magnitude), spectral noise becomes the limiting factor, and controlling temperature- and laser-induced spectral fluctuations is key to high limit of detection values.

3.1.4 Connection and control

As mentioned in the sections before, in our measurement setup, we use a super luminescent diode as broadband light source. The input and output beams in TE mode were connected to the photonics sensors via a 10 µm core cleaved single mode fibre with 10° input and output angles through the grating couplers (GCs). An optical spectrum analyser (OSA) with a resolution bandwidth of 0.06 nm was connected to the output SMF to measure the transmission spectrum of the MRR sensors. To obtain measurement data swiftly, particularly important for fast evaporation solvents such as acetone, an automated measurement system using LabVIEW software based on the general-purpose interface bus (GPIB) connection was employed. For transmission spectrums measurement and sensitivity calculation, different concentrations of solutions or analytes are dropped on the MRR sensing part as shown in Figure 3.4.

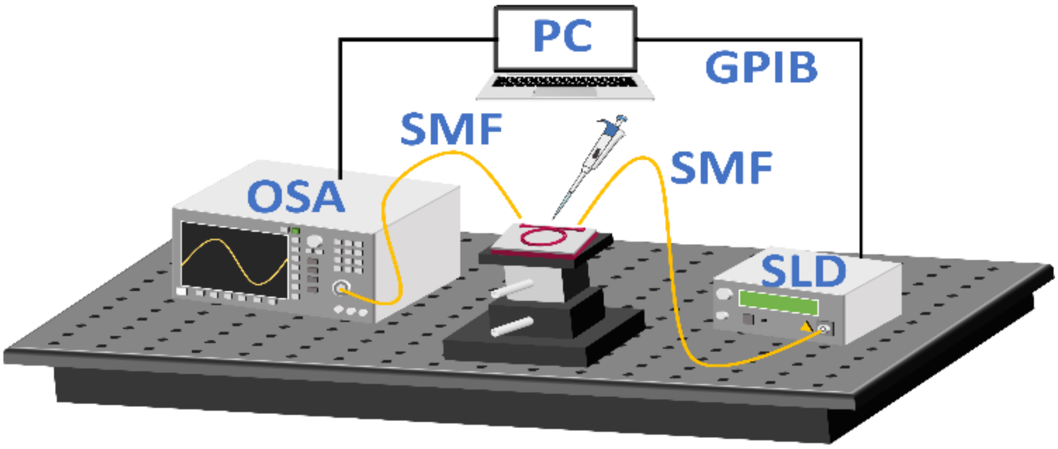

Fig.3.4 Schematic of the measurement setup.

3.2 Refractive index of analytical solution

It could be difficult to acquire reliable refractive indices of typical organic solvents in the near-infrared spectrum region. These RI values are often needed to calibrate new refractive index sensors in areas such as environmental monitoring, food security, environmental monitoring, and chemical detection. Especially for fibre optic refractive index sensors and micro photonic sensors on silicon-on-insulator platform, these devices typically operate in the C-band region of the telecommunications spectrum with wavelength range from 1530 nm to 1565 nm. Both silica fibres and silicon waveguides structures have relatively low attenuation in this wavelength range. The refractive index of the different concentrations of analyte solutions (glucose and sodium chloride) we used for our sensor performance measurement is analysed and calculated based on the references recording the refractive indices of common solvents and solutions at 1550 nm [120-121]. The refractive indices of the common analyte with different concentration are modelled using third order polynomial fits based on the measurement results. It produces a solution of any RI value in 1.3164 to 1.46 range. We used these values for refractive index determination in our simulation and measurement, also for the sensitivity calculation.

3.2.1 RI of different concentration of glucose solution

The D-glucose ($C_6H_{12}O_6$) solutions are used to demonstrate the bulk sensing characteristics of the designed MRR biochemical sensor. The concentration changes (mass%) of glucose results in the RI changes are calculated using a third-order polynomial fit as [120-121]:

$$n = Aw^3 + Bw^2 + Cw + D \tag{41}$$

where *w* is the weight fraction, *A*, *B*, *C* and *D* are the parameters of a polynomial fit, with the values for glucose and sodium chloride solutions listed in Table 3.1.

Table 3.1 Parameters for refractive indexes of glucose solutions

	Glucose
w	0-0.80
A	0.0330
B	0.0456
C	0.1416
D	1.3166

3.2.2 RI of different concentrations of sodium chloride solution

The sodium chloride (NaCl) solutions are used to demonstrate the bulk sensing characteristics of the designed MRR biochemical sensor. The concentration changes (mass%) of sodium chloride results in the RI changes are calculated using a third-order polynomial fit as [120-121]:

$$n = Aw^3 + Bw^2 + Cw + D \tag{42}$$

where *w* is the weight fraction, *A*, *B*, *C* and *D* are the parameters of a polynomial fit, with the values for glucose and sodium chloride solutions listed in Table 3.2.

Table 3.2 Parameters for refractive indexes of sodium chloride solution

	NaCl
w	0-0.25
A	-0.0800
B	0.0740
C	0.1620
D	1.3162

3.3 Biochemical surface binding

To determine the biochemical sensing performance for these photonics sensors (like surface sensitivity), bioreceptor layers on the microring resonator sensor waveguide surface selectively bind analyte molecules in complex fluids, and their mass critically determines the sensor's performance. To obtain large sensitivity, a large affinity for the analyte should be exhibited while maintaining a very low affinity for the other molecules in the solutions to limit unspecified interactions and the resulting false positive results. Also, the bioreceptor layers need to be stable, uniform, and thin (normally a few nanometres). The method to modify the silicon waveguide surfaces biochemically has been presented and reported by multiple groups, like multiplexed label-free quantification of proteins, DNA, and RNA [122-124]. These surface modification methods can be directly applied to the microring resonator biochemical sensors presented in this thesis. Thus, no new methods are developed here. The remainder of this section briefly describes some widespread techniques to biochemically modify the surface of silicon waveguides.

The hydroxyl groups (-OH) of sil’con's natural oxides are ideal anchors for biochemical layers, and their formation can be facilitated by immersing the sensor in a sulfuric acid and hydrogen peroxide (piranha) mixture. Silane reagents are then assembled and covalently bound to the surface, providing a smooth surface with functional groups (such as carboxyl or amine groups) to which receptor molecules can attach. A common technique is to activate the surface with N-hydroxy succinimide (NHS) and couple the acceptor with 1-ethyl-3-[3-dimethylaminopropyl] carbodiimide hydrochloride (EDC). The outward-facing amine groups bind to the surface. Alternatively, receptors can be activated with NHS and then bound to surface functional groups using EDC. Although directly conjugating receptors to silanes is common, it often does not yield sufficiently specific sensors. Coating the silane with a hydrophilic polymer (e.g. polyethylene glycol) prior to coupling to the receptor could enhance specificity [125]. Multiple sensing requires independent surface modifications for individual sensors. This can be achieved with molecular printers such as Nano eNabler or Bioforce [126].

3.4 Microfluidics

The microfluidics channels refer to the handling of fluidic analyte less than millimetre size in length. This could be very challenging because the large surface area to volume ratio leads to the different relative importance of physical effects compared to macroscopic scales. The integration of functions such as pumping, mixing, filtration, cell lysis and polymerase chain reaction is being intensively studied and will provide on-chip sample preparation for advanced on-chip laboratories. Although these additional functionalities could greatly expand the microring resonator sensing applications, the basic operation like liquid delivery control to the sensing MRRs is adequate for reliable and repeatable measurement in this project. On-chip microchannels enable similar processing by laminar flow for all sensors. While they can efficiently transport molecules close to the sensor, the flow rate near the chip surface approaches zero, creating a layer of stagnant liquid of a few microns through which the molecules must diffuse. This limits mass transfer to the sensor. The diffusion in a micro channel determines the limit of detection per unit time. Particularly for low-affinity biochemical interaction mechanisms. This will result in a decreased limit of detection (LOD) value which will require a more advanced mass transport method. For industrial applications, these microfluidic channels are preferably manufactured using high-volume techniques like injection moulding. But in our research, we seek a more flexible approach for our device test instead of complex packaging. The popular microfluidic channel fabrication uses polydimethylsiloxane (PDMS) [127] and the chip package adapting the low-temperature stamp-and-stick method [128]. This method is compatible with biochemical surface modification prior to packaging. The channels are normally micrometre size high to limit the required liquid volume and are several hundred microns wide to achieve alignment tolerances. The layout of the microfluidic channels snakes over different columns of the sensor matrix to address all sensors. The analyte liquid was degassed by vacuum sonication before experiments to reduce the noise contribution of air bubbles and pushed into the channel using a Harvard syringe pump (typical flow rate of 5 µL/min).

Chapter 4 Inner-wall grating double slot microring resonator sensor

This chapter will introduce the novel microring resonator structure: inner-wall grating double slot microring resonator (IG-DSMRR) sensor working for biochemical sensors areas that could solve two current MRR sensors limitations, the sensitivity limitation, and the measurement range limitation. The sections below will detail the working principle, simulation results, fabrication procedures and results, measurement stage and results, and the conclusion about the sensor performance compared with the reported structures before.

We simulate and demonstrate experimentally an inner-wall grating double slot micro ring resonator (IG-DSMRR) with a centre slot ring radius of only 6.72 μm based on the silicon-on-insulator platform. This novel photonic-integrated sensor for optical label-free biochemical analysis boosts the measured refractive index (RI) sensitivity in glucose solutions to 563 nm/RIU with the limit of detection value being 3.7×10^{-6} RIU (refractive index units). The concentration sensitivity for sodium chloride solutions can reach 981 pm/%, with a minimum concentration detection limit of 0.02%. Using the combination of DSMRR and IG, the detection range is enlarged significantly to 72.62 nm, three times the free spectral range of conventional slot micro ring resonators. The measured Q-factor is 1.6×10^{4}, and the straight strip and double slot waveguide transmission losses are 0.9 dB/cm and 20.2 dB/cm, respectively. This IG-DSMRR combines the advantages of a micro ring resonator, slot waveguide, and angular grating and is highly desirable for biochemical sensing in liquids and gases offering an ultra-high sensitivity and ultra-large measurement range. This is the first report of a fabricated and measured double-slot micro ring resonator with an inner sidewall grating structure.

4.1 Working principle

The structure design was inspired by the reported angular grating microring resonator for label-free optical biochemical sensing [148]. This proposed structure design utilized the microring resonator structure with innerwall angular grating. The design principle is first demonstrating the wavelength selectivity, the fundamental modes effective indices of the microring waveguide with and without angular grating are calculated using the mode analysis. Then equivalent index of the angular grating is approximately by Rytov's formula. The bragg wavelength of this bragg angular gratings could be calculated using reflection condition. Meanwhile, the longitudinal modes of the MRR satisfy the resonant condition where the resonance wavelength of the longitudinal mode number can be selected. Based on the angular grating bragg wavelength and the microring resonant wavelength we could decide the final wavelength peak point and the grating and waveguide parameters.

This high sensitivity and large detection range IG-DSMRR sensor is designed based on the general SOI wafer structure. The SOI wafer epilayer and the three-dimensional (3D) schematic of the proposed IG-DSMRR sensing device are illustrated in Figure 4.1. The wafers were purchased through the University wafers company. The SOI wafer structure has a 220 nm top silicon layer and a 2 µm buried oxide (BOX) layer on a 675 µm thick silicon substrate.

The detailed design parameters of IG-DSMRR sensor are shown in Figure 4.2. The structure contains focused grating couplers at the end of the bus waveguide to couple the light between the sensor device to the cleaved single-mode fibre (SMF), and an optimize– "W" - shaped branched tapered coupler is used to couple light between the strip bus waveguide and the slot MRR waveguide. Also, this structure introduces more straight slot waveguide parts in the sensor which could increase the sensitivity and the sensor performance. The inner wall grating combines with the double slot MRR structure enables high-sensitivity sensing over a large detection range.

To achieve homogeneous sensing in the IG-DSMRR structure simulation and measurement, the IG-DSMRR part of the sensing device is immersed in the aqueous solution in both simulations and experiments. Pure water was selected as the top cladding in the process of determining the waveguide geometric parameters. This homogeneous sensing case can be easily extended to surface sensing applications for molecule detections in bioengineering by modelling the device with a thin adsorbed analyte on the top cladding.

The bend radI (R) of the IG-DSMRR sensor is the distance between the centre of the rings and the inner wall of the middle ring and is designed to be 6.72 µm. The gap width between the bus waveguide and the DSMRR is denoted as W_{gap} (200 nm) and the slots in DSMRR have the same slot width named W_{slot}. The strip waveguide width W_{strip} is 630 nm and the bus and ring width W and the slot width W_{slot} are designed as 210 nm and 100 nm respectively, which results in a high mode confinement factor and extremely strong electric field enhancement in the slots. The etched IG has an azimuthal period (*Λ*) of 1.199 µm and duty cycle, or filling factor (*FF*) (ratio of silicon block l_g to the period *Λ*) of 96%, and the corrugation depth of the grating H_g is 24 nm. The propagation of the optical fields in the bus and ring slots is shown in Figure 4.3. Here E_1^+, E_2^+, E_3^+ and E_4^+ represent the input and the output optical field amplitudes with respect to the ring coupling point in the double slots part of the bus waveguide and the double slots of the DSMRR, and E_1^- , E_2^- , E_3^- and E_4^- represent the reflected optical field amplitudes in the corresponding positions.

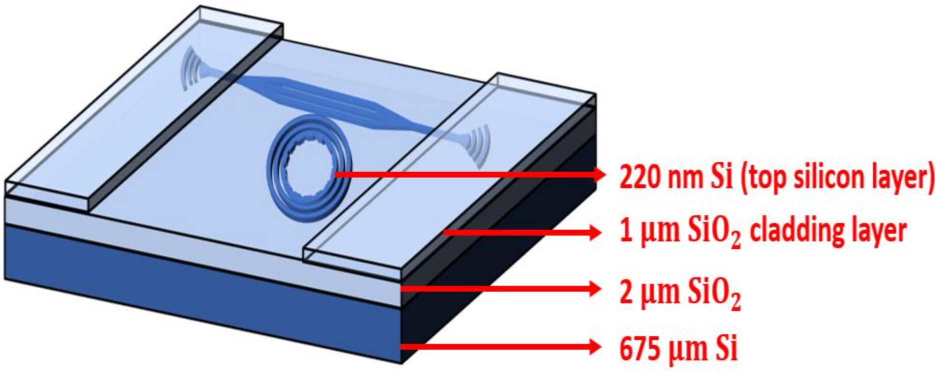

Fig.4.1 Schematic structure of the IG-DSMRR.

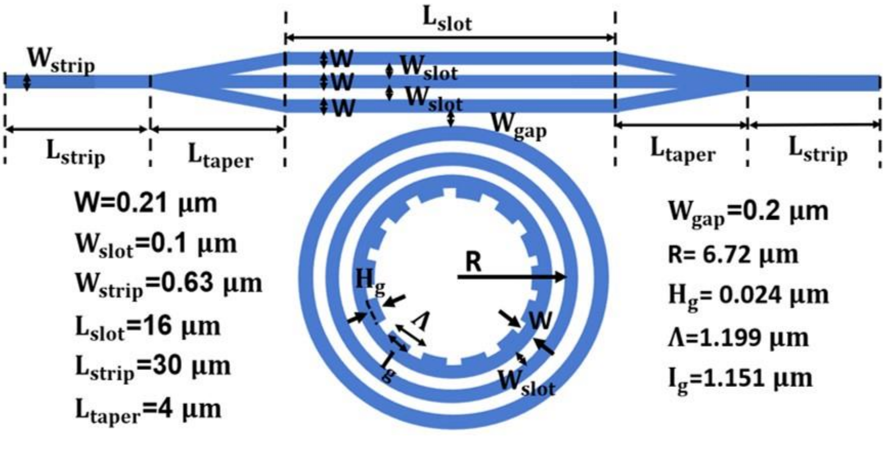

Fig.4.2 Design parameters of the IG-DSMRR structure.

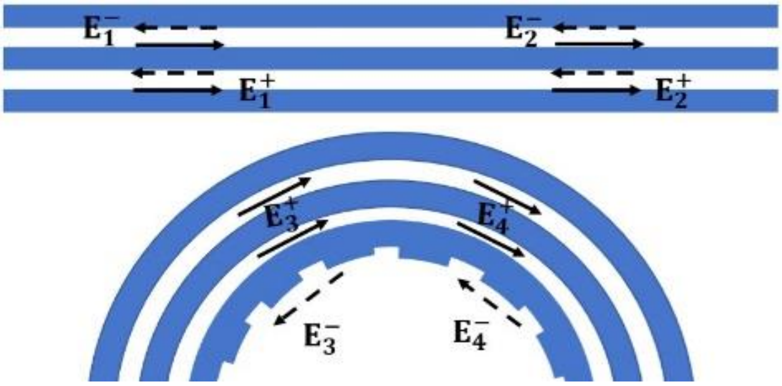

Fig.4.3 Propagating optical fields in the bus and bent double slots.

The resonance equation of the DSMRR can be expressed as:

$$Ln_{eff} = m\lambda_{res}, m = 1,2,3 \ldots \tag{43}$$

where $L = 2\pi R$ is the perimeter of the microring resonator, n_{eff} is the effective refractive index of the DSMRR waveguide, m (positive integer) is the azimuthal resonant order, and λ_{res} is the resonant wavelength.

The optical path is reversible because the input and output ports of the IG-DSMRR device are symmetric. The transmission matrix of incident and reflected optical fields between the bus waveguide and ring waveguide is expressed separately as:

$$\begin{pmatrix} E_2^+ \\ E_4^+ \end{pmatrix} = \begin{pmatrix} \tau & j\kappa \\ j\kappa & \tau \end{pmatrix} \begin{pmatrix} E_1^+ \\ E_3^+ \end{pmatrix} \tag{44}$$

$$\begin{pmatrix} E_1^- \\ E_3^- \end{pmatrix} = \begin{pmatrix} \tau & j\kappa \\ j\kappa & \tau \end{pmatrix} \begin{pmatrix} E_2^- \\ E_4^- \end{pmatrix} \tag{45}$$

where, κ and τ are the amplitude coupling and transmission coefficients. When coupling loss can be ignored, the relation between them is described as:

$$\kappa^2 + \tau^2 = 1 \tag{46}$$

The transmission matrix of the IG [129] is written as:

$$\begin{pmatrix} E_3^+ \\ E_4^- \end{pmatrix} = e^{-\alpha L} \cdot e^{j\beta L} \cdot S \begin{pmatrix} E_3^- \\ E_4^+ \end{pmatrix} = e^{-\alpha L} \cdot e^{j\beta L} \cdot \begin{pmatrix} -jre^{-j\varphi} & t \\ t & jre^{-j\varphi} \end{pmatrix} \cdot e^{j\phi} \begin{pmatrix} E_3^- \\ E_4^+ \end{pmatrix} \quad (47)$$

where S is the scattering matrix of the IG, and α and β are the transmission loss coefficient and propagation constant, respectively. When the transmission loss α is negligible ($\alpha = 0$). The r and t, in the S matrix, are the reflection and transmission coefficients of the IG which satisfy:

$$r^2 + t^2 = 1 \quad (48)$$

Combining Eq. (2)-(6), and setting $E_2^- = 0$ (no reflected signal from the output port), the transfer function of IG-DSMRR is derived as:

$$A = \left|\frac{E_2^+}{E_1^+}\right|^2 = \frac{[t(1+\tau^2)-2\tau cos(\beta L+\phi)]^2}{(1-t^2)[(1+\tau^2)^2-4\tau^2]+[t(1+\tau^2)-2\tau cos(\beta L+\phi)]^2} \quad (49)$$

Here A is the intensity transmission, which is usually expressed in the logarithmic form:

$$T(\lambda) = 10\log_{10}(A) \quad (50)$$

To decide the wavelength selectivity, we calculate the fundamental mode in an angular grating using the mode analysis, the effective indices (n_{avr}) of the fundamental modes and reflection condition of Bragg grating are calculated as below [129]:

$$n_{avr}^2 = FF \cdot n_{eff1}^2 + (1 - FF) \cdot n_{eff2}^2 \quad (51)$$

$$2\lambda_B = 2n_{avr}\Lambda \quad (52)$$

where n_{eff1} and n_{eff2} are the wavelength-dependent effective indices of the ring waveguide at section with and without inner wall grating, *FF* is the filling factor of the IG as denoted above, and λ_B is the Bragg wavelength.

The working principle of the designed sensor is shown in Figure 4.4, where the spectral responses of DSMRR, IG and IG-DSMRR are described. Light transmission can be viewed as two filtering processes. The light in the bus waveguide is first filtered by DSMRR and then the resonant light is filtered by IG. DSMRR and IG have the same resonance wavelength (near 1550 nm), as the main resonance peak of IG-DSMRR, and other resonances of DSMRR are filtered out by IG. IG-DSMRR with wavelength-selective properties is not limited by the FSR of DSMRR. In the second filtering stage, certain side modes can be effectively suppressed by optimizing the ripple depth of IG. Side mode suppression ratio (SMSR) is used to describe the level of suppression.

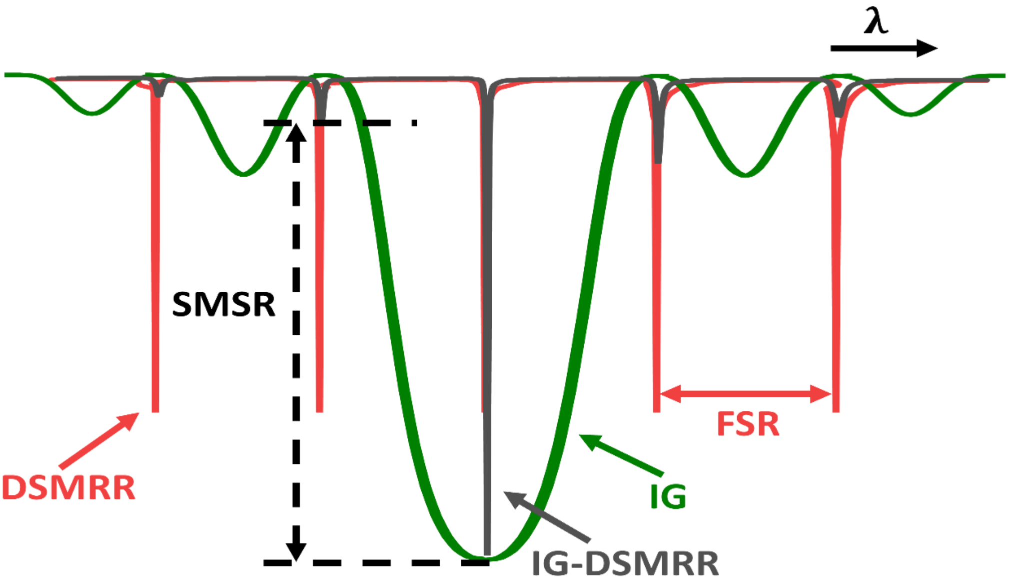

Fig.4.4 Illustration of the operating principle of the IG-DSMRR.

4.2 Simulation

We simulated and optimized the parameters of the IG-DSMRR sensor using Lumerical software to achieve better sensing performance. The introduction of slots in the common bus waveguide can lead to strong confinement of quasi-TE modes in the slot region. This strong confinement will enhance the interaction of light with matter and potentially increase the sensitivity of the sensor. The width of the slot must be carefully designed, since too wide a slot will weaken the electrical strength of the slot waveguide area, while a too narrow slot will prevent biomolecules from entering the slot waveguide area. Here, the width of the gap area is selected to be 100 nm. The mode field distribution of a straight double slot waveguide and of the bent double slot waveguide in the ring are shown in Figure 4.5 and Figure 4.6 respectively.

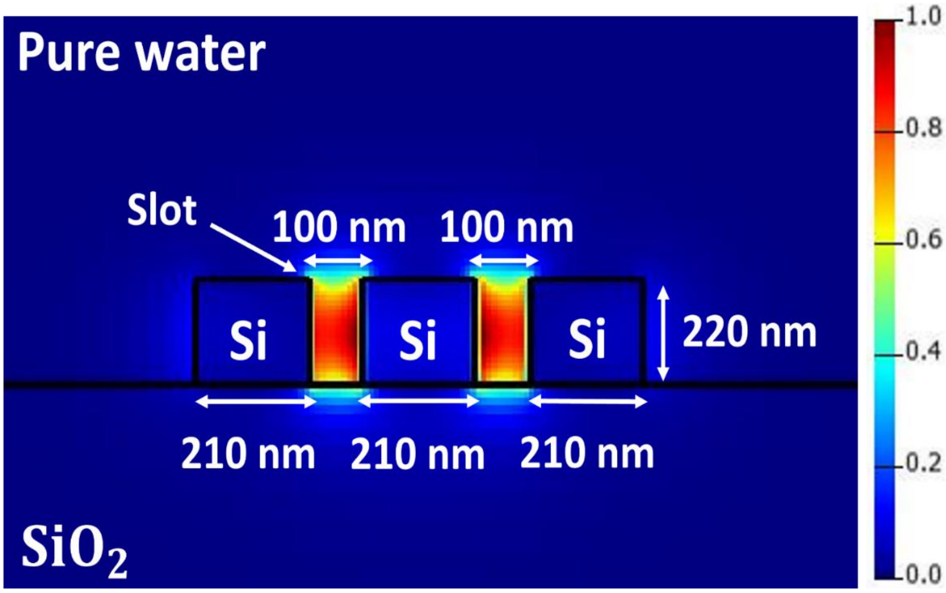

Fig.4.5 Electric field distribution of the bus double slot waveguide.

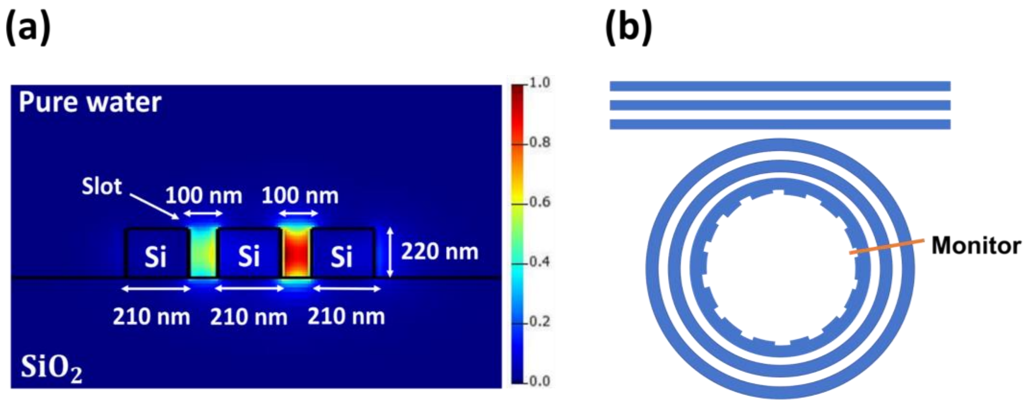

Fig.4.6 (a) Electric field distribution of the bent double slot waveguide, (b) Top view with monitor position.

The straight double slot waveguide has relatively symmetric electric field distribution patterns in the two slots, while the bent double slot waveguide has an asymmetric distribution with the inner slot having a higher electric field strength than the outer one. The simulated high confinement of the TE mode light in the slots 37.2% and 37.8% for the straight waveguide, and 38.7% and 41.2% for the bent slot waveguide. The intensified electric field was realized within the slot region for the applied geometry in both bus and bent waveguide. However, the strong E-field confinements in the slot areas may lead to more losses due to more sidewall scattering and water absorptions as compared with conventional strip waveguides. In the non-sensing state, the measured propagation loss of a straight single strip waveguide in air as top cladding is 0.9 dB/cm, which is close to the result in [130] with similar fabrication processes and waveguide width. The measured propagation loss of a straight double slot waveguide in air (including sidewall scattering loss caused by fabrication) is 20.2 dB/cm. The water absorption loss is 47.5 dB/cm at 1550 nm wavelength based on the reported measurement result [131]. In the sensing state, the estimated propagation loss of the double slot waveguide is therefore about 20.2 dB/cm+(0.372+0.378) ×47.5 dB/cm=55.8 dB/Im.

It is a comparable benefit for the photonics label-free biochemical sensor have high sensitivity. The extinction ratio (ER) value is defined as the ratio between on-resonance and off-resonance transmission, and the Q-factor of the IG-DSMRR are the two key parameters for microring resonator. For Q-factor increasement, it is important to reduce the microring resonator losses. The losses of the IG-DSMRR structure mainly arise from the intrinsic propagation loss in the silicon straight slot waveguide, the bus-ring coupling loss, the bending loss, and the scattering loss. The scattering loss is mainly caused by the IG and waveguide sidewall roughness from the fabrication process. So, in the IG-DSMRR, the coupling loss, bending loss, and scattering loss of IG and the smoothness of the waveguide sidewall in fabrication dominate the total loss, and a small and optimized design bus to ring waveguide coupling distance can effectively decrease the coupling loss. Considering the trade-off between the coupling efficiency from the double slot straight waveguide to the double slot ring resonator and the reactive ion etching (RIE) lag effect in fabrication, the coupling distance W_{gap} between the bus waveguide and ring waveguide was chosen to be 200 nm.

The simulated structure and related parameters of the focused SOI grating coupler are shown in Figure 4.7. The coupling efficiencies as a function of wavelength for the designed and fabricated grating coupler structures are shown in Figure 4.8 for the input cleaved SMF tilted 10˚ from vertical. For the designed grating coupler structure, the optimized grating pitch P is 671.329 nm, the duty cycle d is 39.92%, and the grating height he is 100 nm. The optimum fibre coupling point to maximize coupling from the fibre into the grating is at x =2.745 μm, where x is measured from the narrow end of the taper with gratings. The coupling efficiency can be as high as 42% at the central wavelength of 1555 nm. For the simulation based on the actual fabricated parameters of the grating coupler (taken from the SEM picture), the central wavelength is shifted to 1540 nm with a coupling efficiency of 38%. This is because the grating height h_e of the fabricated grating coupler is around 110 nm, larger than the designed value of 100 nm, which reduces the effective index of the grating and blue shifts the central wavelength from 1555 nm to 1540 nm.

The focused SOI grating coupler was optimized for use with a cleaved SMF angled at 10° from vertical light coupling. The optimized grating pitch P is 671 nm, the duty cycle is 39.9%, and the grating height h_e is 100 nm for operation at a central wavelength of 1550 nm.

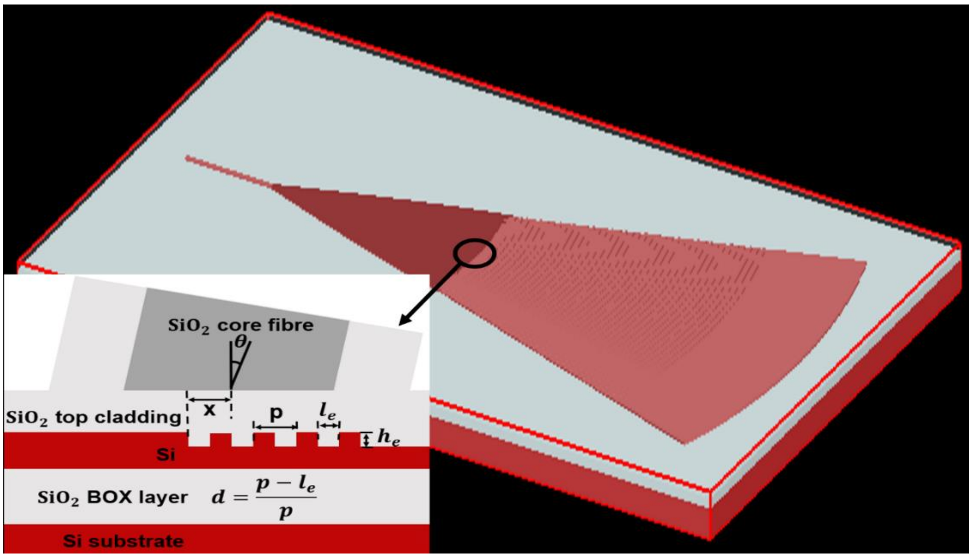

Fig.4.7 Structure and parameters of the focused grating coupler.

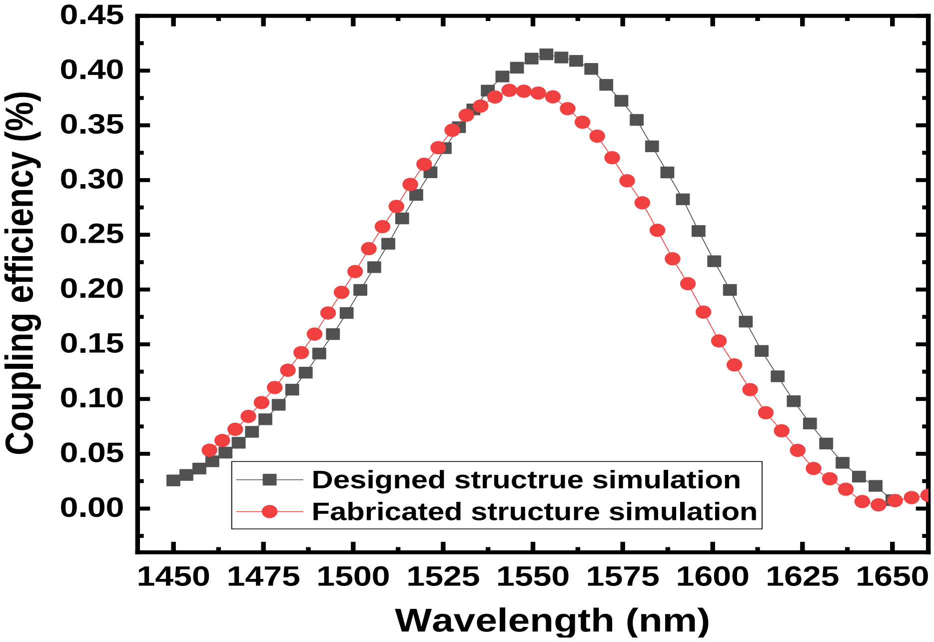

Fig.4.8 The coupling efficiency vs wavelength for designed grating height he of 100 nm (black square dot line) and the fabricated grating height of 110 nm (red circle dotted line).

The simulation of the IG-DSMRR is based on the parameters presented in Figure 4.2 which were chosen to optimize the sensing performance. The electric field distribution of the IG-DSMRR structure is shown in Figure 4.9. The simulated transmission spectra of the designed IG-DSMRR and fabricated parameters IG-DSMRR are shown in Figure 4.10. The relatively low ER (<9 dB) may be due to the coupling efficiency κ between the bus and the ring waveguide being only 1.40% (see section 4.4 measurement results below), also the increased sidewall scattering losses of the double-slot ridge waveguides and the inner wall grating structure should considered. However, there is a trade-off between the Q-factor and the ER since a low value of κ corresponds to a high Q-factor and lower ER [132].

The resonant peak of the dIsigned IG-DSMRR is at 1545 nm, and the resonant peak for the structure with the fabricated parameters is slightly blue shifted to 1543 nm because the grating height of the fabricated inner wall is around 210 nm, smaller than the designed value of 220 nm. Because the hydrogen silsesquioxane (HSQ) resist mask is removed using hydrofluoric acid (HF) following the dry etch to define the ridge waveguide and IGs, the remaining (unetched) near 10 nm thick layer of Si can be used as a wet etch stop layer (see device fabrication in below section 4.3).

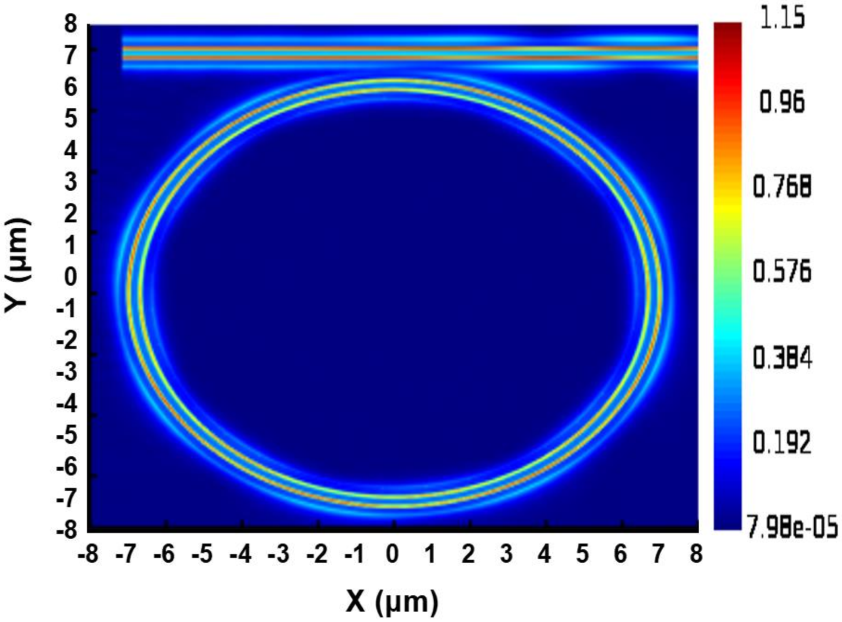

Fig.4.9 The electric field distribution of the IG-DSMRR.

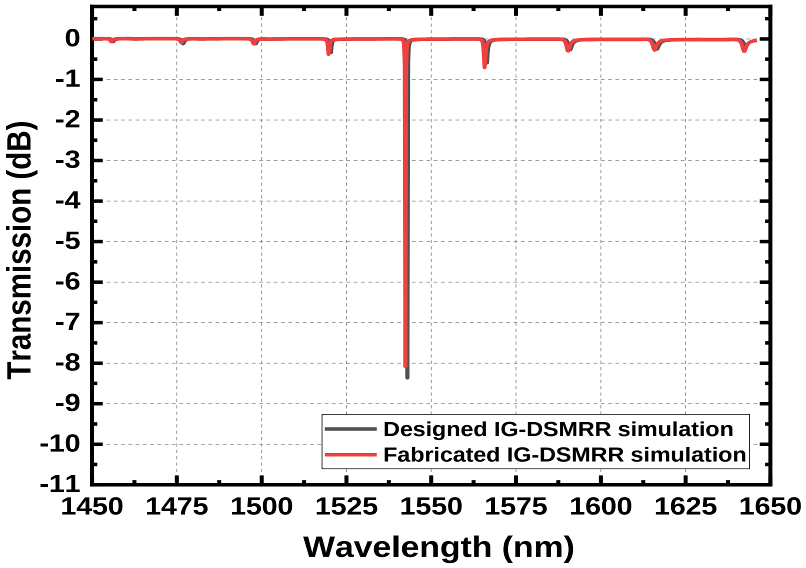

Fig.4.10 The simulated transmission spectrum of the IG-DSMRR for the designed IG height of 220 nm (black curve) and the fabricated IG height of 210 nm (red curve).

An optimized "W" shaped branch tapered coupler was used to couple light between the strip waveguide and the slot waveguide also enhanced the transmission intensity to increase ER [133]. The design and parameters of the "W" shaped branch tapered coupler are shown in Figure 4.11, and the electric field distribution associated with the coupler is shown in Fig. 4.12.

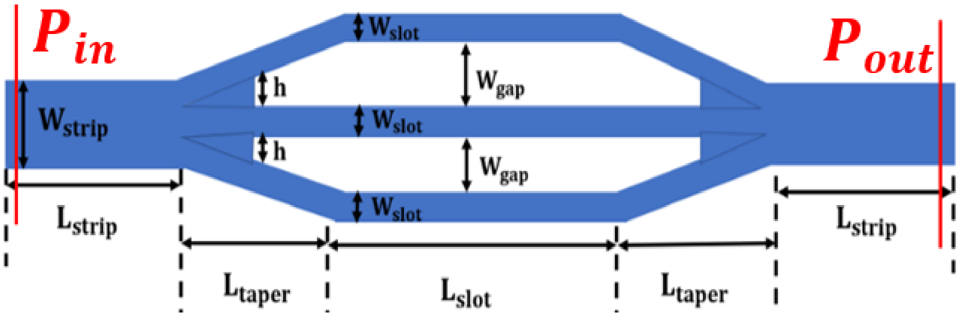

Fig.4.11 The "W" shaped branch tapered coupler design.

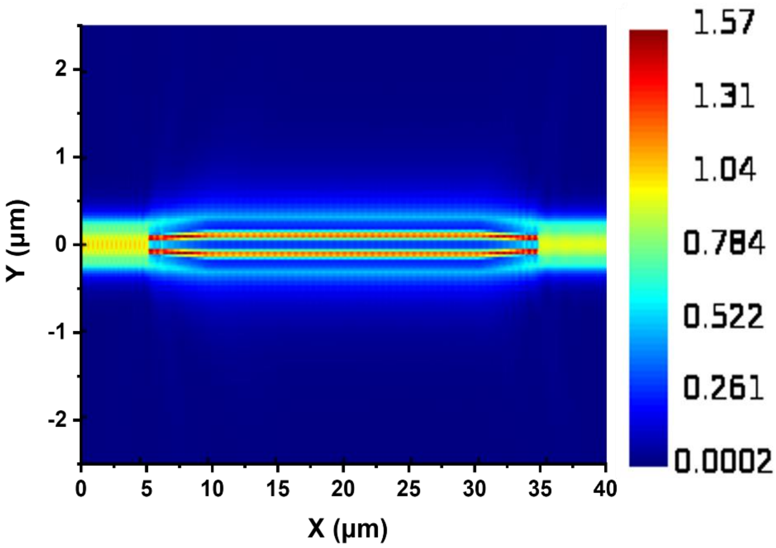

Fig.4.12 The electric field distribution in the "W" shaped branch tapered coupler.

The optimization of the "W" shaped branch tapered coupler is based on the following parameters: the strip waveguide length L_{strip}, the taper waveguide length L_{taper}, the slot waveguide length L_{slot}, the h value arising from limitations in achieved fabrication resolution. The simulated coupling efficiencies of structures with different L_{strip}, L_{taper}, L_{slot}, and h values are shown in Figure 4.13 (a), (b), (c), and (d), respectively. The coupling efficiency decreases for longer L_{strip} and larger h values and fluctuates as L_{taper} and L_{slot} are increased. Based on these simulation curves, the optimized parameters were selected as $L_{strip} = 30$ μm, $L_{taper} = 4$ μm, $L_{slot} = 16$ μm, and $h = 20$ nm. The coupling efficiency of the optimized coupler can reach 96%.

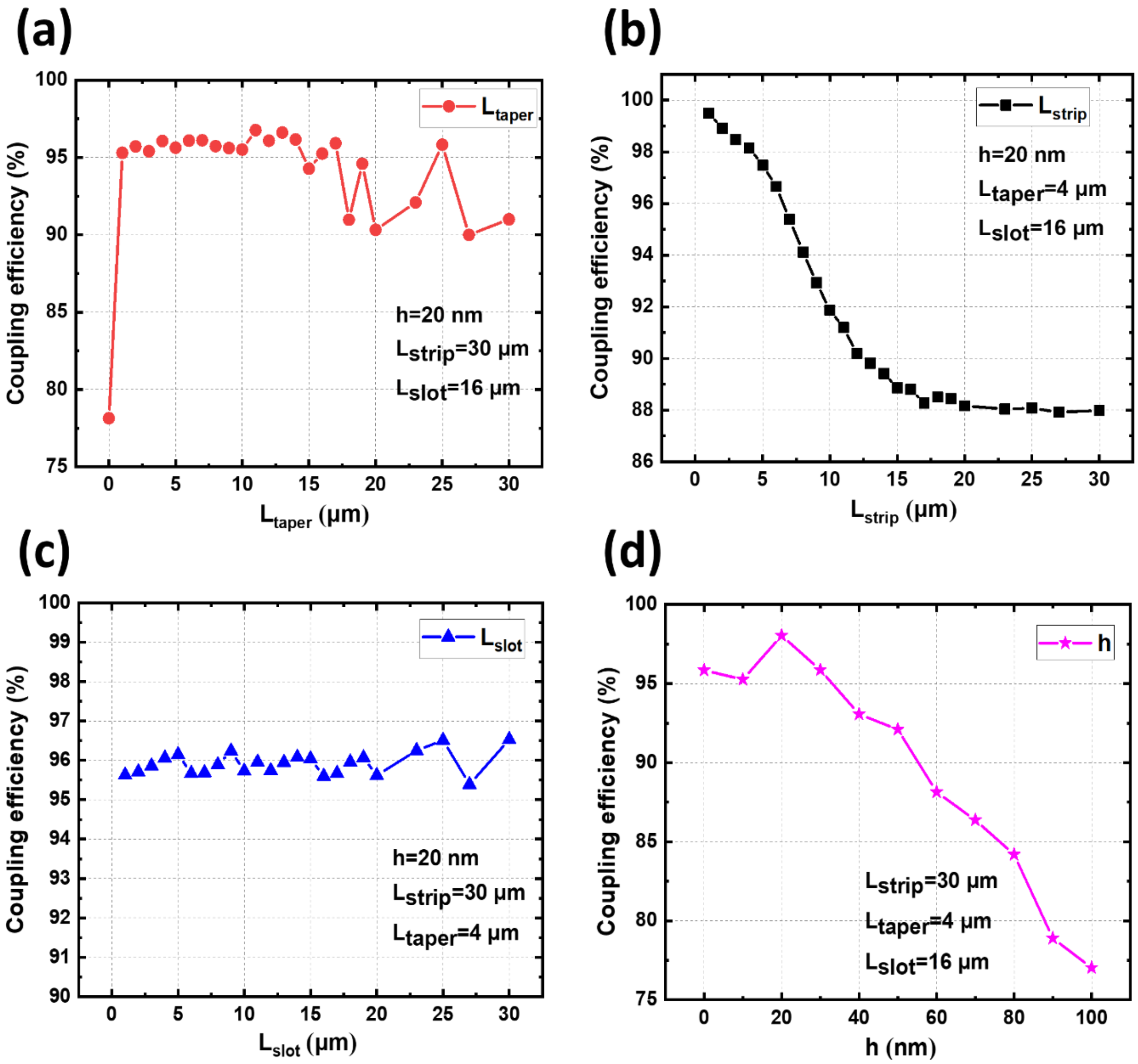

Fig.4.13 The coupling efficiency as a function of (a) strip waveguide length, (b) taper waveguide length, (c) slot waveguide length, and (d) *h* value.

After adding this optimized "W" shaped branch tapered coupler to the IG-DSMRR, the simulation was performed again to confirm the sensing performance. The transmission spectra with and without the taper coupler are shown in Figure 4.14 (a). There is a measured principal resonant peak at 1543 nm. The transmission intensity in the spectrum is slightly enhanced which brings a higher ER and confirms the optimized taper coupler will not affect the transmission spectrum of the IG-DSMRR. The simulated transmission spectra for different concentrations of glucose and sodium chloride as the top cladding mediums are shown in Figure 4.14 (b) and Figure 4.14 (c), respectively. The RI of the cladding solution on the top of the sensor influences the field of the optical mode, which results in a change in the effective index and a shift in the resonant frequencies of the

MRR. Here, the strong resonant optical field inside the slots plays a crucial role in the sensing process. The simulated surface sensitivity S_s is 0.219 nm/nm as shown in Figure 4.14 (d).

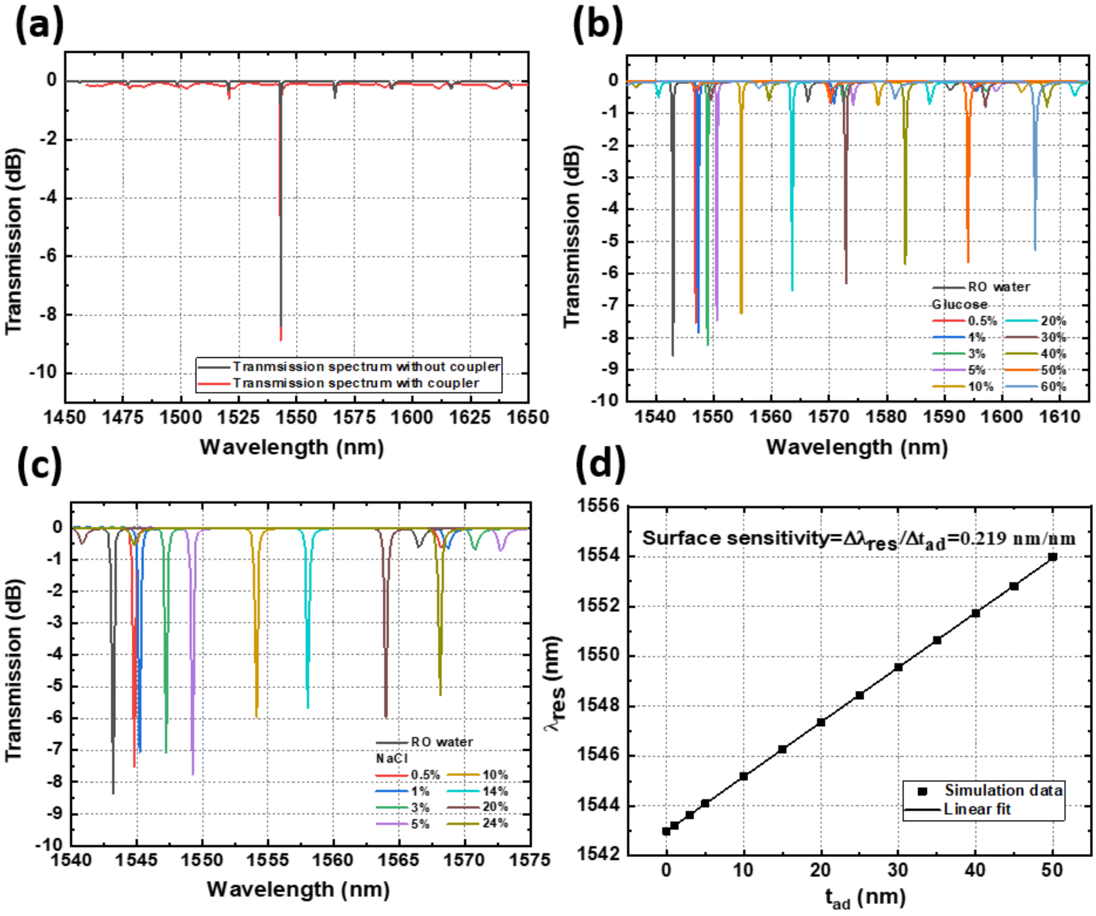

Fig.4.14 (a) Simulated transmission spectra of IG-DSMRR without (black curve) and with tapered coupler (red curve). (b) Simulated transmission spectra for different concentrations of glucose solutions. (c) Simulated transmission spectra for different concentrations of sodium chloride solutions. (d) Simulated surface sensitivity S_s.

4.3 Fabrication

In this section, the fabrication techniques used to realize the fabricated sensing structures are described. The process details of each fabrication step are reported later in this section. The section starts with the introduction of the properties of the wafer material used within this work which is the Silicon-on-Insulator (SOI) platform. The process steps used to fabricate the device are then explained in sequence. Each small section includes a detailed description of the specific process to realize photonics sensor structures. The necessary optimization and developed process are also presented in the thesis.

4.3.1 The material

The substrate platform used in this project is a Silicon-On-Insulator (SOI) UNIBOND wafer produced by the Smart-Cut technique from University Wafers and SOITEC company. The technology is based on the implantation of hydrogen ions like protons and the bonding of two wafers to create the SOI wafer. A detailed description of the process can be found in [134]. The schematic view of wafer fabrication process is shown in Figure 4.15 with following steps:

1) The wafer A covered with a dielectric layer (such as thermally grown SiO2) is hydrogen implanted at room temperature to introduce a thin buried layer with a sufficiently high density of hydrogen ions.

2) The second step involves chemical cleaning and hydrophilic bonding of wafer A to handle wafer B via van der Waals forces at room temperature. The processed wafer acts as a stiffener and provides bulk silicon beneath the buried SiO2 in the final SOI structure.

3) The third step is to segment and anneal the two bonded wafers, including two stages of heating, a medium temperature annealing stage (400-600°C) and a high temperature stage (about 1100°C). In the first stage, a thin highly damaged layer appears in the implanted wafer A at the depth where the hydrogen ion concentration is maximum, and this layer splits into two parts, creating the SOI structure and the remainder of wafer A. Subsequent high-temperature heat treatment removes radiation defects in the silicon layer and strengthens the chemical bond between the two wafers.

4) Use chemical mechanical methods to polish the top silicon layer to obtain a high-quality surface. Therefore, because of the processing, the SOI wafer and the residual wafer A are obtained, and the latter can be used again as a supporting wafer.

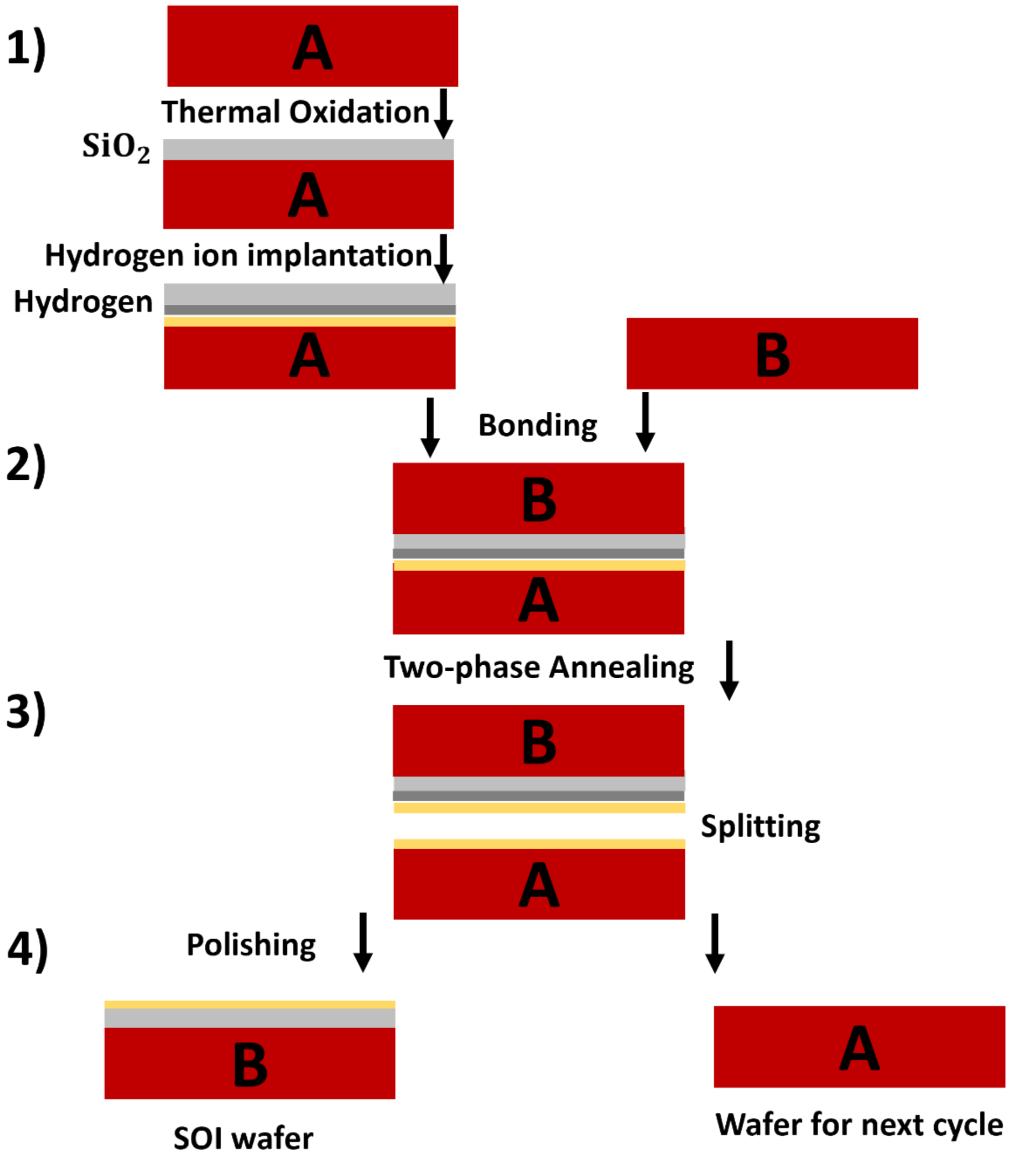

Fig.4.15 Schematic of the production process of silicon on insulator wafers [94].

These SOI wafers are commercially available and consist of three layers: For the present work, the top layer is silicon with a nominal thickness of 220 nm. This layer is the guiding core of the optics. Below the core there is a silicon dioxide layer (BOX) with a nominal thickness of 2 µm, which forms the lower cladding of the optical waveguide. The interface between the top layer and the BOX layer is very sharp with a small roughness. The silicon layer is usually lightly acceptor (boron) doped with a conductivity of 20 Ωcm, corresponding to a doping concentration of approximately 10^{15} cm^{-3} [135]. The optical loss caused by this doping value is negligible. Finally, the substrate layer is made of 675µm thick bulk silicon, which gives the wafer mechanical strength.

4.3.2 Process steps

The SOI wafer structure was shown in Figure 2.4. The fabrication process consisted of 5 main steps, as shown in Figure 4.16.

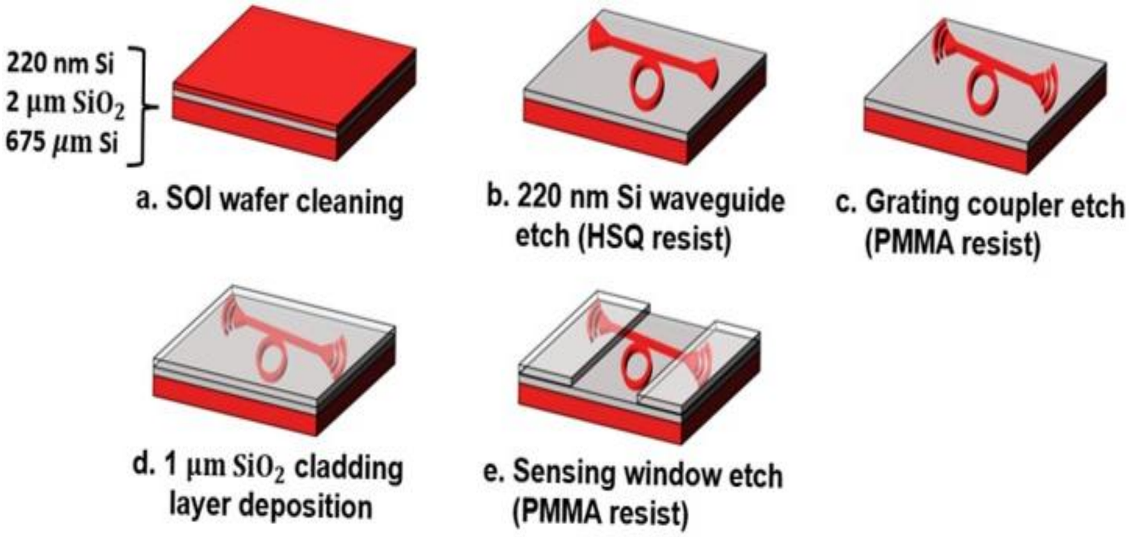

Fig.4.16 Fabrication steps of the device.

The basic samples preparation process includes the SOI wafer cleaning. The specific cleaning process is submerging the SOI substrates in acetone, isopropanol (IPA) and RO water with ultrasonic bath.

The fabrication of markers is included in our fabrication since we defined the microring resonator waveguide structure and the grating coupler structure in two layers. The markers aim for the alignment of different layers in Electron beam lithography. For marker fabrication, we use the lift-off process to deposit titanium and gold markers.

The fabrication process uses three etching steps to create the waveguides and ring resonators, the grating couplers, and the sensing windows. First, the SOI substrates were cleaned by submerging in acetone, isopropanol (IPA) and RO water. Second, an electron beam lithography (EBL) resist 1:3 HSQ: MIBK film was spin-coated and baked at 90 °C. After that, EBL (Raith EBPG 5200) was used to define all the waveguides and the IGs. Then, the exposed samples were developed with 25% tetramethylammonium hydroxide (TMAH). After that, the top silicon patterns of the ridge waveguides and IGs were dry etched using an inductively coupled plasma (ICP) STS 100 tool with a gas flow of SF6/C4F8 (30:90 sccm). Third, another EBL resist layer, of polymethyl methacrylate (PMMA, AR-P 642 200k Anisole 12% PMMA), was spin-coated and the samples were baked using a hotplate at 180 ℃. Then, EBL was carried out to the input and output grating couplers, and the exposed samples were developed with an IPA/MIBK (2.5:1) solution. Then, the silicon layer of the grating coupler was dry etched using an ICP STS 100 system with flow rates of SF6/C4F8 (30:90 sccm). Fourth, a 1 µm silicon oxide layer was deposited on the whole sample using plasma-enhanced chemical vapor deposition (PECVD) to form a cladding layer to increase the coupling efficiency of the grating coupler with a SMF. Fifth, a 1-µm-thick SiO2 window over the ring resonator section was opened by using three PMMA (AR-P 642 200k Anisole 15% PMMA) resist layers and dry-etching in CHF3/Ar (25/18 sccm). Here we note that the EBL resist thicknesses, EBL doses and beam step size (BSS) had been optimized according to our designed structure previously.

4.3.3 Patterning using Electron Beam Lithography (EBL)

Photolithography is to transfer a desired pattern onto a wafer surface. The desired pattern is defined by exposing a radiation-sensitive polymer or sensitized resin that spins on the sample surface. The exposure wavelength defines the minimum feature size achievable using a specific lithography tool. Nowadays, there are multiple techniques for exposure to define patterns. Researchers in each field are trying to develop and improve the technique to achieve smaller resolutions. Developments in optical lithography supported by the CMOS industry, this pattern transfer method involves a single exposure of a large area of the wafer through a mask is fast and cheap. On the other hand, electron beam lithography (EBL) is characterized by extremely high resolution (in nanometre scale). It involves raster scanning of a collimated beam across the wafer surface to define structures and is more flexible in pattern definition (no mask preparation required). Therefore, it is suitable for our research with multiple pattern changes, a small total writing area and a high-resolution requirement.

Because of the small size of our sensing device required for this research, we use a state-of-the-art electron beam lithography machine (Raith EBPG5200 HS electron beam tool) to define the patterns. This electron beam lithography machine available in our facilities was limited to a resolution comparable with the electron wavelength used (less than 8 nm minimum feature size).

The patterI design in th”s re’earch is using Ledit software. After the pattern definition and the final layout generation using Ledit, the patterns are processed with another EBL control software (Beamer) to preset some parameters that could dramatically influence the final pattern structure writing quality. It could divide each area to be exposed into small areas (trapezoids) that correspond to each exposure position of the electron beam. Here, the Resolution is the minimum distance between the points of the trapezia positioned over a square lattice grid. The beam scans the grid horizontally row by row and exposing dots separated by a fixed gap, this gap is called the Beam Step Size (BSS, an integer multiple of the resolution). The finite width of beam is defined by the Spot Size parameter (SS) and depends on the aperture diameter and the beam current. Therefore, the pattern is a discrete set of exposed pixels. The Beam Step Size (BSS) should be a fraction of the Minimum Feature Size (MFS), guidance suggests choosing BSS=MFS/5. There is a point where the BSS starts to affect the integrity of a single pixel line, then the line-edge roughness becomes a problem in this situation. It is suggested the SS always chosen to be around 1.2 times bigger than the BSS. This is the best combination in terms of small line edge roughness (Small SS and BSS) and minimum beam time (Large SS and BSS). The beam time can be further reduced by designing a non-critical device with a larger spot (i.e., a wide strip waveguide), and this choice does not affect the final result for isolated patterns.

The characteristic wavelength of the elecIron beam is so small that diffraction no longer defines lithography resolution. Resolution is primarily limited by electron scattering in the resist and underlying substrate. These electron scattering effects, often called proximity effects, result in the exposure of areas surrounding the area where the electron beam is incident. Due to proximity effect, any written pattern may vary significantly from its intended size. The EBL tool used in this work has a proximity correction function that reduces the proximity effect by adjusting the exposure dose according to the density of the pattern to be defined, thereby eliminating additional exposure due to the limited size of the electron beam. The effect of proximity is the smoothing of pixels and lines.

The EBL tools have a limited writing field because electrons cannot be deflected beyond a certain amount without distortion. The complete pattern is divided into blocks that must be stitched together by movements of the stage. Therefore, platform misalignment can lead to stitching errors when patterns extend beyond the field boundaries. The accuracy of platform positioning is a key parameter characterizing EBL tools. Therefore, it is important during design and fracturing processes to avoid situations where critical structures are located at the boundaries of the field (leave dislocation values of up to 30 nm are possible at each field boundary).

The patterns and mask Iayers are initially created and designed using L-edit, a Mask Editor Software. Subsequently, these designs are saved as GDSII files and undergo processing in Beamer, where fracturing, pattern optimization, and layer output exposure design take place. Following this, the files are further processed in Belle to define critical beam parameters such as dose test, dose value, beam spot size, and step size. Finally, the prepared files are transferred to the ebeam tool for the exposure process.

4.3.4 Resists

Resists are radiation-sensitive compounds. During exposure, their chemical structure changes and they dissolve in the developer. Based on their response to electron exposure, they can be divided into 1) Positive resists: the exposed regions become more soluble with the net result of the pattern formed is the reverse of the mask. 2) Negative resists: the exposed regions become less soluble, and the pattern formed is the same as in the mask.

There are two important parameters that define the resist structure: 1) Sensitivity: defined as the energy required to retain 100 % of the thickness of the exposed region after development (for negative resist). The resist has a finite solubility in its developer even without exposure to radiation. 2) Contrast: corresponds to the selectivity between exposed and unexposed regions. A high contrast is required in the ideal EBL resist to allow vertical profiles after the development and a high sensitivity which allows a low writing dose and a faster exposure process.

Table 4.1 The characteristics of the resist

Resist	Tone	Contrast	Sensitivity	Etching resistance
PMMA	Positive	Low	High	Poor
HSQ	Negative	High	Medium	Good
ZEP	Positive	Low	High	Poor
NEB	Negative	High	Low	Medium

Table 4.1 above summarizes the characteristics of some resists available in our James Watt Nanofabrication Centre (JWNC). The fabrication process for photonic structures varies depending on the specific resist utilized.

The characteristics of the resist available in our department are summarized in Table 4.4. The fabrication processes changes according to the photonics structures and the resists utilized. In some work, positive electron-beam resists such as PMMA and ZEP are used to transfer the required patterns into the substrate, but their poor etching resistance (generally 1:1 selectivity) may require the use of a transfer mask layer using silica or silicon nitride when using deep etch. Thus, the imperfection in the mask is amplified from the double step mask transfer process. In our sensor structure design, we only need shallow etch of the top silicon layer, thus the resist layer thickness is carefully designed to avoid running out of the positive resist during dry etch process. The process steps for transferring the patterns based on resists and dry etch is illustrated in Figure 4.17. This schematic is suitable for all the Ebeam photoresists we mentioned above.

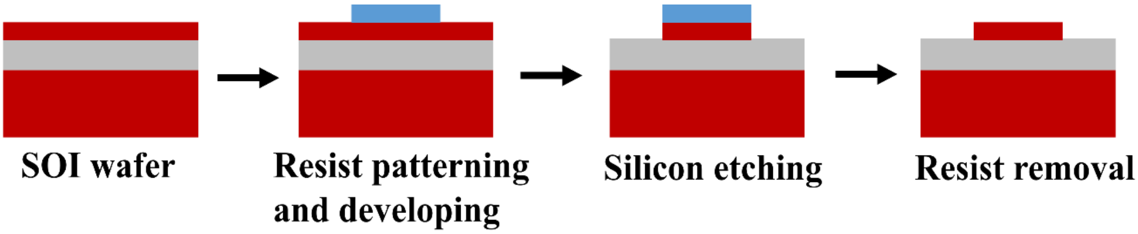

Fig.4.17 Schematic of the process steps for patterns transfer.

Nowadays Hydrogen Silsesquioxane (HSQ) has become popular electron-beam resist because it combines high resolution with moderate sensitivity and minimal line edge roughness with a high level of etch resistance. The fabrication process used in this work for the definition of the microring resonator waveguide structure was based on HSQ resist and consists of four main steps resist spinning, exposure (Electron-beam lithography), and development (tetramethylammonium hydroxide, TMAH), and silicon dry etch using inductively coupled plasma (ICP STS 100/ ICP SpTS Rapier DSiE tool). Even though the sensitivity of HSQ is lower compared to many positive photoresists, the area to be written is greatly reduced because only the waveguide structure is written and not the negative photoresist, making this parameter important in choosing the best photolithography Glue is of only marginal importance when compared with other data such as etch resistance and contrast ratio.

The chemical structure of HSQ resist consists of silicon, oxygen and hydrogen atoms that are initially arranged in a three-dimensional cage-like manner. When energy is applied (e.g., by electron beam), the SiH bonds, which are weaker than SiO bonds, are replaced and form a three-dimensional network structure more similar to silica.

The exposed areas have varying degrees of reactivity with the developer tetramethylammonium hydroxide (TMAH). The choice of the resist thickness (dependent on concentration of the resist and spin speed), pre and post baking (time and temperature), dose value in exposure and development process (concentration, time, and temperature) has different influences on the final quality of the pattern mask for the etching. The resist should be thick enough to protect the guide layer and contain a minimum level of roughness that can be transferred directly to the guide core during the etching process. The main properties of HSQ are reported as when increasing the developer concentration, the contrast and reproducibility of the process increase while the sensitivity reduces. Also, increasing the baking temperature also increases the sensitivity, but reduces the contrast: the effect of thermal curing is to start bond division and recombination, thereby favouring the transition to a network structure and reducing the cage/network ratio. Baking can be considered as a sort of pre-exposure, which enhances the sensitivity but reduces the contrast. Another important aspect that must be considered is surface roughness, which depends on the baking temperature and is a function of the concentration of developer (smaller roughness for larger concentration). Based on the information mentioned above and the goal is to achieve high contrast at reasonably high sensitivity, maximize repeatability and reduce roughness. The concluded HSQ process should include low temperature baking, minimum delay between baking and exposure, and high-concentration developer.

Considering the various physical properties of the mentioned resist materials, we have carefully selected a specific set of values optimized for our sensing structure. Specifically, we have employed a developer solution consisting of 25% TetraMethyl Ammonium Hydroxide (TMAH) for the HSQ resist. The HSQ resist layer is precisely 500 nm thick, and a 15-minute bake at 90 degrees has been determined to provide the best performance for our structure. Achieving this nominal thickness involves a 3:1 dilution of HSQ in Methyl Isobutyl Ketone (MIBK), followed by spinning at 4000 rpm for 60 seconds. The best dose for our tiny grating and slot microring structure was found to be 1800 $\mu C/cm^2$. The unexposed resist was removed during the development in TMAH at 22 degrees. The development time in TMAH solution is typically 30 seconds and no post exposure bake is necessary. This temperature is a critical aspect of the process, and the temperature value was controlled accurately by a digital thermometer (with a precision of ± 0.1℃). A subsequent rinse in Reverse Osmosis (RO) water for 60 seconds was used to remove the development from the surface of the sample. A final rinse with IPA for 30 seconds is useful for high aspect-ratio features because IPA has a lower surface tension than water. Then the sample is dried using the nitrogen gun.

4.3.5 Dry etch techniques

Another fundamental step in transferring patterns onto the wafer surface to create waveguide structures involves the use of the dry etching method. This method selectively removes material in the unmasked areas through a combination of physical and chemical processes. Dry etching techniques are preferred due to their ability to meet specific requirements, such as anisotropy (i.e., vertical sidewalls), uniformity, and precise control over etching time. The general dry etching process can be broken down into the following steps:

1) Generation of reactive gas species through a radio frequency discharge of reactive gases introduced into the chamber. This process involves electron impact dissociation and ionization reactions.

2) Diffusion of active species from the discharged bulk plasma to the wafer surface.

3) Reaction steps, including the absorption of surface free radicals and simultaneous ion bombardment. This results in a chemical reaction between the adsorbed active material and the material to be etched.

4) Extraction of volatile chemical by-products.

For a visual representation of the etching process, please refer to Figure 4.18.

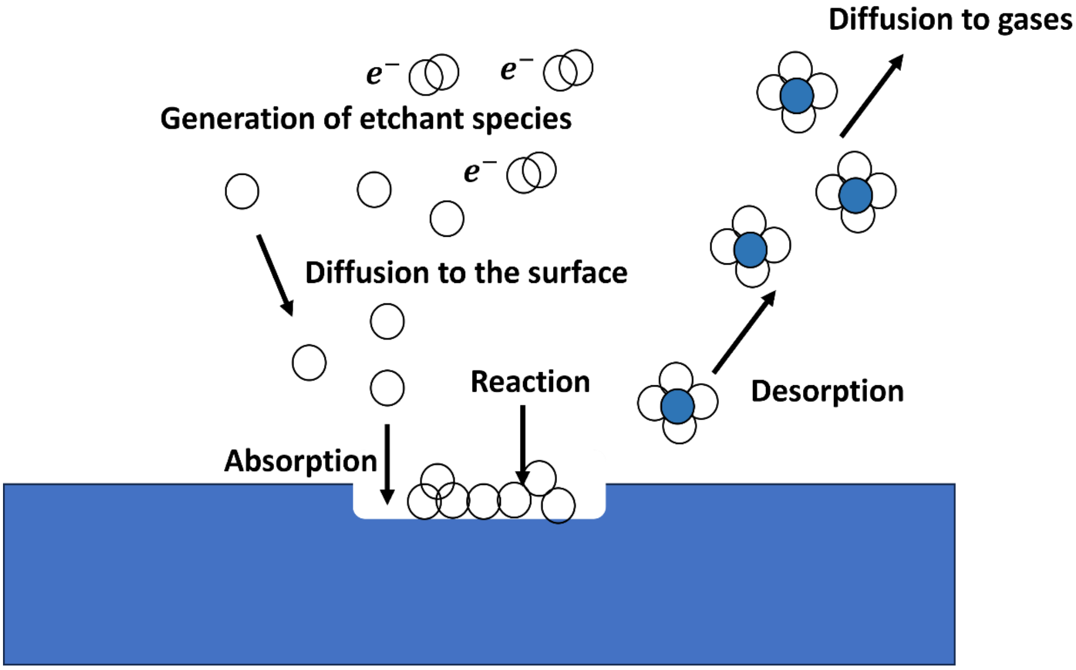

Fig.4.18 Schematic of an dry etching process [94].

The two types of dry etching methods we use in manufacturing are:

1) RIE (Reactive Ion Etching): a technique that removes unwanted material through the combined effects of chemical and physical interactions of accelerated ions. Under certain conditions, RIE can produce strong anisotropic profiles and good selectivity between the mask layer and the material to be etched. RF power applied to the two parallel plates is used to control plasma generation and ion acceleration; the etch rate depends directly on the plasma density. An increase in RF power increases the self-bias voltage on the cathode where the sample is located. The result is an increase in ion bombardment energy, leading to deterioration of etch selectivity and increased sample damage.

2) ICP: Plasma generation is separated from the etch chamber, with two different RF

power generators coupled to the plasma to independently control ion energy and ion density. An inductively coupled RF generator controls the density of the plasma across the chamber walls, and in addition, a capacitively coupled RF power source is used to vary the ion acceleration toward the material. ICP can produce very high plasma densities with low ion bombardment energies. The independent processes of ion generation and acceleration allow the selection of a well-balanced set of operating parameters to produce the desired etch profile.

In this research, we employed the RIE 80+ machine by Oxford Plasma Instruments for etching silica and the STS-ICP 100 as well as the ICP SPTS Rapier DSiE by Surface Technology Systems for etching silicon.

The silicon etching process using ICP-RIE method in STS-ICP 100 and ICP SPTS Rapier DSiE dry etch machine was performed with SF_6-C_4F_8 chemistry, with the parameters given in Table 4.2.

Table 4.2 Silicon Etching Parameters in STS ICP and Rapier SPTS ICP

Parameters	STS-ICP 100)	ICP SPTS Rapier DSiE
Gas	SF_6/C_4F_8	SF_6/C_4F_8
Flow (SCCM)	30/80	30/90
Platen Power (W)	12	14
Coil Power (W)	600	600
Pressure (mT)	10	20
Etch Rate (nm/s)	2.2	3.5

For this process, the vertical etching is assisted by deposition on the sidewalls: This technique is based on the idea that the vertical sidewall etching is protected by a deposited non-reactive film, but the horizontal surfaces are exposed and open to etching. An etch resistant film layer can be coated on the sidewalls to prevent or weaken lateral etching. Thus, a repeated etching passivation process is obtained by introducing alternating gases in the chamber.

In the etching recipes, the etching gas is SF_6 and the passivation gas is C_4F_8. The C_4F_8 gas in the plasma can form a fluorine-carbon compound which can prevent F^+ from further reacting with the silicon once deposited on the silicon surface. Etching and passivation are switched every few seconds during the cycle. Although pure SF_6 gas reacting with silicon leads to isotropic etching, the etched surface is soon passivated by C_4F_8. In the next SF_6 circle, ion bombardment removes the deposited film in the depth direction allowing SF_6 to react further with the fresh silicon surface, whereas it cannot sputter-etch the sidewalls. The etching rates using different machines are tested as follows: the Si etch rate is around 2.2 nm/s and 3.5 nm/s with a Si/SiO_2 selectivity of $\simeq 10$ and 3.2 for ICP-STS 100 and ICP-SPTS Rapier respectively. Utmost caution must be exercised when fabricating intricate patterns with minimal gap dimensions. The occurrence of RIE-lag can impact the etching depth of patterns, causing a reduction in depth as the gap dimension decreases. This phenomenon and its constraints are of particular significance in devices like coupled waveguides, arrays, and structures with small holes.

4.3.6 Silica deposition

During the manufacturing process, a thin film layer of silicon dioxide needs to be deposited. The purpose of this layer is to provide a relatively higher refractive index layer on the grating couplers structures compared to the air to increase the coupling efficiency of the grating couplers, or simply to protect the structure from the external environment like dust to reduce unwanted scattering. The silicon dioxide film deposition in this research utilizes the Plasma Enhanced Chemical Vapor Deposition (PECVD) method.

The PECVD method is a low-temperature deposition method at approximately 300°C in which the energy to dissociate reactants is provided by radiofrequency (RF), microwave and photon excitation [136]. Generally, gas phase precursors are delivered into a deposition chamber where free electrons are accelerated by an electric field to create plasma. Excited atoms are accelerated from the plasma region towards the deposition substrate, thereby assisting in the silica coating growth. Reacts with adsorbed species forming chemical bonds on the surface to produce the desired stable film. The nature of the deposition is determined by two main factors: 1) Plasma initiates chemical reactions that produce free radicals and ions. 2) The energy with which these reactive species reach the substrate. The variables should be taken into account: RF power, temperature, and the relative proportions of the input precursor. These variables affect the reactions that occur in the plasma and the interaction that occur at the substrate interface. We used a standard recipe in Oxford Instruments Plasmalab 80+ PECVD tool for silica film deposition with the recipe parameters summarized in Table 4.3.

Table 4.3. Silica Deposition Parameters

Parameter	Value		
Gas	SiH_4	N_2O	N_2
Flow (SCCM)	4.7	150	85
Power (W)	19		
Pressure (mT)	1000		
Temperature (°C)	300		

The deposition film thickness of silicon dioxide is slightly varied from the nominal value about ±5%. The refractive index value of the deposited silicon dioxide is measured as $n_{SiO_2} = 1.48$ using ellipsometry. Quality issues observed during the deposition, such as limited plasma penetration into narrow gaps and the resulting granular surface, should be taken into account when evaluating the fabrication outcomes.

4.3.7 Metal deposition and lift off techniques

The metal deposition process is required in our device fabrication for markers definition, plasmonic structures, and slot hybrid plasmonic MRR structures. This process could also be used in electrodes fabrication as part of a photonic device, such as a thermo-optically tuneable microcavity. In this process, we use the PMMA resist and lift-off processes.

The marker structures definition is mandatory before the fabrication of the core layer patterns. This is important for the alignment of all different layers (like waveguide structure layer, grating coupler layer, metal deposition layer).

The metal deposition is carried out using Plassys IV or Evap 7 E-Beam two evaporators in JWNC. The metal deposition and evaporation are illustrated as follows, the source material metal for deposition is heated by an electron beam to the point it starts to boil and evaporate. The whole process is carried out inside the vacuum chamber to enable the molecules evaporate freely until reach and condensate on the substrate surface in the chamber. The marker deposition process consists of the following steps and the flow diagram is shown in the Figure 4.19.

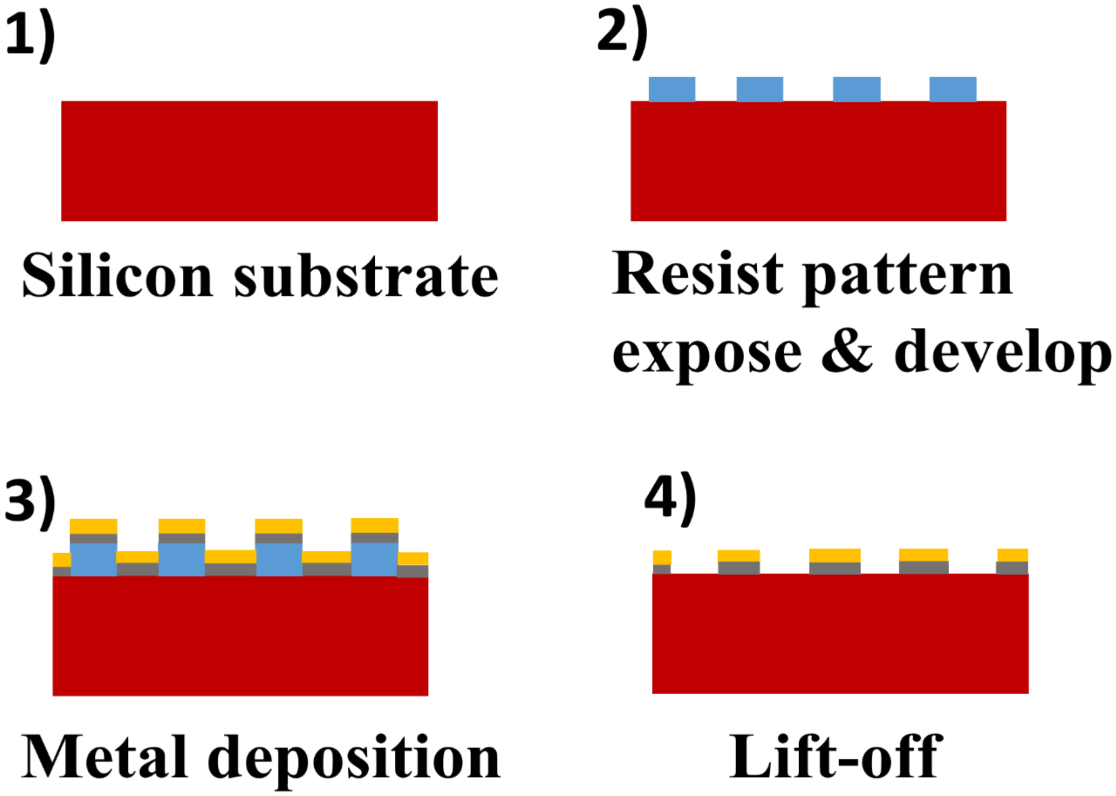

Fig.4.19 Schematic of the metal deposition by lift-off process.

1) Double layers PMMA resist spinning and baking,

   a) Layer 1 PMMA resist: 15% 2010 Anisole (4000 rpm), at 155℃ hotplate 2 min.

   b) Layer 2 PMMA resist: 4% Ethyl Lactate (4000 rpm), at 155℃ hotplate 4 min.

2) E-beam exposure with a dose value 1000 $\mu C/cm^2$.

3) Development: The development solution we use after the exposure is the dilution of isopropyl alcohol (IPA): methyl isobutyl ketone (MIBK)=2.5:1 for 30 seconds – and then two subsequent rinses in IPA and RO water for 30 seconds and 1 min each.

4) Metal layer evaporation and deposition onto the sample.

5) Lift-off step in acetone 50℃ water bath (30 min+).

The two different PMMA resists layers consist of different sensitivities which allows the realization of undercut of the mask layer. Thus, the deposited metal layer has a step between the resist top surface and the sample pattern area, which allows an easier removal of the undesired metal and providing sharp edges. The lift-off steps in acetone is following by the deposition step for at least 30 min until time is sufficient to remove all the unwanted part of metals from the samples. The metal deposition layers for markers are 30 nm NiCr and 100 nm Au respectively.

The PMMA resist layer and metal deposition recipes are different for the fabrication of the markers and plasmonic structures. The marker deposition contains NiCr/Au metals with 30/100 nm thickness. The plasmonic structures normally deposit a few nanometre titanium before gold deposition to guarantee good adhesion onto the silicon surface and the gold (Au) layer. The gold layer is selected as the top layer because of its brightness under electron beam irradiation, it produces an excellent contrast ratio compared to silicon substrates, enabling alignment accuracies on the order of a few nanometres.

4.3.8 Wet etch techniques

The wet etch techniques are also studied and investigated based on the project fabrication requirement. The fabrication of plasmonic structures on transparent and non-reflective sample surfaces like silicon dioxide. This kind of material does not reflect enough of the incident laser to read sample height in the Ebeam calibration process. In this case, a metal charge conduction layer is usually used (like 10 nm gold/aluminium layer) which provides a reflective surface of the height meter. Therefore, the wet etch of the gold/aluminium layer is researched. Also, the wet etch of deposited silicon dioxide layer using

Hydrofluoric acid (HF) is investigated as an alternative method for silica dry etch using RIE 80+ machine.

The measured wet etch rate of PECVD deposited silicon dioxide layer using buffered oxide etchant (BOE) 6:1 hydrofluoric acid (HF) is 96 nm/sec in room temperature. However, the undercut problem is quite severe in this HF wet etch method with 7 µm undercut in 1 µm wet etch depth. This should be taken into consideration for the structure fabrication.

The wet etch process of deposited gold (Au) layer is using KI/I2 solutions and the measured etch rate is 0.67 nm/sec. The wet etch process of deposited aluminium (Al) layer is using mixed solvents (Nitric acid: Orthophosphoric acid: RO water = 1:16:2) with the measured etch rate value of 10 nm/min.

4.3.9 IG-DSMRR fabrication results

As mentioned in the section before, the IG-DSMRR or similar MRR structures are fabricated using three main etching steps to create the waveguides and microring resonators, the grating couplers, and the sensing windows. The brief conclusion of the fabrication processes are shown below.

1) The SOI wafers were cleaned by subsequently submerging in acetone, isopropanol (IPA) and RO water with ultrasonic bath.
2) The 1:3 HSQ: MIBK Ebeam lithography (EBL) resist spinning.
3) Ebeam exposure and 25% tetramethylammonium hydroxide (TMAH) development.
4) Silicon dry etch (ICP STS 100 tool).
5) The polymethyl methacrylate (PMMA) resist spinning.
6) Ebeam exposure and IPA/MIBK (2.5:1) development.
7) Silicon dry etch (ICP STS 100 tool).
8) PECVD silicon dioxide deposition.
9) Silica dry etch (RIE 80+ tool).

It should be noted that the EBL resist thicknesses, EBL doses and beam step size (BSS) had been optimized to achieve better structure fabrication results.

The pattern for IG-DSMRR waveguide layers is carefully designed in Beamer software to make sure the precise pattern writing result is achieved in especially tiny sidewall grating structure (ten nanometres scale). There are several things to improve the result when writing tiny and high-resolution structures in Beamer:1) In the PEC module the isodose grid should be set to a multiple of your beam step size (10nm in our design). 2) In the Export module, the resolution should be set to 0.001 and the beam step size is better at 5 nm (the PG can write up to 100 MHz and for an 8 nA beam and typical doses, this is fine). 3) The field size value should set to 1000 µm and the fracture mode to "Shape Detection". 4) Shape Filling in the Export should set to "High Res". The zoomed in version of the final inner wall grating export pattern is shown in Figure 4.20, Figure 4.21 and Figure 4.22 below. The dose tests did for this structure and the final result shows the better dose value for inner wall grating writing is 1800 $\mu C/cm^2$.

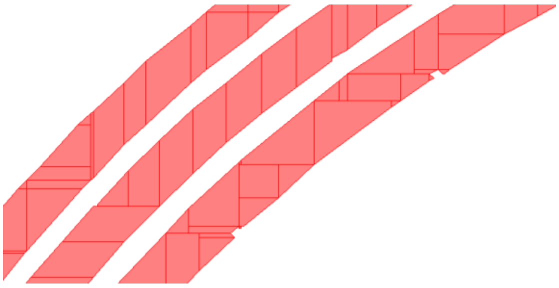

Fig.4.20 Pattern before Beamer parameter optimising.

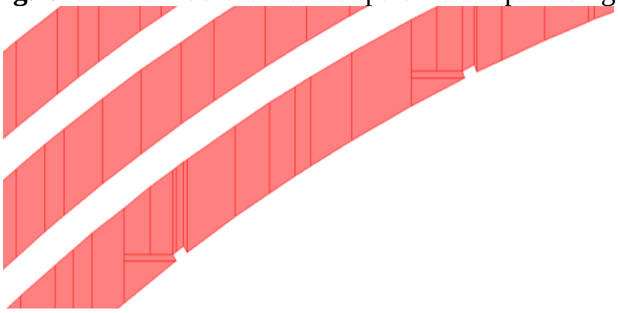

Fig.4.21 Pattern after Beamer parameter optimising.

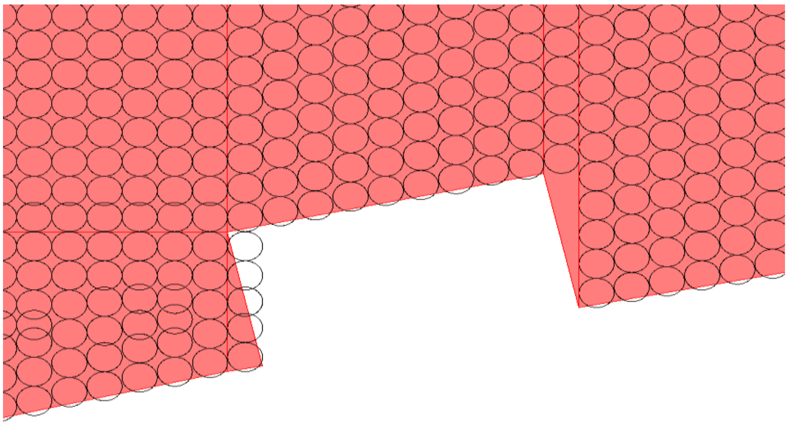

Fig.4.22 Zoomed final inner wall grating export result in Ebeam.

Following the detailed process introduction and optimization outlined earlier, we present the fabrication results and SEM images in this section. Figure 4.23(a) displays a top-view scanning electron microscope (SEM) image of the completed IG-DSMRR device, while Figure 4.23(b) provides a magnified SEM view of the inner sidewall grating. The fabricated grating coupler is shown in Figure 4.23(c), from which the period and duty cycle are 672 nm and 39.9% with an etch depth of 110 nm. These parameters are close to the designed period and duty cycle (671 nm and 39.9%), the differences being due to the fabrication errors which result from proximity effects in EBL and side wall etching during the ICP-RIE process [37]. The open window on the ring resonator for high-sensitivity sensing is shown in Figure 4.23(d).

Here, it is essential to highlight the performance of the devices on the wafer sample we have manufactured. The wafer area scale we use in fabrication is 11×12 mm^2. Normally we can fabricate 30 devices each column with 5 columns of different designed structures. In measurement, we tested 30 IG-DSMRR sensors in one column with 24 devices could work well and perform the designed transmission spectrum (80% yield percentage). The measurement results reported here for the IG-DSMRR sensor are based on the optimal best performance sensor selected for analysis. For the 80% yield our analysis is the dry etch non uniformity and the resist development which may bring some difference between the designed parameters and the fabricated parameters. This may cause the unsatisfied performance.

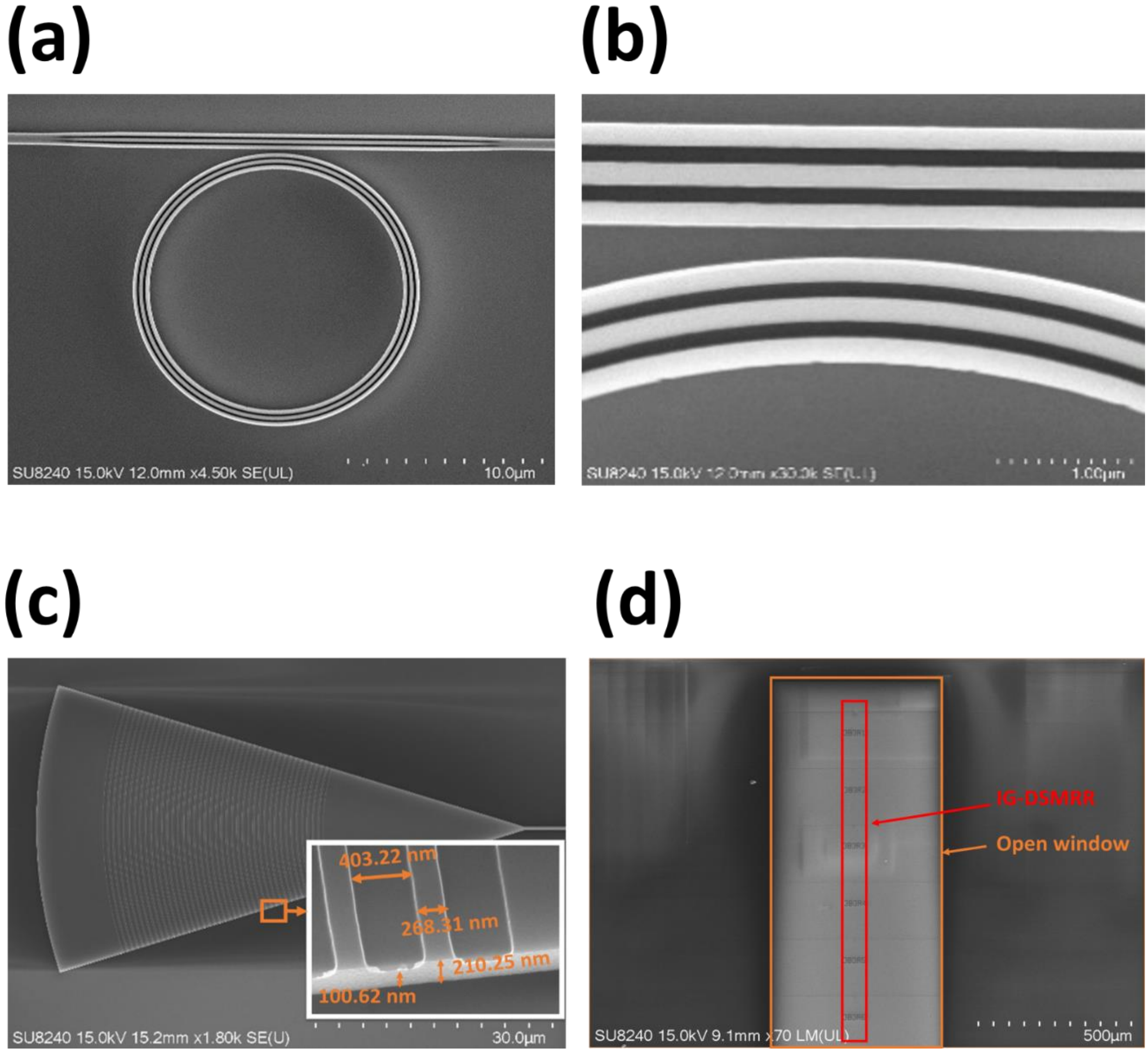

Fig.4.23 SEM images of (a) the IG-DSMRR. (b) zoomed bus, ring waveguides, and the inner sidewall grating. (c) the grating coupler, and the inset shows the grating period of 672 nm and dry etched grating height of around 110 nm. (d) the dry-etched open window for a series IG-DSMRRs.

4.4 Measurement

As mentioned in chapter 3 before, the experimental setup for these MRR photonics sensors contains a Super Luminescent Diode (SLD) broadband light source with a central wavelength of 1550 nm, and maximum output power of 22 mW with a 50 nm 3 dB bandwidth to measure the spectral response. The input and output TE mode light were connected to the IG-DSMRR sensors via a 10 µm core cleaved SMF with 10° input and output angles through the grating couplers (GCs). The optical spectrum analyser (OSA) with a resolution bandwidth of 0.06 nm was connected to the output SMF to measure the transmission spectrum of the IG-DSMRR. To measure the sensitivity of the sensor to different RIs, sample liquids were dropped on the sensing part of the sensors. To obtain measurement data swiftly, particularly important for fast evaporation solvents such as acetone and IPA, an automated measurement system using LabVIEW software based on the general-purpose interface bus (GPIB) connection was employed for the whole measurement and data acquisition.

In the experiments, the coupling efficiency of the grating coupler, the transmission loss of the straight SOI waveguide, and the transmission spectra of the IG-DSMRR with different concentrations of glucose and sodium chloride solutions were measured. The simulated and measured coupling efficiencies as a function of wavelength of the output grating coupler are shown in Figure 4.24(a). The central wavelength and coupling efficiency of the simulated grating coupler based on the fabricated parameters are 1548±0.1 nm and 38% respectively. For the real measured grating coupler, the central wavelength and coupling efficiency are 1540 nm and 34% respectively. The differences in the central wavelength and coupling efficiency may be due to deviations in the tilt angle of the output SMF. The transmission spectra of the simulated and measured IG-DSMRR are shown in Figure 4.24(b). There is a measured principal resonant peak at 1547.7±0.1 nm, which can be tuned from 1450 nm to 1650 nm. Nearly 5-nm redshift in the resonant peak compared with the simulation result in Figure 4.24(a) may be due to the fabrication errors of the IG period and FF.

The distance between the main resonant peak and its right-third subsidiary peak is denoted as quasi-FSR. In the spectrum, the quasi-FSR of the IG-DSMRR is 72.6±0.1 nm, compared to the FSR of a conventional SMRR of 20.4±0.1 nm. This magnification of the detection wavelength range can be defined using Eq. (53) to give a measure of the degree of broadening of the detection range:

$$A_{EF} = \frac{quasi-FSR}{FSR} \tag{53}$$

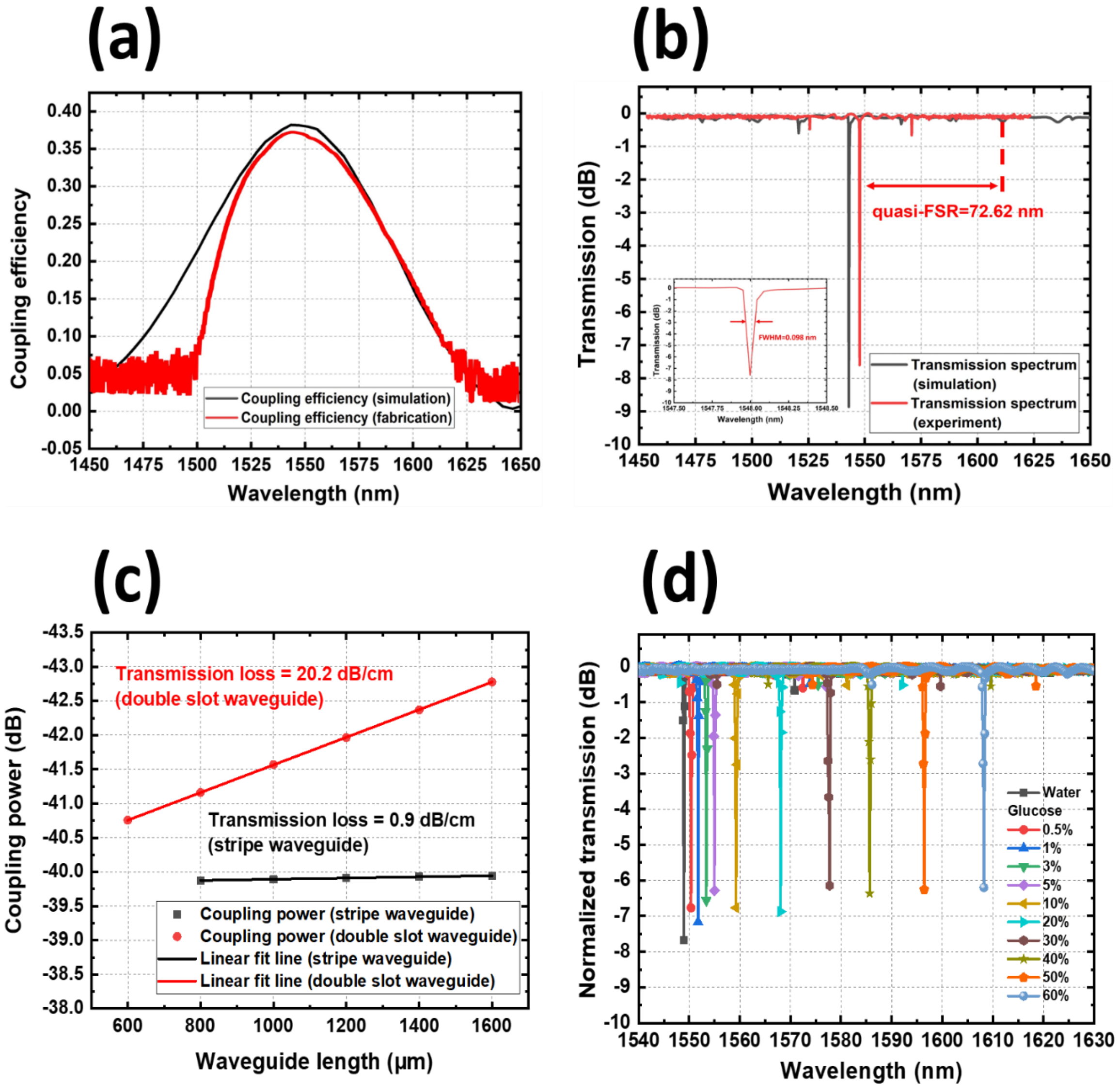

Fig.4.24 (a) Coupling efficiency of the simulated (black line) and fabricated (red line) focused grating coupler. (b) Transmission spectra of the simulated (black line) and measured (red line) IG-DSMRR. (c) Coupling power of the strip and double slot SOI waveguide vs waveguide length. (d) Measured transmission spectra for different concentrations of glucose solution.

The calculated enlargement factor of this device is up to 3.55, hence the operating range of the proposed IG-DSMRR is expanded significantly. The large FSR of the IG-DSMRR also brings advantages. Conventional MRRs can only detect glucose concentrations below 20% [137], while the large quasi-FSR of the IG-DSMRR allows higher concentrations to be measured without ambiguity. The Q-factor can be calculated from Eq. (26): from the transmission spectrum the resonant wavelength is 1547.7±0.1 nm and the FWHM is 0.09 nm, giving the Q-factor as 1.6×10^4. The measured coupling efficiency κ between the bus and the ring waveguide is about 1.40%.

The measured transmission losses of the straight strip and double slot SOI waveguides are shown in Figure 4.24(c) and are calculated from the coupled output power using different lengths of waveguides. The transmission loss is 0.9 dB/cm for the straight strip SOI waveguide, and 20.2 dB/cm for the straight double slot waveguide with air cladding. Under sensing condition, the calculated propagation loss of straight double slot waveguide is 55.8 dB/cm as noted above.

The transmission spectra for different concentrations of glucose and sodium chloride are shown in Figure 4.24(d) and Figure 4.25(b) respectively. Samples with different concentrations of glucose and sodium chloride were dropped onto the ring resonator. The resonant peak starts at 1547.7±0.1 nm and as the concentration of solute is increased, the waveguide effective index increases and the resonant peak in the spectrum is red shifted. The wavelength sensitivity can be calculated from the changes in the resonance and in the refractive index.

The simulated and measured sensitivities of the device to glucose and sodium chloride concentration are shown in Figure 4.25(a) and Figure 4.25(c) respectively. The simulated bulk sensitivities to glucose and sodium chloride are both 576 nm/RIU, while the measured structure bulk sensitivities are 552±5 nm/RIU and 563±5 nm/RIU respectively. The achieved bulk sensitivity is more than two times that of optimized designed single strip SOI-based quasi-TM MRRs [138]. It is also higher than that of reported SMRRs [139, 140]. The measured LOD values related to these sensitivities are 3.6×10^{-6} RIU and 3.7×10^{-6} RIU respectively. The concentration sensitivities are also shown in Figure 4.25(d), where the simulated concentration sensitivities are 1015 pm/% and 1004 pm/% for glucose and sodium chloride solutions respectively, with the experiment concentration sensitivities being 975±8 pm/% and 981±8 pm/% respectively. The corresponding measured concentration LOD values are both 0.02%. Experimentally, the central coupling wavelength of the grating couplers and the transmission peak of the IG-DSMRR were 10 nm blue shifted and 5 nm red shifted respectively compared with the simulation results, which may be because of fabrication errors and the analytes RIs fluctuations between the reference and the experiment.

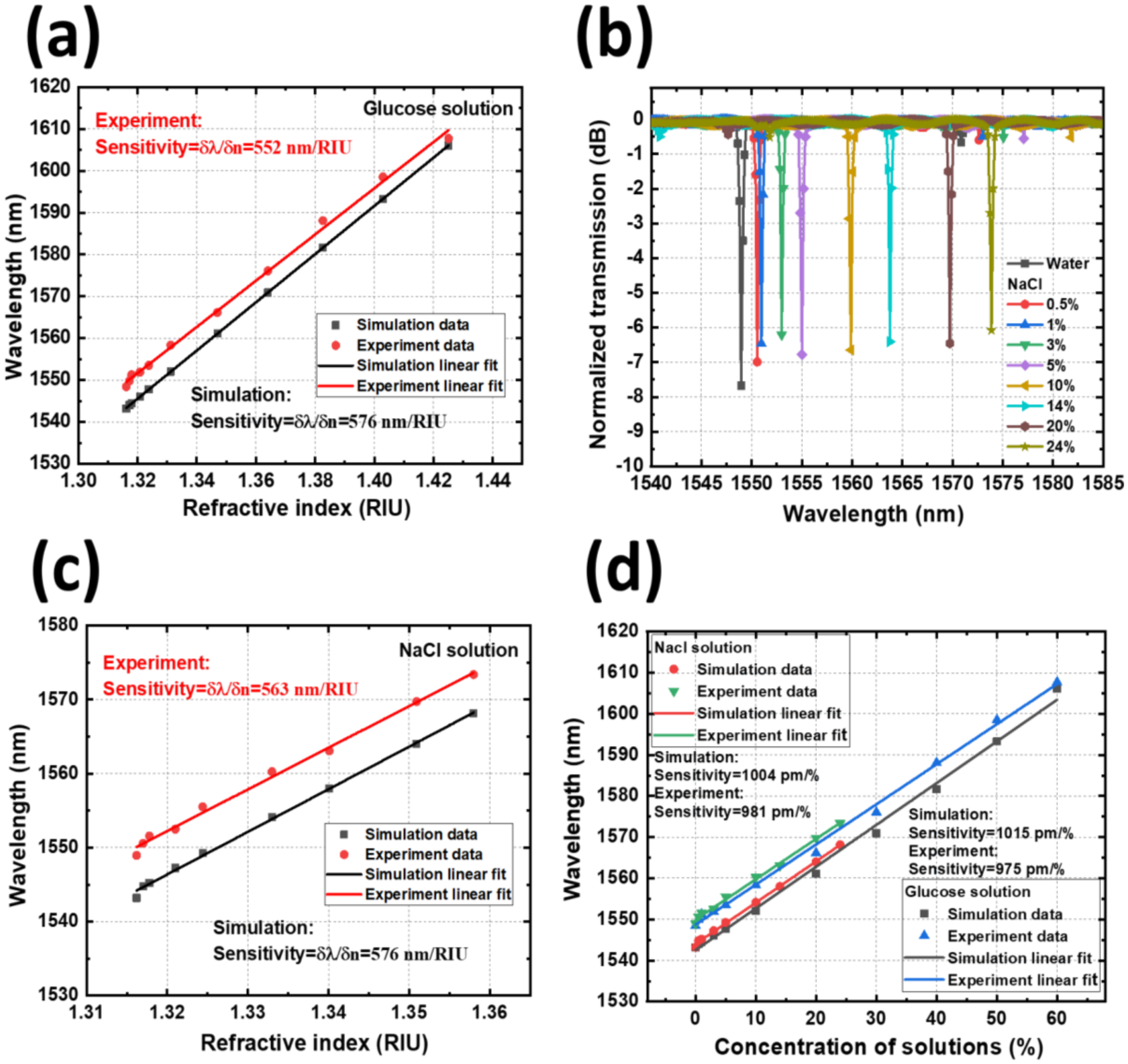

Fig.4.25 (a) The RI sensitivity of IG-DSMRR of simulation (square black line) and experiment (red dot line) (glucose). (b) measured transmission spectrum of different concentrations of NaCl solution. (c) The RI sensitivity of IG-DSMRR of simulation (square black line) and experiment (red dot line) (NaCl). (d) The simulation and experiment concentration sensitivity of IG-DSMRR for glucose and NaCl solutions respectively.

It is necessary to note that due to the lack of an accurate tool to measure the protein layer thickness t_{ad}, the measured surface sensitivity S_S could not be determined. However, we estimate that the experimental S_S value should be close to the simulated value of 0.219 nm/nm because the measured bulk sensitivity is nearly the same as that of the simulation.

4.5 Conclusions

In summary, this chapter provides a detailed introduction to all the fabrication tools and techniques involved in this research work. We invest a lot of time and effort into optimizing almost all key process steps. The high-quality fabrication achieved in this work allows various novel and state-of-the-art silicon photonics building blocks development. With the help of the stable and repeatable behaviour of these basic tools and techniques, more complex structures designed to meet the desired system requirements can be developed.

Furthermore, a compact size IG-DSMRR highly sensitive biochemical sensor was developed. The sensor is a combination of a double slot microring resonator and an inner wall angle grating. Compared with previously reported work on a similar dual-slot waveguide configuration, this structure with inner wall gratings is designed to have only one resonant peak, while the other peaks are suppressed. The new design therefore provides a combination of high sensitivity and large detection range in the compact size of a 6.72 µm centre radius non-levitated ring resonator structure. After design and modelling, high-precision EBL and dry etching were used to manufacture the device, and a groove waveguide ring resonator with micron-level radius and nano-level IG was realized. As a result, a record high sensitivity of 563±5 nm/RIU was achieved with a minimum LOD of 3.7×10^{-6} RIU. The concentration sensitivity can reach 981±8 pm/%, and the lowest concentration detection limit is less than 0.02%. The sensing structure achieves a high resonator Q-factor of 1.6×10^{4} and low propagation loss of 0.9 dB/cm for a straight single-strip waveguide in air and 20.2 dB/cm for a double-slot straight waveguide in air background environment.

Compared with ring resonator sensors based on a single SOI reported so far, its sensitivity is more than 2 times that of specially designed MRR, and its detection range is more than 3 times that of traditional slit MRR. Additionally, it is the first fabricated sensor to simultaneously combine an ultra-compact footprint, ultra-high sensitivity, and an ultra-large detection range. Although the IG-DSMRR is fabricated using EBL, it can also be fabricated using mass production CMOS processes. The SOI platform-based IG-DSMRR reported in this project can be applied to a variety of chemical, biomedical, and environmental applications.

It should be noted that the high sensitivity biochemical sensors compared with the current reported biochemical SOI sensors in many references to understand our novelty and improvement stage. The measured slot waveguide based microring resonator on SOI platform with similar radius is reported in [152] with sensitivity 298 nm/RIU. Thus our IG-DSMRR sensors shows two times than this measured sensitivity in reference. Therefore, we could conclude that our designed IG-DSMRR sensor design shows a sensitivity improvement (563 nm/RIU) than the current reported subwavelength grating biochemical sensor on SOI platform.

Chapter 5 Sidewall grating slot microring resonator

This chapter will introduce the novel microring resonator structure: sidewall grating slot microring resonator (SG-SMRR) biochemical sensor that could deal with two current MRR sensors limitations, the sensitivity limitation, and the detection range limitation. The sections below will also detail the working principle, simulation results, fabrication procedures and results, measurement stage and results, and the conclusion about the sensor performance compared with the reported structures before.

In this paper, we propose and experimentally demonstrate a compact label-free optical sensor using a combination of sidewall grating and slot micro ring resonator (SG-SMRR) structures. This sensor offers an FSR-free large detection range (84.5 nm in lab measurement), four times that of a conventional MRR, and high measured bulk sensitivity (620 nm/RIU) with a limit of detection (LOD) value of 1.4×10^{-4} RIU. The concentration sensitivity for a sodium chloride solution was as high as 1120 pm/% with a minimum concentration detection limit of 0.05%. The measured slot waveguide transmission loss is 5.2 dB/cm, and the Q-factor of the sensor is 5.2×10^{3}. This is the first demonstration of a fabricated SG-SMRR based on the SOI platform offering both FSR-free large detection range and high sensitivity.

5.1 Working principle

The structure design was inspired by the reported angular grating microring resonator for label-free optical biochemical sensing [148]. The sidewall grating slot waveguide idea was inspired by the reported straight sidewall grating slot waveguide reference demonstration [149]. This proposed structure design utilized the microring resonator structure with innerwall angular grating. The design principle is first demonstrating the wavelength selectivity, the fundamental modes effective indices of the microring waveguide with and without angular grating are calculated using the mode analysis. Then equivalent index of the angular grating is approximately by Rytov's formula. The bragg wavelength of this bragg angular gratings could be calculated using reflection condition. Meanwhile, the longitudinal modes of the MRR satisfy the resonant condition where the resonance wavelength of the longitudinal mode number can be selected. Based on the angular grating bragg wavelength and the microring resonant wavelength we could decide the final wavelength peak point and the grating and waveguide parameters. Then the transmission spectrum of the slot waveguide microring resonator and the sidewall grating slot waveguide are simulated and compared together to ensure the wavelength selective performance.

The SG-SMRR sensor was designed based on a standard SOI wafer structure consisting of a 220 nm top silicon layer and a 2 µm buried oxide (BOX) layer on a 675 µm thick silicon substrate. A three-dimensional (3D) schematic of the proposed sensing device with detailed parameters is illustrated in Figure 5.1. The structure parameters were calculated and optimized using the 2D and 3D Finite Difference Time Division (FDTD) and MODE solutions software from Lumerical Inc. (Vancouver, BC, Canada). The grating couplers were simulated to optimize the grating pitch, duty cycle, and fibre coupling position to achieve the highest coupling efficiency of 44%. The effective indices of the SMRR and SG were designed to achieve an operation wavelength near 1550 nm. The SG-SMRR structure was simulated using the Finite Difference Eigenmode (FDE) solver and variational-FDTD to calculate the mode field distribution and transmission spectral responses. A tuneable laser of TE-polarization (to match the TE0 fundamental mode of the waveguide) was injected into the strip bus waveguide, and pure water was chosen as the cladding material for the structural parameters' optimization. The structure contains focused grating couplers at the ends of the bus waveguides to couple the device optically to cleaved single mode fibres (SMF). The SMRR with sidewall grating enables sensing with high sensitivity over a large detection range. Homogeneous sensing was achieved by immersing this sensor device in aqueous solutions in both simulation and experiment. This sensing investigation can easily be extended to surface sensing applications by modelling the device with a thin adsorbed analyte layer covering the SG-SMRR.

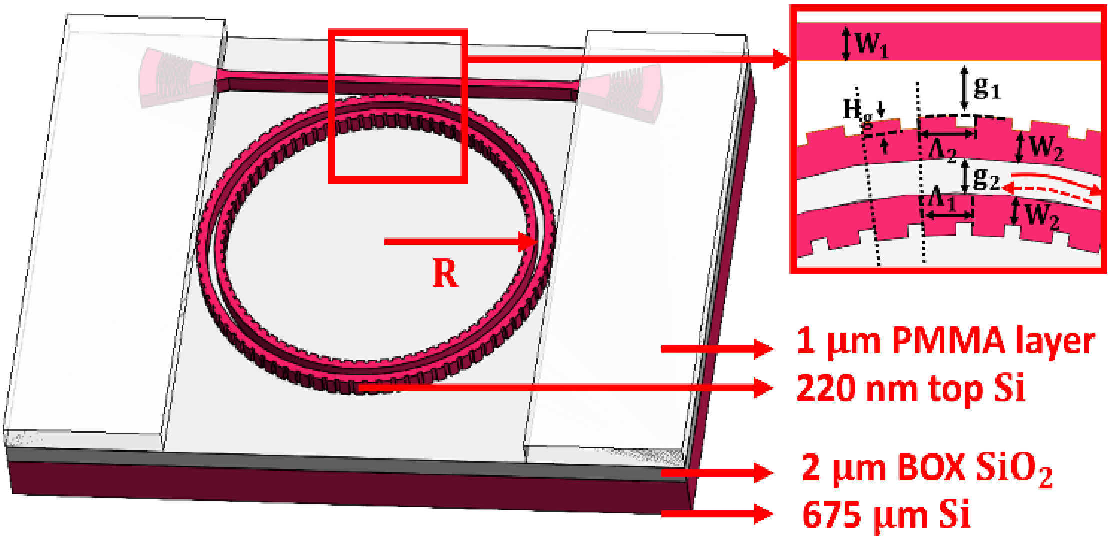

Fig.5.1 Schematic of the SG-SMRR device.

The bend radius (R) of the SG-SMRR is the distance between the centre of the rings and the centre of the slot, which was designed to be 5 µm. The gap width between the bus and the outer ring waveguide is denoted as g_1 (240 nm) and the slot width between the two ring waveguides is g_2 (100 nm). The bus waveguide width W_1 and slot waveguide width W_2 are both set to 200 nm, which results in a high mode confinement factor and extremely strong electric field enhancement in the slot. The etched SGs on the inner and outer slot waveguides have azimuthal periods of Λ_1(345 nm) and Λ_2 (368 nm) respectively. The duty cycle, or filling factor (FF, ratio of the silicon grating length to the period) is 85%, and the corrugation depth of the grating H_g is 10 nm.

The theory of the double peak transmission spectrum generated by this sensing structure is mainly based on the electromagnetically induced transparency (EIT)-like effect. Part of the injected light field propagates through the coupling region of the bus and microring waveguide in a clockwise direction and a part of the field is reflected counterclockwise by the gratings. The interactions between the two different propagating modes in the MRR produce the EIT-like effect. As is well known, a uniform Bragg grating is a partially reflective element. After optimization, the grating reflection spectrum stopband was centred at a specified resonant peak of the transmission spectrum of the MRR, and these double peaks then dominate with others suppressed. With the help of the reflection spectrum, only one EIT-like spectrum is retained over a relatively wide wavelength range. Thus, the EIT-like effect can be generated by the interaction between slot waveguide micro-ring resonators and sidewall gratings.

5.2 Simulation

First, the single-mode condition analysis simulation based on the structure parameters and sensing cladding layer we designed, and the result is shown in Figure 5.2 (a) and Figure 5.2 (b). It can be seen in Figure 5.2 (a) when the ridge waveguide W_1=200 nm, there is only TE_{00} mode because the cut-off ridge waveguide width for TE_{01} mode is 260 nm. When the slot gap is set to 100 nm, and the result in Figure 1(b) shows when the slot ridge waveguide W_2=200 nm, there is only TE_{00} mode because the cut-off ridge waveguide width for TM_{01} mode is 230 nm.

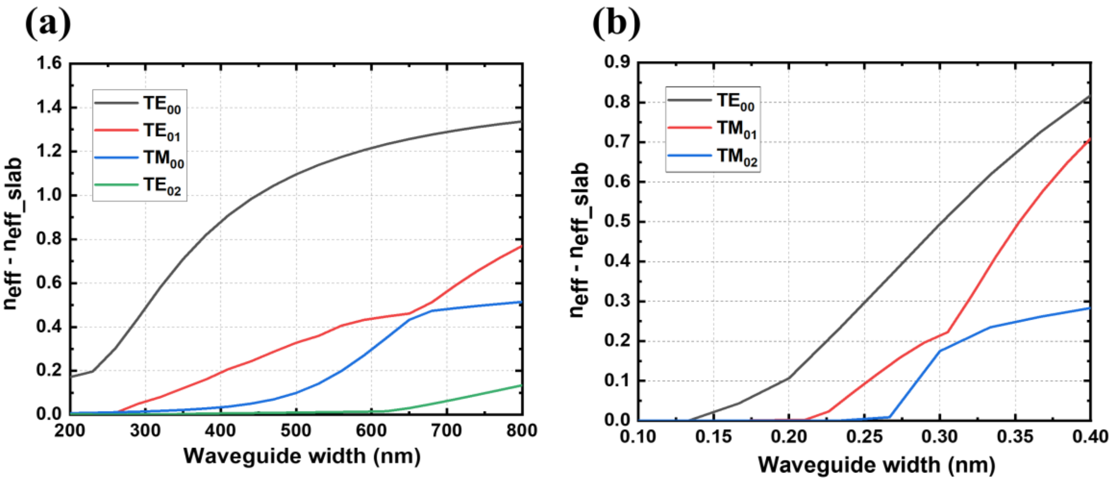

Fig.5.2 **(a) The transmission modes of different waveguide widths in bus waveguide, (b) The transmission modes of different waveguide widths in slot waveguide.**

Then simulated the mode field distribution of the slot sidewall grating and the electric field distribution of the SG-SMRR, and the results are shown in Figure 5.3 (a) and (b) respectively. The optical confinement factor in the slot is 0.4.

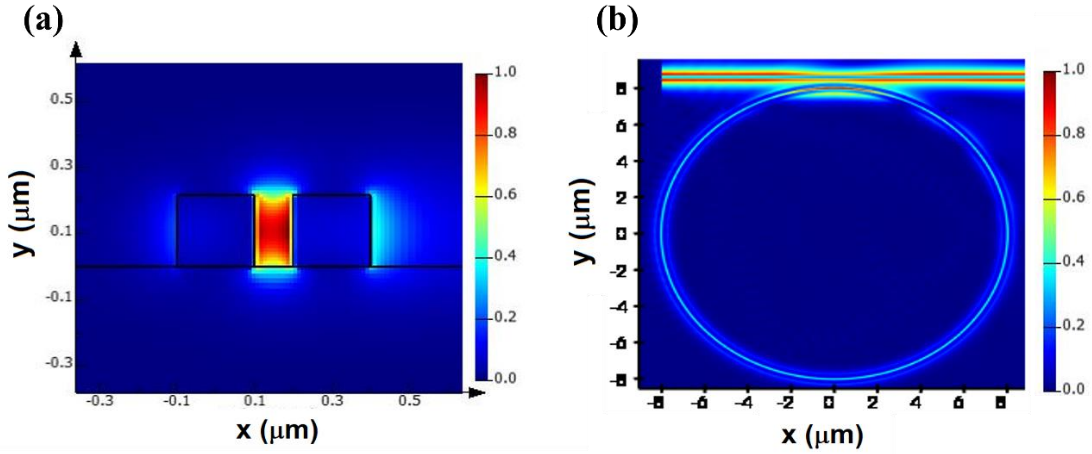

Fig.5.3 (a) The E_x-field of TE polarized light in the designed slot waveguide structure, (b) the electric field distribution of the SG-SMRR.

After that, the simulated transmission spectrum of the slot waveguide with sidewall grating and the SG-SMRR is simulated to ensure the filtering is operating at the resonant peak of SG-SMRR near 1550 nm. The other resonant peaks of the SMRR structures are suppressed. The simulated results are shown in Figure 5.4.

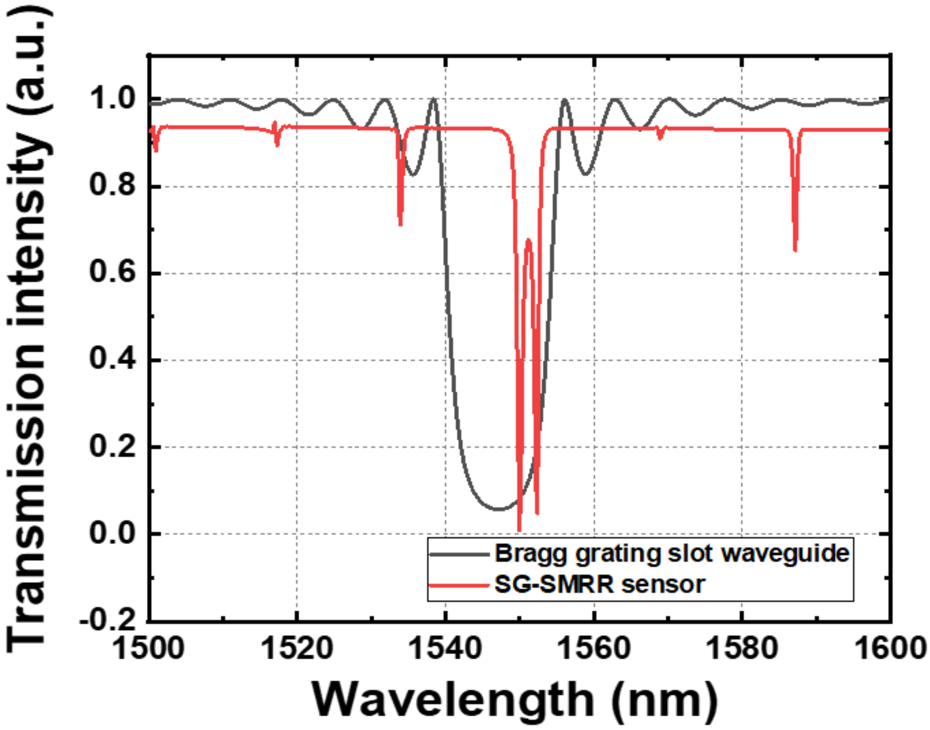

Fig.5.4 **Transmission spectrum of designed sidewall grating slot waveguide and the SG-**SMRR sensor.

The simulated coupling efficiencies as a function of the wavelength of the output grating coupler are shown in Figure 5.5. In simulation, the central wavelength and coupling efficiency of the designed grating coupler are 1556 nm and 44% respectively. The transmission spectra of the simulated SG-SMRR with RO water cladding layer are shown in Figure 5.6. The simulated principal resonant double peaks are at 1554.2 nm and 1556.6 nm respectively and can be tuned from 1555.5 nm to 1650 nm with different RIs solutions as cladding layers.

The distance between the first main peak and the maximum measurement range that could be achieved in the experiment is defined as the quasi-FSR. In theory and simulation, this proposed sensor is free of FSR limitation, and the detection range is unbounded.

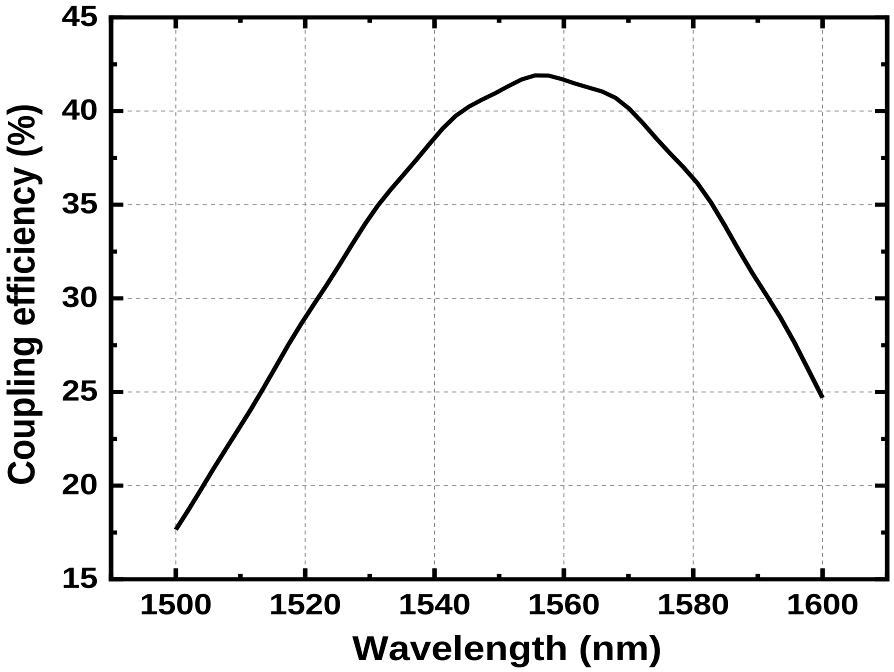

Fig.5.5 Coupling efficiency of the simulated focused grating coupler.

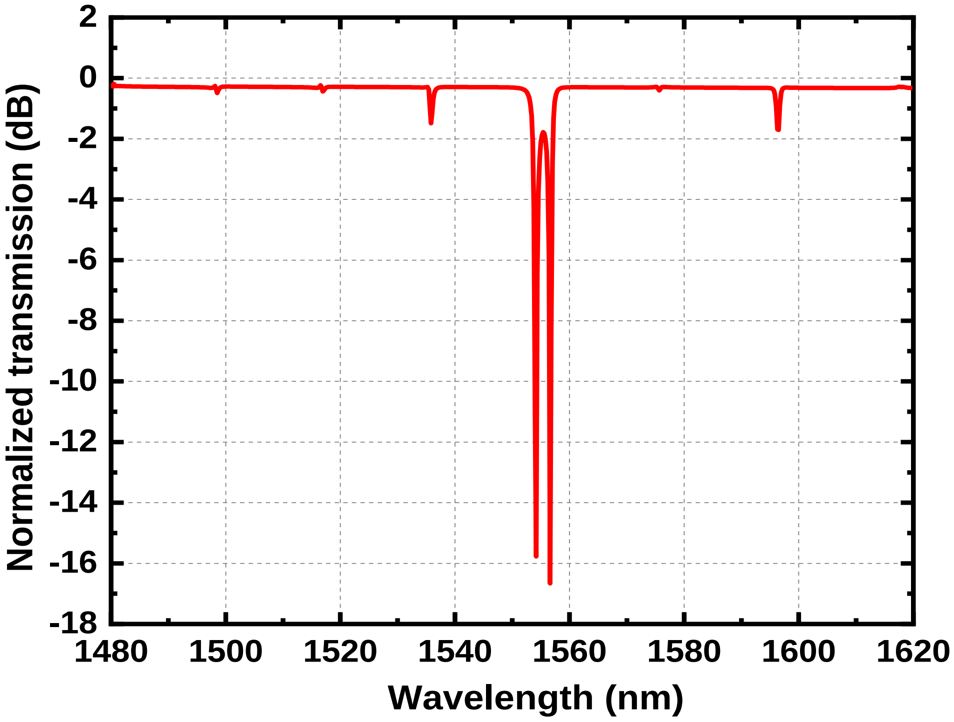

Fig.5.6 The simulated transmission spectrum of SG-SMRR sensor with RO water cladding.

In the bulk and concentration sensitivity measurement, different concentrations of sodium chloride (NaCl) and D-glucose ($C_6H_{12}O_6$) were used as analytes and dropped onto the SG-SMRR. Concentration changes (mass%) of sodium chloride and glucose result in the

RI changes, which can be derived using a third-order polynomial fit described in section 3.2. The simulated transmission spectra for different concentrations of glucose and sodium chloride are shown in Figure 5.7 (a) and (b) respectively. The resonant double peaks initially start at 1554.2 nm and 1556.6 nm respectively and are red shifted when the concentration of solution is increased. The simulated RI sensitivities (S_{RI}) for sodium chloride are 650 nm/RIU, and for glucose are 646 nm/RIU.

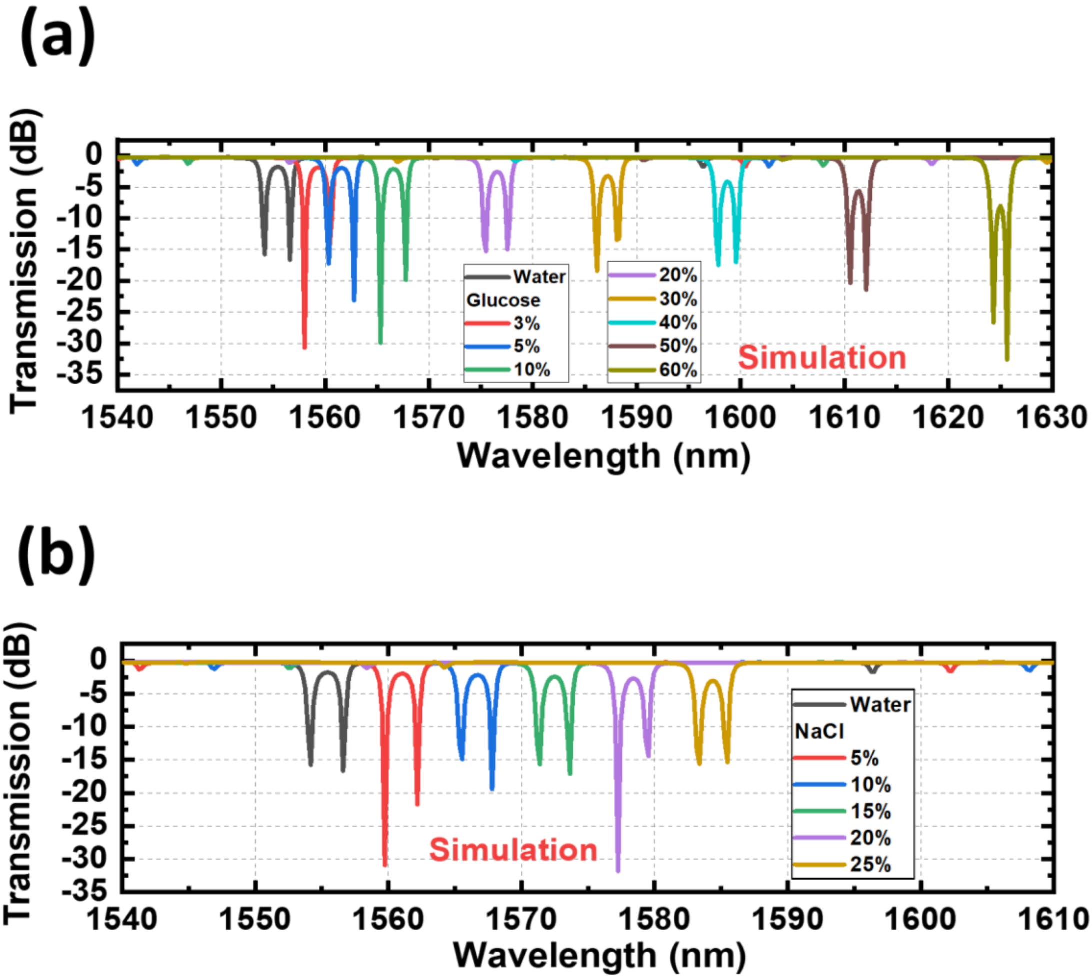

Fig.5.7 (a) Simulated transmission spectra of different concentrations of glucose solutions, (b) Simulated transmission spectra of different concentrations of NaCl solutions.

5.3 Fabrication

The fabrication process consisted of 4 main steps, as shown in Figure 5.8. The steps are similar to those illustrated in section 4.3.2 except the fourth step, a 1 μm polymethyl methacrylate (AR-P 642 200k Anisole 12% PMMA) resist layer was spun, exposed, and developed to create an open window on the ring resonator part for sensing. The electron-beam lithography (EBL) resist thicknesses, EBL doses, and beam step size (BSS) were optimized to give a high-resolution sidewall grating and smooth sidewall waveguide.

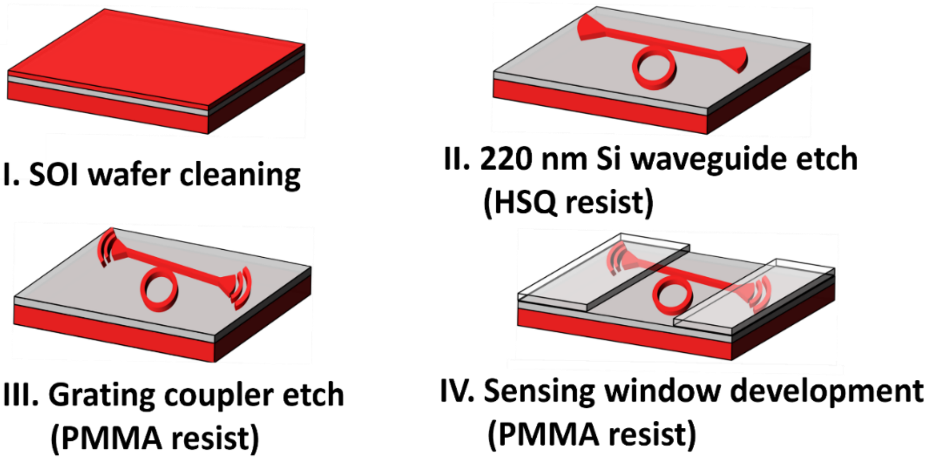

Fig.5.8 Fabrication steps of the device.

A top-view scanning electron microscope (SEM) picture of a fabricated SG-SMRR device is shown in Figure 5.9 and a zoomed SEM picture of the SMRR with SG is shown in Figure 5.10. The measured period and duty cycle of the fabricated grating coupler are 672 nm and 39.9% with an etch depth of 100 nm (close to the designed period of 671 nm and duty cycle of 39.9%). The differences are due to proximity effects during the EBL writing and sidewall etching errors during the inductively coupled plasma (ICP)-reactive ion etching (RIE) process.

Here, it is essential to highlight the performance of the devices on the wafer sample we have manufactured. The wafer area scale we use in fabrication is 11×12 mm^2. Normally we can fabricate 30 devices each column with 5 columns of different designed structures. In measurement, we tested 30 SG-SMRR sensors in one column with 25 devices could work well and perform the designed transmission spectrum (80% yield percentage). The measurement results reported here for the SG-SMRR sensor are based on the optimal best performance sensor selected for analysis. For the 80% yield our analysis is the dry etch non uniformity and the resist development which may bring some difference between the designed parameters and the fabricated parameters. This may cause the unsatisfied performance.

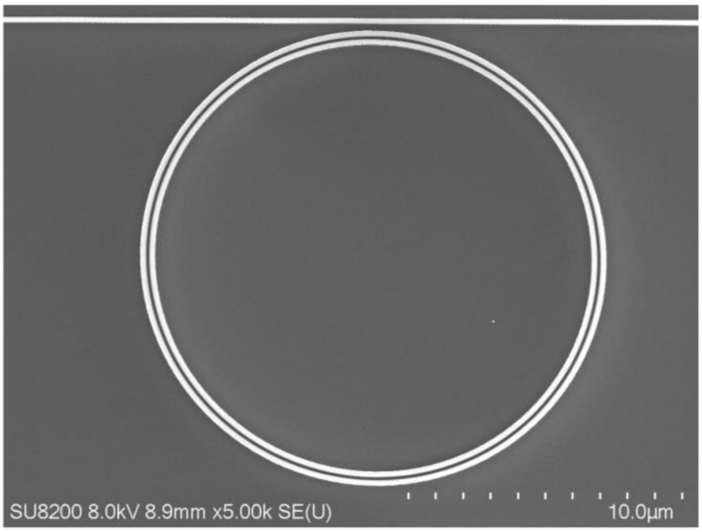

Fig.5.9 SEM images of the SG-SMRR sensor.

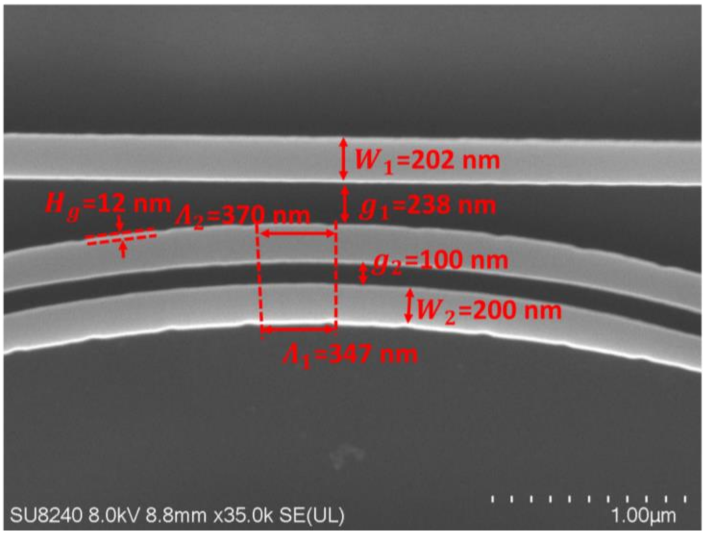

Fig.5.10 Zoomed bus waveguide, SMRR, and SG.

5.4 Measurement

The measurement setup for SG-SMRR sensor is the same as the measurement setup shown in chapter 3. The Super Luminescent Diode (SLD) from THORLABS with central wavelength of 1550 nm and maximum output power 22 mW is used as the broadband light source, and optical spectrum analyser (OSA) with 0.06 nm resolution bandwidth (RBW) is used as the transmission spectrum measurement. The TE polarized input and output light were coupled into and out of the sensor via 10 µm cleaved SMFs with 10˚ input and output angles through the grating couplers (GCs). For sensitivity measurement and calculation, different concentrations of solutions or analytes are dropped on the sensing MRR structure's part. An automated measurement system using LABVIEW software based on the general-purpose interface bus (GPIB) connection was employed for swift data acquisition, especially important for quickly evaporating solvents like acetone and IPA.

The simulated and measured coupling efficiencies as a function of the wavelength of the output grating coupler are shown in Figure 5.11. In measurement, the central wavelength and coupling efficiency of the fabricated grating coupler are 1555 nm and 41% respectively (the simulated central wavelength and coupling efficiency are 1556 nm and 44% respectively). The difference in central wavelength and coupling efficiency may be due to deviations in the coupling tilt angle of the SMFs. The transmission spectra of the simulated and measured SG-SMRR with water cladding layer are shown in Figure 5.12. The measured principal resonant double peaks are at 1555.5±0.1 nm and 1557.6±0.1 nm respectively and can be tuned from 1555.5 nm to 1650 nm with different RIs solutions as cladding layers (the simulated resonant double peaks are at 1554.2 nm and 1556.6 nm respectively). The small 1-nm redshift of the measured resonant peak compared with the simulation result is due to fabrication errors in the SG period and FF.

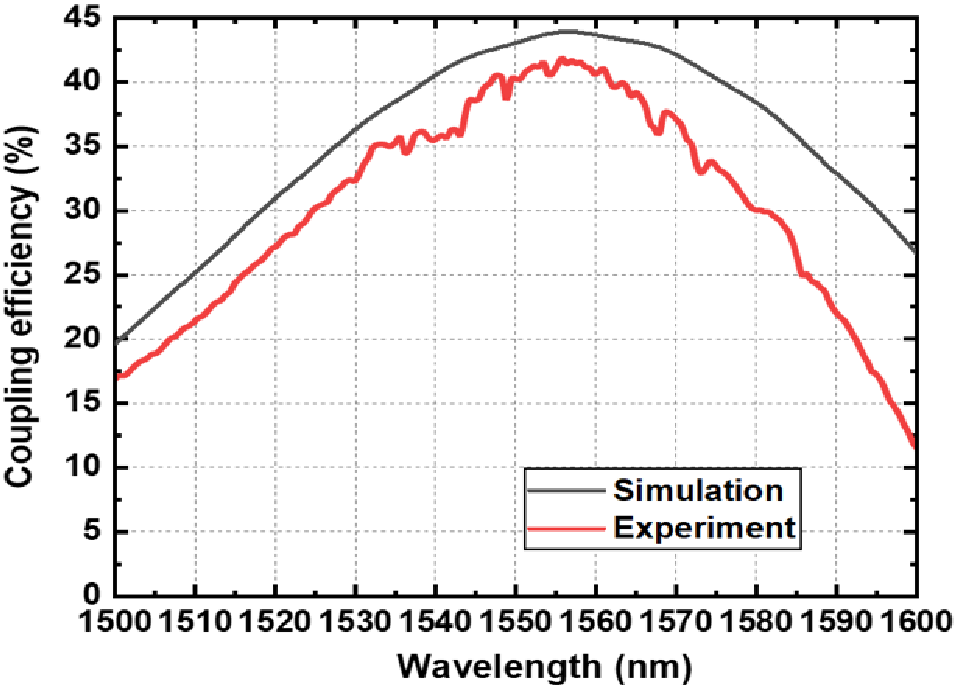

Fig.5.11 Coupling efficiency of the simulated (black line) and measured (red line) focused grating coupler.

The distance between the first main peak and the maximum measurement range that could be achieved in the experiment is defined as quasi-FSR. In theory and simulation, this proposed sensor is free of FSR limitation, and the detection range is unbounded. Due to the wavelength range limit of the SLD broadband light source and the OSA used in lab measurement, the practical limit of the measured quasi-FSR is 84.5 nm, 4.2 times that of the FSR of the conventional SMRR (20.4 nm). Hence the operating range of the proposed SG-SMRR is expanded significantly. This wide operating range brings the advantage of wide dynamic range (in terms of analyte concentration) and enabling measurement of high-concentration analytes. The Q-factor can be calculated as the resonant wavelength (1555.5 nm) divided by the FWHM (0.3 nm) of the measured transmission spectrum. The calculated Q-factor is 5.2×10^3, which is two times that of the SMRR with a grating structure reported in [141]. The transmission loss of the slot SOI waveguides is measured from the coupled output power using different lengths of waveguide. The transmission loss is 5.2 dB/cm for the straight slot SOI waveguide with air cladding. The water absorption loss is 47.5 dB/cm at a wavelength of 1.55 μm [131] and the optical confinement factor in the slot is 0.4. Thus, the propagation loss of the straight slot waveguide is 5.2 dB/cm+0.4×47.5 dB/cm=24.2 dB/cm under sensing conditions.

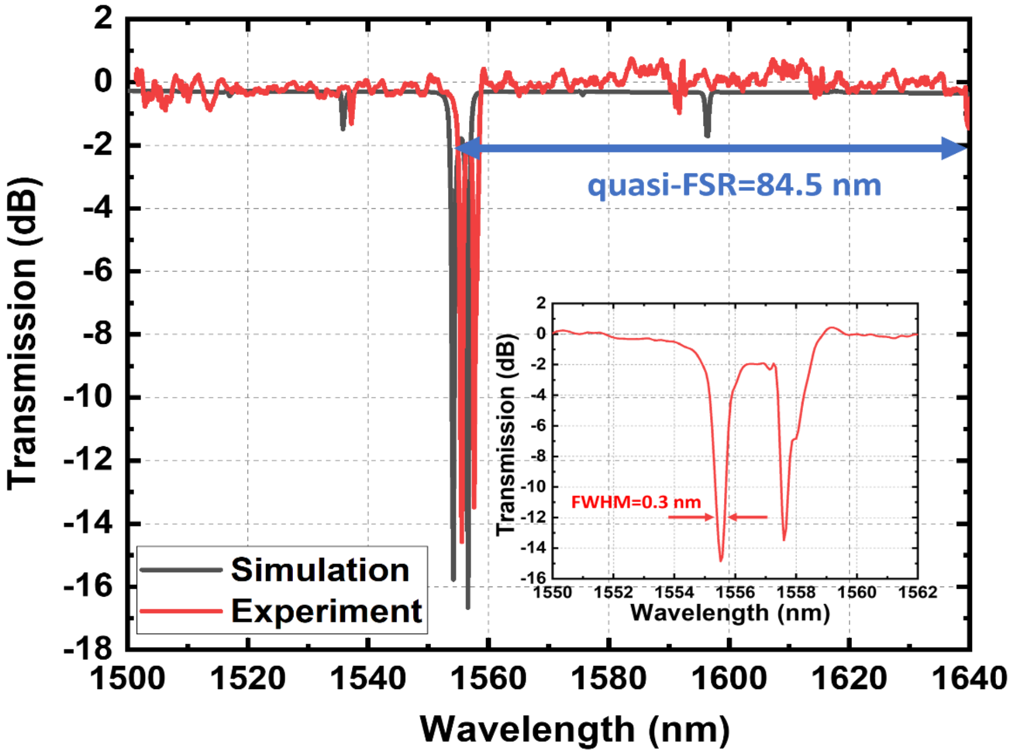

Fig.5.12 Transmission spectra of the simulated (black line) and measured (red line) SG-SMRR with water cladding layer.

In the bulk and concentration sensitivity measurement, different concentrations of sodium chloride (NaCl) and D-glucose ($C_6H_{12}O_6$) were used as analytes dropped onto the SG-SMRR. Concentration changes (mass%) of sodium chloride and glucose result in the RI changes, which can be derived using a third-order polynomial fit described in [142]. The simulated and measured transmission spectra for different concentrations of glucose and sodium chloride are shown in Figure 5.13(a), (c), and Figure 5.13(b), (d) respectively. The resonant double peaks initially start at 1555.5 nm and 1557.6 nm respectively and are red shifted when the concentration of solution is increased.

The simulated and measured RI and concentration sensitivities of the device to glucose and sodium chloride concentration are shown in Figure 5.14 and Figure 5.15 respectively. The simulated and measured RI sensitivities (S_{RI}) for sodium chloride are 650 nm/RIU and 620±2 nm/RIU respectively, and for glucose are 646 nm/RIU and 616±2 nm/RIU respectively. The derivation of the two measured sensitivities is limited by RBW of the OSA. The measured RI sensitivity is more than two times that of optimized designed single strip SOI-based quasi-TM MRRs, and higher than that of previously reported SMRRs in [143-144]. The related measured RI LOD value for NaCl is 1.4×10^{-4} RIU. The measured concentration sensitivities (Sc) are 1120±5 pm/% and 1095±5 pm/% for NaCl and glucose solutions respectively, and the corresponding simulation values are 1156 pm/%

and 1139 pm/%. The corresponding measured concentration LOD values for NaCl is 0.05%. It should be noted that the surface sensitivity (Ss) could not be determined experimentally due to the lack of an accurate molecules binding and protein layer thickness measurement tool. However, we estimate that the experimental Ss value should be close to the simulated value of 5.2 nm/nm based on the RI and concentration sensitivity results.

A comparison of the performance of different SOI MRR sensors is shown in Table 5.1. Our sensor shows advantages in terms of its simple structure (single bus waveguide), FSR free detection range, higher Q-factor and extinction ratio (ER), and high sensitivity verified experimentally. The SRI in [145] is comparable to ours but is based only on simulation results.

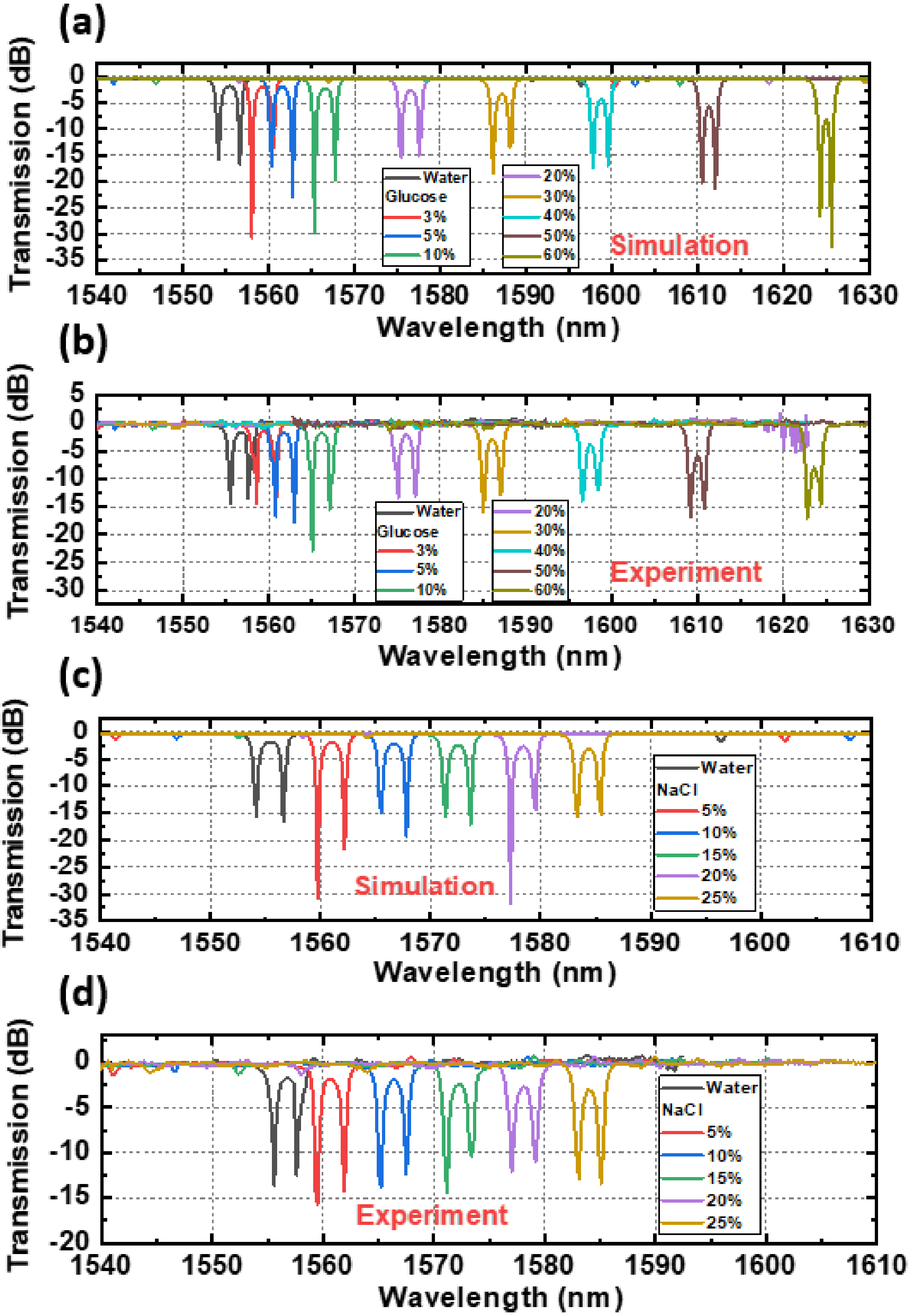

Fig.5.13 (a) Simulated and measured (b) transmission spectra of different concentrations of glucose solutions, (c) Simulated and measured (d) transmission spectra of different concentrations of NaCl solutions.

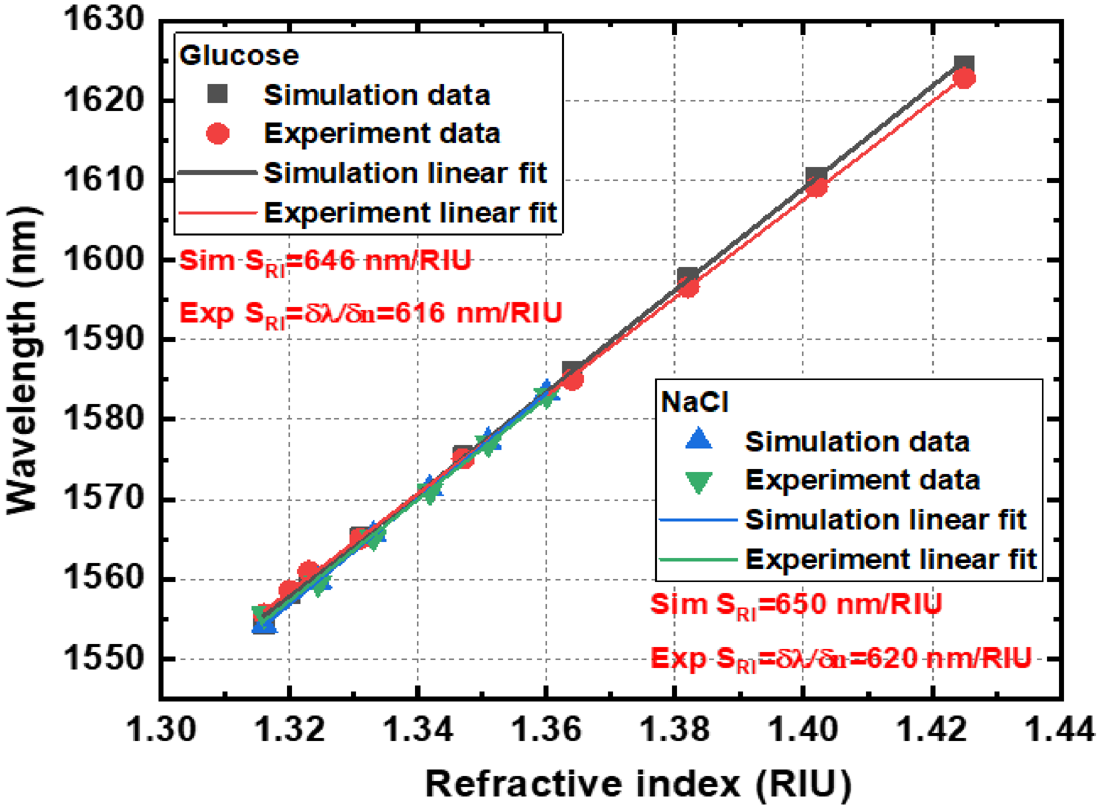

Fig.5.14 Simulation and experimental RI sensitivities of SG-SMRR for glucose and NaCl solutions respectively.

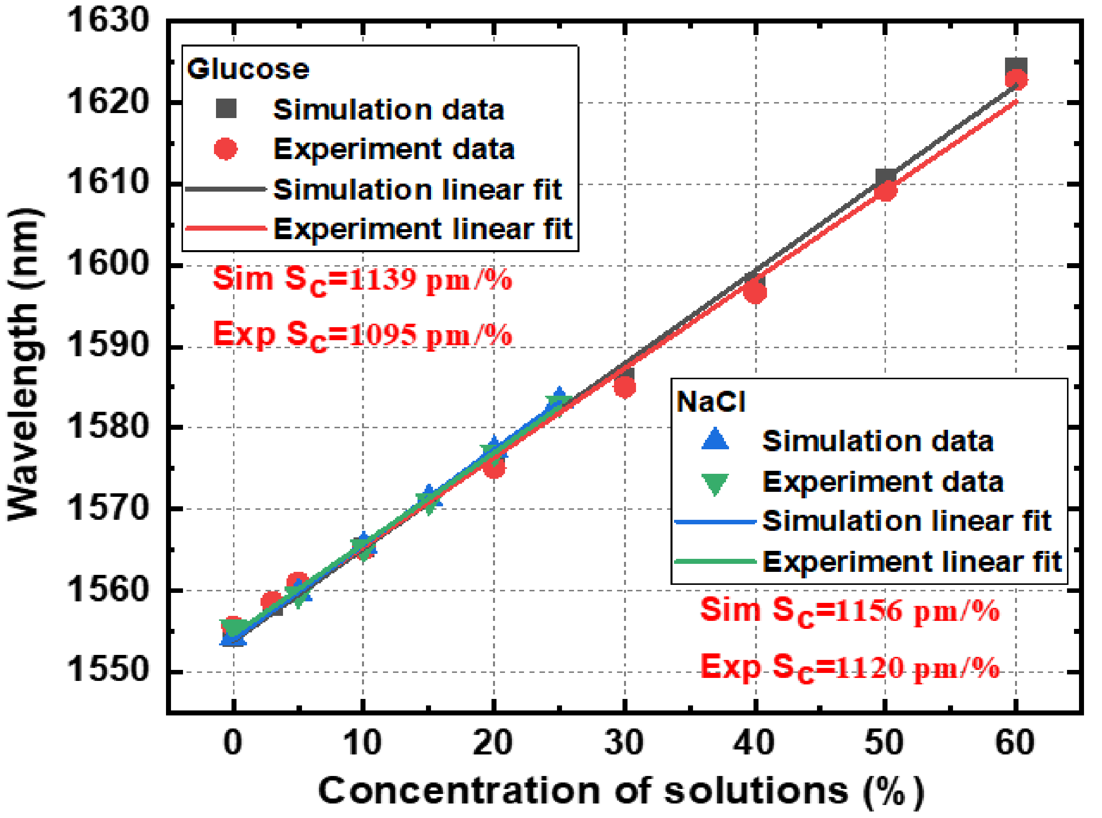

Fig.5.15 Simulation and experimental concentration sensitivities of SG-SMRR for glucose and NaCl solutions respectively.

Table 5.1 Some features comparison of SOI MRR sensors

	S_{RI} (nm/RIU)	Q	ER (dB)	FSR (nm)
Optimized SMRR [146]	403	1.2×10^3	14	23
Grating DSMRR [147]	433	4.3×10^3	10	Free
IG-SMRR [145]	643	1.4×10^3	11	
This work	650/620	5.2×10^3	15	Free

5.5 Conclusion

A novel and compact SG-SMRR biochemical sensor (5 μm radius) based on the SOI platform has been proposed and demonstrated experimentally. The measured bulk sensitivity and LOD values are 620±2 nm/RIU and 1.4×10^{-4} RIU, respectively. The concentration sensitivity and minimum concentration detection limit are 1120±5 pm/% and 0.05%. Moreover, the theoretical detection range is FSR free, and the experimental detection range is significantly enlarged to 84.5 nm, four times that of the free spectral range of conventional slot MRRs. Under sensing conditions, the measured Q-factor is 5.2×10^3 and the straight slot waveguide transmission loss is 24.2 dB/cm under sensing conditions.

It should be noted that the high sensitivity biochemical sensors compared with the current reported biochemical SOI sensors in many references to understand our novelty and improvement stage. The measured slot waveguide based microring resonator on SOI platform with similar radius is reported in [152] with sensitivity 298 nm/RIU. Thus our SG-SMRR sensors shows two times than this measured sensitivity in reference. Therefore, we could conclude that our designed SG-SMRR sensor design shows a sensitivity improvement (620 nm/RIU) than the current reported subwavelength grating biochemical sensor on SOI platform.

Chapter 6 Subwavelength grating cascaded microring resonator sensor

This chapter introduces a novel microring resonator structure designed to achieve high sensitivity photonics biochemical sensors: the Subwavelength Grating Cascaded Microring Resonator (SWG-CMRR) sensor. This innovative design aims to address current limitations associated with conventional MRR sensors and offers the potential for ultra-high sensitivity. The sections below will provide a comprehensive overview of the SWG-CMRR sensor, including its working principle, simulation results, fabrication procedures and outcomes, measurement stages and results, and a conclusion that assesses the sensor's performance relative to previously reported MRR sensing structures.

6.1 Working principle

The structure design was inspired by the reported multi-slot sub-wavelength Bragg grating refractive index sensor on SOI platform [150]. This reported structure mainly focused on the straight waveguide sensor design and demonstration. While the second reference inspire us is the subwavelength multibox waveguide microring resonator label-free biosensors on SOI platform [151]. Our proposed structure intends to combine both advantages from multi-slot subwavelength Bragg grating and the microring resonator structure and improve the sensitivity based on the reported subwavelength sensors on SOI platform.

The novel structure of subwavelength grating cascaded microring resonator sensing structure is shown in Figure 6.1. This sensor mainly utilizes the combination of subwavelength grating microring resonator and multi-box straight waveguide structures. These two structures are widely recognized as the primary configurations for achieving high sensitivity in biochemical and bimodal sensing . Our primary objective, which is sensitivity, can be significantly enhanced by integrating these two structures.

The three-dimensional structure illustration is shown in Figure 6.1, where the sensor combines subwavelength grating microring resonator and multi-box straight waveguide together to achieve ultra-high sensitivity. The detailed parameters are shown in Figure 6.2. The multi-box straight waveguide width is defined as W_1=1.2 μm, the multi-box segment length is defined as a=150 nm and the multi-box grating period is defined as p=250 nm (the filling factor FF is 0.6). The slot width between each multi-box grating row is defined as s=80 nm. The subwavelength grating microring resonator has the same grating segment width and grating period as straight multi-box waveguide. The gap between the straight multi-box waveguide and the subwavelength microring resonator is defined as g=100 nm. The radius of the subwavelength microring resonator is defined as the distance between the centre of the ring to the outer radius of the inner subwavelength microring resonator, with a value of R=5 μm.

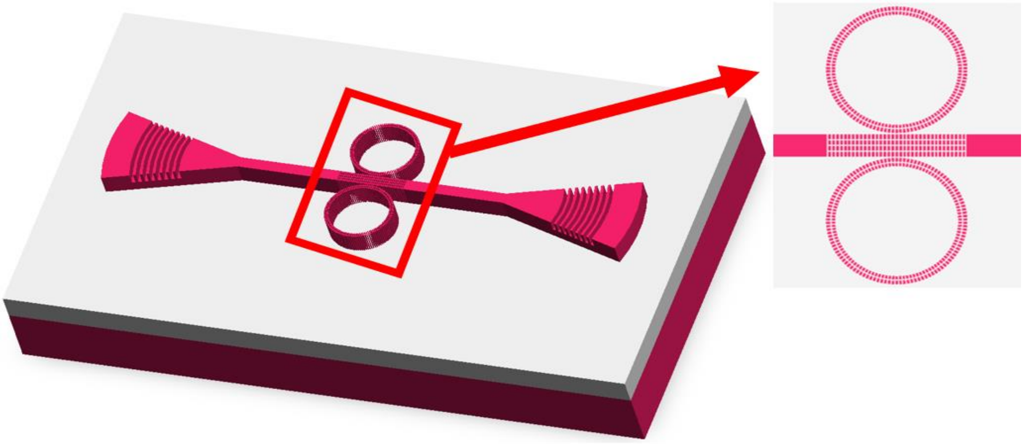

Fig.6.1 Structure of the subwavelength waveguide microring resonator.

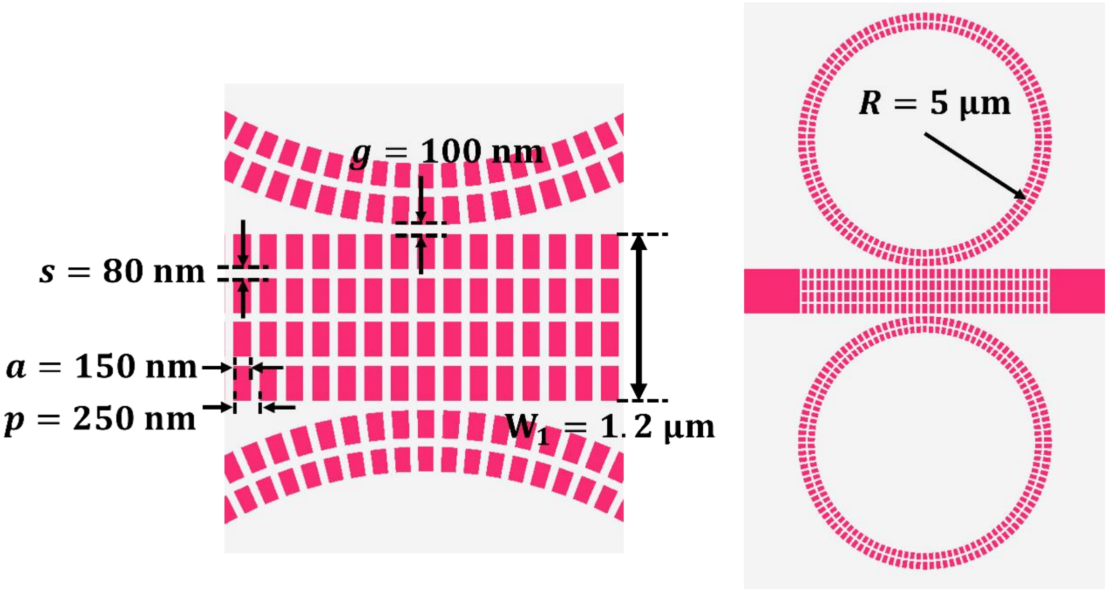

Fig.6.2 The design parameters of SWG-CMRR sensor.

6.2 Simulation

The structure has been meticulously designed through the simulation of a multi-box straight waveguide and a subwavelength grating microring resonator. The subwavelength grating dimensions have been carefully optimized to ensure optimal performance of the multibox waveguide, the subwavelength grating microring resonator, and the coupling between these cascaded subwavelength microring resonators and the multi-box bus waveguide. The period and filling factor (FF) of the subwavelength grating have been precisely tailored to achieve an effective refractive index (RI) suitable for guiding light within the subwavelength grating waveguide, and to enable strong light confinement within the slots between subwavelength gratings for evanescent field sensing. In pursuit of compact biochemical sensors, we have chosen a radius as a compromise between the microring resonator size and the transmission loss in the bend waveguide.

The simulated electric field distribution of the subwavelength grating cascaded microring resonator are shown in Figure 6.3 as follows. This sensing structure utilize both sub wavelength multi-box straight waveguide and subwavelength microring resonator to achieve ultra-high sensitivity in MRR sensing structures. The strong light confinement inside the slots of the subwavelength straight waveguide and the subwavelength microring resonator could be achieved using our structure parameters design. The sensitivity of this biochemical sensors could be dramatically enhanced compared with other microring resonator sensing structures reported before. Additionally, we have conducted in-depth simulations to analyse the electric field (Ex) distribution within the multi-box straight waveguide and the subwavelength microring resonator. The simulation results, providing insights into this distribution, are illustrated in Figure 6.4 and Figure 6.5.

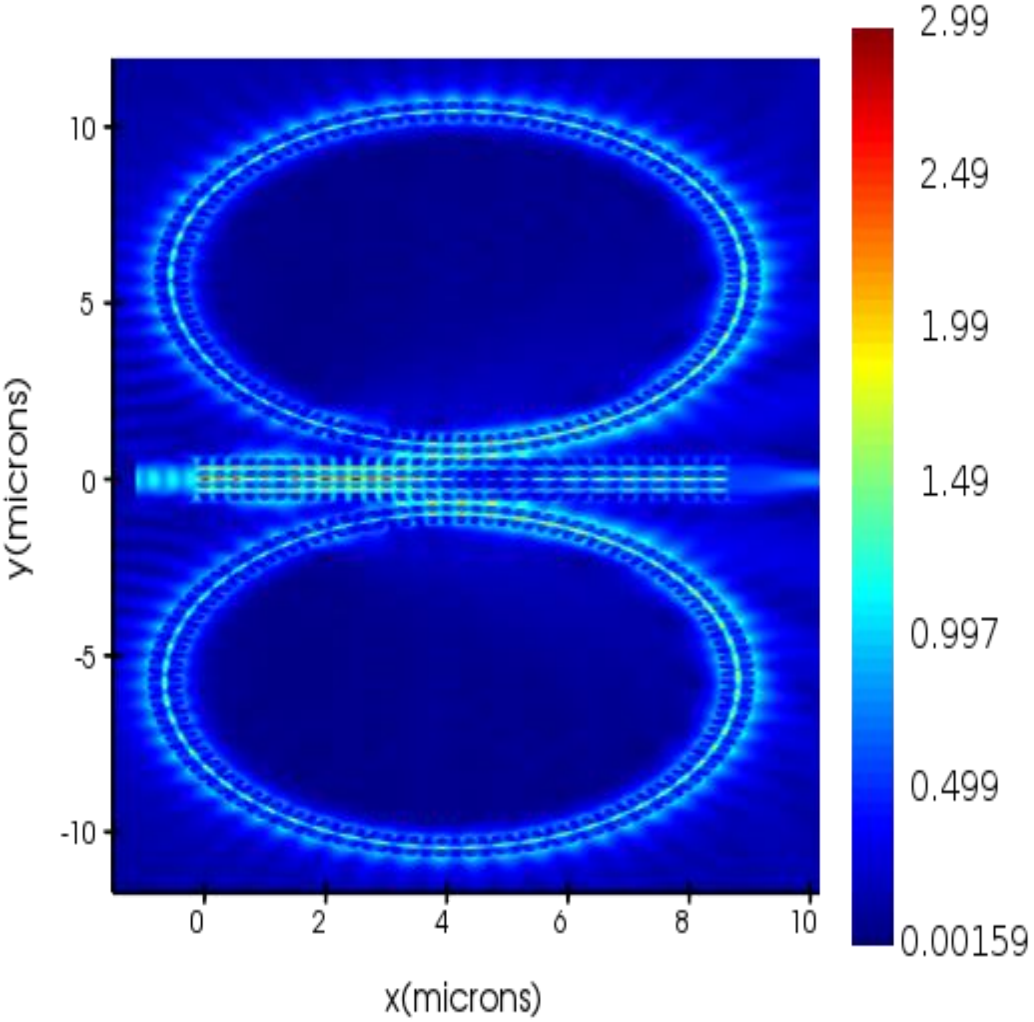

Fig.6.3 The electric field distribution of the SWG-CMRR.

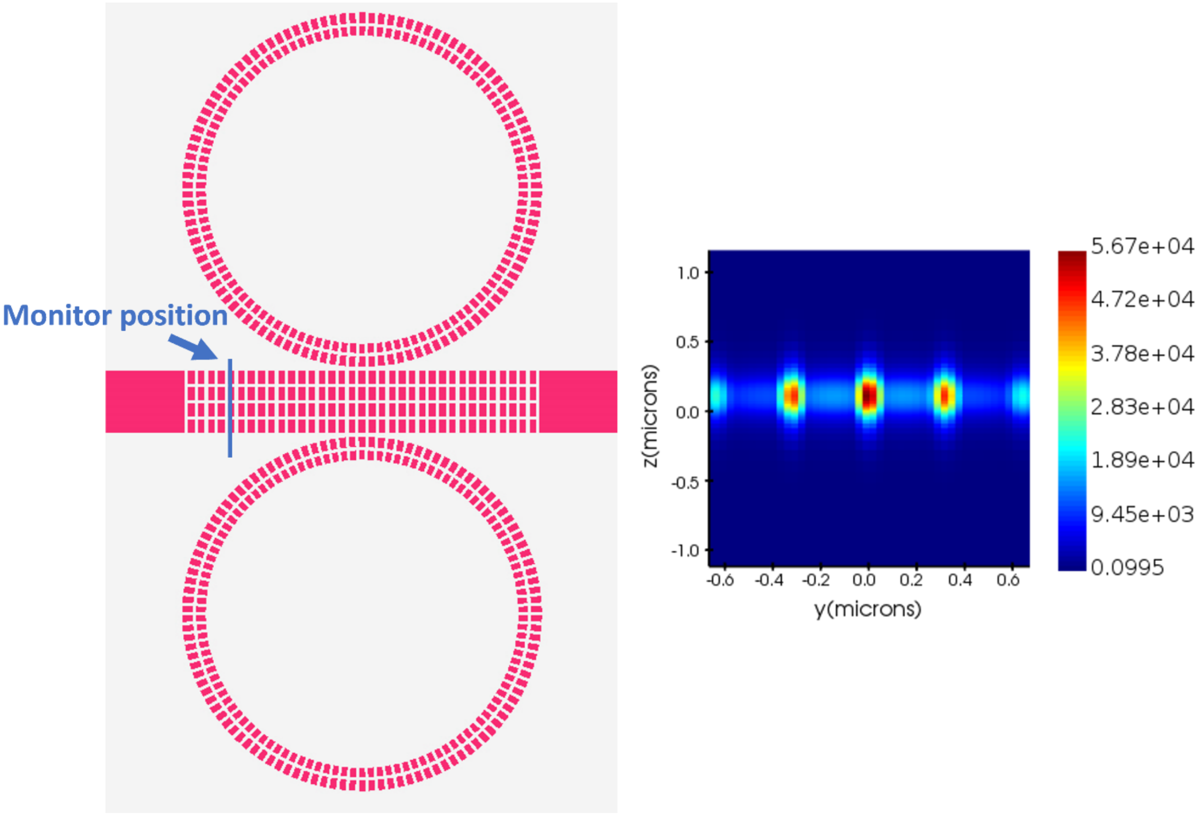

Fig.6.4 **The Ex field distribution of the multi-box straight waveguide.**

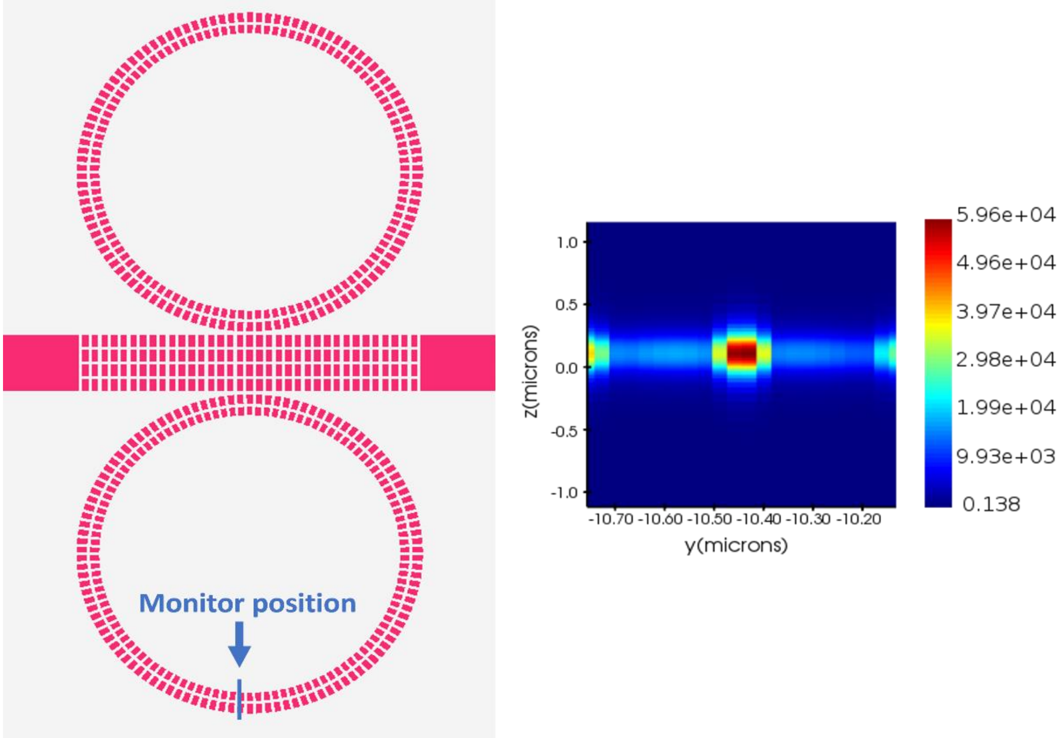

Fig.6.5 The E_x field distribution of the subwavelength grating microring resonator.

We have simulated the transmission spectrum of the subwavelength grating cascaded microring resonator sensor with RO water as the cladding background, as illustrated in

Figure 6.6. The graph exhibits five distinct resonant peaks within a wavelength range of 1450 nm to 1650 nm. For our subsequent sensitivity measurement and calculations, we focus on the resonant peak occurring near 1550 nm, specifically at 1547.7 nm. The simulated Free Spectral Range (FSR) value is determined to be 39.8 nm, and the Extinction Ratio (ER) value is measured at 18.1 dB.

In the bulk and concentration sensitivity measurement, different concentrations of sodium chloride (NaCl) and D-glucose ($C_6H_{12}O_6$) were used as analytes as cladding layers covering the sensing part. Concentration changes (mass%) of sodium chloride and glucose result in the RI changes, which can be derived using a third-order polynomial fit described in section 3.2. The simulated transmission spectra for different concentrations of glucose and sodium chloride are shown in Figure 6.7 and Figure 6.8 respectively. The resonant peak using RO water refractive index as cladding layer background initially starts at 1547.7 nm and are red shifted when the concentration of analyte solution is increased, the tuning range starts from 1547.7 nm to 1638 nm.

The calculated RI sensitivities (S_{RI}) based on simulation results are shown in Figure 6.9 and Figure 6.10 for glucose is 802 nm/RIU and for sodium chloride is 838 nm/RIU.

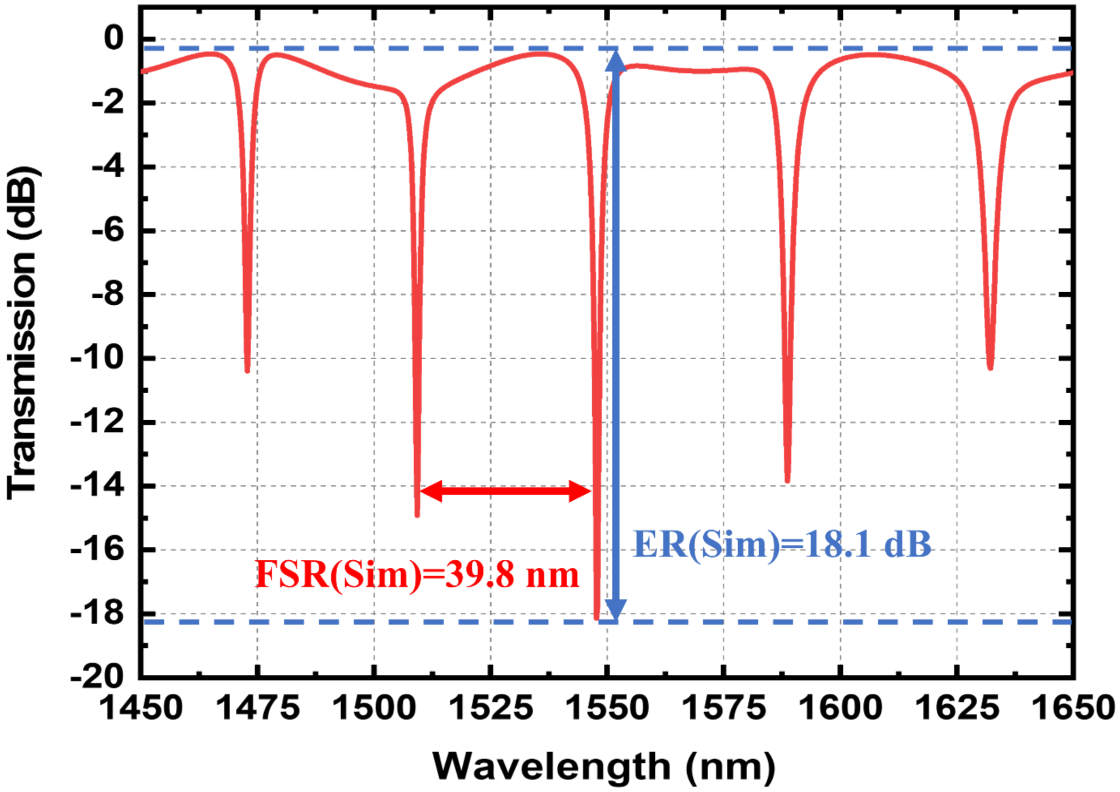

Fig.6.6 Simulated transmission spectrum of the SWG-CMRR.

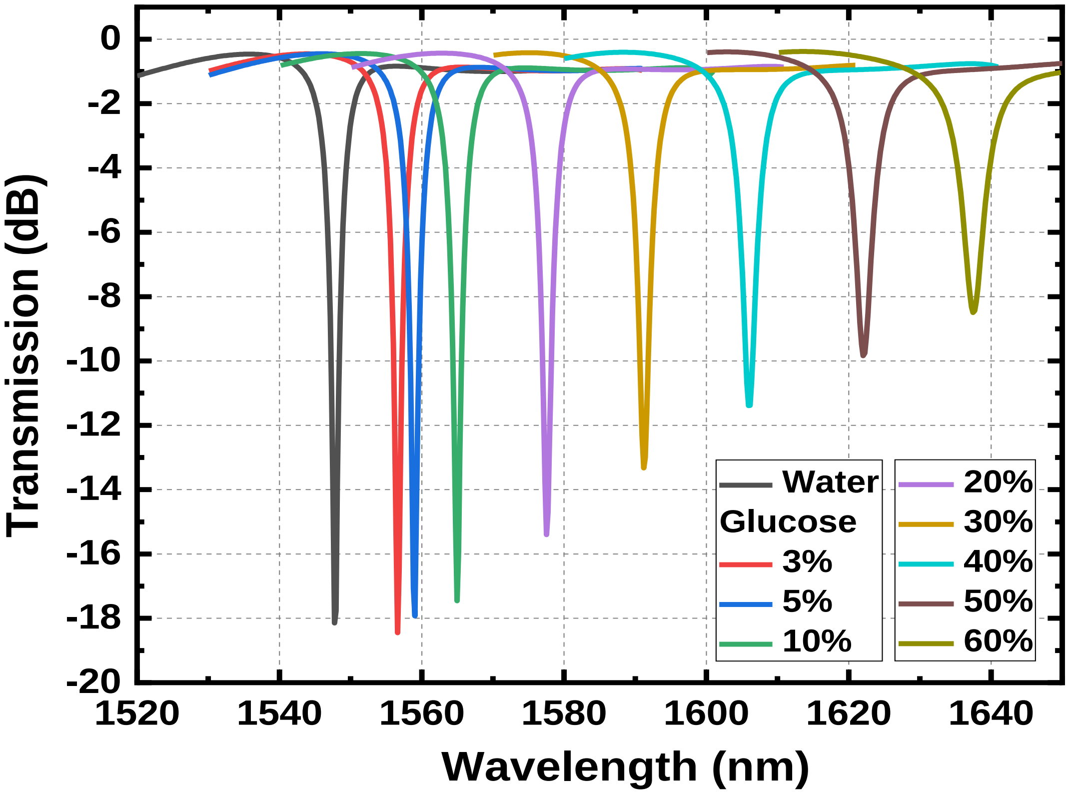

Fig.6.7 Simulated transmission spectra for different concentrations of glucose solutions.

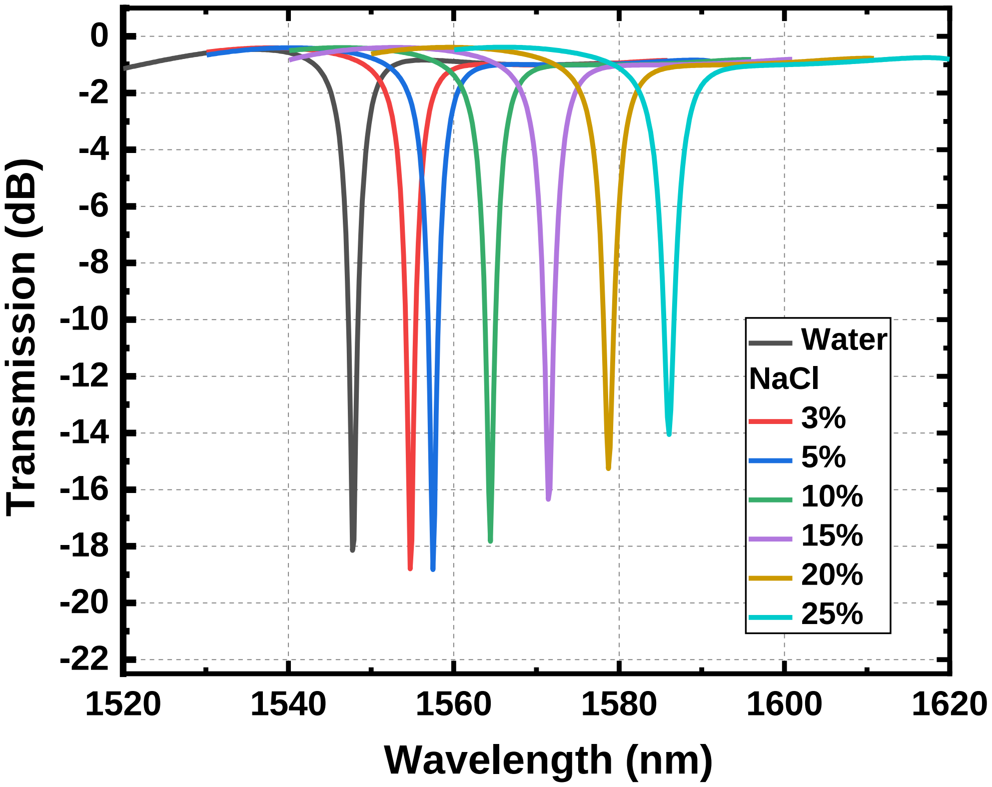

Fig.6.8 Simulated transmission spectra for different concentrations of sodium chloride solutions.

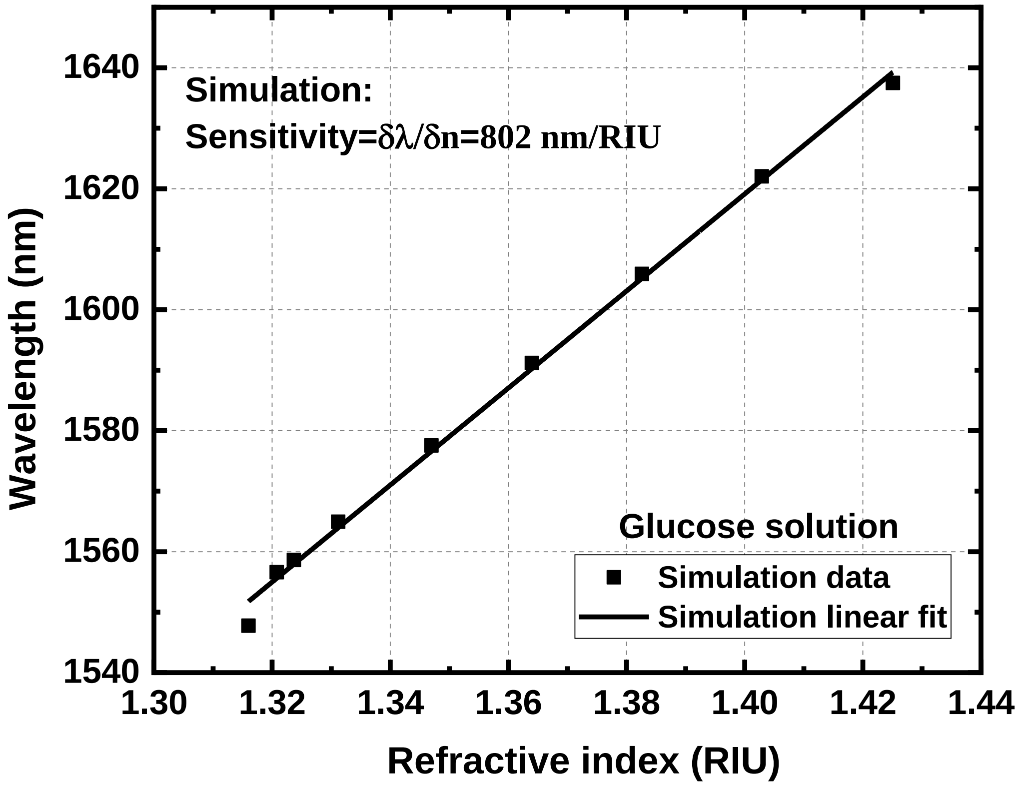

Fig.6.9 Simulated RI sensitivity for different concentrations of glucose solutions.

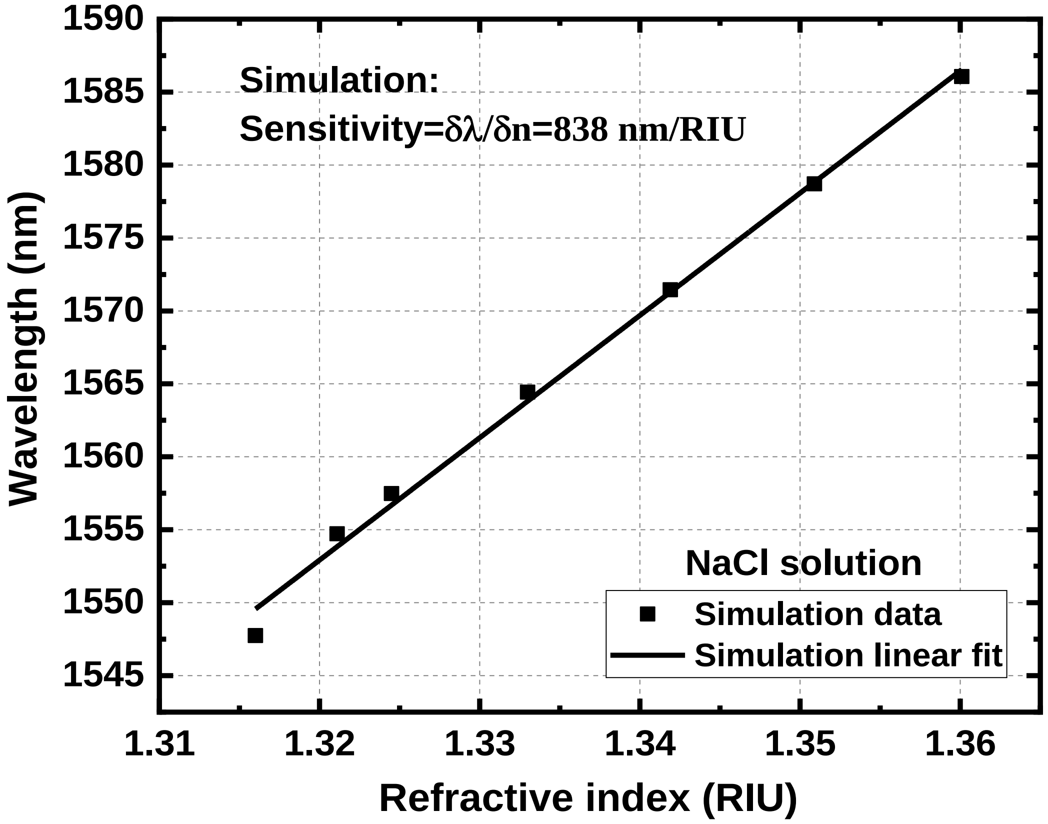

Fig.6.10 Simulated RI sensitivity for different concentrations of glucose solutions.

6.3 Fabrication

The fabrication process steps are shown in Figure 6.11, which is similar to those illustrated in section 4.3.2 and section 5.3. In the fourth step, a 1 μm polymethyl methacrylate (AR-P 642 200k Anisole 12% PMMA) resist layer was spun, exposed, and developed to create an open window on the ring resonator part for sensing. The electron-beam lithography (EBL) resist thicknesses, EBL doses, and beam step size (BSS) were optimized according to the designed structures to give a high-resolution subwavelength grating and smooth sidewall waveguide.

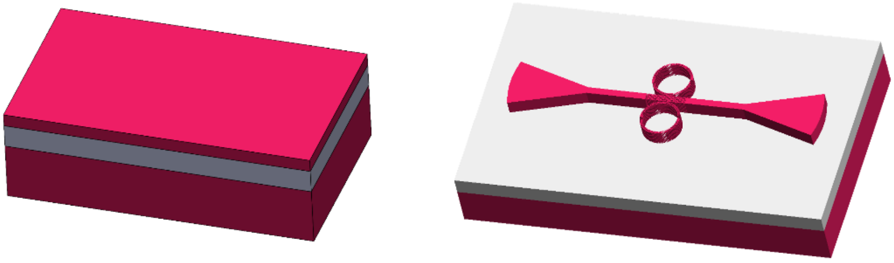

I. SOI wafer cleaning

II. 220 nm Si waveguide etch (HSQ resist)

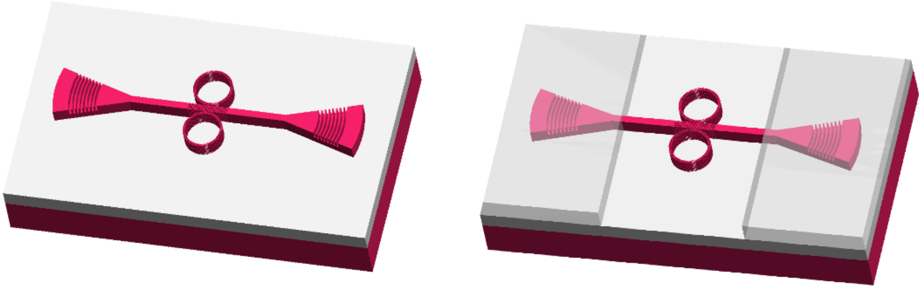

III. Grating coupler etch (PMMA resist)

IV. Sensing window development (PMMA resist)

Fig.6.11 Fabrication steps of the SWG-CMRR device.

A top-view scanning electron microscope (SEM) picture of a fabricated SWG-CMRR device is shown in Figure 6.12 and a zoomed SEM picture of the subwavelength grating parts of SWG-CMRR is shown in Figure 6.13. Based on the fabrication results, it is evident that our optimization of electron-beam lithography (EBL) resist thicknesses, EBL doses, and beam step size (BSS), as previously mentioned, has been successful, and the structure has been faithfully fabricated according to the intended design.

Here, it is essential to highlight the performance of the devices on the wafer sample we have manufactured. The wafer area scale we use in fabrication is 11×12 mm^2. Normally we can fabricate 30 devices each column with 5 columns of different designed structures. In measurement, we tested 30 SWG-CMRR sensors in one column with 21 devices could work well and perform the designed transmission spectrum (70% yield percentage). The measurement results reported here for the SWG-CMRR sensor are based on the optimal best performance sensor selected for analysis. For the 70% yield our analysis is the dry etch non uniformity and the resist development which may bring some difference between the designed parameters and the fabricated parameters. This may cause the unsatisfied performance.

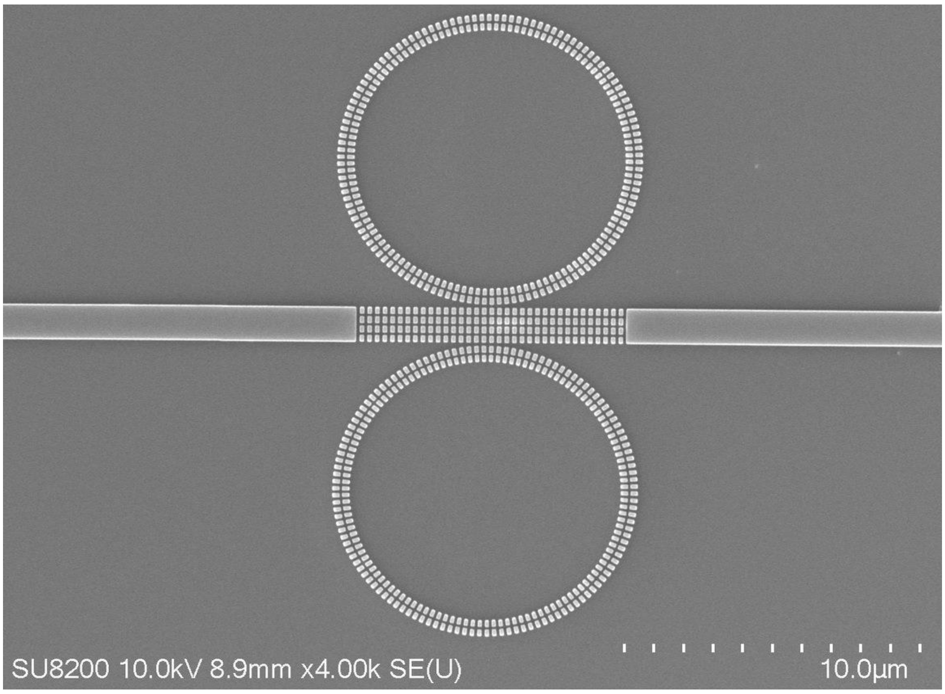

Fig.6.12 Fabrication results of the SWG-CMRR sensor.

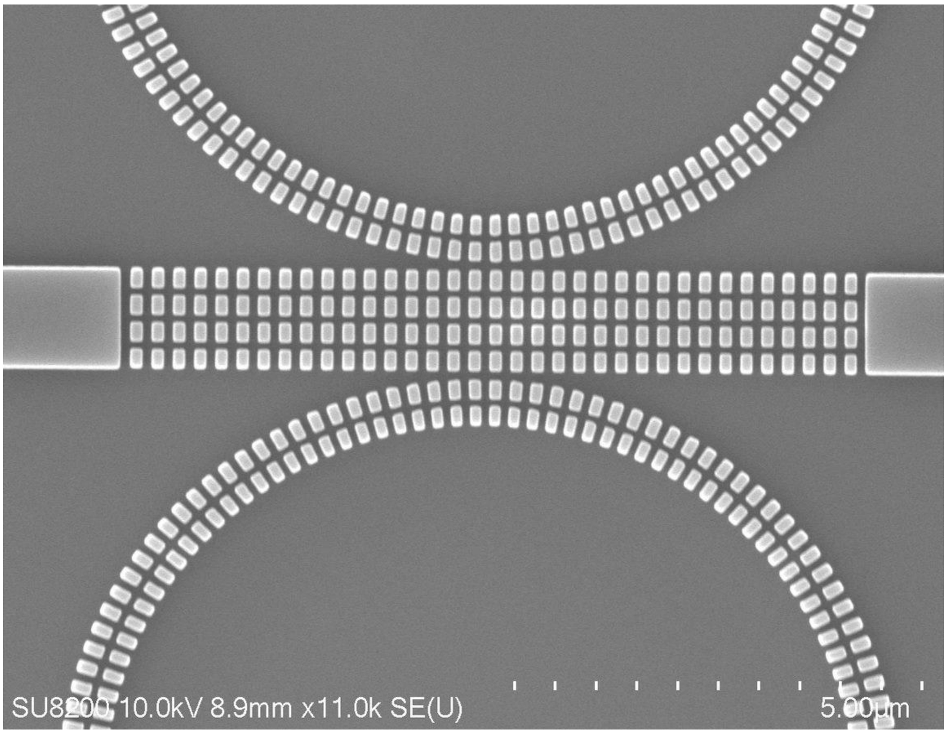

Fig.6.13 Zoomed-in **subwavelength grating parts of SWG-CMRR.**

6.4 Measurement

The measurement setup for the SWG-CMRR sensor is the same as shown in Chapter 3. The broadband light source is using a THORLABS super light-emitting diode (SLD) with a centre wavelength of 1550 nm and a maximum output power of 22 mW. The transmission spectra of the sensor were measured as transmission spectra using an analyser (OSA) with a minimum resolution bandwidth (RBW) of 0.06 nm. The TE-polarized input and output light are introduced into and extracted from the sensor using a 10 μm diameter cleaved single-mode fibre (SMF) through a grating coupler (GC) at input and output angles of 10°. The sensitivity measurements and calculations are performed by dropping various concentrations of solutions or analytes onto portions of the sensing MRR structure. The General-Purpose Interface Bus (GPIB) connected measurement systems using LABVIEW software enable automated and fast data acquisition, which is especially important for rapidly evaporating solvents such as acetone and IPA.

The simulated and measured coupling efficiencies as a function of the wavelength of the output grating coupler are same as the results shown in Figure 5.11. In measurement, the central wavelength and coupling efficiency of the fabricated grating coupler are 1555 nm and 41% respectively (the simulated central wavelength and coupling efficiency are 1556 nm and 44% respectively). The difference in central wavelength and coupling efficiency may be due to deviations in the coupling tilt angle of the SMFs.

The transmission spectra of the simulated and measured SGC-MRR with RO water cladding layer are shown in Figure 6.14 and Figure 6.15. The measured peak we monitored for biochemical sensing is at 1548.9±0.1 nm and can be tuned from 1548.9 nm to 1650 nm with different RIs solutions as cladding layers (the simulated resonant peak is at 1547.7 nm). The small 1-nm redshift of the measured resonant peak compared with the simulation result is due to solution or slightly fabrication etch thickness than design or refractive background difference between theory and experiment. The measured Free Spectral Range (FSR) of the SWG-CMRR is 35.8±0.1 nm, which is slightly lower than the simulated FSR of 39.8 nm, as previously discussed. The 4 nm variance between the simulated and measured FSR values could be attributed to disparities in group indices between the simulated material modules and the real wafer material.

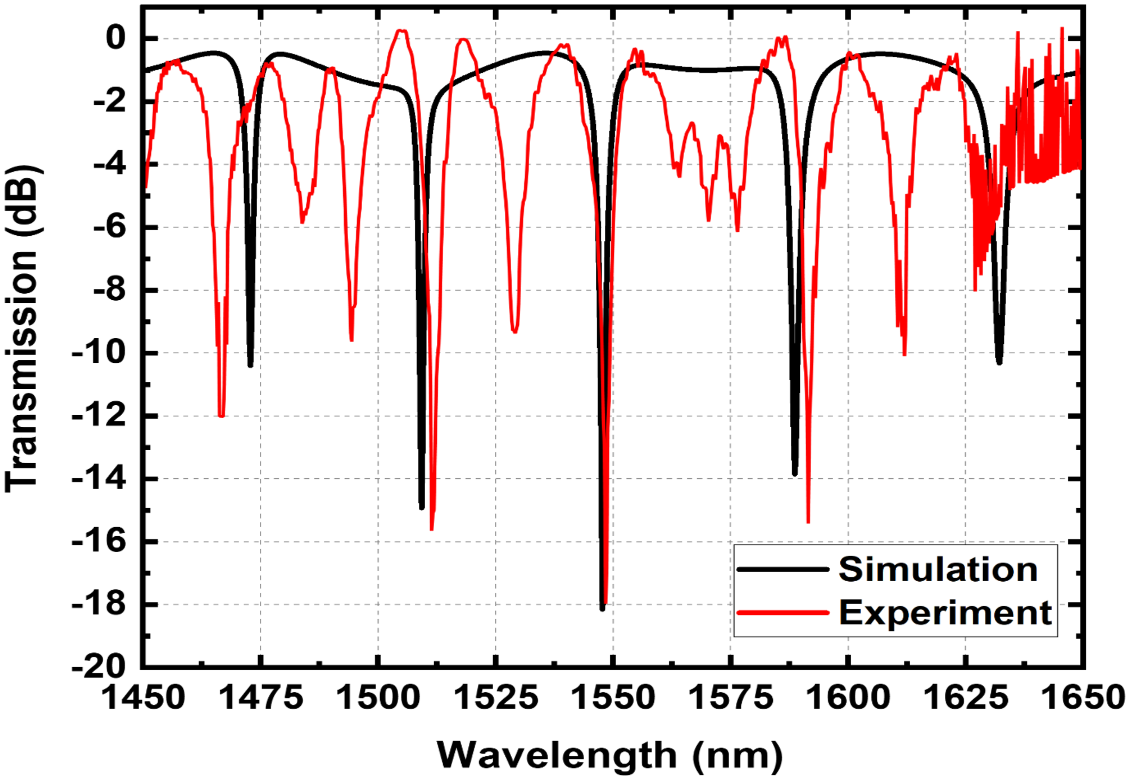

Fig.6.14 Transmission spectra of the simulated (black line) and measured (red line) SWG-CMRR with water cladding layer.

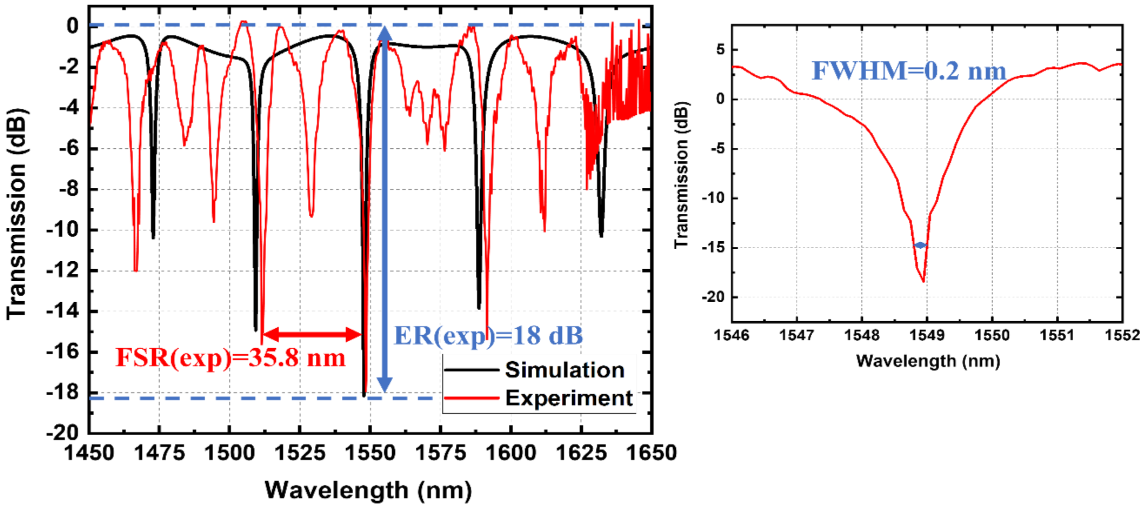

Fig.6.15 The zoomed-in resonant peak of measured transmission spectrum for Q factor calculation.

Here, based on the transmission spectrum we get in the measurement. We estimate that there are some reflections inside the straight waveguide cavity which will cause the low extinction ratio resonant peaks with smaller FSR between the main MRR resonant peaks. Based on the FSR calculation of the straight waveguide cavity (cavity length 28.8 µm, group index 2.7). The FSR of straight waveguide cavity is 15.4 nm which is close to the transmission result we get.

The zoomed resonant peak for Q factor calculation is shown in Figure 6.15. The measured resonant peak is at 1548.9 nm and the Full Width Half Max (FWHM) is 0.2 nm. Thus, the calculated Q factor value is 7.7×10^3. The measured extinction ratio (ER) value for the resonant peak is 18 dB (the simulated ER 18.1 dB).

In the bulk and concentration sensitivity measurement, different concentrations of sodium chloride (NaCl) and D-glucose ($C_6H_{12}O_6$) were used as analytes dropped onto the SWG-CMRR. Concentration changes (mass%) of sodium chloride and glucose result in the RI changes, which can be derived using a third-order polynomial fit. The simulated and measured transmission spectra for different concentrations of glucose and sodium chloride are shown in Figure 6.16 and Figure 6.17 respectively. The resonant peak initially starts at 1548.9 nm and is red shifted when the concentration of solution is increased.

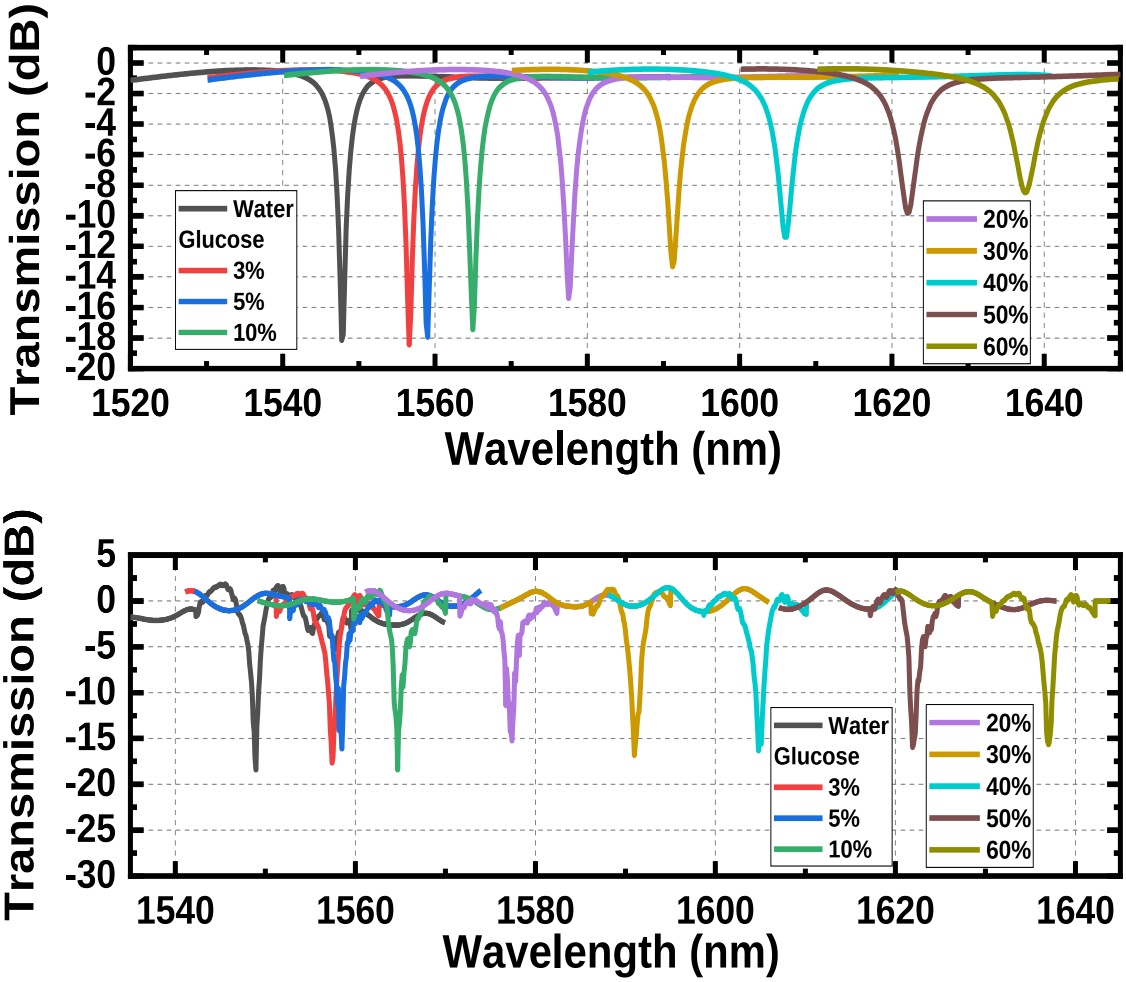

Fig.6.16 (a) Simulated and measured (b) transmission spectra of different concentrations of glucose solutions.

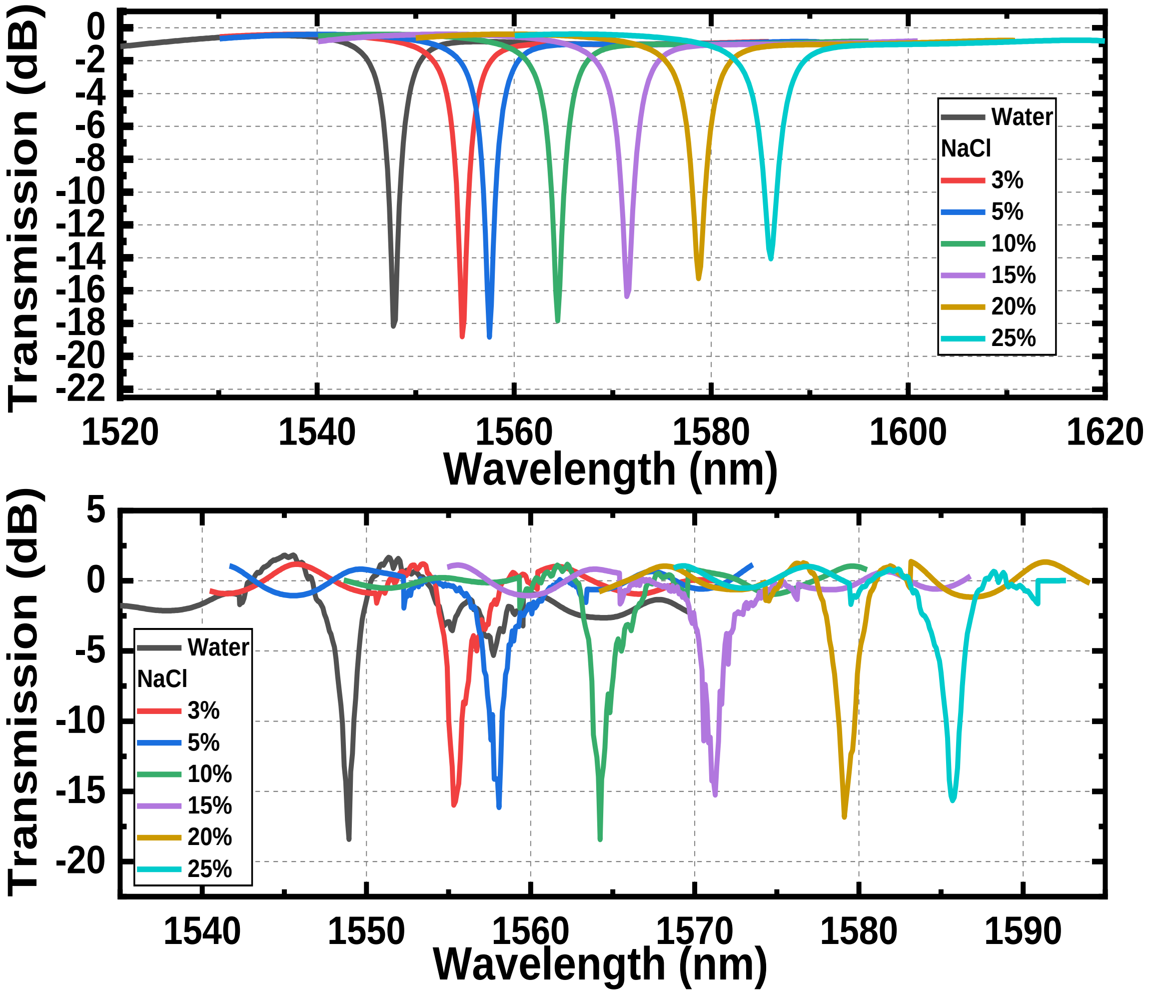

Fig.6.17 (a) Simulated and measured (b) transmission spectra of different concentrations of NaCl solutions.

The simulated and measured RI and concentration sensitivities of the device to glucose and sodium chloride concentration are shown in Figure 6.18 and Figure 6.19 respectively. The simulated and measured RI sensitivities (S_{RI}) for glucose are 802 nm/RIU and 792±4 nm/RIU respectively, and for glucose are 838 nm/RIU and 810±4 nm/RIU respectively. The related measured refractive index limit of detection (LOD) value of glucose and sodium chloride solutions are 2.08×10^{-5} RIU and 2.04×10^{-5} RIU respectively.

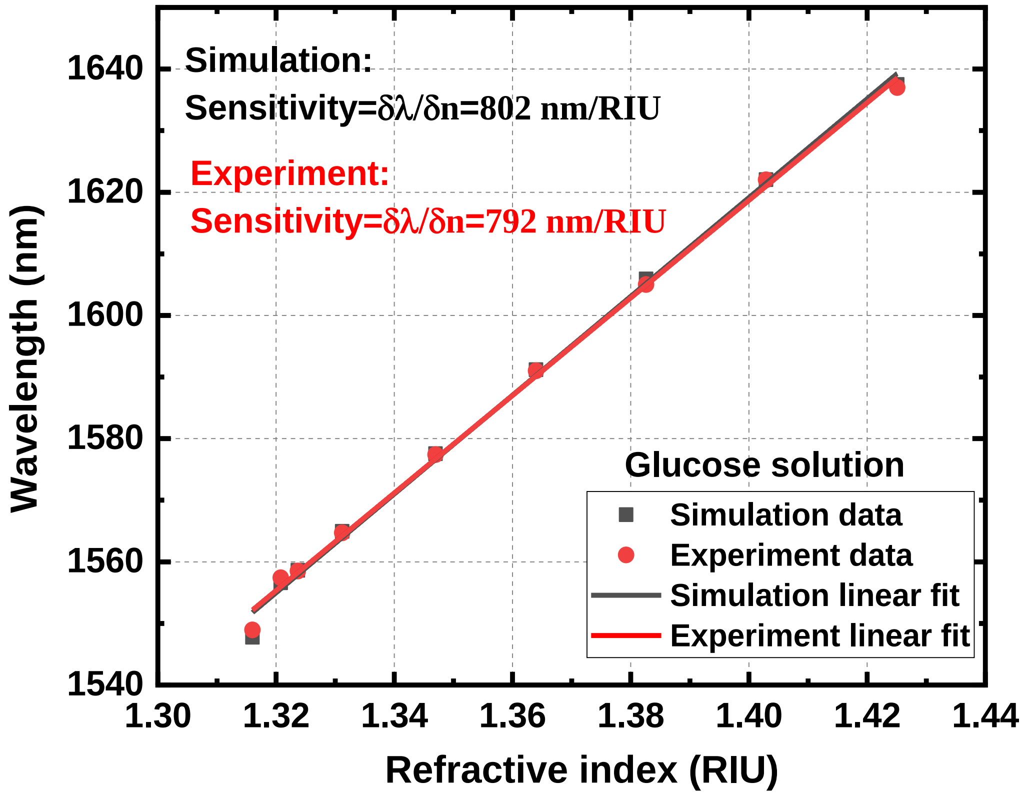

Fig.6.18 Simulation and experimental RI sensitivities of SWG-CMRR for glucose solutions.

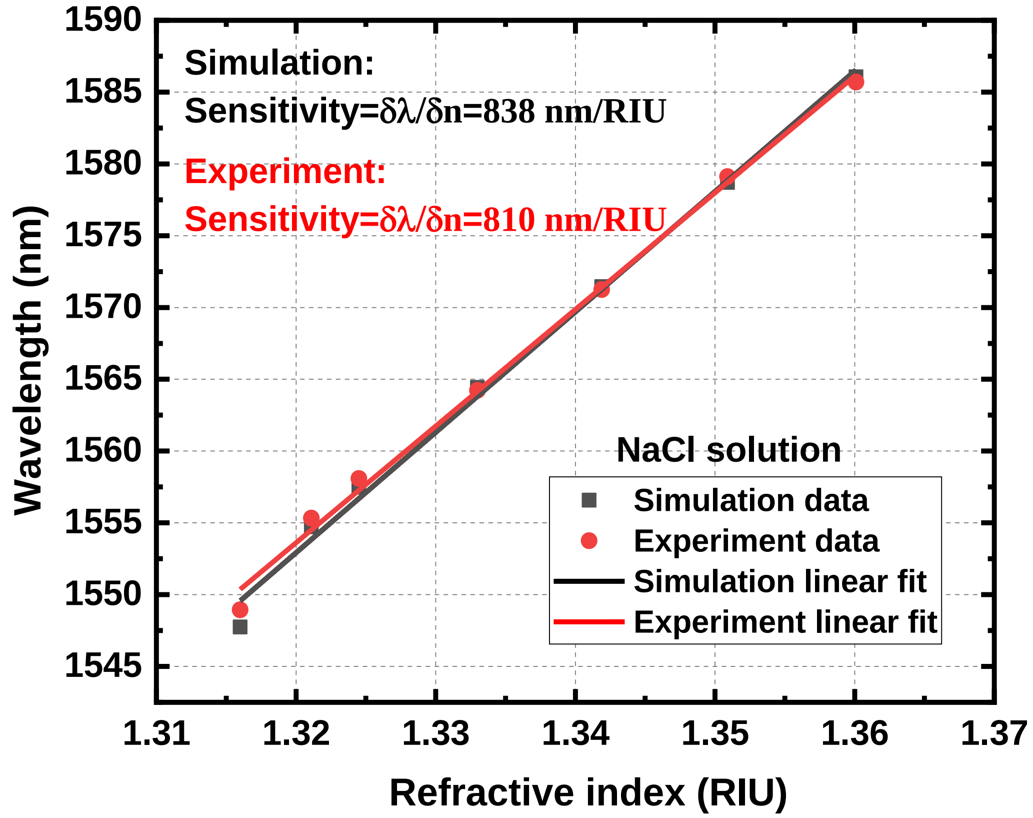

Fig.6.19 Simulation and experimental RI sensitivities of SWG-CMRR for NaCl solutions.

The simulated and measured concentration sensitivities (S_C) of different concentrations of glucose and sodium chloride solutions are shown in Figure 6.20 and Figure 6.21. The measured concentration sensitivities (S_C) are 1415±5 pm/% and 1430±5 pm/% for glucose and NaCl solutions respectively, and the corresponding simulation values are 1434 pm/% and 1478 pm/%. The corresponding measured concentration LOD values for glucose and sodium chloride solutions are 0.04%. It should be noted that the surface sensitivity (Ss) could not be determined experimentally due to the lack of an accurate molecules binding and protein layer thickness measurement tool. However, we estimate that the experimental Ss value should be close to the simulated value of 10.4 nm/nm based on the RI and concentration sensitivity results.

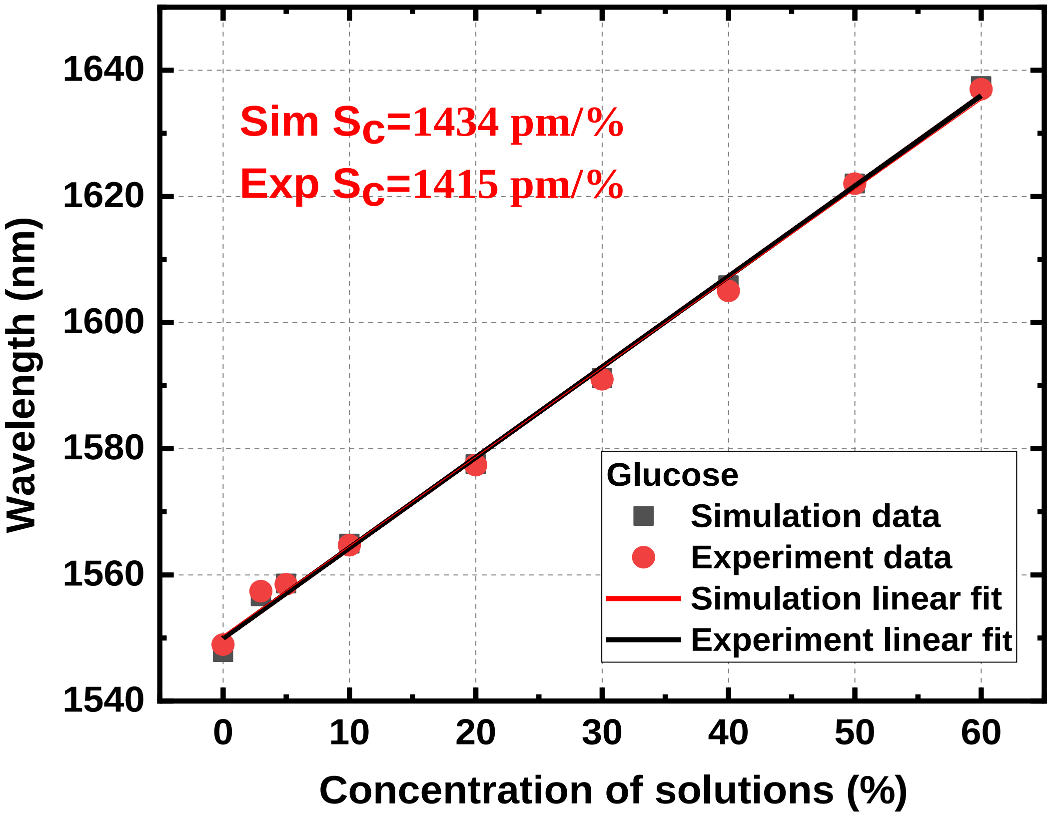

Fig.6.20 Simulation and experimental concentration sensitivities of SWG-CMRR for glucose solutions.

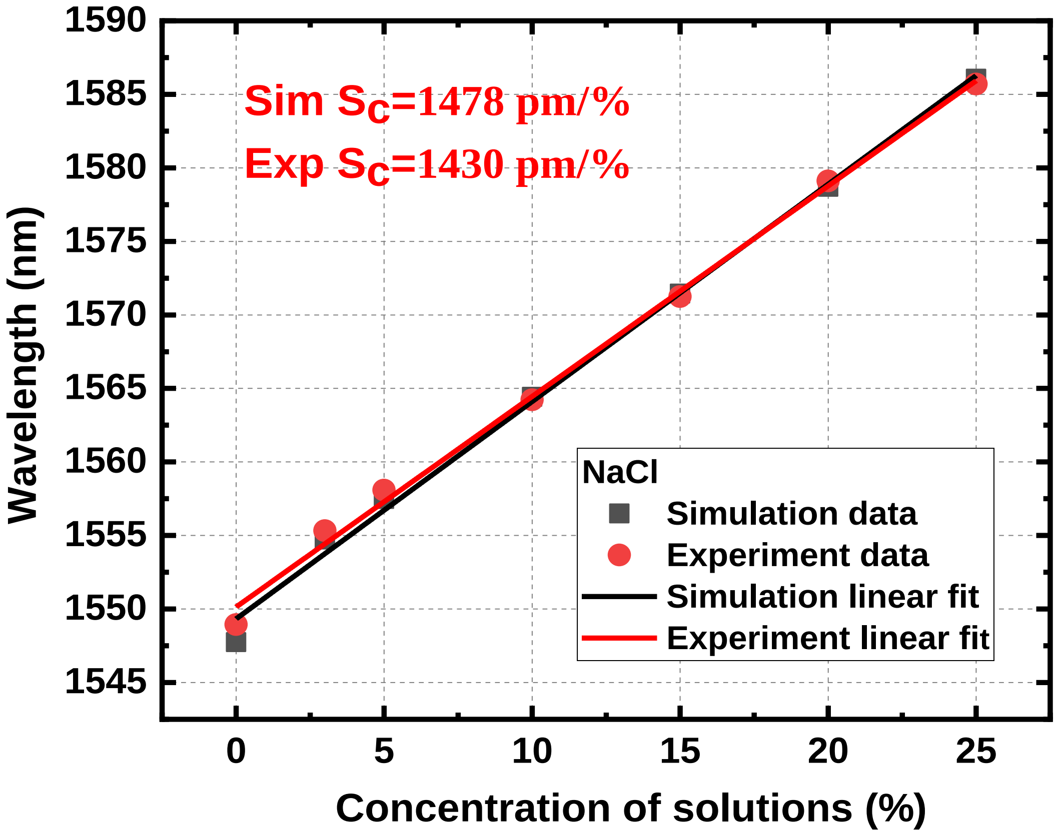

Fig.6.21 Simulation and experimental concentration sensitivities of SWG-CMRR for NaCl solutions.

6.5 Conclusion

We have successfully demonstrated a compact photonic biochemical sensor based on the SOI platform, featuring a 5 µm radius. This innovative design incorporates a combination of cascaded microring resonators, subwavelength gratings, and a multi-box bus waveguide structure, leading to a substantial improvement in sensitivity for analyte and biomolecule detection. Our experimental results reveal a bulk sensitivity of 810±4 nm/RIU and a Limit of Detection (LOD) of 2.04×10^{-4} RIU. The concentration sensitivity is 1430±5 pm/%, with a minimum concentration detection limit of 0.04%. Additionally, the measured Free Spectral Range (FSR) is 35.8±0.1 nm, and the Extinction Ratio (ER) is 18 dB. The Q factor for this structure measures 7.7×10^{3}, and the estimated surface sensitivity is 10.4 nm/nm. With its exceptional sensitivity, this biochemical sensor finds promising applications in areas such as blood tests, disease diagnosis, and environmental protection.

It should be noted that the high sensitivity biochemical sensors compared with the current reported biochemical SOI sensors in many references to understand our novelty and improvement stage. The measured slot waveguide based microring resonator on SOI platform with similar radius is reported in [152] with sensitivity 298 nm/RIU. Thus our slot waveguide MRR sensors (IG-DSMRR and SG-SMRR) shows two times than this measured sensitivity in reference. For the multi-slot subwavelength grating structures, we can compare our results with the measured subwavelength grating straight waveguide and microring resonator structures reported in [150, 151], the sensitivities are 579.5 nm/RIU and 730 nm/RIU respectively. Therefore, we could conclude that our designed SWG-CMRR shows a sensitivity improvement than the current reported subwavelength grating biochemical sensor on SOI platform.

Chapter 7 Double slot microring resonator

This chapter introduces a novel microring resonator structure known as the Double Slot Microring Resonator (DSMRR) sensor, designed for applications in the field of biochemical sensing. The DSMRR sensor aims to overcome existing limitations of traditional MRR sensors and offer enhanced sensitivity. The following sections will delve into the working principle, simulation results, fabrication procedures and their outcomes, measurement stages and results, and conclude by evaluating the sensor's performance.

Dr. Shengwei Ye supported with the fabrication of DSMRR devices discussed in this chapter.

7.1 Working principle

This structure is designed to test our proposed biochemical sensor based on double slot waveguide microring resonator structure. We design this double slot waveguide microring resonator with the similar radius scale of IG-DSMRR to have a basic idea of this DSMRR performance.

This novel structure of double slot microring resonator sensing structure is shown in Figure 7.1. This sensor uses double slot waveguide structure to enhance light confinement in the double slot waveguides and perform better light-matter interaction compared with the traditional strip waveguides. This structure could boost the sensitivity of current MRR biochemical sensors on SOI platform. The fabrication platform we use is Electron Beam Lithography which could perform better sidewall smoothness of the slot waveguides and perform a lower slot waveguide transmission loss results compared to other slot MRR measurement results.

The three-dimension structure graph of the double slot microring resonator is shown in Figure 7.1, and the detailed design parameters are shown in Figure 7.2. The slot waveguides are simulated in Lumerical FDE to ensure the strong optical confinement inside the slots and perform TE mode transmission at the same time. The bus waveguide width W_1 is 365 nm, the slot waveguide width W_2 is 200 nm, and the gap between the bus waveguide, the double slot microring resonator g_1 is set as 160 nm, and the gap between the slot waveguides g_2 are set as 100 nm.

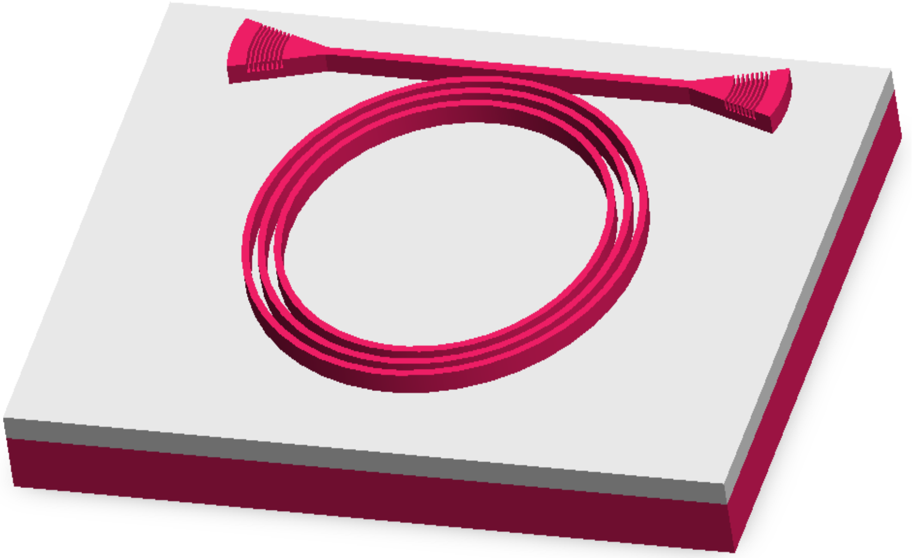

Fig.7.1 Structure of double slot microring resonator.

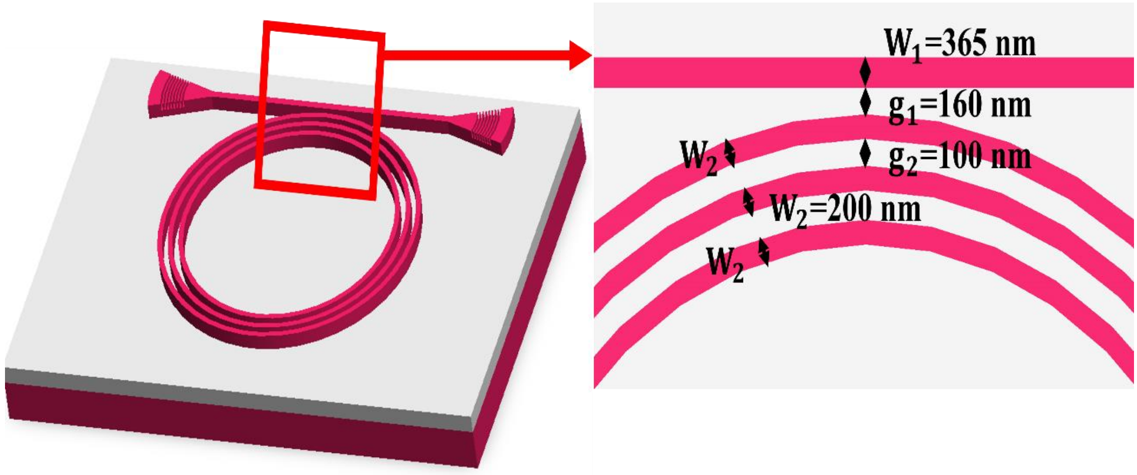

Fig.7.2 Parameters of double slot microring resonator.

7.2 Simulation

Firstly, the mode field simulation of the basic double slot waveguide structure is simulated based on the SOI wafer structure we used in our design and fabrication. The double slot waveguides are simulated and designed to have strong light confinement (fundamental TE mode) inside the slots which could ensure high light-matter interaction when used for sensing purposes.

The designed parameters of double slot waveguide structures are shown in Figure.7.2 with waveguide width of 200 nm with slot width 100 nm. The simulated Ex-field of TE polarized light in the designed straight double slot waveguide structure is shown in Figure 7.3, and the simulated Ex-field of TE polarized light in the designed bent double slot waveguide structure (with bent radius 5 µm) is shown in Figure 7.4.

The simulated electric field distribution of the proposed double slot microring resonator is shown in Figure 7.5. This light distribution figure of the proposed sensing structure verifies our bus and double slot waveguide design.

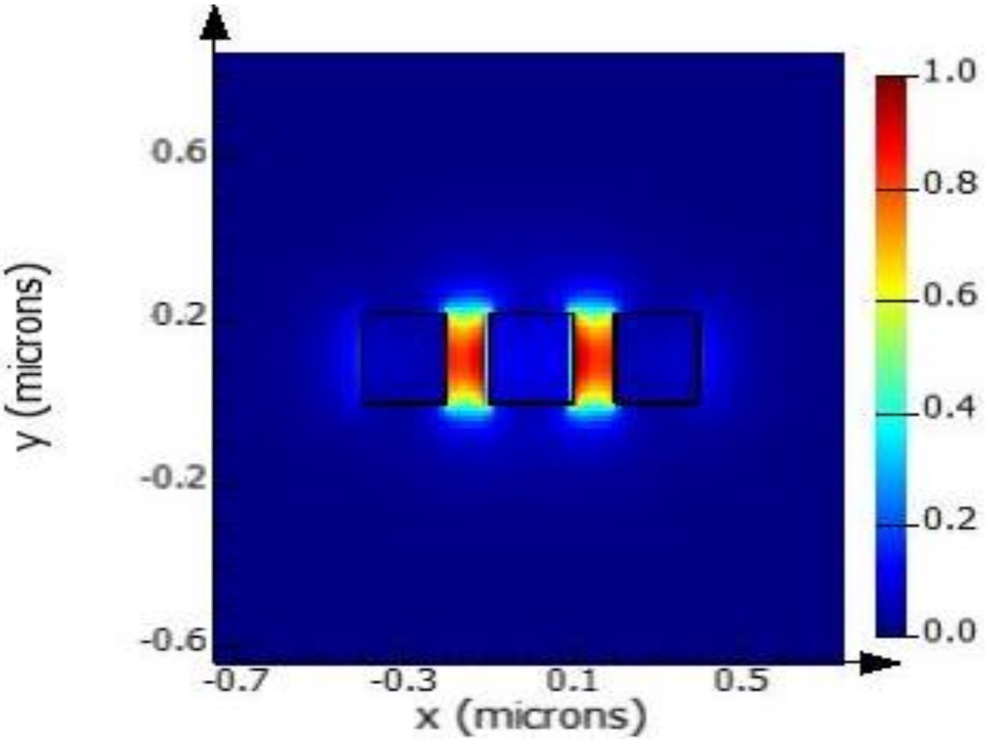

Fig.7.3 The E_x field of TE polarized light in the straight double slot waveguide structure.

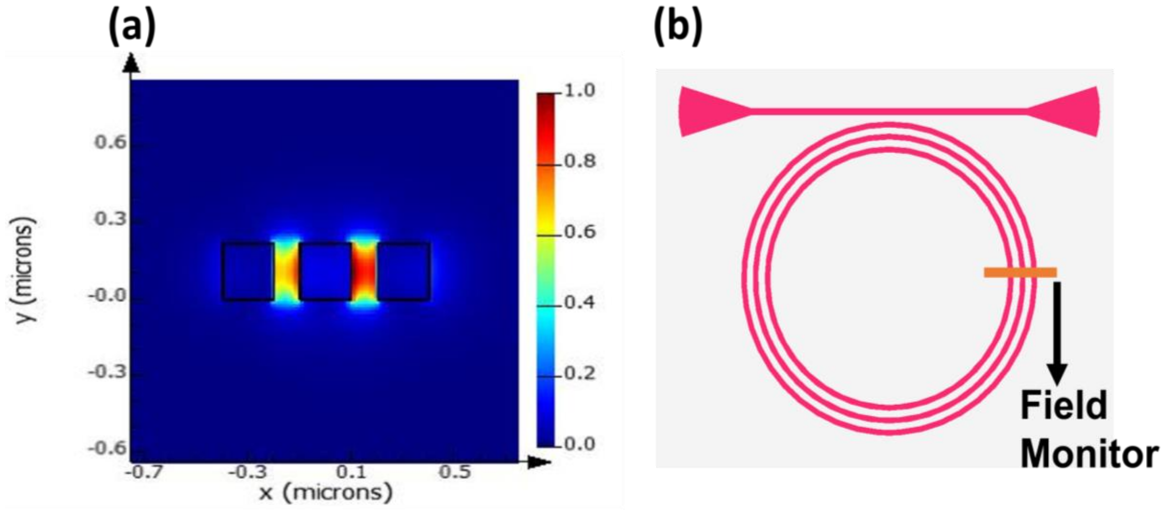

Fig.7.4 (a) The E_x field of TE polarized light in the bent double slot waveguide structure. (b) The top view of DSMRR with field monitor.

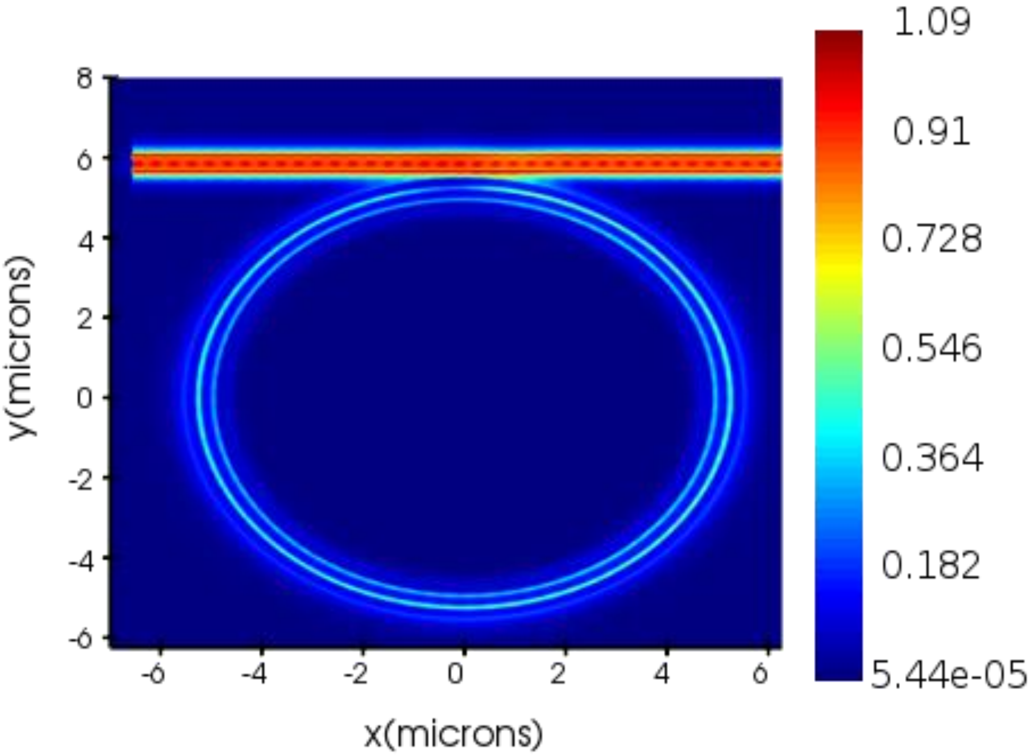

Fig.7.5 The E_x electric field distribution of the double slot MRR.

The simulated transmission spectrums of the double slot microring resonator are shown in Figure 7.6. The graph shows three resonant peaks from wavelength range from 1500 nm to 1600 nm. In our further sensitivity measurement and calculation, we use the one resonant peak near 1550 nm.

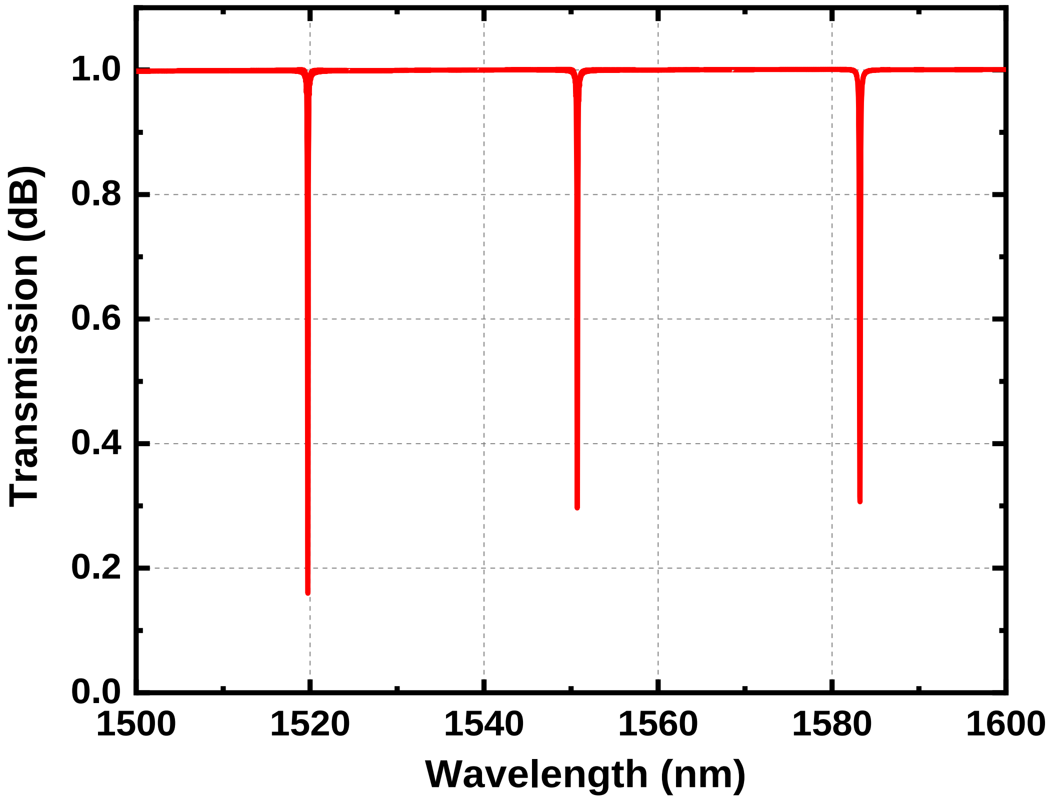

Fig.7.6 The simulated transmission spectrums of the double slot MRR.

In the bulk and concentration sensitivity measurement, different concentrations of sodium chloride (NaCl) and D-glucose ($C_6H_{12}O_6$) were used as analytes and dropped onto the DSMRR. Concentration changes (mass%) of sodium chloride and glucose result in the RI changes, which can be derived using a third-order polynomial fit described in section 3.2. The simulated transmission spectra for different concentrations of glucose and sodium chloride are shown in Figure 7.7 and Figure 7.8 respectively. The resonant double peaks initially start at 1550.7 nm in RO water background refractive index and are red shifted when the concentration of solution is increased. The calculated RI sensitivities (S_{RI}) based on simulation results are shown in Figure 7.9 and Figure 7.10 for glucose is 604 nm/RIU and for sodium chloride is 602 nm/RIU.

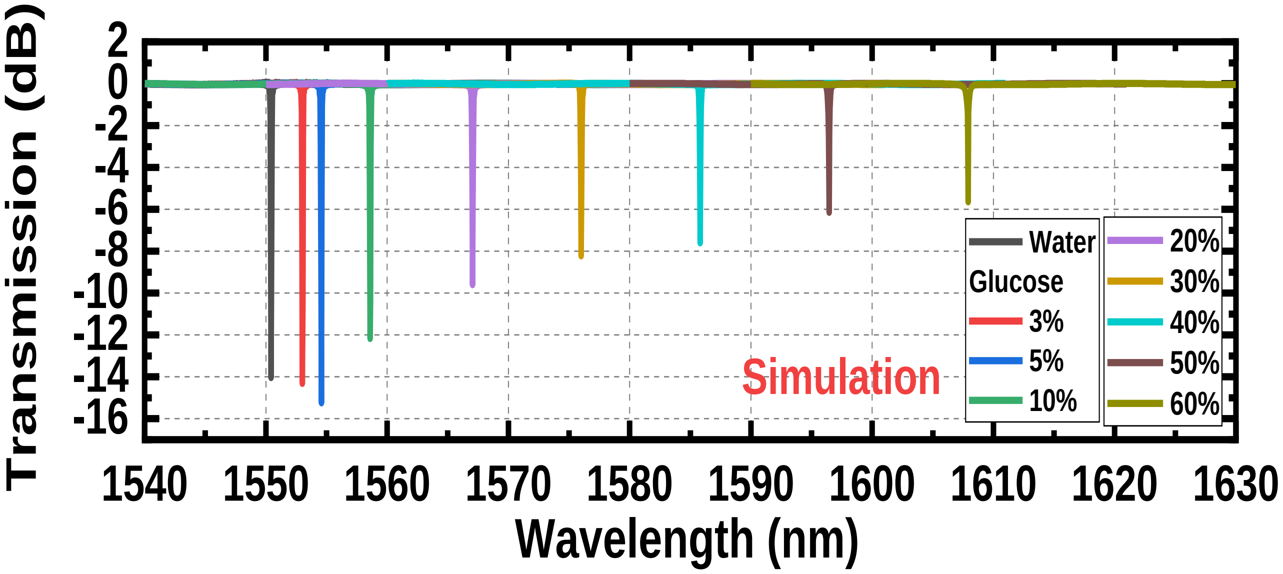

Fig.7.7 Simulated transmission spectra for different concentrations of glucose solutions.

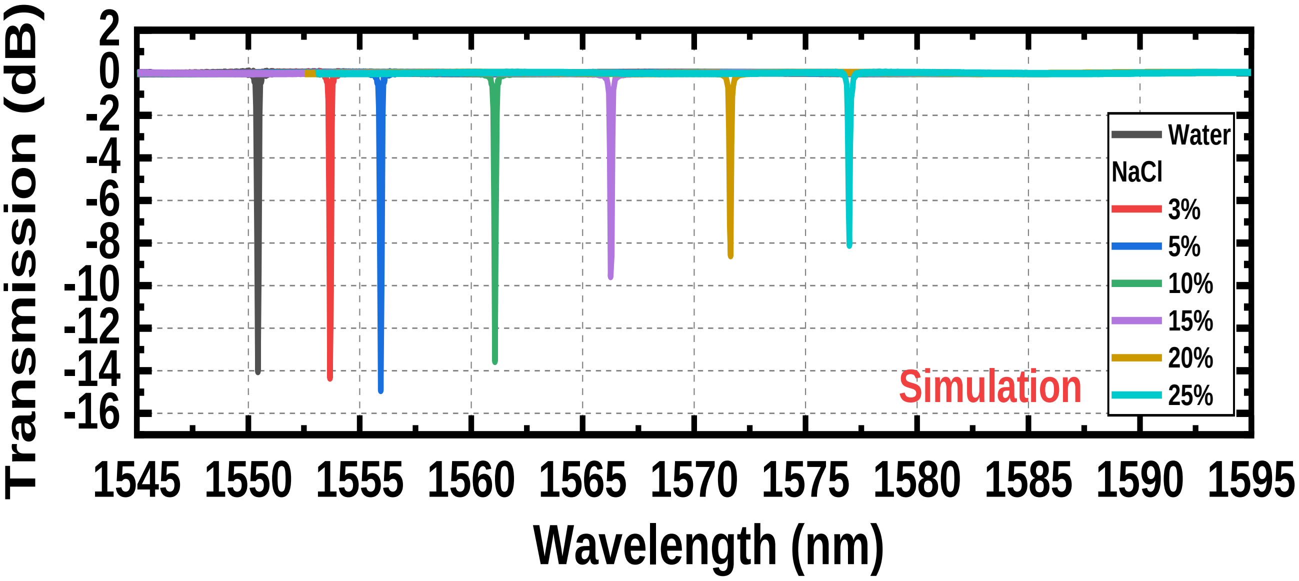

Fig.7.8 Simulated transmission spectra for different concentrations of sodium chloride solutions.

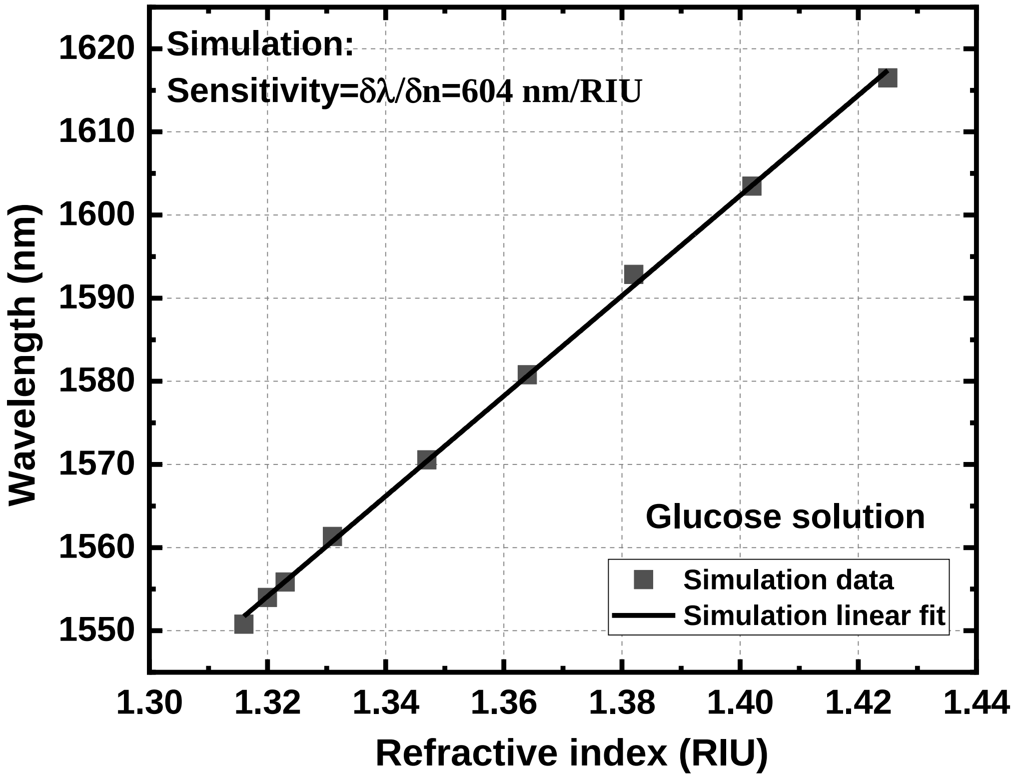

Fig.7.9 Simulated RI sensitivity for different concentrations of glucose solutions.

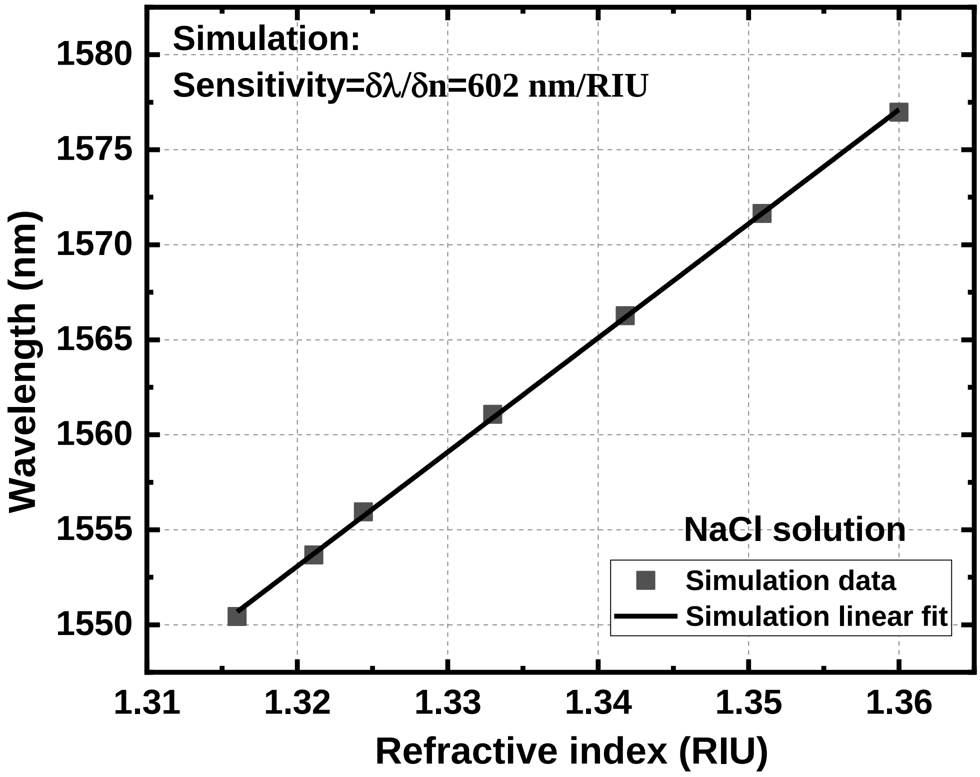

Fig.7.10 Simulated RI sensitivity for different concentrations of sodium chloride solutions.

7.3 Fabrication

Before delving into the illustration of the fabrication process, it is essential to acknowledge that the construction of this structure is a collaborative effort between Dr. Shengwei Ye and myself. The fabrication process steps are shown in Figure 7.11, which is similar to those illustrated in section 4.3.2 and section 5.3. This device uses 1 μm top silicon dioxide layer as cladding layer to increase coupling efficiency of grating couplers. The sensing parts for the DSMRR structure are created using silicon dioxide dry etch as open window patterns. The electron-beam lithography (EBL) resist thicknesses, EBL doses, and beam step size (BSS) were optimized to give a high-resolution double slot waveguide microring resonator, 100 nm tiny slot gaps and smooth sidewall double slot waveguide.

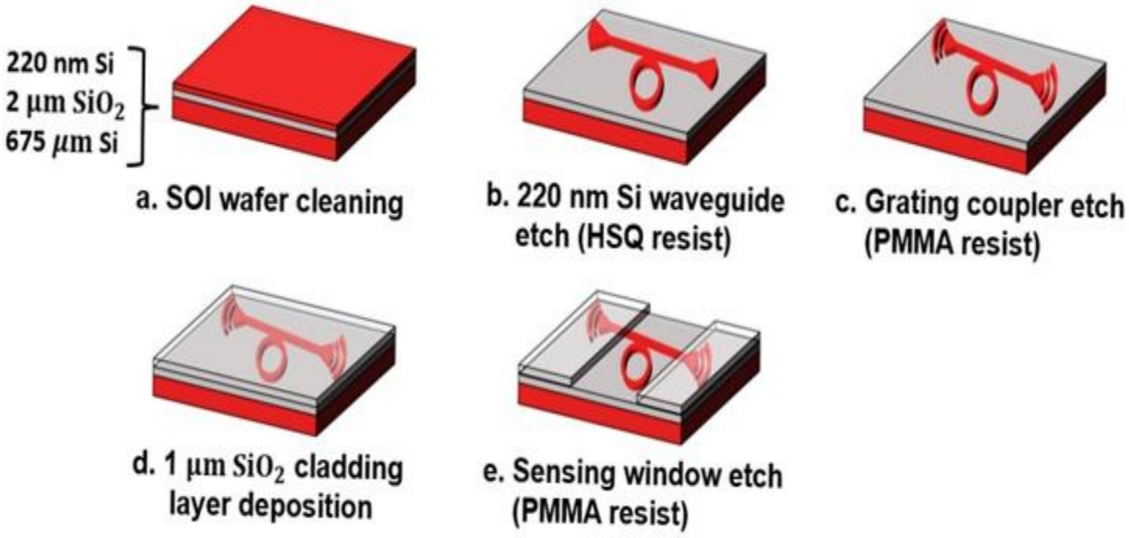

Fig.7.11 Fabrication steps of the device.

Figure 7.12 presents a top-view scanning electron microscope (SEM) image of a completed DSMRR device. This SEM image vividly illustrates the exceptional fabrication outcomes achieved through the utilization of Electron Beam Lithography with pattern optimization and the precisely optimized silicon dry etching method, resulting in smooth sidewalls.

Here, it is essential to highlight the performance of the devices on the wafer sample we have manufactured. The wafer area scale we use in fabrication is 11×12 mm^2. Normally we can fabricate 30 devices each column with 5 columns of different designed structures. In measurement, we tested 30 DSMRR sensors in one column with 27 devices could work well and perform the designed transmission spectrum (90% yield percentage). The measurement results reported here for the DSMRR sensor are based on the optimal best performance sensor selected for analysis. For the 90% yield our analysis is the dry etch non uniformity and the resist development which may bring some difference between the designed parameters and the fabricated parameters. This may cause the unsatisfied performance.

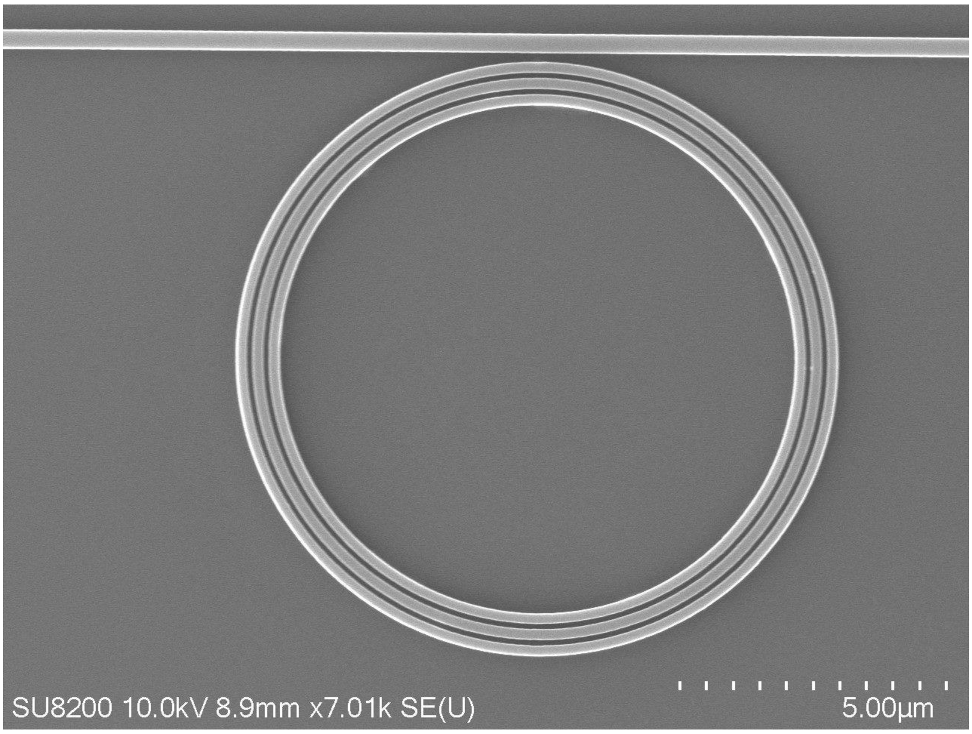

Fig.7.12 Fabrication results of the DSMRR sensor.

7.4 Measurement

The measurement setup for the DSMRR sensor is the same as that shown in Chapter 3.

Using a THORLABS super light-emitting diode (SLD) with a centre wavelength of 1550 nm and a maximum output power of 22 mW as a broadband light source, the spectra were measured as transmission spectra using an analyser (OSA) with a resolution bandwidth (RBW) of 0.06 nm. TE polarized input and output light is coupled into and out of the sensor through a 10 μm diameter cleaved SMF via a grating coupler (GC) with input and output angles of 10°. To perform sensitivity measurements and calculations, solutions or analytes of varying concentrations are dropped onto portions of the sensing MRR structure. An automated measurement system using LABVIEW software based on a General Interface Bus (GPIB) connection enables fast data acquisition, which is especially important for rapidly evaporating solvents such as acetone and IPA.

The simulated and measured coupling efficiencies as a function of the wavelength of the output grating coupler are same as the results shown in Figure 5.11. In measurement, the central wavelength and coupling efficiency of the fabricated grating coupler are 1555 nm and 41% respectively (the simulated central wavelength and coupling efficiency are 1556 nm and 44% respectively). The difference in central wavelength and coupling efficiency may be due to deviations in the coupling tilt angle of the SMFs.

The transmission spectra of the simulated and measured DSMRR with water cladding layer are shown in Figure 7.13. The measured peak we monitored for biochemical sensing is at 1553.2±0.1 nm and can be tuned from 1553.2 nm to 1650 nm with different RIs solutions as cladding layers (the simulated resonant double peaks are at 1550.7 nm). The small 3-nm redshift of the measured resonant peak compared with the simulation result is due to solution or slightly fabrication etch thickness than design. The Free Spectral Range (FSR) of the simulated DSMRR is 26.8 nm and the measured FSR is 24.9±0.1 nm. The difference between the simulated and measured FSR values may be because of the group index difference between the simulation material modules and the actual wafer material.

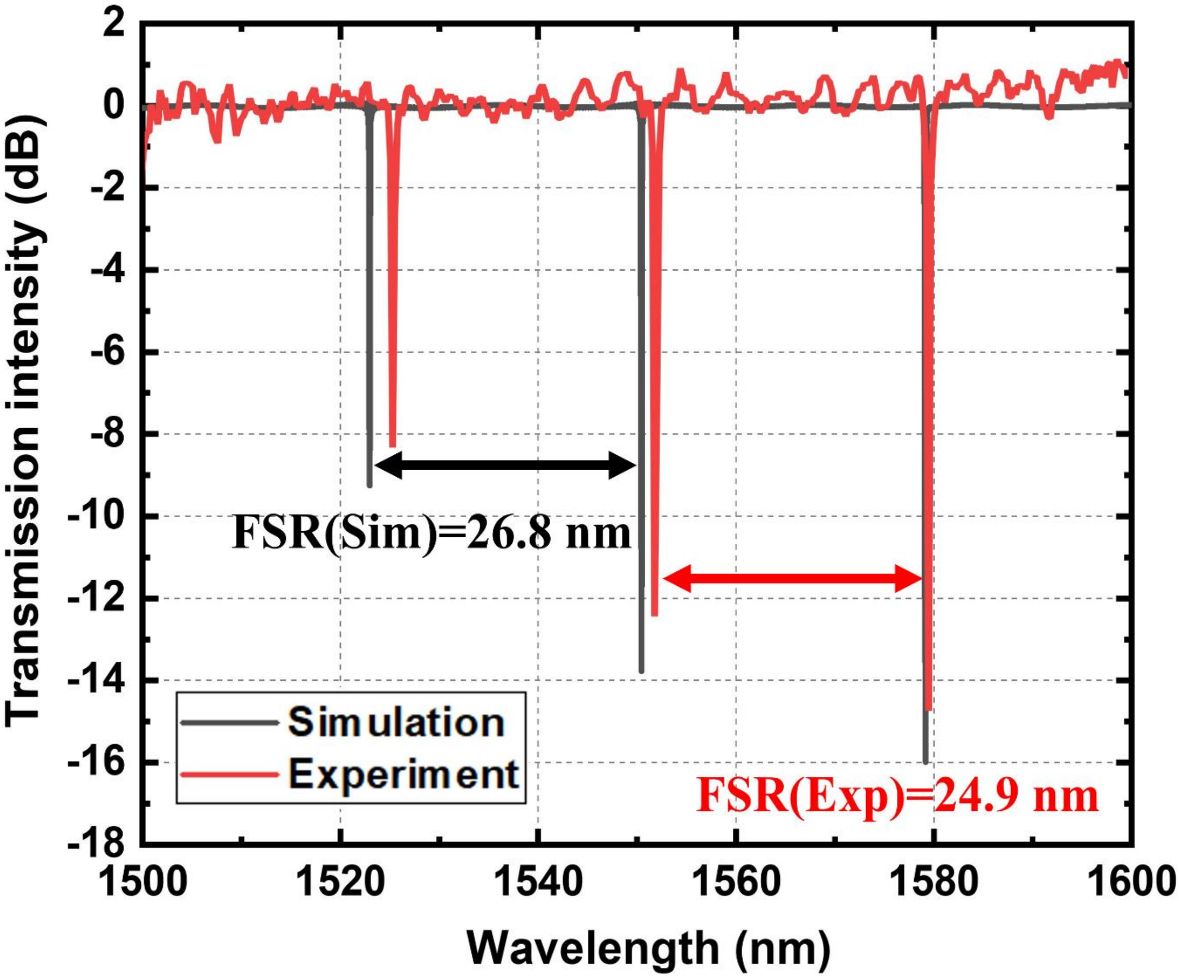

Fig.7.13 Transmission spectra of the simulated (black line) and measured (red line) DSMRR with water cladding layer.

The calculated for measured quality factor (Q factor) is shown in Figure 7.14. The zoomed resonant peak for Q factor calculation is shown in Figure 6.14. The measured resonant peak is at 1553.2 nm and the Full Width Half Max (FWHM) is 0.06 nm. Thus, the calculated Q factor value is 2.6×10^4. The measured extinction ratio (ER) value for the resonant peak is 12.8 dB.

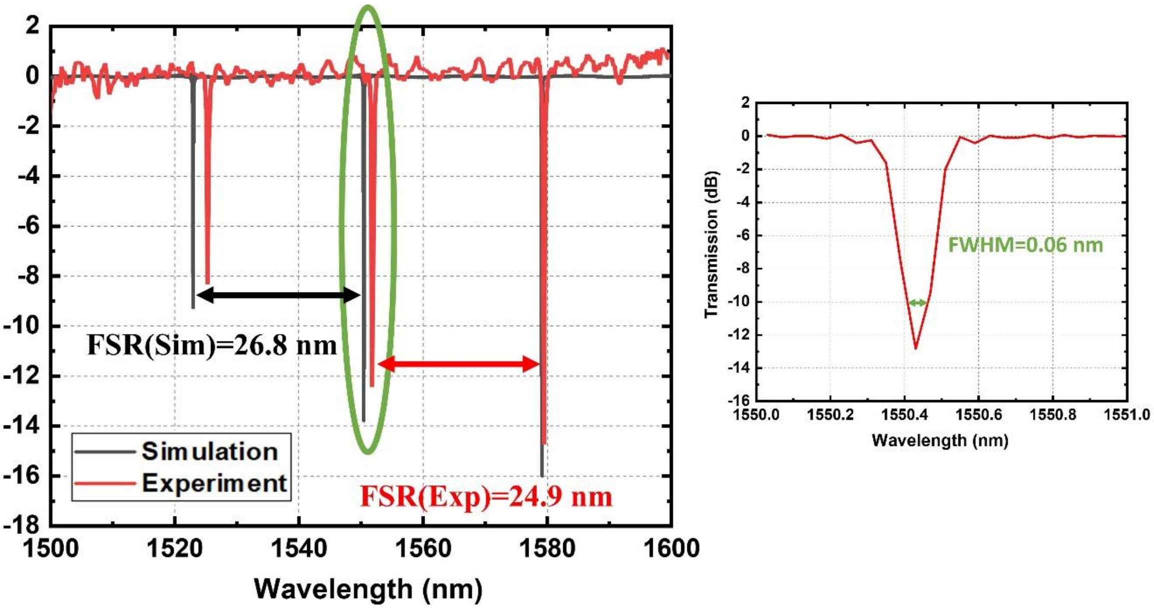

Fig.7.14 The zoomed-in resonant peak of measured transmission spectrum for Q factor calculation.

In the bulk and concentration sensitivity measurement, different concentrations of sodium chloride (NaCl) and D-glucose ($C_6H_{12}O_6$) were used as analytes dropped onto the SG-SMRR. Concentration changes (mass%) of sodium chloride and glucose result in the RI changes, which can be derived using a third-order polynomial fit. The simulated and measured transmission spectra for different concentrations of glucose and sodium chloride are shown in Figure 7.15 and Figure 7.16 respectively. The resonant double peaks initially start at 1553.2±0.1 nm and are red shifted when the concentration of solution is increased.

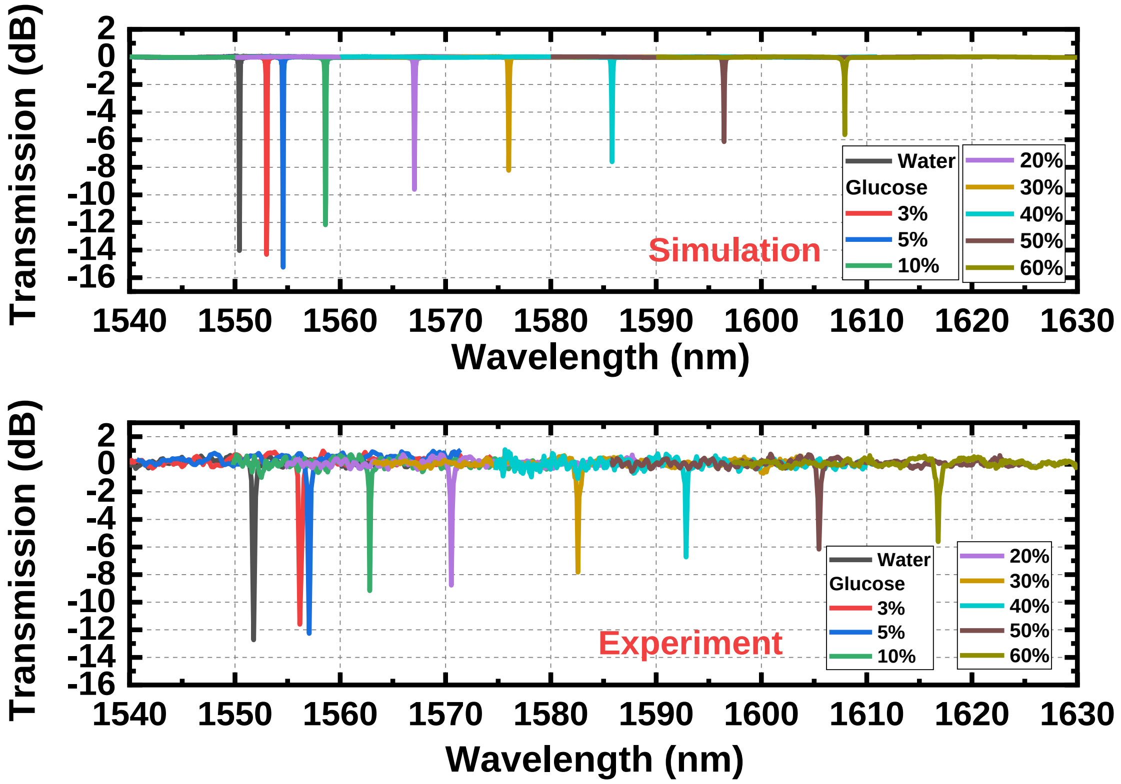

Fig.7.15 (a) Simulated and measured (b) transmission spectra of different concentrations of glucose solutions.

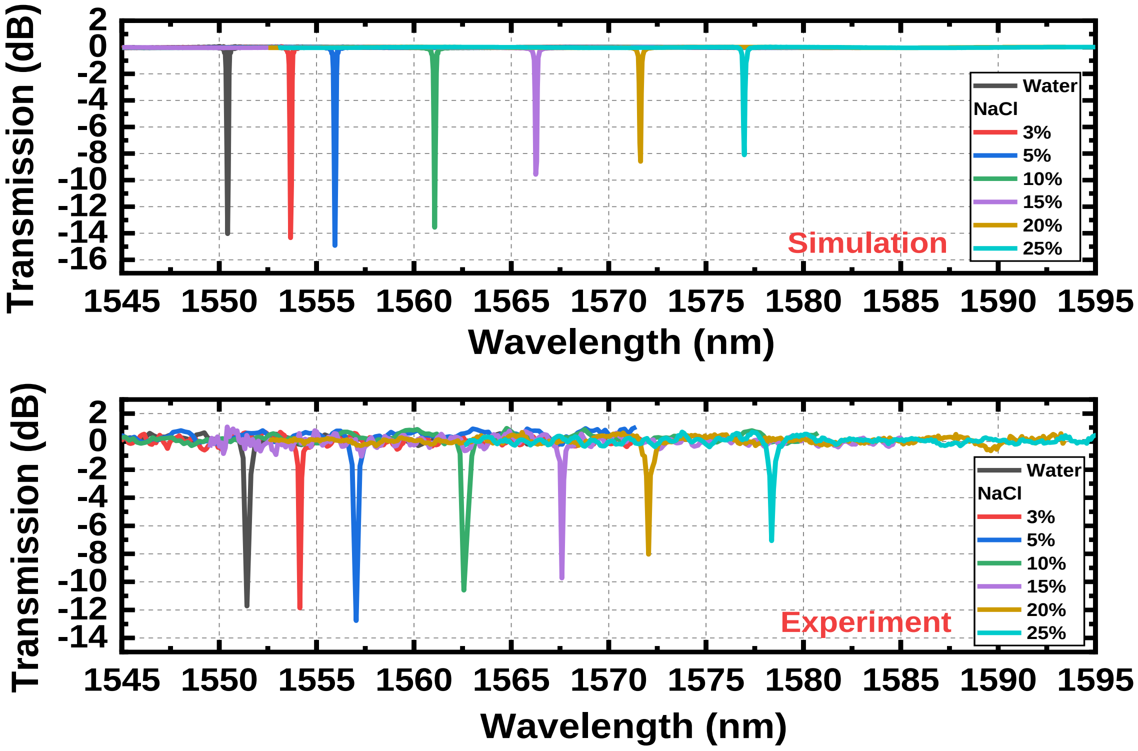

Fig.7.16 (a) Simulated and measured (b) transmission spectra of different concentrations of NaCl solutions.

The simulated and measured RI and concentration sensitivities of the device to glucose and sodium chloride concentration are shown in Figure 7.17 and Figure 7.18 respectively. The simulated and measured RI sensitivities (S_{RI}) for glucose are 604 nm/RIU and 598±2 nm/RIU respectively, and for glucose are 602 nm/RIU and 600±2 nm/RIU respectively. The related measured refractive index limit of detection (LOD) value is 1.15×10^{-6} RIU.

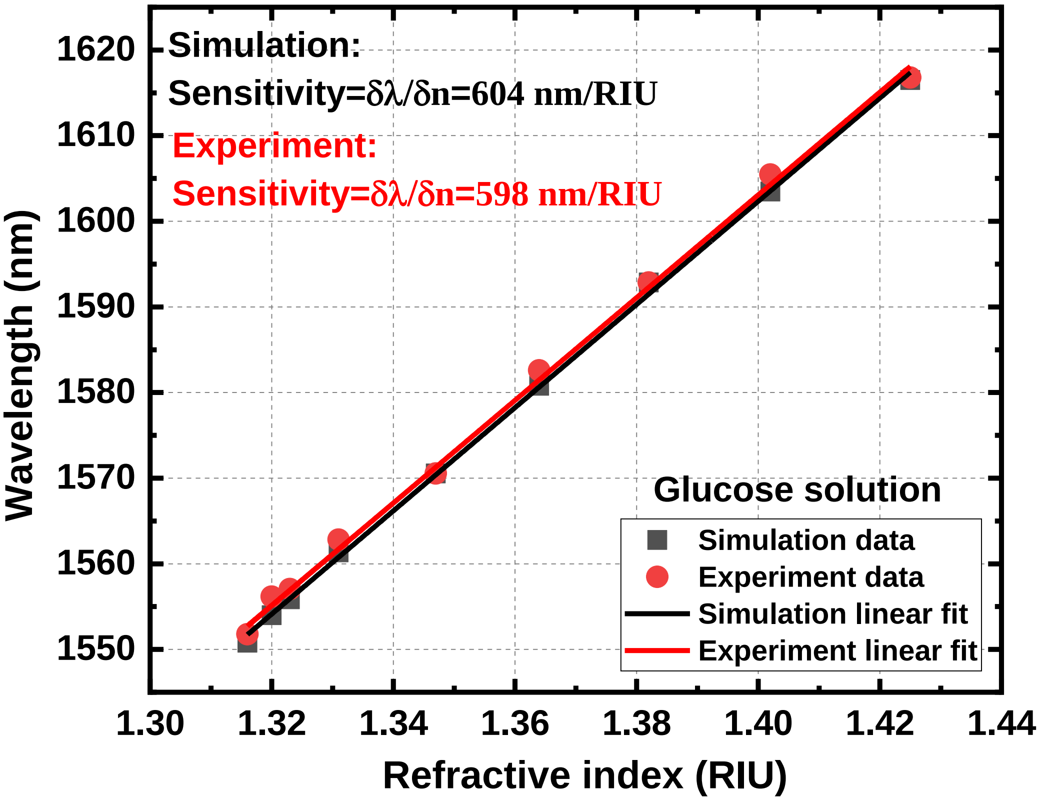

Fig.7.17 Simulation and experimental RI sensitivities of DSMRR for glucose solutions.

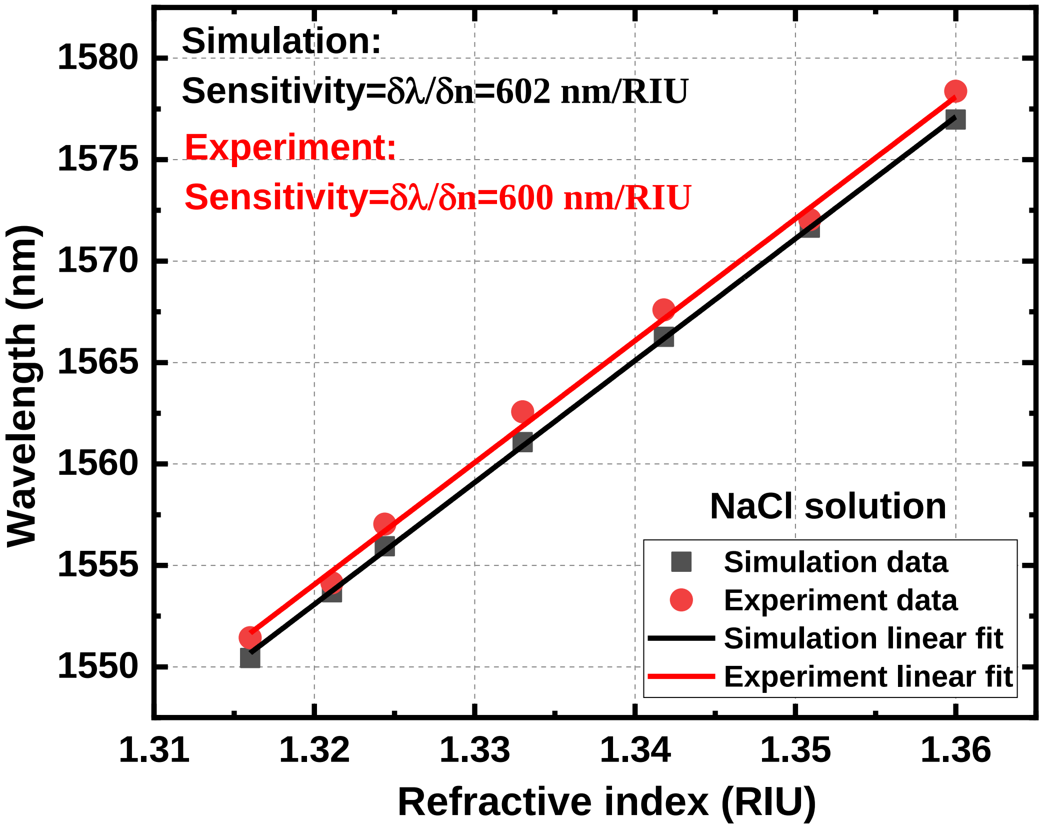

Fig.7.18 Simulation and experimental RI sensitivities of DSMRR for NaCl solutions.

The simulated and measured concentration sensitivities (Sc) of different concentrations of glucose and sodium chloride solutions are shown in Figure 7.19 and Figure 7.20. The measured concentration sensitivities (Sc) are 1065±4 pm/% and 1057±4 pm/% for glucose and NaCl solutions respectively, and the corresponding simulation values are 1176 pm/% and 1063 pm/%. The corresponding measured concentration LOD values is 0.05%. It should be noted that the surface sensitivity (Ss) could not be determined experimentally due to the lack of an accurate molecules binding and protein layer thickness measurement tool. However, we estimate that the experimental Ss value should be close to the simulated value of 6.4 nm/nm based on the RI and concentration sensitivity results.

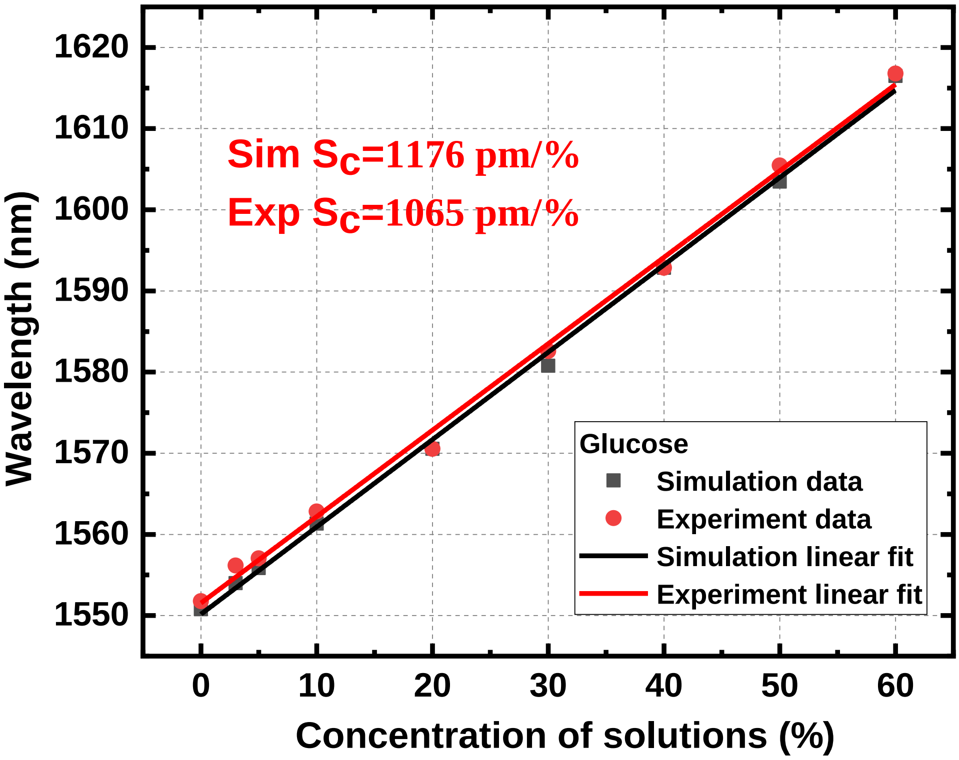

Fig.7.19 Simulation and experimental concentration sensitivities of DSMRR for glucose solutions.

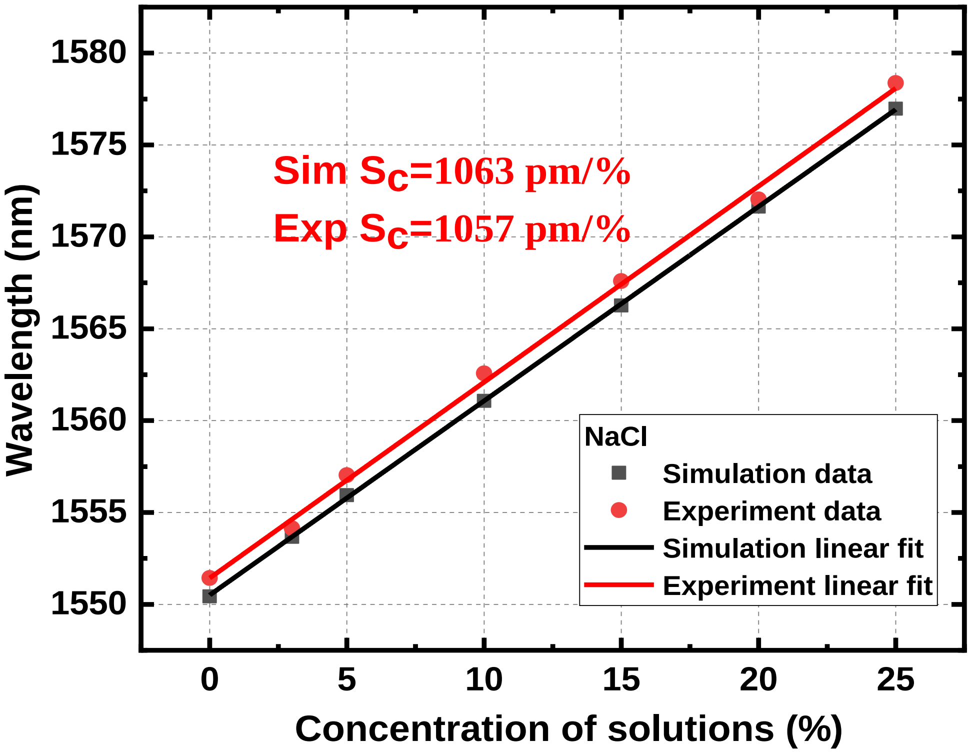

Fig.7.20 Simulation and experimental concentration sensitivities of DSMRR for NaCl solutions.

7.5 Conclusion

This proposed sensing structure contains the double slot waveguide to enhance sensitivity and combines with microring resonator structure. The sensor has compact size with 5 µm central radius. The structure has high Q factor as 2.6×10^4 and measured ER value for the resonant peak as 12.8 dB. This high sensitivity biochemical sensor with 600±2 nm/RIU RI sensitivity and RI LOD value of 1.15×10^{-6} RIU. The measured concentration sensitivities (Sc) of different concentrations of glucose and sodium chloride solutions are 1065±4 pm/% and 1057±4 pm/% for glucose and NaCl solutions respectively. The corresponding measured concentration LOD values is 0.05%. This high sensitivity and ultra compact double slot MRR could be used in photonic integrated circuits for many applications like blood test, disease diagnosis, and environment protection.

It should be noted that the high sensitivity biochemical sensors compared with the current reported biochemical SOI sensors in many references to understand our novelty and improvement stage. The measured slot waveguide based microring resonator on SOI platform with similar radius is reported in [152] with sensitivity 298 nm/RIU. Thus, our slot waveguide DSMRR sensors shows two times than this measured sensitivity in reference, and we could conclude that our designed DSMRR shows a sensitivity improvement (600 nm/RIU) than the current reported subwavelength grating biochemical sensor on SOI platform.

Chapter 8 Gold nanodots plasmonic sensing structure

This chapter will introduce the design, simulation and fabrication works of some gold nanodots based plasmonic structures collaborates with NJUST university in China. The detection of far-field mode distribution under the resonant wavelength is using Polarization Indirect Microscopic Imaging (PIMI) technique. The PIMI parameters $\boldsymbol{sin\delta}$ and ϕ could be used as nano device structural characterization and sensing.

8.1 Working principle

The detail of the working principle is shown in section 2.4. Plasmon resonators can efficiently achieve high quality factors and local field strengths, which can enhance surface-enhanced Raman scattering (SERS) or photoluminescence. Additionally, bioparticle detection methods are used to sense viruses or particles in plasma structures. This method has a significant impact on the scattering spectra and fields when molecules are added to structures that are highly desirable for high-sensitivity detection.

The PIMI technique was used to detect the far field mode distribution at the resonant wavelength. The optical system is built based on the PIMI method and is used to measure the orientation angle of the polarization ellipsoid and the phase difference between two orthogonal directions of light transmitted, reflected or scattered by the sample.

8.2 Simulation

The simulation is performed using the finite-difference time-domain (FDTD) method to calculate the electric field intensity under different conditions. The boundary conditions are set as perfectly matched layer (PML) boundary. The PIMI algorithm results are derived by processing the simulation results under ten different incident linear polarization directions.

In PIMI, the contrast of the indirect parametric images arises from the different coupling between the modulated optical field and the sample structure. When a linearly polarized beam is incident at different polarization azimuthal angles and coupled to the sample, information related to the nanoscale anisotropic features of the sample can be collected and enhanced. During the modulation process, the scattering spatial distribution changes from one polarization angle to another due to the different coupling between the illuminating light and the anisotropic characteristics of the sample.

The intensity changes of the image pixel corresponding to each object point can be expressed by using the Jones model. Experimental space points that meet a certain level of adjusted fitting criteria. Square roots can be considered to fit the theoretical modelling curve well and they are treated as real points. On the other hand, those spatial points that do not meet the fitting criteria are regarded as noise and filtered out. In this way, the diffraction effect of adjacent object points on the imaging sensor is suppressed and the point spread function (PSF) is narrowed, thereby improving the spatial resolution and contrast of the indirect parametric image.

The PIMI results when the monitors are at different heights (the length of the monitor from the surface of the sample) are shown in Figure 8.1. The black circle in the results is the edge of the gold nano disk. It can be seen from the results that there are two elliptical vortices formed simultaneously in the far field. Moreover, as the propagation distance of the electromagnetic field becomes longer, the electromagnetic field will also diffuse outward, but the phase difference of the light fields always exists, which also ensures the stability of the propagation orbit. Based on the relationship between electric field and surface charge density in Maxwell equations, the charge distribution on the surface of gold nano-disk can be calculated by FDTD, as shown in Figure 8.2. Compared with the results of normal incidence, it can be found that the charge density on the surface of gold nano-disk is no longer linear oscillation, but hybridization appears. This verifies the result that the interaction between surface plasmon polariton (SPP) wave and spin electrons leads to electron hybridization.

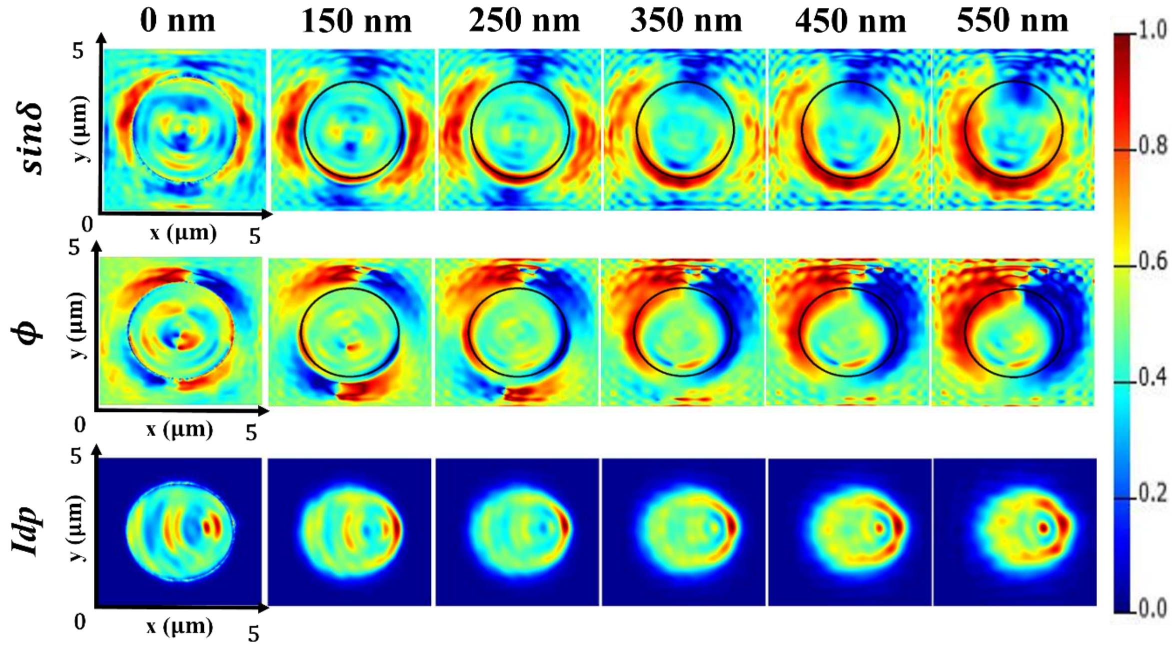

Fig.8.1 PIMI results obtained at NA=0.9 while varying the distance between the monitor lens and the sample surface from 0 nm to 550 nm.

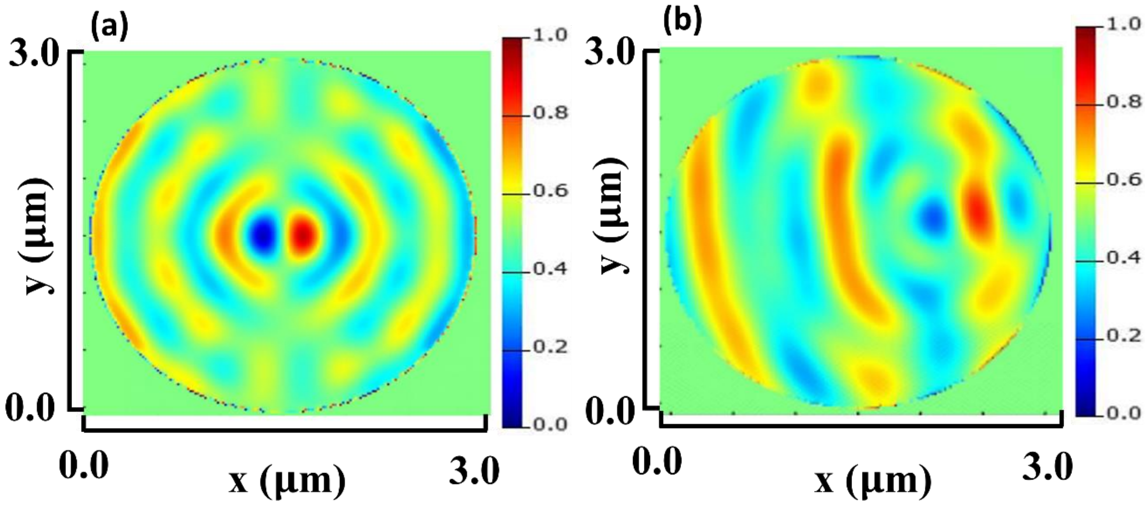

Fig.8.2 The electron distribution on the disk by vertical(a) and corned illumination(b) simulated by FDTD.

In order to verify the role of SPP waves generated by metals in scattering, the results of focused light irradiation on nano-disks of different materials (gold and silicon dioxide) were simulated and compared, and the results are shown in Figure 8.3. It can be clearly seen from the results that nano-disks of different materials can scatter photons with orbital angular momentum outward, which once again verifies that the focused light field plays a decisive role in the process of generating orbital angular momentum photons. However, the electromagnetic field scattered by gold nano-disks is stronger and more obvious, because only the metal surface can generate SPP, and SPP scatters to the far field after encountering the edge. There is also a weak light field scattering result at the edge of the silica disk, which is caused only by the scattered field at the edge of the nano-disk.

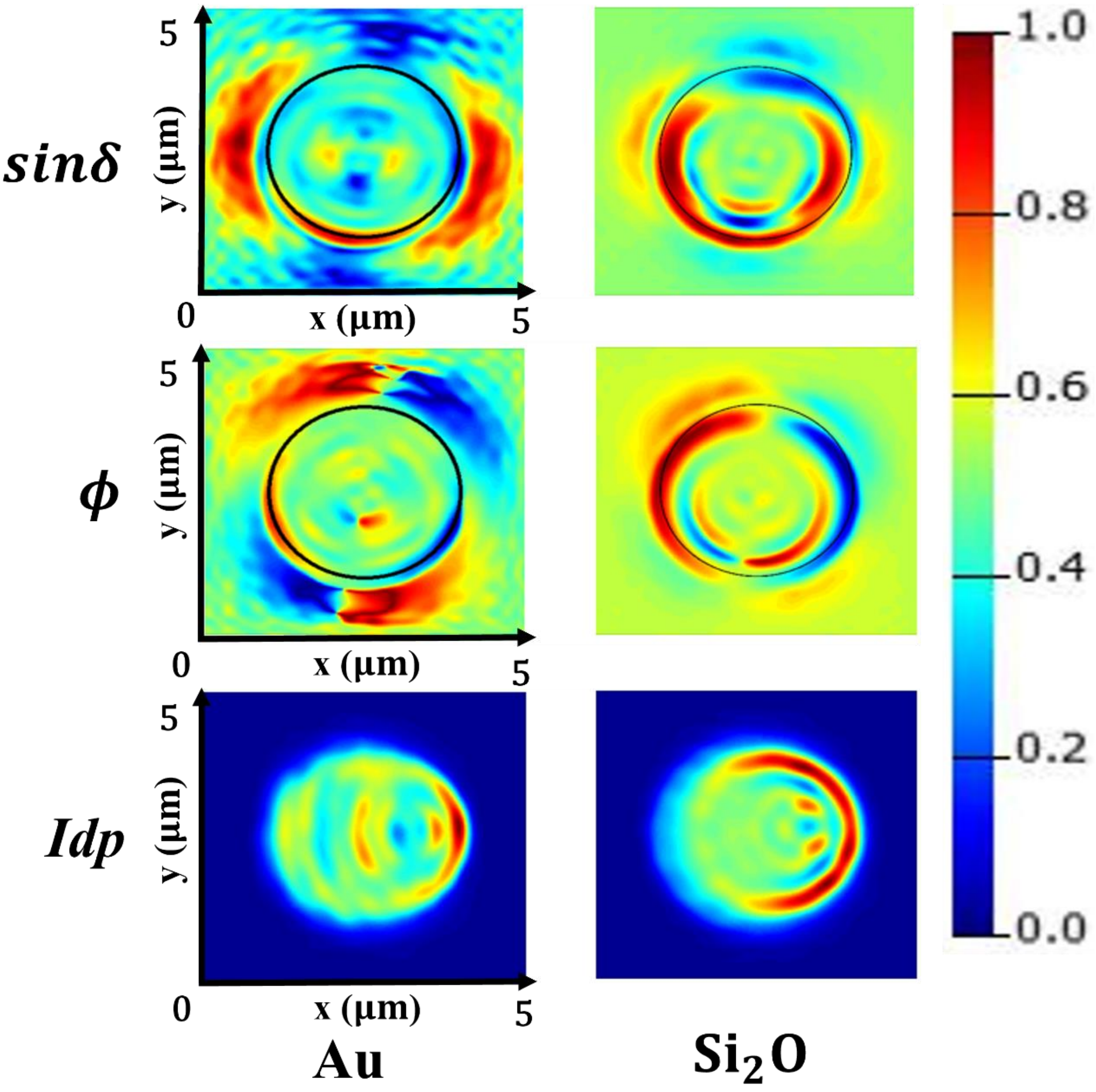

Fig.8.3 PIMI results at NA=0.9 when the disk has different materials under linear polarization incidence.

8.3 Fabrication

The fabrication processes are illustrated in the Figure 8.4 below with detailed fabrication processes,

1) Glass sample (silicon dioxide) cleaving and cleaning.

2) Two layers of PMMA resists spinning and baking.

3) 10 nm gold or aluminium metal layer deposition.

4) Ebeam exposure, wet etch the 10 nm Au/Al metal layer.

   PMMA resist development.

5) Metal layers (Titanium and gold here) deposition.

6) Lift-off.

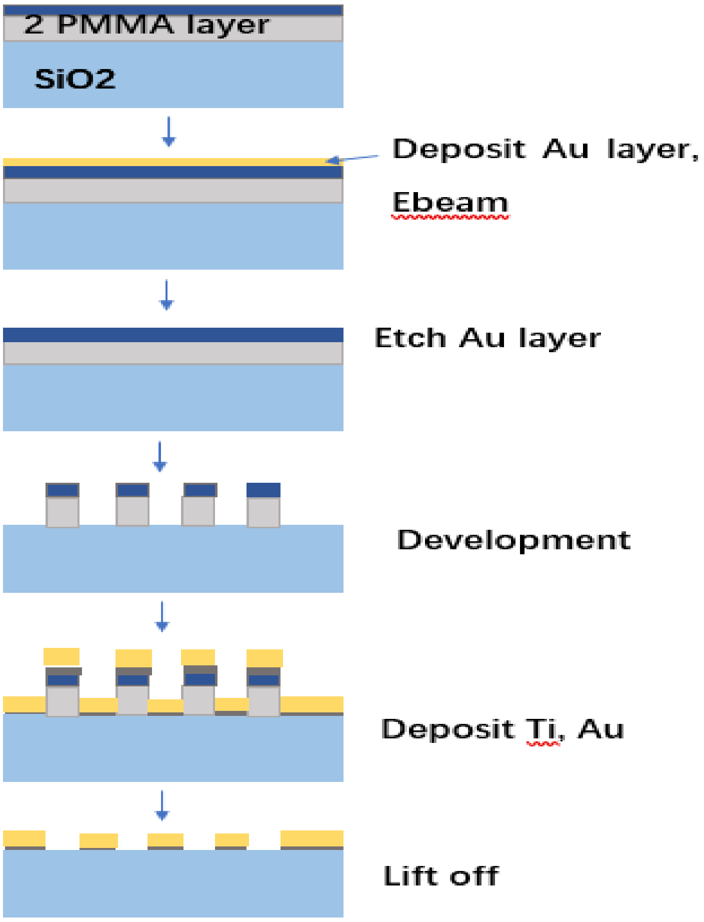

Fig.8.4 Fabrication processes flow chart.

The fabrication results of gold dot and gold ring structure with different dimensions are shown in Figure 8.5 to Figure 8.8, respectively. The fabricated large gold dot and gold ring structure has outer and inner diameter of the gold ring of 3 µm and 2 µm respectively with the diameter of gold dot of 400 nm. The fabricated small gold dot and gold ring structure has outer and inner diameter of the gold ring of 400 nm and 250 nm respectively with the diameter of gold dot of 100 nm. The metal thickness contains 10 nm Titanium (Ti) and 70 nm gold (Au).

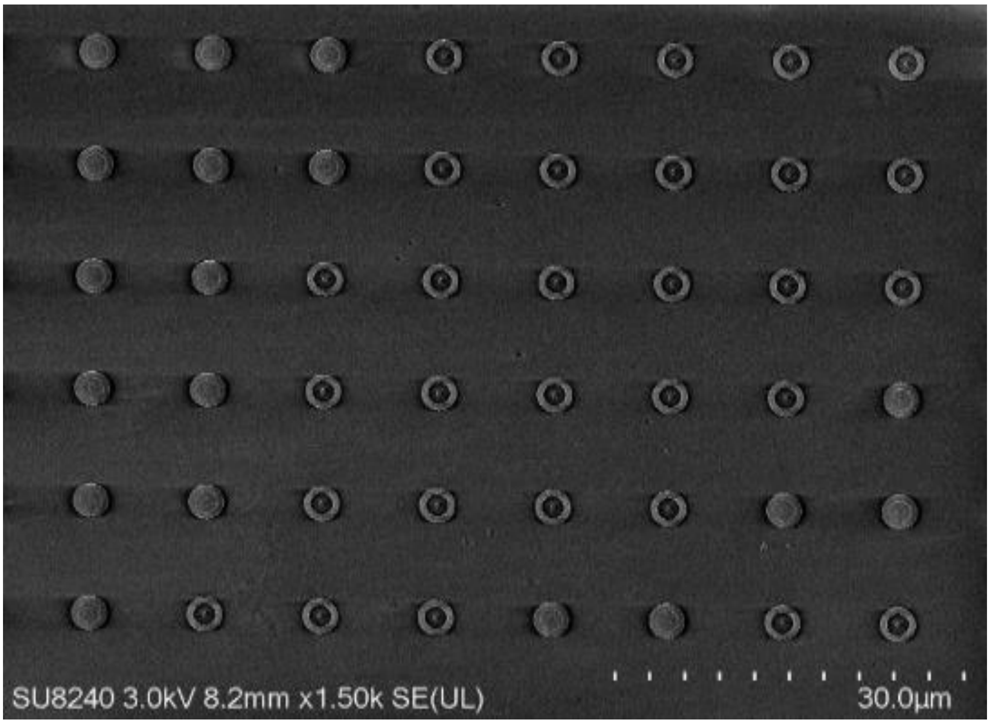

Fig.8.5 SEM image of a large-sized gold dot and gold ring array over a wide range.

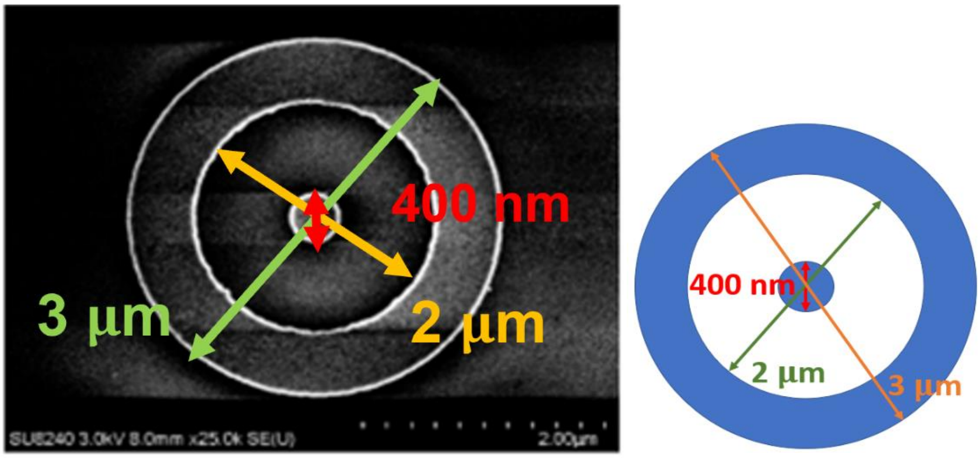

Fig.8.6 A scanning electron microscope (SEM) image of an individual large gold dot and gold ring structure (left) and corresponding schematic diagram (right).

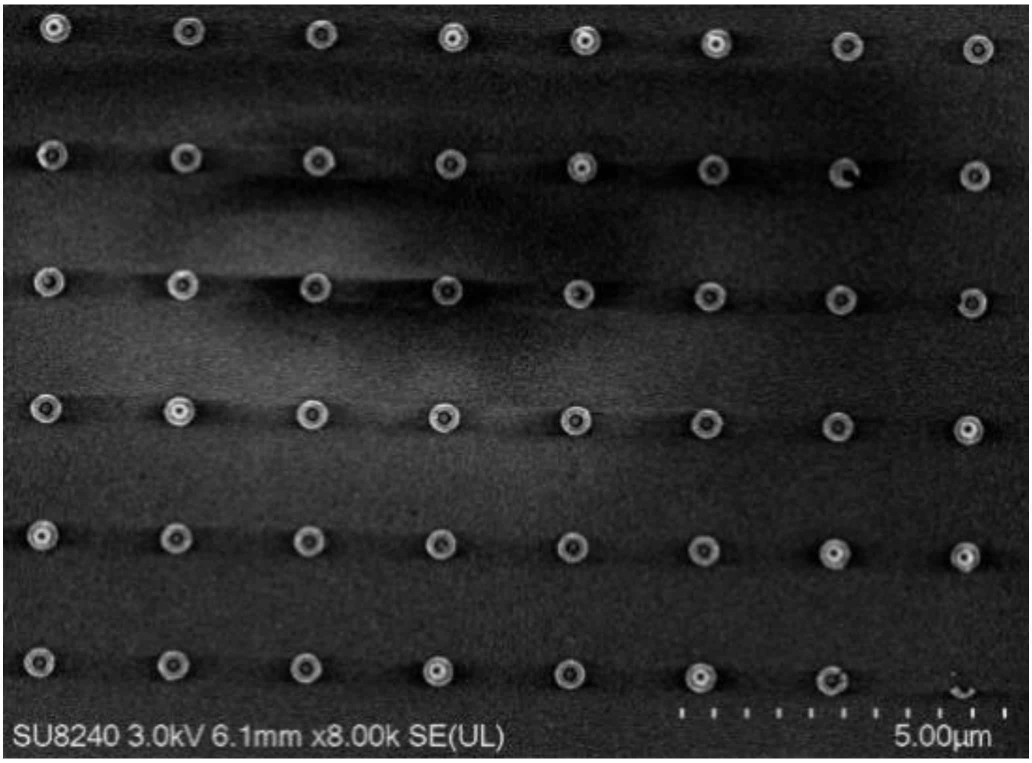

Fig.8.7 A SEM of small size gold dot and gold ring array.

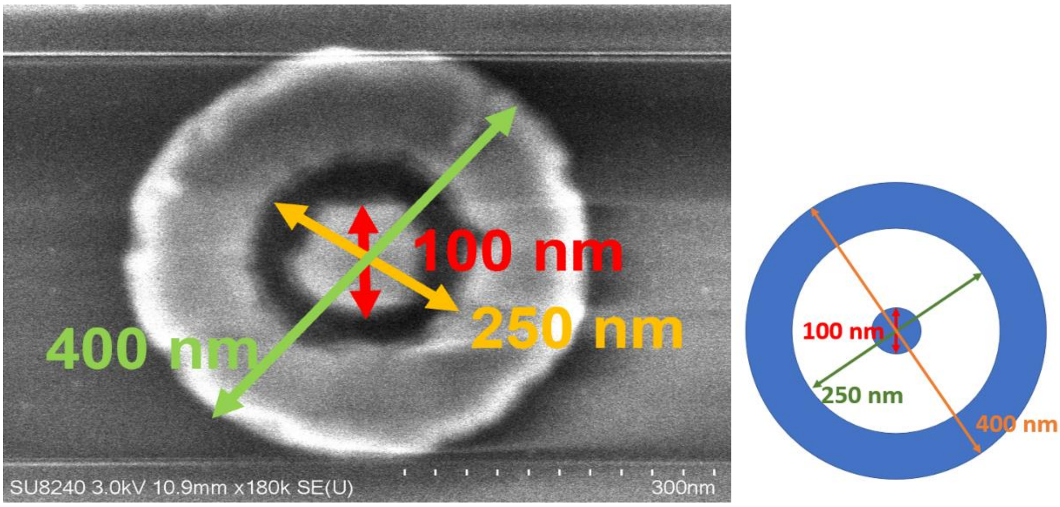

Fig.8.8 A SEM of single small size gold dot and gold ring structure(left) and corresponding schematic diagram (right).

The Atomic Force Microscopy (AFM) measurements of single gold dot and gold ring structures are presented in Figures 8.9 to 8.11. By examining the results from both Scanning Electron Microscopy (SEM) and AFM measurements (Figures 8.6, 8.8, and 8.9 to 8.11), we can deduce the fabrication parameters of the large size gold dot and ring structures. Specifically, the outer and inner diameters of the gold ring are 3 µm and 2 µm, respectively, while the gold dot has a diameter of 400 nm. The fabricated small gold dot and gold ring structure has outer and inner diameter of the gold ring of 400 nm and 250 nm respectively with the diameter of gold dot of 100 nm. The metal structure consists of a 10 nm layer of Titanium (Ti) followed by a 70 nm layer of gold (Au).

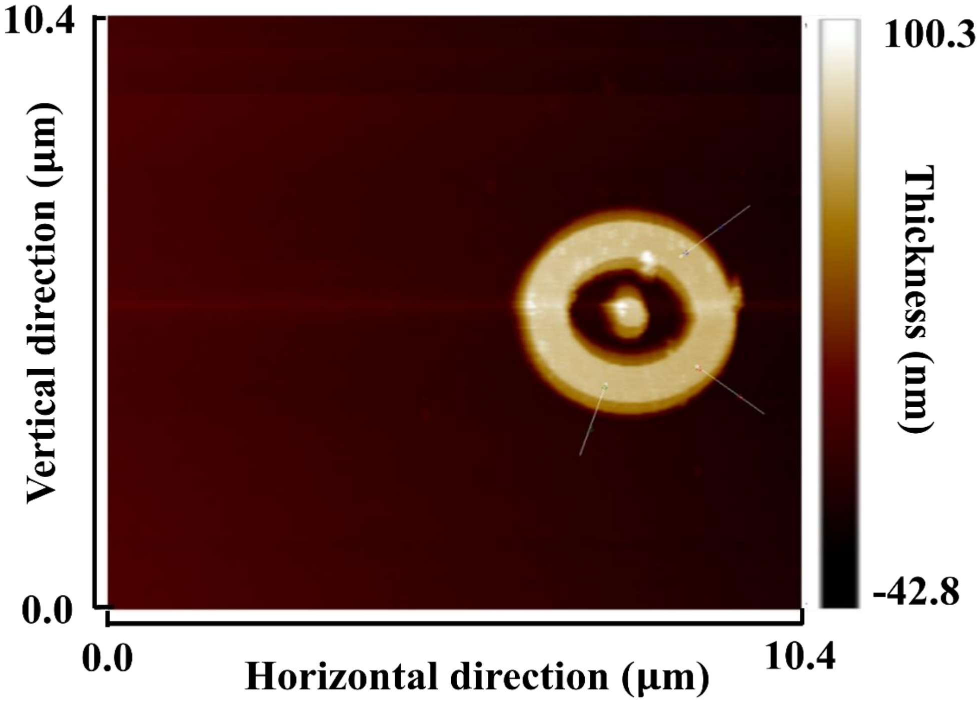

Fig.8.9 A top view AFM image of a large size single gold dot and gold ring structure.

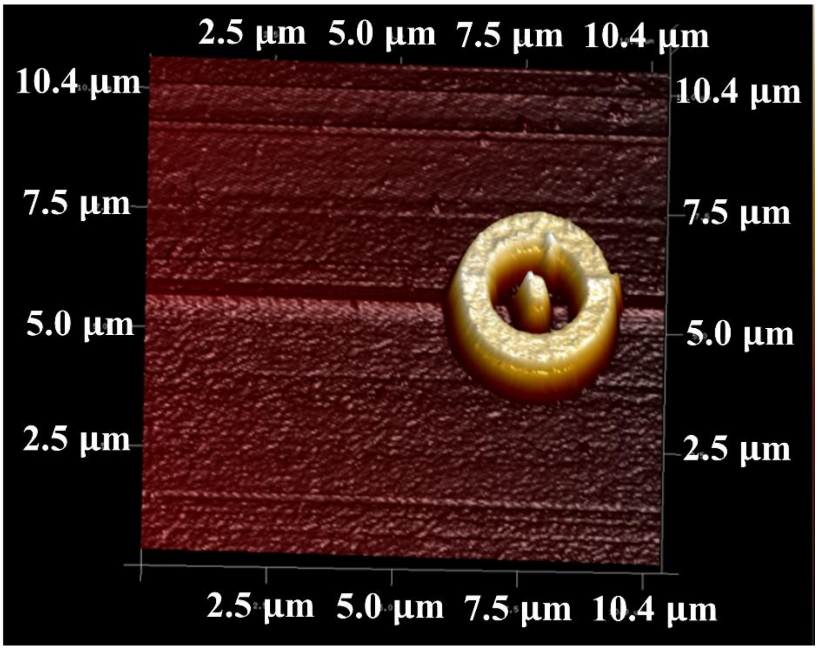

Fig.8.10 An 3D view AFM image of a large size single gold dot and gold ring structure.

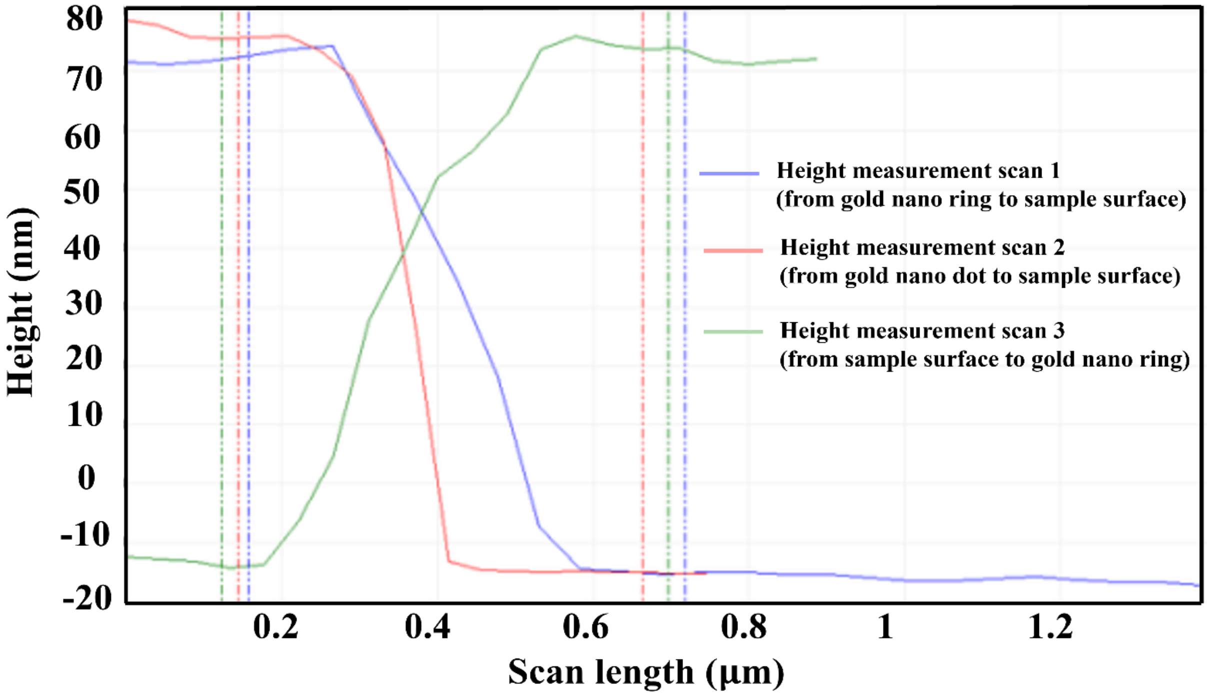

Fig.8.11 The AFM height sensor scan of the large size single gold dot and gold ring structure.

8.4 Measurement

The far-field scattering characteristics of nanostructures have been widely used in light field modulation, sensing and other fields. Although there are far-field detection methods for scattering characteristics of metasurfaces, there are still few far-field detection methods for the scattering characteristics of a single nano unit. Exploring the characteristics of a single nano structure is significant for the design of metasurfaces, and the regulation of near field (surface plasmon field) and far field (scattering field). The measured results are shown in Figures 8.12-8.14. In the measurement, kohler illumination focused linearly polarized light was used to illuminate the gold nano disk, so that the surface plasmon polariton （SPP） were excited and far-field scattering occurred. The scattered field was detected by far-field imaging, and it was found that the scattered field was vortex light field. This is due to the different optical paths of SPP excited by the edge of the nano disk when spreading on the surface.

Figure 8.12-8.14 depict the outcomes of far-field scattering experiments involving micro-nano structures obtained through the PIMI method. In Figure 8.12, we observe the scattering of light by a solitary gold nano disk. The PIMI results reveal that this disk simultaneously scatters two light fields, each possessing elliptical orbital angular momentum.

In Figure 8.13, we examine the scattering of light by a composite structure consisting of a ring and a cylinder. The PIMI findings demonstrate that both the inner and outer layers of the ring scatter light fields with elliptical orbital angular momentum concurrently, but with identical phases.

In Figure 8.14, the illustration depicts the scattering of light by a composite structure consisting of a ring and a cylinder, with PMMA filling the space between them. The PIMI results show that the inner and outer layers of the ring simultaneously scatter light fields with elliptical orbital angular momentum. However, the presence of PMMA introduces phase shifts, leading to the generation of light fields with elliptical orbital angular momentum between the inner and outer layers.

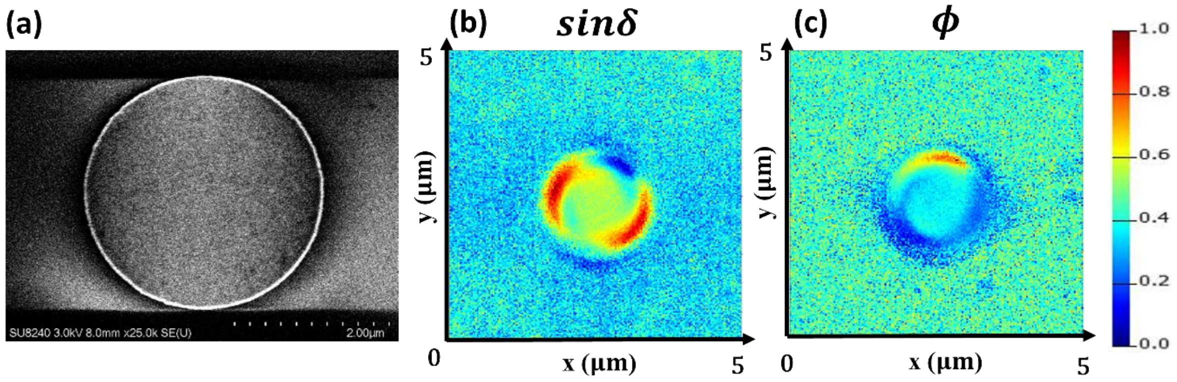

Fig.8.12 (a) SEM picture of gold disk structure, and measured (b) **sinδ** and (c) ϕ of the gold disk structure.

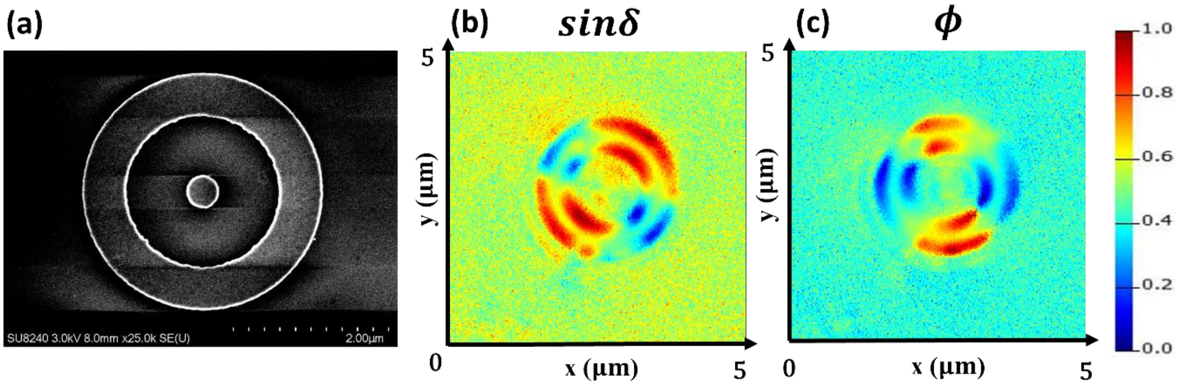

Fig.8.13 (a) SEM picture of gold nanodot and ring. Measured (b) sinδ and (c) ϕ of the gold nanodot and ring.

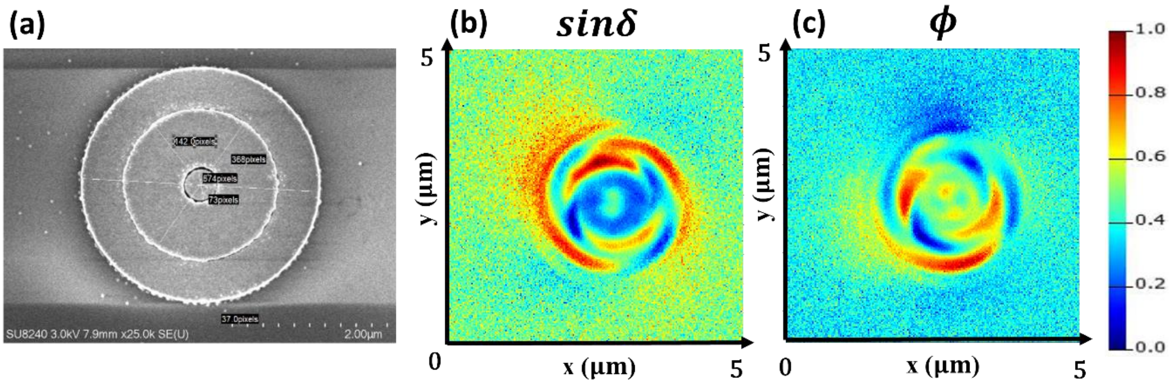

Fig.8.14 (a) SEM picture of gold nanodot and ring with PMMA left in the slot. Measured (b) sinδ and (c) ϕ of the gold nanodot and ring with PMMA left in the slot.

Ten groups of results are processed by the PIMI algorithm, and the results are shown in Figure 8.15. In this graph, the experimental results are compared with the simulation results, and it is found that the two groups of results are very consistent, which also verifies the correctness of our theory from the experimental point of view. The angle rotation between the simulation results and the experimental results is caused by the different starting angles used in the experiment, which will not affect the correctness of the results.

Sensing measurements, such as virus detection, utilizing the mentioned gold dot and gold ring arrays are currently being conducted by the research group at Nanjing University of Science and Technology (NJUST).

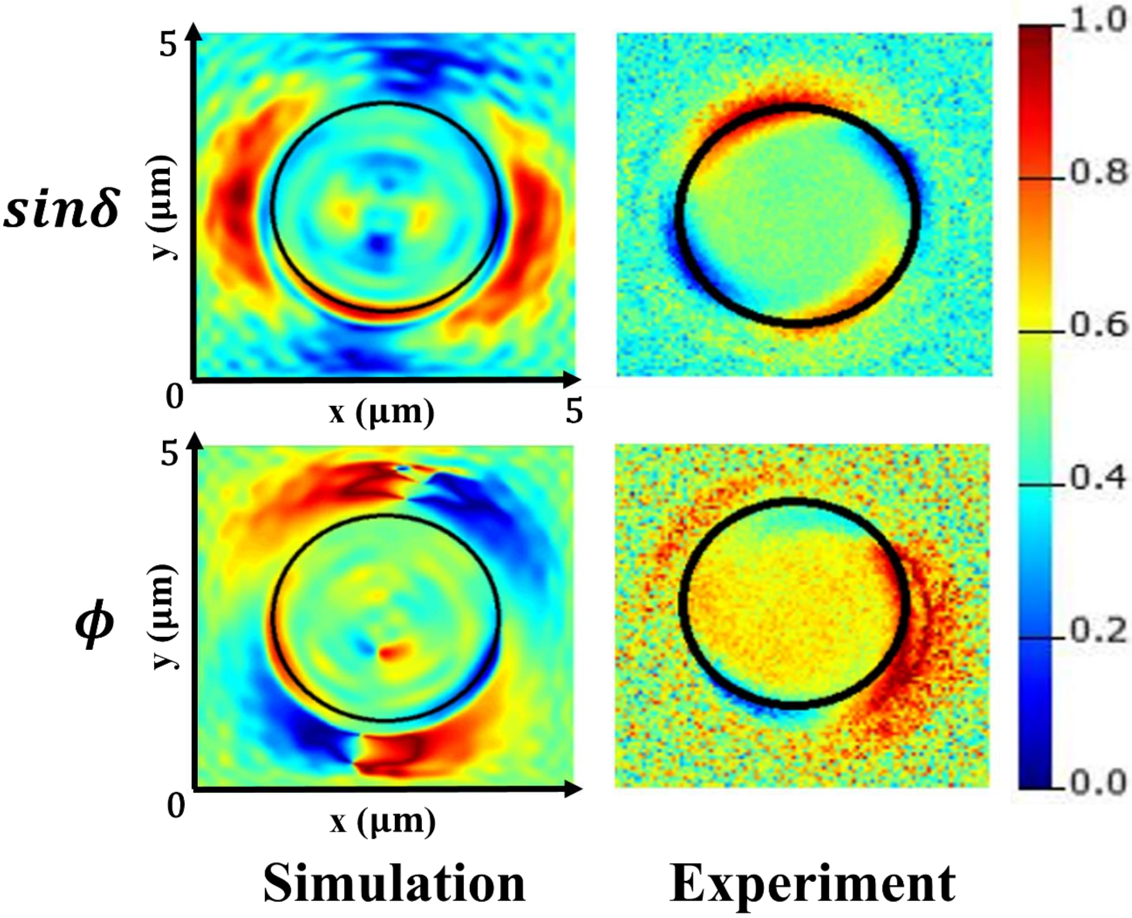

Fig.8.15 PIMI results, with simulation on the left and experimental data on the right, both at NA=0.9 under linear polarization incidence.

8.5 Conclusion

In summary, this chapter presents a collaborative effort with NJUST in China, focusing on the design, simulation, and fabrication of gold plasmonic nanostructures. The chapter employs the PIMI technique to detect far-field mode distribution at the resonant wavelength. Structural characterization and nano-device sensing are performed using parameters such as sinδ and ϕ.

The PIMI technique plays a pivotal role in examining the far-field mode distribution at the resonant wavelength. An optical system based on the PIMI method has been established, enabling the measurement of the polarization ellipsoid's orientation angle and the phase difference between two orthogonal directions of light transmitted, reflected, or scattered by the sample.

These plasmon resonators exhibit the capability to efficiently achieve high-quality factors and local field strengths, leading to enhanced surface-enhanced Raman scattering (SERS) and photoluminescence. Additionally, bioparticle detection methods are applied for sensing viruses or particles within plasmonic structures, significantly impacting scattering spectra and fields, and providing high-sensitivity detection capabilities.

.

Chapter 9 Conclusions and future work

In conclusion, this project and thesis reported the design, simulation, fabrication and measurement work aimed to achieve better performance integrated photonics biochemical sensors and especially focus on the optimized design of MRR structure based biochemical sensors.

Several biochemical photonics sensors are proposed to solve the two main limitations: sensitivity limitations and detection limitation. The transmission loss of fabricated optical waveguides (strip, slot waveguides) is measured. The sensor performances are experimentally verified based on different aspects of parameters.

The inner-wall grating double slot micro ring resonator (IG-DSMRR) with 6.72 μm radius based on the silicon-on-insulator (SOI) boosts the measured refractive index (RI) sensitivity in glucose solutions to 563 nm/RIU with the limit of detection (LOD) value being 3.7×10^{-6} RIU. The concentration sensitivity for sodium chloride solutions can reach 981 pm/%, with a minimum concentration detection limit of 0.02%. The detection range is enlarged significantly to 72.6 nm with measured Q-factor is 1.6×10^{4}. The straight strip, slot and double slot waveguide transmission losses are 0.9 dB/cm, 5.2 dB/cm and 20.2 dB/cm.

The novel sidewall grating slot microring resonator (SG-SMRR) with a compact size (5 μm centre radius) based on the silicon-on-insulator (SOI) platform is proposed and demonstrated experimentally. The measured refractive index (RI) sensitivity and the limit of detection (LOD) value are 620 nm/RIU and 1.4×10^{-4} RIU, respectively. The concentration sensitivity and minimum concentration detection limit are 1120 pm/% and 0.05%. Moreover, the significantly enlarged detection range based on grating structure is 85.8 nm, four times the free spectral range of conventional slot MRRs. The measured Q-factor is 5.2×10^{3}.

The designed subwavelength grating cascaded microring resonator (SWG-CMRR) structure could achieve ultra-high sensitivity as 810 nm/RIU with a limit of detection (LOD) value of 2.04×10^{-4}. The measured Q-factor is 7.7×10^{3}.

Also, the double slot microring resonator (DSMRR) structure are fabricated and verified in this project. The measured RI sensitivity is 600 nm/RIU with a limit of detection (LOD) value of 1.15×10^{-6}. The measured Q factor is 2.6×10^{4}.

Table 9.1 summarizes the above four MRR sensors performances. The design, simulation, and fabrication of surface plasmonic sensing structures, such as nano dots and nano rings, have been undertaken to enable the detection of hybrid photons and map the anapole-like electronic modes.

Table 9.1 A comparison of key features among the four SOI MRR sensors

	S_{RI} (nm/RIU)	Q	LOD (RIU)	FSR (nm)
IG-DSMRR	563	1.6×10^{4}	3.7×10^{-6}	72.6
SG-SMRR	620	5.2×10^{3}	1.4×10^{-4}	Free
SGC-MRR	810	7.7×10^{3}	2.04×10^{-4}	35.8
DSMRR	600	2.6×10^{4}	1.15×10^{-6}	24.9

It should be noted that the high sensitivity biochemical sensors compared with the current reported biochemical SOI sensors in many references to understand our novelty and improvement stage. The measured slot waveguide based microring resonator on SOI platform with similar radius is reported in [152] with sensitivity 298 nm/RIU. Thus our slot waveguide MRR sensors (IG-DSMRR and SG-SMRR) shows two times than this measured sensitivity in reference. For the multi-slot subwavelength grating structures, we can compare our results with the measured subwavelength grating straight waveguide and microring resonator structures reported in [150, 151], the sensitivities are 579.5 nm/RIU and 730 nm/RIU respectively. Therefore, we could conclude that our designed SWG-CMRR shows a sensitivity improvement than the current reported subwavelength grating biochemical sensor on SOI platform.

The future prospects for this research can be divided into two main avenues. First, there is the optimization of sensor performance, which involves refining sensor structure design and making modifications to the wafer material, such as SiN material, to enhance sensing and detection capabilities. Second, there is the integration of photonic sensors and circuits, encompassing the incorporation of cascaded or parallel MRR sensors for multiple sensing applications on the same chip. This is particularly relevant in the fields of medicine and environmental monitoring. Additionally, integrating these sensors with light sources (lasers) and detectors on various wafer structures, beyond just SOI, has the potential to significantly reduce the size of existing sensing platforms, resulting in ultra-compact sensing systems.

Here, we need to consider the possibility to apply these sensors in biomedical area for protein and virus measurement and detection. Some commonly used sensors for large molecules detection are mass spectrometers, X-ray Crystallography, biolayer interferometry. Especially for the MRR based on SOI platform tested for biomedical area, some examples could be found in [151, 152]. These shows our sensor could be used as biomedical sensors after rinsing with PBS buffer (pH = 7.39, n = 1.35) for baseline before functionalization. Then some protein detection can be performed with parameters 0.5 mg/mL, MW ~42 kDa, a globular protein with a diameter of 3 nm and a refractive index of 1.48. These reported protein detection shows our sensor has the potential in biomedical area in the future work.

References

1. R. Lequin, "Enzyme immunoassay (EIA)/enzyme-linked immunosorbent assay (ELISA)," Clinical chemistry **51**(12), 2415-2418 (2005).

2. E. Mylonakis, M. Paliou, M. Lally, T. P. Flanigan, and J. D. Rich, "Laboratory testing for infection with the human immunodeficiency virus: established and novel approaches," The American journal of medicine, **109**(7), 568-576 (2000).

3. U. B. Nielsen, and B. H. Geierstanger, "Multiplexed sandwich assays in microarray format," Journal of Immunological Methods, **290**(1-2), 107-120 (2004).

4. M. T. Arellano-Garcia, S. Hu, J. Wang, B. Henson, H. Zhou, D. Chia, and D. T. Wong, "Multiplexed immunobead-based assay for detection of oral cancer protein biomarkers in saliva," Oral Diseases, **14**(8), 705-712 (2008).

5. S. Schultz, D. R. Smith, J. J. Mock, and D. A. Schultz, "Single-target molecule detection with nonbleaching multicolor optical immunolabels," Proceedings of the National Academy of Sciences of the United States of America, **97**(3), 996-1001 (2000).

6. J. L. Arlett, E. B. Myers, and M. L. Roukes, "Comparative advantages of mechanical biosensors." Nature Nanotechnology, **6**(4), 203–215 (2011).

7. M. L. Phelan, and S. Nock, "Generation of bioreagents for protein chips." Proteomics, **3**(11), 2123-2134 (2003).

8. J. Q. Abraham, A. L. Washburn, J. Y. Byeon, and R. C. Bailey, "Label-free technologies for quantitative multiparameter biological analysis." Anal. Bioanal. Chem., **394**(1), 121-135 (2009).

9. M. Nirschl, F. Reuter, and V. Janos, "Review of Transducer Principles for Label-Free Biomolecular Interaction Analysis." Biosensors, **1**(3), 70–92 (2011).

10. J. Homola, "Surface plasmon resonance sensors for detection of chemical and biological species," Chemical Reviews, **108**(2), 462–493 (2008).

11. B. M. S. Richard and J. T. Anna editors, "Handbook of surface plasmon resonance," RSC Publishing (2008).

12. C. T. Campbell and G. Kim, "SPR microscopy and its applications to high-throughput analyses of biomolecular binding events and their kinetics," Biomaterials, **28**(15), 2380–2392 (2007).

13. C. Boozer, G. Kim, S. Cong, H. W. Guan, and T. Londergan, "Looking towards label-free biomolecular interaction analysis in a high-throughput format: a review of new surface plasmon resonance technologies," Current Opinion In Biotechnology, **17**(4), 400–405 (2006).

14. T. C. Brian and L. Laing, "Microplate-based, label-free detection of biomolecular interactions: applications in proteomics," Expert Review of Proteomics, **3**(3), 271–281 (2006).

15. D. Grieshaber, R. MacKenzie, J. Voeroes, and E. Reimhult, "Electrochemical biosensors - Sensor principles and architectures," Sensors, **8**(3), 1400–1458 (2008).

16. G. F. Zheng, F. Patolsky, Y. Cui, W. U. Wang, and C. M. Lieber, "Multiplexed electrical detection of cancer markers with nanowire sensor arrays," Nature Biotechnology, **23**(10), 1294–1301 (2005).

17. G.H. Wu, R. H. Datar, K. M. Hansen, T. Thundat, R. J. Cote, and A Majumdar," Bioassay of prostate-specific antigen (PSA) using microcantilevers," Nature Biotechnology, **19**(9), 856–860 (2001).

18. J. H. Lee, K. S. Hwang, J. Park, K. H. Yoon, D. S. Yoon, and T. S. Kim, " Immunoassay of prostate-specific antigen (PSA) using resonant frequency shift piezoelectric nanomechanical microcantilever," Biosensors & Bioelectronics, **20**(10), 2157–2162 (2005).

19. D. G. Rabus, "Integrated Ring Resonators," Springer series in optical sciences (2007).

20. J. Heebner, R. Grover, and T. Ibrahim, "Optical microresonators," Springer series in optical sciences (2008).

21. W. Bogaerts, P. D. Heyn, V. V. Thomas, K. D. Vos, S. K. Selvaraja, T. Claes, P. Dumon, P. Bienstman, D. V. Thourhout, and R. Baets, "Silicon microring resonators," Laser & Photonics Reviews, **6**(1), 47–73 (2012).

22. F. Xia, L. Sekaric, and Y. Vlasov, "Ultracompact optical buffers on a silicon chip," Nature Photonics, **1**(1), 65–71 (2007).

23. B. E. Little, J. S. Foresi, G. Steinmeyer, E. R. Thoen, S. T. Chu, H. A. Haus, E. P. Ippen, L.C. Kimerling, and W. Greene, "Ultra-compact Si-SiO2 microring resonator optical channel dropping filters," IEEE Photonics Technology Letters, **10**(4), 549–551 (1998).

24. Q. Xu, S. Manipatruni, B. Schmidt, J. Shakya, and M. Lipson, "12.5 Gbit/s carrier-

injection-based silicon micro-ring silicon modulators," Opt. Express, **15**(2), 430–436 (2007).

25. B. R. Koch, A. W. Fang, O. Cohen, and J. E. Bowers, "Mode-locked silicon evanescent lasers," Opt. Express, **15**(18), 11225–11233 (2007).
26. S. L. Mccall, A. F. J. Levi, R. E. Slusher, S. J. Pearton, and R. A. Logan, "Whispering-gallery mode microdisk lasers," Applied Physics Letters, **60**(3), 289–291 (1992).
27. C. Y. Chao, L. J. Guo, "Design and optimization of microring resonators in biochemical sensing applications," J. Lightwave Technol. **24**(3), 1395–1402 (2006).
28. M. S. Luchansky, A. L. Washburn, T. A. Martin, M. Iqbal, L. C. Gunn, and R. C. Bailey, "Characterization of the evanescent field profile and bound mass sensitivity of a label-free silicon photonic microring resonator biosensing platform," Biosensors and Bioelectronics, **26**(4), 1283 – 1291 (2010).
29. S. K. Selvaraja, P. Jaenen, W. Bogaerts, D. V. Thourhout, P. Dumon, and R. Baets, " Fabrication of Photonic Wire and Crystal Circuits in Silicon-on-Insulator Using 193-nm Optical Lithography, " J. Lightw. Technol., **27**(18), 4076–4083 (2009).
30. S. K. Selvaraja, "Wafer-Scale Fabrication Technology for Silicon Photonic Integrated Circuits, " PhD thesis, Universiteit Gent, 2011.
31. J. T. Robinson, K. Preston, O. Painter, and M. Lipson, "First-principle derivation of gain in high-index-contrast waveguides, " Optics Express, **16**(21), 16659–16669 (2008).
32. R. B. M. Schasfoort and A. J. Tudos, editors, "Handbook of surface plasmon resonance, " RSC Publishing, (2008).
33. A. Currie, "Detection: International update, and some emerging dilemmas involving calibration, the blank, and multiple detection decisions," Chemometrics and Intelligent Laboratory Systems, **37**(1), 151– 181 (1997).
34. M. S. Luchansky, and R. C. Bailey, "Silicon Photonic Microring Resonators for Quantitative Cytokine Detection and T-Cell Secretion Analysis," Analytical Chemistry, **82**(5), 1975–1981 (2010).
35. M. S. Luchansky, A. L. Washburn, M. S. McClellan, and R. C. Bailey, "Sensitive on-chip detection of a protein biomarker in human serum and plasma over an extended dynamic range using silicon photonic microring resonators and sub-micron beads," Lab on a Chip, **11**(12), 2042–2044 (2011).

36. J. J. Hu, X. C. Sun, A. Agarwal, and L. C. Kimerling, "Design guidelines for optical resonator biochemical sensors," Journal of the Optical Society of America B, **26**(5),1032–1041 (2009).

37. K. B. Gylfason, C. F. Carlborg, A. Kazmierczak, F. Dortu, H. Sohlström, L. Vivien, C. A. Barrios, W. Wijngaart, and G. Stemme, "On-chip temperature compensation in an integrated slot-waveguide ring resonator refractive index sensor array," Opt. Express, **18**(4), 3226–3237 (2010).

38. D. Xu, M. Vachon, A. Densmore, R. Ma, S. Janz, A. Delage, J. Lapointe, P. Cheben, J. H. Schmid, E. Post, S. Messaoudene, and J. M. Fedeli, "Real-time cancellation of temperature induced resonance shifts in SOI wire waveguide ring resonator label-free biosensor arrays," Opt. Express, **18**(22), 22867–22879 (2010).

39. A. L. Washburn, L. C. Gunn, and R. C. Bailey, "Label-Free Quantitation of a Cancer Biomarker in Complex Media Using Silicon Photonic Microring Resonators," Analytical Chemistry, **81**(22), 9499– 9506 (2009).

40. http://www.dow.com/cyclotene/.

41. K. S. Ulaganathen, "Attenuation Measurement On Cyclotene (Bcb Photo Resin) Polymer Based Slab Waveguide," Master’s thesis, Faculty of Electrical Engineering, Universiti Teknologi Malaysia (2005).

42. C. B. Kim, and C. B. Su, "Measurement of the refractive index of liquids at 1.3 and 1.5 micron using a fibre optic Fresnel ratio meter," Measurement Science and Technology, **15**(9), 1683 (2004).

43. D. X. Xu, A. Densmore, A. Delâge, P. Waldron, R. McKinnon, S. Janz, J. Lapointe, G. Lopinski, T. Mischki, E. Post, P. Cheben, and J. H. Schmid, "Folded cavity SOI microring sensors for highsensitivity and real time measurement of biomolecular binding," Optics Express, **16**(19),15137–15148 (2008).

44. T. M. Squires, R. J. Messinger, and S. R. Manalis, "Making it stick: convection, reaction and diffusion in surface-based biosensors," NATURE BIOTECHNOLOGY, **26**(4), 417–426 (2008).

45. A. J. Qavi, T. M. Mysz, and R. C. Bailey, "Isothermal Discrimination of Single-Nucleotide Polymorphisms via Real-Time Kinetic Desorption and Label-Free Detection of DNA Using Silicon Photonic Microring Resonator Arrays," Analytical Chemistry, **83**(17), 6827– 6833 (2011).

46. www.bioforcenano.com.

47. A. Renaudin, V. Chabot, E. Grondin, V. Aimez, and P. G. Charette, "Integrated active mixing and biosensing using surface acoustic waves (SAW) and surface plasmon resonance (SPR) on a common substrate," Lab On a Chip, **10**(1), 111–115 (2010).

48. X. Chen, D. Cui, and J. Chen, "Integrated Design, fabrication and characterization of nano-filters in silicon microfluidic channels based on MEMS technology," Electrophoresis, **30**(18), 3168–3173 (2009).

49. C. Xing, D. F. Cui, C. C. Liu, and H. Y. Cai, "Microfluidic biochip for blood cell lysis," Chinese Journal of Analytical Chemistry, **34**(11), 1656–1660 (2006).

50. J. J. Haddad, "Cytokines and related receptor-mediated signaling pathways," Biochemical and Biophysical Research Communications, **297**(4), 700–713 (2002).

51. N. L. Anderson and N. G. Anderson, "The Human Plasma Proteome," Molecular and Cellular Proteomics, **1**(11), 845–867 (2002).

52. A. J. Qavi and R. C. Bailey, "Multiplexed Detection and Label Free Quantitation of MicroRNAs Using Arrays of Silicon Photonic Microring Resonators," Angewandte Chemie, **49**(27), 4608–4611 (2010).

53. A. J. Qavi, J. T. Kindt, M. A. Gleeson, and R. C. Bailey, "Anti-DNA:RNA Antibodies and Silicon Photonic Microring Resonators: Increased Sensitivity for Multiplexed microRNA Detection," Analytical Chemistry, **83**(15), 5949–5956, (2011).

54. M. S. McClellan, L. L. Domier, and R. C. Bailey, "Label-free virus detection using silicon photonic microring resonators," Biosensors & Bioelectronics, **31**(1), 388–392, (2012).

55. J. Wang, and D. Dai, "Highly sensitive Si nanaowaire-based optical sensor using a Mach-Zehnder interferometer coupled microring," Opt. Lett. **35**(24), 4229-4231, (2010).

56. V.R. Kolli, T. Srinivasulu, G. Hegde, T. Badrinarayana, and S. Talabattula, "Design and analysis of serially coupled double microring resonator-based force sensor for 1 µN range measurement," Optik. **131**, 1063-1070 (2017).

57. W. Shi, X. Wang, W. Zhang, H. Yun, C. Lin, L. Chrostowski, and N. A. Jaeger, "Grating-coupled silicon microring resonators," Appl. Phys. Lett. **100**(12), 12118 (2012).

58. T. Ma, L. Sun, J. Yuan, X. Sang, B. Yan, K. Wang, and C. Yu, "Integrated label-free optical biochemical sensor with a large measurement range based on an angular grating-microring resonator," Appl. Opt. **55**(18), 4784-4790 (2016).

59. K. De Vos, I. Bartolozzi, E. Schacht, P. Bienstman, and R. Baets, "Silicon-on-insulator microring resonator for sensitive and label-free biosensing," Opt. Express **15**(12), 7610-7615 (2007).
60. T. Sahba, S. Shon, W. Shi, W. Wu, N. A. F. Jaeger, E. Kwok, D. M. Ratner, and L. Chrostowski, "Optimized sensitivity of silicon-on-insulator (SOI) strip waveguide resonator sensor," Biomed. Opt. Express **8**, 500-511 (2017).
61. T. Claes, J. G. Molera, K. De Vos, E. Schacht, R. Baets and P. Bienstman, "Label-free biosensing with a slot-waveguide-based ring resonator in silicon on insulator," IEEE Photonics Journal **1**(3), 197-204 (2009).
62. V. Mere, H. Muthuganesan, Y. Kar, C. V. Kruijsdijk and S. K. Selvaraja, "On-chip chemical sensing using slot-waveguide-based ring resonator," IEEE Sensors Journal **20**(11), 5970-5975 (2020).
63. R. C. Bailey, "Informative diagnostics for personalized medicine," Nature Chemical Biology, **6**(12), 857–859 (2010).
64. K. R. Rogers, "Recent advances in biosensor techniques for environmental monitoring," Analytica Chimica Acta, **568**(1-2), 222–231 (2006).
65. F. S. Ligler, "Perspective on Optical Biosensors and Integrated Sensor Systems," Analytical Chemistry, **81**(2), 519–526 (2009).
66. G. P. Agrawal, "Fiber-optic communication systems," John Wiley & Sons, (2012).
67. Y. Yu, Z. J. Yu, Z. Y. Zhang, H. K. Tsang, and X. K. Sun, "Wavelength-Division Multiplexing on an Etchless Lithium Niobate Integrated Platform," ACS Photonics, **9**(10), 3253-3259 (2022).
68. Selvaraja, S. Kumar, and P. Sethi, "Review on optical waveguides." Emerging Waveguide Technology, **95**(458), (2018).
69. Y. H. Ding, L. Liu, C. Peucheret, and H. Y. Ou, "Fabrication tolerant polarization splitter and rotator based on a tapered directional coupler," Opt. Express **20**, 20021-20027 (2012).
70. T. Barwicz, C. W. Holzwarth, P. T. Rakich, M. A. Popović, E. P. Ippen, H. I. T. Smith, "Optical loss in silicon microphotonic waveguides induced by metallic contamination," Applied Physics Letters, **92**(13), (2008).
71. K. Kinoshita, T. Horikawa, D. Shimura, H. Takahashi, T. Mogami, "Study of O3-TEOS SiO2 Cladding for Silicon Photonics Devices," In APS Annual Gaseous Electronics Meeting Abstracts, NR2-002, (2015).

72. D. K. Sparacin, "Process and design techniques for low loss integrated silicon photonics," Massachusetts Institute of Technology, (2006).

73. Y. A. Vlasov, S. J. McNab, "Losses in single-mode silicon-on-insulator strip waveguides and bends," Optics express, **12**(8), 1622-1631 (2004).

74. R. Orobtchouk, N. Schnell, T. Benyattou, J. M. Fedeli, "Compact building block for optical link on SOI technology," Proceedings of the 12th European Conference on Integrated Optics (ECIO'05), 221-224 (2005).

75. D. K. Sparacin, S. J. Spector, L. C. Kimerling, "Silicon waveguide sidewall smoothing by wet chemical oxidation," Journal of lightwave technology, **23**(8), 2455 (2005).

76. W. Bogaerts, R. Baets, P. Dumon, V. Wiaux, S. Beckx, D. Taillaert, V. Thourhout, " Nanophotonic waveguides in silicon-on-insulator fabricated with CMOS technology, " Journal of Lightwave Technology, **23**(1), 401 (2005).

77. T. Tsuchizawa, K. Yamada, H. Fukuda, T. Watanabe, J. I. Takahashi, M. Takahashi, H. Morita, "Microphotonics devices based on silicon microfabrication technology," IEEE Journal of selected topics in quantum electronics, **11**(1), 232-240 (2005).

78. F. Xia, L. Sekaric, and Y. Vlasov, "Ultracompact optical buffers on a silicon chip," Nature photonics, **1**(1), 65-71 (2007).

79. M. Gnan, S. Thoms, D. S. Macintyre, R. M. De La Rue, and M. Sorel, "Fabrication of low-loss photonic wires in silicon-on-insulator using hydrogen silsesquioxane electron-beam resist," Electronics Letters, **44**(2), 115-116 (2008).

80. G. Murdoch, A. Milenin, C. Delvaux, P. Ong, S. Pathak, D. Vermeulen, and P. Absil, " Advanced 300-mm waferscale patterning for silicon photonics devices with record low loss and phase errors," In 17th Opto-Electronics and Communications Conference (OECC-2012) IEEE, 15-16 (2012).

81. A. Novack, M. Streshinsky, R. Ding, Y. Liu, A. E. J. Lim, G. Q. Lo, T. B. Jones, and M. Hochberg, "Progress in silicon platforms for integrated optics," Nanophotonics, **3**(4-5), 205-214 (2014).

82. W. Bogaerts, S. K. Selvaraja, P. Dumon, J. Brouckaert, K. De Vos, D. V. Thourhout, and R. Baets, "Silicon-on-insulator spectral filters fabricated with CMOS technology," IEEE journal of selected topics in quantum electronics, **16**(1), 33-44 (2010).

83. N. Hirayama, H. Takahashi, Y. Noguchi, M. Yamagishi, and T. Horikawa, "Low-loss Si waveguides with variable-shaped-beam EB lithography for large-scaled photonic

circuits," In Extended Abstracts of the International Conference on Solid State Devices and Materials, 530-531 (2012).

84. S. K. Selvaraja, P. De Heyn, G. Winroth, P. Ong, G. Lepage, C. Cailler, and P. Absil, "Highly uniform and low-loss passive silicon photonics devices using a 300mm CMOS platform, " In Optical Fiber Communication Conference, Th2A-33 (2014).

85. S. K. Selvaraja, P. Jaenen, W. Bogaerts, D. V. Thourhout, P. Dumon, and R. Baets, " Fabrication of Photonic Wire and Crystal Circuits in Silicon-on-Insulator Using 193-nm Optical Lithography, " Journal of Lightwave Technology, **27**(18), 4076-4083 (2009).

86. E. A. Marcatili, "Dielectric rectangular waveguide and directional coupler for integrated optics," Bell System Technical Journal, **48**(7), 2071-2102 (1969).

87. E. C. M. Pennings, L. B. Soldano, "Optical multi-mode interference devices based on self-imaging: principles and applications," Journal of Lightwave Technology, **13**(4), 615-627 (1995).

88. P. D. Trinh, S. Yegnanarayanan, and B. Jalali, "Integrated optical directional couplers in silicon-on-insulator," Electronics Letters, **31**(24), 2097-2098 (1995).

89. T. T. Le and L.W. Cahill, "The design of soi-mmi couplers with arbitrary power splitting ratios using slotted waveguide structures," In LEOS Annual Meeting Conference Proceedings, IEEE, 246–247 (2009).

90. G. E. Bachmann, B. Melchior-H, "P.A.New 2 times;2 and 1 times;3 multimode interference couplers with free selection of power splitting ratios," Journal of Lightwave Technology, **14**(10), 2286 –2293 (1996).

91. J. Leuthold and C. H. Joyner, "Multimode interference couplers with tunable power splitting ratios," J. Lightwave Technol., **19**(5), 700 (2001).

92. L. B. Soldano and E. C. M. Pennings, "Optical multimode interference devices based on self-imaging - principles and applications," Journal of Lightwave Technology, **13**(4), 615–627 (1995).

93. W. Bogaerts, S. K. Selvaraja, P. Dumon, J. Brouckaert, K. De Vos, D. Van Thourhout, and R. Baets, "Silicon-on-Insulator Spectral Filters Fabricated With CMOS Technology," IEEE Journal of Selected Topics in Quantum Electronics, **16**(1), 33–44 (2010).

94. A. Samarelli, "Micro ring resonators in silicon-on-insulator," Doctoral dissertation, University of Glasgow, (2011).

95. D. V. Katrien, "Label-free Silicon Photonics Biosensor Platform with Microring Resonators," PhD thesis, Universiteit Gent, (2010).

96. C. Sada, and D. G. Rabus, "Integrated Ring Resonators A Compendium," 1-405 (2020).

97. G. Reed, G. Mashanovich, F. Gardes, D. Thomson, (2010). Silicon optical modulators [Review]. Nature Photonics. **4**(179), 518-526, (2010).

98. X. Mu, S. Wu, L. Cheng, and H. Y. Fu, "Edge Couplers in Silicon Photonic Integrated Circuits: A Review," Appl. Sci. **10**(4), 1538, (2020).

99. S. Nambiar, P. Sethi, and S. Selvaraja, "Grating-Assisted Fiber to Chip Coupling for SOI Photonic Circuits," Appl. Sci. **8**(7), 1142 (2018).

100. R. Marchetti, C. Lacava, L. Carroll, K. Gradkowski, P. Minzioni, "Coupling strategies for silicon photonics integrated chips, " Photonics Res. **7**(2), 201–239 (2019).

101. Y. Fu, T. Ye, W. Tang, T. Chu, "Efficient adiabatic silicon-on-insulator waveguide taper, " Photonics Res. **2**(3), A41–A44 (2014).

102. F. V. Laere, T. Claes, J. Schrauwen, S. Scheerlinck, W. Bogaerts, D. Taillaert, L. O’Faolain, D. Van Thourhout, R. Baets, "Compact focusing grating couplers for silicon-on-insulator integrated circuits, " IEEE Photonics Technol. Lett. **19**(23), 1919–1921 (2007).

102. Achieve More with Light. Available online: http://www.lumerical.com.

103. J. R. Mejía-Salazar, Oliveira and Jr, O. N. , "Plasmonic biosensing: Focus review, " Chemical reviews, **118**(20), 10617-10625 (2018).

104. S. Unser, I. Bruzas, and J. He, "Localized surface plasmon resonance biosensing: current challenges and approaches, " Sensors, **15**(7), 15684-15716 (2015).

105. D. Conteduca, I. Barth, G. Pitruzzello, "Dielectric nanohole array metasurface for high-resolution near-field sensing and imaging, " Nature communications, **12**(1), 1-9 (2021).

106. J. F. Li, C. Y. Li, and R. F. Aroca, "Plasmon-enhanced fluorescence spectroscopy, " Chemical Society Reviews, **46**(13), 3962-3979 (2017).

107. X. Jin, L. Xue, S. Ye, W. Cheng, J. Hou, L. Hou, J. H. Marsh, M. Sun, X. Liu, J. Xiong, B. Ni, "Asymmetric parameter enhancement in the split-ring cavity array for

virus-like particle sensing, " Biomed Opt Express, **14**(3), 1216-1227 (2023).

108. X. Liu, B. Qiu, Q. Chen, Z. Ni, Y. Jiang, M. Long, and L. Gui, "Characterization of graphene layers using super resolution polarization parameter indirect microscopic imaging, " Optics Express **22**(17), 20446-20456 (2014).

109. T. Claes, "Advanced Silicon Photonic Ring Resonator Label-Free Biosensors, " PhD thesis, Universiteit Gent, (2011).

110. A. Densmore, D. X. Xu, P. Waldron, S. Janz, P. Cheben, J. Lapointe, A. Delage, B. Lamontagne, J. H. Schmid, and E. Post, "A silicon-on- insulator photonic wire based evanescent field sensor, " IEEE Photonics Technology Letters, **18**(21-24), 2520–2522 (2006).

111. K. Tiefenthaler and W. Lukosz, "Sensitivity of grating couplers as integrated optical chemical sensors, " Journal of the Optical Society of America B Optical Physics, **6**(2), 209–220 (1989).

112. B. Lillis, M. Manning, H. Berney, E. Hurley, A. Mathewson, and M. M. Sheehan, " Dual polarisation interferometry characterisation of DNA immobilisation and hybridisation detection on a silanised support, " Biosensors & Bioelectronics, **21**(8), 1459–1467 (2006).

113. F. Hook, J. Voros, M. Rodahl, R. Kurrat, P. Boni, J. J. Ramsden, M. Textor, N. D. Spencer, P. Tengvall, J. Gold, and B. Kasemo, "A comparative study of protein adsorption on titanium oxide surfaces using in situ ellipsometry, optical waveguide lightmode spectroscopy, and quartz crystal microbalance/dissipation, " Colloids and Surfaces B-Biointerfaces, **24**(2), 155–170 (2002).

114. J. Voros, " The density and refractive index of adsorbing protein layers, " Biophysical Journal, **87**(1), 553–561 (2004).

115. P. I. Nikitin, B. G. Gorshkov, E. P. Nikitin, and T. I. K. Picoscope, " a new label-free biosensor, " Sensors and Actuators B-Chemical, 111, 500–504 (2005).

116. J. T. Robinson, K. Preston, O. Painter, and M. Lipson, " First-principle derivation of gain in high-index-contrast waveguides, " Optics Express, **16**(21), 16659–16669 (2008).

117. E. Luan, H. Yun, L. Laplatine, Y. Dattner, D. M. Ratner, K. C. Cheung, and L. Chrostowski, "Enhanced sensitivity of subwavelength multibox waveguide microring resonator label-free biosensors," IEEE Journal of Selected Topics in Quantum Electronics **25**(3), 1-11 (2018).

118. A. Currie, " Detection: International update, and some emerging dilemmas involving calibration, the blank, and multiple detection decisions, " Chemometrics and Intelligent Laboratory Systems, 37(1), 151– 181 (1997).

119. I. M. White, X. Fan, " On the performance quantification of resonant refractive index sensors," Optics Express, 16(2), 1020-1028 (2008).

120. S. Hui, and H. Xu, "Fresnel-reflection-based fiber sensor for on-line measurement of solute concentration in solutions." Sens. Actuat. B: Chem. **126**(2), 579-582 (2007).

121. J. E. Saunders, C. Sanders, H. Chen, and H. P. Loock, "Refractive indices of common solvents and solutions at 1550 nm," Appl. Opt. **55**, 947-953 (2016).

122. A. L. Washburn, M. S. Luchansky, A. L. Bowman, and R. C. Bailey, " Quantitative, Label-Free Detection of Five Protein Biomarkers Using Multiplexed Arrays of Silicon Photonic Microring Resonators, " Analytical Chemistry, **82**(1), 69–72 (2010).

123. A. J. Qavi, T. M. Mysz, and R. C. Bailey, " Isothermal Discrimination of Single-Nucleotide Polymorphisms via Real-Time Kinetic Desorption and Label-Free Detection of DNA Using Silicon Photonic Microring Resonator Arrays, " Analytical Chemistry, **83**(17), 6827– 6833 (2011).

124. A. J. Qavi and R. C. Bailey, " Multiplexed Detection and Label-Free Quantitation of MicroRNAs Using Arrays of Silicon Photonic Microring Resonators, " Angewandte Chemie, **49**(27), 4608–4611 (2010).

125. K. D. Vos, J. Girones, S. Popelka, E. Schacht, R. Baets, and P. Bienstman, " SOI optical microring resonator with poly(ethylene glycol) polymer brush for label-free biosensor applications, " Biosens Bioelectron, **24**(8), 2528–33 (2009).

126. www.bioforcenano.com.

127. J. C. McDonald, D. C. Duffy, J. R. Anderson, D. T. Chiu, H. K. Wu, O. J. A. Schueller, and G. M. Whitesides, "Fabrication of microfluidic systems in poly (dimethylsiloxane), " Electrophoresis, **21**(1), 27–40 (2000).

128. S. Satyanarayana, R. N. Karnik, and A. Majumdar, "Stamp-and-stick room-temperature bonding technique for microdevices, " Journal of Microelectromechanical Systems, **14**(2), 392–399 (2005).

129. Y. M. Kang, A. Arbabi, and L. L. Goddard, "A microring resonator with an integrated Bragg grating: A compact replacement for a sampled grating distributed Bragg

reflector," Opt. Quant. Electron. **41**, 689–697 (2009).

130. M. Gnan, S. Thoms, D. S. Macintyre, De La Rue, R. M., and M. Sorel, "Fabrication of low-loss photonic wires in silicon-on-insulator using hydrogen silsesquioxane electron-beam resist," Electronics Letters. **44**(2), 115-116 (2008).
131. K. F. Palmer and D. Williams, "Optical properties of water in the near infrared," JOSA. **64**(8), 1107-1110 (1974).
132. C. Ciminelli, F. Dell'Olio, D. Campanella, C.M., and M. N. Armenise, "High performance SOI microring resonator for biochemical sensing," Optics & laser technology. **59**, 60-67 (2014).
133. Passaro, M. N. Vittorio, and L. N. Mario, "Optimizing SOI slot waveguide fabrication tolerances and strip-slot coupling for very efficient optical sensing," Sensors **12**(3), 2436-2455 (2012).
134. M. Bruel, B. Aspar, and A.J. Auberton-Herv´e, " Smart-cut: A new silicon on insulator material technology based on hydrogen implantation and wafer bonding, " Japanese Journal of Applied Physics **36**(1), 1636–1641 (1997).
135. R. Thurber, R. L. Mattis, Y. M. Liu, and J. J. Filliben, " Resistivity dopant density relationship for phosphorus-doped silicon, " Journal of The Electrochemical Society **127**(8), 1807–1812 (1980).
136. Oxford instruments, surface technology systems, URL http://www.oxinst.com/products/etching-deposition-growth/processes-techniques/plasma-deposition/pecvd/Pages/pecvd.aspx.
137. C. Ciminelli, F. Dell'Olio, D. Campanella, C.M., and M. N. Armenise, "High performance SOI microring resonator for biochemical sensing," Optics & laser technology **59**, 60-67 (2014).
138. T. Sahba, S. Shon, W. Shi, W. Wu, N. A. F. Jaeger, E. Kwok, D. M. Ratner, and L. Chrostowski, "Optimized sensitivity of silicon-on-insulator (SOI) strip waveguide resonator sensor," Biomed. Opt. Express 8, 500-511 (2017).
139. T. Claes, J. G. Molera, K. De Vos, E. Schacht, R. Baets and P. Bienstman, "Label-free biosensing with a slot-waveguide-based ring resonator in silicon on insulator," IEEE Photonics Journal 1(3), 197-204 (2009).
140. V. Mere, H. Muthuganesan, Y. Kar, C. V. Kruijsdijk and S. K. Selvaraja, "On-chip chemical sensing using slot-waveguide-based ring resonator," IEEE Sensors Journal

20(11), 5970-5975 (2020).

141. C. Zhao, P. Chen, and C. Zhang, "Numerical analysis of Bragg grating-based slot-micro-ring coupling resonator system for electromagnetically-induced transparency-like effect," Modern Physics Letters B 34(28), 2050307 (2020).

142. W. Cheng, X. Sun, S. Ye, B. Yuan, J. Xiong, X. Liu, Y. Sun, J. H. Marsh, and L. Hou, "Double slot micro ring resonators with inner wall angular gratings as ultra-sensitive biochemical sensors," Opt. Express 31(12), 20034-20048 (2023).

143. T. Claes, J. G. Molera, K. De Vos, E. Schacht, R. Baets, and P. Bienstman, "Label-free biosensing with a slot-waveguide-based ring resonator in silicon on insulator," IEEE Photonics Journal **1**(3), 197-204 (2009).

144. V. Mere, H. Muthuganesan, Y. Kar, C. Van Kruijsdijk, and S. K. Selvaraja, "On-chip chemical sensing using slot-waveguide-based ring resonator," IEEE Sensors Journal **20**(11), 5970-5975 (2020).

145. C. Zhao, P. Chen, and C. Zhang, "Numerical analysis of Bragg grating-based slot-micro-ring coupling resonator system for electromagnetically-induced transparency-like effect," Modern Physics Letters B 34(28), 2050307 (2020).

146. B. Shi, X. Chen, Y. Cai, S. Zhang, T. Wang, and Y. Wang, "Compact Slot Microring Resonator for Sensitive and Label-Free Optical Sensing," Sensors 22(17), 6467 (2022).

147. C. Liu, C. Sang, X. Wu, J. Cai, and J. Wang, "Grating double-slot micro-ring resonator for sensing," Optics Communications 499, 127280 (2021).

148. T. Ma, L. Sun, J. Yuan, X. Sang, B. Yan, K. Wang, and C. Yu, "Integrated label-free optical biochemical sensor with a large measurement range based on an angular grating-microring resonator," Appl. Opt. 55, 4784-4790 (2016).

149. X. Wang, S. Grist, J. Flueckiger, N. A. F. Jaeger, and L. Chrostowski, "Silicon photonic slot waveguide Bragg gratings and resonators," Opt. Express 21, 19029-19039 (2013).

150. S. Heinsalu, Y. Isogai, Y. Matsushima, H. Ishikawa, and K. Utaka, "Record-high sensitivity compact multi-slot sub-wavelength Bragg grating refractive index sensor on SOI platform," Opt. Express 28, 28126-28139 (2020)

151. E. Luan, H. Yun, L. Laplatine, Y. Dattner, D. M. Ratner, K. C. Cheung, L.

Chrostowski, "Enhanced sensitivity of subwavelength multibox waveguide microring resonator label-free biosensors," IEEE Journal of Selected Topics in Quantum Electronics, 25(3), 1-11 (2018).

152. T. Claes, J. Girones Molera, K. De Vos, E. Schacht, R. Baets and P. Bienstman, "Label-Free Biosensing With a Slot-Waveguide-Based Ring Resonator in Silicon on Insulator," IEEE Photonics Journal, 1(3), 197-204, (2009).